

University of Naples “Federico II”



***Development of Kytoon Station
for Meteorological and Air Pollution
Measurements in a Mediterranean
Urban Climate***

by
Mario Panelli

Thesis

PhD's School in Aerospace, Naval and Quality Management
Engineering.

2010

*To Giovanna
and those who believed in me.*

Acknowledgements

A lot of people I would like to thank at the end of this experience but I'm afraid that I'd need of write other thesis to well serve each one. In this contest it is strictly due at least some formal acknowledgements, leaving the most in the brief dedication above.

God bless: Prof. G. Cardone, Prof. A. Moccia, Prof. G. M. Carlomagno and Prof. T. Astarita; Giuseppe Sicardi; PhD's students: Engineers A. Ianiro, M. Imbriale, S. Discetti; the graduated students: R. Spinelli, T. Piscitelli, D. Amato, R.A. De Stefano, G. Pagliuca, L. Staibano and M. Girfoglio; Eng. E. De Lucia and all the staff of SVG (Caserta); Prof. G. Bronzone (ENAC, Naples).



Naples, February 9th 2009, 8:10 AM

¹"Signori, in un secolo in cui l'uomo intende così vittoriosamente a strappare dal seno della natura i suoi più riposti ed intimi segreti, era della più grande ed urgente importanza l'erezione di un Osservatorio deputato particolarmente allo studio attuale e pratico della meteorologia e della fisica terrestre..."

²...Signori, noi abbiamo rapiti i fulmini al cielo; ma quel che è e quel che segue a poca profondità sotto questa terra che tutti calpestiamo e dove tutti abbiamo vita e morte, è ancora un gran mistero per noi. Dio mi guardi di presumere tanto di me stesso, ch'io ardisca promettermi di sollevare questo grave velo, dove mani sterminate più vigorose sentirono pur troppo la loro impotenza!"

(M. Melloni, 28 Settembre 1845: *Discorso per l'inaugurazione dell'Osservatorio Meteorologico Vesuviano*).

Introduction

Our survival instinct led always us to want to foresee the natural catastrophic events. The only way to do this had been, and is still nowadays, by observing nature in order to "...finally extort from nature's stomach her most hidden and closest secrets..."¹. On 28th of September 1845 the regal meteorological Vesuvius observatory was inaugurated and it started to work in 1852. The new director L. Palmieri, completed the set of observatory instruments with a weather tower, saying that "The observatory's mission was to explore all the phenomena of the Vesuvius".

During last years in all world researches focused their attention on other catastrophic phenomena, not less serious than that of the Vesuvius observatory.

The concern for the state of health of our planet is not new and has been constantly increasing during the last three decades. The will to improve the quality of life through strong investments in the industrial and technological sector inevitably has to deal with the negative aspects ensuing from this sector's development.

Environmental air pollution is one of these negative aspects, if not the main one. In particular, controlling, monitoring, and predicting the emission and the dispersion of pollutants are necessary to elaborate territorial strategies which can safeguard human health in the best possible way. This activity is especially critical in urban areas for various reasons: more than half of the world's population lives in urban areas (according to UN survey); areas account for the majority of the air pollutants' emission, mostly from motor vehicle exhaust; the particular geographical situation of urban areas generates distinctive meteorological phenomena which interact with other local- and global-scale phenomena, complicating the prediction of the pollutants' dispersion.

Particularly, there are few data about this topic in the typical urban climate of Mediterranean cities, characterized by the interaction between Urban Heat Island (UHI), sea/land breezes and slope/valley flows.

Consequently, this PhD's thesis describes the development of a meteoric-climatic kytoon station for measurements of vertical profile of pressure, wind velocity (module and direction) turbulent spectrum, temperature, humidity and concentration of pollutants, very useful to study such phenomena.

A brief introduction to Boundary Layer (BL) meteorology is given in chapter I, in order to introduce an inexperienced reader to the topic; on the same aim, chapter II deals about the air pollution, describing the most dangerous pollutants, their production mechanisms and effects.

The bibliographical review (Chapter III) attests the originality of the thesis' work: using the developed kytoon station (Chapter IV), in addition to the classic meteorological vertical profiles (e.g. wind, virtual potential temperature, specific humidity), it is possible to calculate four air pollution concentration profiles (no publication about) and, thanks to the highest sampling frequency of wind speed (32Hz), accurately turbulent energy spectra and all the turbulent statistics.

To verify the launch site procedures (Chapter V) and the data reduction process (Chapter VI), a field tests campaign was necessary.

The results of the measurements made up during this flight tests (Caserta, Italy 6th- 17th September 2010) are discussed in Chapter VII.

Index

Acknowledgements	v
Introduction	viii
Index	10
List of figures	13
List of tables	18
I Boundary Layer Meteorology	22
I.1. Boundary Layer Definition	22
I.2. Wind and flow	22
I.3. Virtual Potential Temperature	22
I.4. Turbulent Transport	23
I.5. Kinematic Flux	24
I.5.1. Vertical Eddy Heat Flux	25
I.5.2. Turbulent Kinetic Energy and Energy spectra of atmospheric Turbulence	25
I.6. Boundary Layer Structure and Evolution	26
I.7. Urban Heat Island	28
I.8. Land and Sea Breeze	30
I.9. Valley, Katabatic and anabatic winds	32
II Air pollution	36
II.1. Air pollutants	36
II.1.1. Carbon monoxide	37
II.1.2. Nitrogen oxides	37
II.1.3. Ozone	38
II.1.4. Benzene and volatile organic compounds	39
II.2. Air quality	39
II.3. Dispersion of pollutants	40
III Bibliographic Review	44
III.1. Micrometeorology research (UHI, sea breeze, valley flows)	44
III.2. Overview of atmospheric turbulence studies over cities	44
III.2. Experiments using kytoon station	46
III.2.1. Wallops “Aeropalynologic Survey Project”	46
III.2.2. Boulder Observatory Experiments	46

III.2.3. Observation of land sea breeze in Tokyo, Japan	46
III.2.4. ASCOT Field Study	48
III.2.5. Polar Experiments	48
III.2.6. Lower Fraser Valley Experiment	48
IV. Kytoon Station Description	52
IV.1. Selection of Sensor Station	52
IV.2. Sensor Requirements.....	54
IV.3. Sensors and Subsystems.....	55
IV.3.1. <i>Gill Windmaster</i> – 3D Sonic Anemometer.....	56
IV.3.2. <i>Vaisala HMP50</i> – ThermoHygrometer	57
IV.3.3. <i>UniTech-Sens3000</i> – Air pollution sensor.....	58
IV.3.4. <i>Sbg Systems IG 500N</i> – Navigation System/Barometer	59
IV.3.5. <i>Vortex86</i> – On board computer	62
IV.3.6. <i>Datex MUX 3017 V</i> – Multiplexer	62
IV.3.7. <i>ACCU Li Ion battery</i>	63
IV.3.8. <i>BeeLine APRS</i> – Automatic Reporting Position System.....	63
IV.3.9. Mass budget Table	64
IV.4. Kytoon station	65
IV.4.1. <i>Floatograph SkyDoc#18</i> - Kytoon	65
IV.4.2. CATFISH gondola	74
IV.4.3. Trailer.....	83
IV.5. Flight requirements	91
V. Launch site and procedures	94
V.1. Selection of launch site	94
V.2. Launch operations	98
V.2.1. Weather forecast.....	98
V.2.2. Inflation of kytoon.....	98
V.2.3. Preparation for mounting of payload.....	100
V.2.4. Preparation of the acquisition.....	101
V.2.5. Garaging or deflating balloon	101
V.3. Description of the Caserta Experimental Field tests	102
V.4. Safety test	103
VI. Data reduction	106
VI.1. Raw parameters	106
VI.2. Data synchronization.....	107

VI.3. Air pollution sensors calibration	109
VI.4. Magnetometer calibration	110
VI.5. Wind calculation	113
VI.6. Profile mode calculations	116
VI.6.1. Richardson Number.....	116
VI.7. Tower mode calculations	117
VI.7.1. Turbulent energy spectra.....	118
VI.7.2. Vertical eddy heat flux	121
VI.7.3. Linear correlation coefficient.....	122
VII.1. Caserta Wind profiles (7/9/2010).....	124
VII.2. Temperature profiles (7/9/2010)	127
VII.3. Air pollution concentrations profiles (7/9/2010).....	133
VII.4. Wind profiles (13/9/2010).....	135
VII.5. Temperature profiles (13/9/2010)	137
VII.6. Air pollution concentration profiles (13/9/2010)	139
VII.7. Wind profiles (15/9/2010).....	141
VII.8. Temperature profiles (15/9/2010)	143
VII.9. Air pollution concentration profiles (15/9/2010)	145
VII.10. Wind profiles (16/9/2010).....	147
VII.11. Temperature profiles (16/9/2010)	149
VII.12. Air pollution concentration profiles (16/9/2010)	151
VII.13. Wind profiles (17/9/2010).....	153
VII.14. Temperature profiles (17/9/2010)	155
VII.15. Air pollution concentration profile (17/9/2010).....	157
VII.16. Analysis of atmospheric turbulence (7/9/2010)	159
VII.16.1. Turbulent fluctuations	159
VII.16.2. Turbulent statistics	163
VII.16.3. Turbulent fluxes	164
VII.16.4. Turbulent kinetic energy	166
VII.16.5. Turbulent power density spectra	166
Conclusions.....	169
Symbols.....	170
Super/Subscripts.....	171
Abbreviations	171
Bibliography.....	172

Appendix A: Sensor and equipment datasheets	176
Appendix B: CATFISH gondola drawings	193
Appendix C: IG 500 N Configuration Document.	197
Appendix D: Weather forecast.....	201
Appendix E: Failure Analysis	205

List of figures

Figure I-1 Idealization of (a) Mean Wind alone, (b) waves alone, (c) turbulence alone. In reality waves or turbulence are superimposed on a mean wind (Stull, 1988). U is the component of wind along the dominant direction.	22
Figure I-2 Idealization of the small eddy mixing process, showing (a) net upward turbulent heat flux in a statically unstable environment and (b) net downward turbulent heat flux in a stable environment (Stull, 1988).	25
Figure I-3 Evolution of the Boundary Layer during the day.....	26
Figure I-4 Virtual potential temperature vertical profiles taken at different instants during the day, identified by S1-S6 in figure I-3.....	28
Figure I-5 UHI: air circulation.	28
Figure I-6 Urban Heat Island: profile of air/soil temperature during daytime and nighttime.	29
Figure I-7 CFD simulation of an urban canyon.	30
Figure I-8 Land and Sea breezes circulations scheme.	31
Figure I-9 Scheme of the sea breeze circulations.....	31
Figure I-10 recent topics of interest in high-resolution numerical modeling studies of sea breezes including: horizontal convective roll (HCR), convective boundary layer (CBL), Kelvin–Helmholtz instability (KHI), and the thermal internal boundary layer (TIBL).	32
Figure I-11 Katabatic and anabatic winds scheme with virtual potential temperature profiles. .	33
Figure I-12 3D circulation pattern of winds in a valley during the night (a), morning (b), and afternoon (c).	33
Figure I-13 Valley winds scheme; (a) day; (b) night.	34
Figure IV-1 Typical atmospheric flow sensor deployment in a field campaign.	52
Figure IV-2 Scheme of operation (left) of the <i>Gill WindMaster</i> anemometer (Right).....	56
Figure IV-3 Cartesian <i>WindMaster</i> reference system of velocities.....	57
Figure IV-4 Notches identifies the North Spar (U^+ direction of the cartesian <i>WindMaster</i> reference system).	57
Figure IV-5 <i>Vaisala HMP50</i> temperature and humidity probe.....	58
Figure IV-6 <i>UniTec SENS3000</i> pollutants sensor.	58
Figure IV-7 <i>SBG IG 500N</i> INU (left); Block diagram of the Kalman filter integration (right)..	59
Figure IV-8 <i>IG 500N</i> : Physical location of the 3D accelerometer (device coordinate system); dimension are in mm.	61
Figure IV-9 <i>IG 500N</i> : Representation of the sensor in the fixed coordinate system (NED).....	61
Figure IV-10 <i>Vortex86</i>	62
Figure IV-11 <i>Datex MUX 3017 V</i>	62
Figure IV-12 <i>ACCULi-Ion</i> battery.....	63
Figure IV-13 Altitude monitoring system: land receiver (left) and APRS transmitter (right). ...	63
Figure IV-14 Kytoon Station: Kytoon blimp, gondola and trailer in a schematic representation (left) and in a photo (right).	65
Figure IV-15 Photo of <i>Floatograph Skydoc #18</i>	66

Figure IV-16 Front view of the upper surface of the kytoon. The direction of harness straps are put in evidence. The helium valves can be seen.....	67
Figure IV-17 Loops at the ends of the control line, which are connected to the payload (left). Detail of the keel line and its knots. Notice that the line is set on the 3rd knot, which gives an AoA of 0° (right).....	67
Figure IV-18 (Left) EDD kytoon unit. The actuated arm with the circular electrical resistance is shown on the left. EDD land unit (Right).	68
Figure IV-19 Typical two-dimensional cable configuration and forces acting on cable.	69
Figure IV-20 Obstruction Marking flags and stripes.	70
Figure IV-21 Tether strain resulting by <i>SkyDoc</i> wind tunnel tests.	72
Figure IV-22 <i>SkyDoc</i> Height (ft) vs. wind speed (mph) considering a fix cable length of 500ft.	72
Figure IV-23 3D CAD model of the CATFISH gondola; Maximum allowed rotation (30°) of CATFISH nacelle at 7 m/s of wind speed.....	75
Figure IV-24 CATFISH gondola: they are visible the Gill Windmaster anemometer and the GPS's antenna (black rhomboid object); silver tape cover the CATFISH's body to surely avoid over heating due to the sun light. It can be seen the cable to regulate AoA of the nacelle.	76
Figure IV-25 From the top: left front tube, back tube, front tube. The nacelle support tube spans between the others.....	77
Figure IV-26 Lower triangular chassis. The elastic cable which is normally linked to the nacelle's back, can be seen.	77
Figure IV-27 Upper triangular chassis.....	77
Figure IV-28 (Right) Holding bridle in position: the stopper blocks the bridle, while the snap hook links the bridle to the control lines (bottom left); circular plastic sleeves (top left).....	78
Figure IV-29 CATFISH gondola connections: scheme (left) and photo (right).	78
Figure IV-30 Top part of CATFISH gondola: Battery, Ethernet port (set/warm-up phase), GPS antenna.	79
Figure IV-31 Top part of CATFISH nacelle: warning led, fuse, ON/OFF switch and AHRS-GPS external data input port (calibration phase).....	80
Figure IV-32 Belly of the CATFISH nacelle; the thermo-hygrometer probe , the led light, the four circular air intakes of the chemical sensors and the six straight intakes for the inside cooling are visible.	81
Figure IV-33 Position of the <i>Sbg IG500-N</i> , AHRS-GPS (yellow parallelepiped), device and its support structure inside the cover of the CATFISH gondola; they are also visible: the chemical sensors (violet), and the led light's battery.	81
Figure IV-34 Aerodynamic interference of the balloon on the anemometer's measurements. DV is the difference between the velocity module, calculated with RANS simulation, and the value of free wind stream (7m/s). The stream lines are shown, too.....	82
Figure IV-35 <i>Umbra Rimorchi TM100B/D</i> . Front connection trunk is on the right.	83
Figure IV-36 Front support of the trailer.	83
Figure IV-37 View of the ensemble trailer.	84
Figure IV-38 Gas cylinder cage after welding of the bars. The support platforms and the gas cylinders supports are still missing at this stage of setup.....	85
Figure IV-39 Loaded gas cylinder cage. The upper blocking bars are visible.....	85
Figure IV-40 Detail of the closing butterfly screw.	86
Figure IV-41 Open back end of the gas cylinder cage. The stopper bar is visible and the cylinder caps are pushing against it. The swiveling back end of the planking is open to permit access to the cylinders.	86
Figure IV-42 Pressure regulator mounted on the cylinder valve during inflation.....	87
Figure IV-43 Inflating wand and hose.	87

Figure IV-44 <i>SKYDOC winch</i> .	88
Figure IV-45 <i>Toshiba inverter</i> .	88
Figure IV-46 Winch in operation during a test flight. The roller fairlead is in the center.	89
Figure IV-47 220 V motor plug.	90
Figure IV-48 <i>Honda EU30is</i> power generator. The control panel with the DC cable is clearly visible (Left). (Right) fixing bracket (connection with trailer).	90
Figure IV-49 Garaging of the balloon (left) on the collapsible cradle (Right).	91
Figure IV-50 Information extracted from NOTAM.	92
Figure V-1 Kytoon clearance and orientation – top view.	95
Figure V-2 Kytoon clearance and orientation – side view.	95
Figure V-3 Overview of the Caserta (Italy) metropolitan area at 20 km of altitude (Google image).	96
Figure V-4 Airport no flight zone (green circle); potential points of analysis (blue circle).	96
Figure V-5 the topography near Caserta city (Italy)	97
Figure V-6 Location of the selected launch site (B point); note the proximity to city center.	97
Figure V-7 Training Camp, Servizio Volontario Giovanile (SVG)	98
Figure V-8 Tarp positioning.	99
Figure V-9 Blimp deployed on the tarp.	99
Figure V-10 Sail effect during inflating phase.	99
Figure V-11 Fully inflated kytoon linked to the ground.	100
Figure V-12 Pulley.	100
Figure V-13 Kytoon bounded trough the pulley (Red circle).	101
Figure V-14 Test launch site location at Capua City Airport (41° 7'3.88"N, 14°11'1.12"E). The red circle outlines a clear area 40 meters wide.	103
Figure V-15 CATFISH gondola: dummy version used during Capua (CE, Italy) safety flight test (26 th February 2010).	104
Figure VI-1 Scheme of the synchronization way.	107
Figure VI-2 Structure of the Anemometer data file; Time mark in evidence (black circle)	107
Figure VI-3 Structure of the “slow” data file; 10 th column reports the TSR.	108
Figure VI-4 Synchronization test: experimental apparatus (left) and expected results (Right).	108
Figure VI-5 Synchronization test result.	109
Figure VI-6 Magnetometer Calibration: x-axis of DEV coordinate system (line between the Nord spar on anemometer's mounting flange and the yellow screw's head) is aligned with magnetic Nord fixed by compass; <i>IG 500N</i> device connected to external PC via USB connection cable (white).	111
Figure VI-7 Magnetometer calibration; INU disconnected: Hard Iron effects' heading deviation; average (μ) and standard deviation (σ) are shown.	112
Figure VI-8 Magnetometer calibration; INU connected: Hard Iron effects' heading deviation; average (μ) and standard deviation (σ) are shown.	112
Figure VI-9 Magnetometer calibration verification; average (μ) and standard deviation (σ) are shown.	113
Figure VI-10 Relative motions correction.	114
Figure VI-11 Wind velocity correction (7/9/2010): Anemometer's ($U_{NED}, V_{NED}, W_{NED}$) and GPS's ($U_{GPS}, V_{GPS}, W_{GPS}$) measurements; average (μ) and standard deviation (σ) are shown.	115
Figure VI-12 Accuracies of the speed (GPS) and position measurements; average (μ) and variance (σ^2) are shown.	115
Figure VI-13 Relationship between the bulk Richardson number, over a layer and the probability of turbulence within that layer.	117

Figure VI-14 Horizontal wind-speed spectrum at Brookhaven National Laboratory at about 100m height (Van Der Hoven, 1957).....	120
Figure VI-15 Power density spectra (m^2/s) of longitudinal velocity in log-log space (Grachev, 1994); $-5/3$ power law is shown.	120
Figure VI-16 Dimensionless power density spectra of longitudinal velocity in log-log space (Roth, 2000); n is the frequency; z_s' is the altitude of the measurements; U is the mean horizontal wind; $-2/3$ power law is shown.	121
Figure VII-1 Altitude profile; 7/9/2010, 9:10-12:50 UTC+1.....	124
Figure VII-2 Climbing (black) and descending (red) phases: wind direction and wind speed profiles; 7/9/2010, 9:10 - 12:50 UTC+1.....	124
Figure VII-3 Altitude profile; 7/9/2010, 13:20-16:20 UTC+1.....	125
Figure VII-4 Climbing (black) and descending (red) phases: wind direction and wind speed profiles; 7/9/2010, 13:20 – 16:20 UTC+1.....	125
Figure VII-5 Altitude profile; 7/9/2010, 16:20-19:00 UTC+1.....	126
Figure VII-6 Climbing (black) and descending (red) phase: wind direction and wind speed profiles; 07/09/2010, 16:20 – 19:00 UTC+1.....	126
Figure VII-7 Climbing phase: static, potential and virtual potential temperature profiles; 7/9/2010, 9:10 – 10:30 UTC+1.	127
Figure VII-8 Descending phase: static, potential and virtual potential temperature profiles; 7/9/2010, 10:30 – 12:50 UTC+1.	127
Figure VII-9 Climbing phase: static, potential and virtual potential temperature profiles; 7/9/2010, 13:20 – 13:55 UTC+1.	128
Figure VII-10 Descending phase: static, potential and virtual potential temperature profiles; 7/9/2010, 13:55 – 16:20 UTC+1.	128
Figure VII-11 Climbing phase: static, potential and virtual potential temperature profiles; 7/9/2010, 16:20 – 18:40 UTC+1.	129
Figure VII-12 Descending phase: static, potential and virtual potential temperature profiles; 7/9/2010, – 18:40- 19:00 UTC+1.....	129
Figure VII-13 The time variation combined north-south wind component and the vertical wind profiles (Ogawa Y., 1986); dashed line denote the sea breeze front (1 m/s); red line identify the approximate location of the most particular wind and temperature vertical profiles.	130
Figure VII-14 The diurnal variation of the vertical potential temperature profiles on June 11, 1982 ,Lake Eire, Canada. (Ogawa Y., 1986)	131
Figure VII-15 Stability of virtual potential profiles (Stull, 1988).	131
Figure VII-16 Bulk Richardson number over altitude compared to virtual potential temperature profiles; 7/9/2010 UTC+1.....	132
Figure VII-17 Climbing (black) and descending (red) phases: pollutants' profiles; 7/9/2010, 9:10-12:50 UTC+1.	133
Figure VII-18 Climbing (black) and descending (red) phases: pollutants profiles; 7/9/2010, 13:20 – 16:20 UTC+1.	133
Figure VII-19 Climbing (black) and descending (red) phase: pollutants profiles; 7/9/2010, 16:20 – 19:00 UTC+1.	134
Figure VII-20 Altitude profile 13/09/2010, 10:20 – 13:30 UTC+1.	135
Figure VII-21 Climbing (black) and descending (red) phases: wind direction and wind speed profiles; 13/09/2010, 10:20 – 13:30 UTC+1.....	135
Figure VII-22 Altitude profile; 13/09/2010, 14:00 – 17:35 UTC+1	136
Figure VII-23 Climbing and descending phases: wind direction and wind speed profiles; 13/09/2010, 14:00 – 17:35UTC+1.	136
Figure VII-24 Climbing phase: static, potential and virtual potential temperature profiles; 13/09/2010, 10:20 – 11:35 UTC+1.	137

Figure VII-25 Descending phase: static, potential and virtual potential temperature profiles; 13/09/2010, 11:35 – 13:30 UTC+1.	137
Figure VII-26 Climbing phase: static, potential and virtual potential temperature profiles; 13/09/2010, 14:00 – 15:20 UTC+1.	138
Figure VII-27 Descending phase: static, potential and virtual potential temperature profiles; 13/09/2010, 15:20 – 17:35 UTC+1.	138
Figure VII-28 Climbing (black) and descending (red) phases: pollutants profiles; 13/09/2010, 10:20 – 13:30 UTC+1.	139
Figure VII-29 Climbing (black) and descending (red) phases: pollutants profiles; 13/09/2010, 14:00 – 17:35 UTC+1.	140
Figure VII-30 Altitude profile; 15/09/10, 9:30 - 13:10 UTC+1.	141
Figure VII-31 Wind direction and wind speed profiles (ascent); 15/09/2010, 9:30 - 13:10 UTC+1.	141
Figure VII-32 Altitude profile; 15/09/2010, 14:15 - 18:00 UTC+1.	142
Figure VII-33 Wind direction and wind speed profiles (ascent); 15/09/2010, 14:15 - 18:00 UTC+1.	142
Figure VII-34 Only climbing phase: static, potential and virtual potential temperature profiles; 15/09/2010, 9:30 - 13:10 UTC+1.	143
Figure VII-35 Only climbing phase: static, potential and virtual potential temperature profiles; 15/09/2010, 14:15 to 18:00 UTC+1.	143
Figure VII-36 Wind roses; 9:30 - 13:10 (up) and 14:15 to 18:00 UTC+1 (down).	144
Figure VII-37 Trajectory of the kytoon; 9:30 - 13:10 (red) and 14:15 to 18:00 UTC+1 (black).; 15/9/2010.	145
Figure VII-38 Only climbing phase: pollutants profiles; 15/09/2010, 9:30-13:10 UTC+1.	145
Figure VII-39 Only climbing phase: pollutants profiles; 15/09/2010, 14:15 – 18:00 UTC+1.	146
Figure VII-40 Altitude profile; 16/09/2010, 9:40 - 11:50 UTC+1.	147
Figure VII-41 Climbing (black) and descending (red) phases: wind direction and wind speed profiles. 16/09/2010, 9:40 - 11:50 UTC+1.	147
Figure VII-42 Altitude profile. 16/09/2010, 12:00 - 14:40 UTC+1.	148
Figure VII-43 Climbing (black) and descending (red) phases: wind direction and wind speed profiles. 16/09/2010, 12:00 – 14:40 UTC+1.	148
Figure VII-44 Climbing phase: static, potential and virtual potential temperature profiles. 16/09/2010, 9:40 - 10:50 UTC+1.	149
Figure VII-45 Descending phase: static, potential and virtual potential temperature profiles. 16/09/2010, 10:50 - 11:50 UTC+1.	149
Figure VII-46 Climbing phase: static, potential and virtual potential temperature profiles. 16/09/2010, 12:00 - 13:10 UTC+1.	150
Figure VII-47 Descending phase: static, potential and virtual potential temperature profiles. 16/09/2010, 13:10 - 14:40 UTC+1.	150
Figure VII-48 Climbing (black) and descending (red) phases: pollutants profiles.	151
Figure VII-49 Climbing (black) and descending (red) phases: pollutants profiles.	152
Figure VII-50 Altitude profile. 17/09/2010, 9:30 - 12:20 UTC+1.	153
Figure VII-51 Climbing (black) and descending (red) phases: wind direction and wind speed profiles. 17/09/2010, 9:30 – 12:20 UTC+1.	153
Figure VII-52 Altitude profile. 17/09/2010, 12:30 to 15:30 UTC+1.	154
Figure VII-53 Climbing (black) and descending (red) phases: wind direction and wind speed profiles. 17/09/2010, 12:30 - 15:30 UTC+1.	154
Figure VII-54 Climbing phase: static, potential and virtual potential temperature profiles. 17/09/2010, 9:30 - 10:40 UTC+1.	155

Figure VII-55 Descending phase: static, potential and virtual potential temperature profiles. 17/09/2010, 10:40 - 12:20 UTC+1.....	155
Figure VII-56 Climbing phase: static, potential and virtual potential temperature profiles. 17/09/2010, 12:30 - 13:50 UTC+1.....	156
Figure VII-57 Descending phase: static, potential and virtual potential temperature profiles. 17/09/2010, 13:50 - 15:30 UTC+1.....	156
Figure VII-58 Climbing (black) and descending (red) phases: pollutants profiles. 17/09/2010, 9:30 – 12:20 UTC+1.	157
Figure VII-59 Climbing (black) and descending (red) phases: pollutants profiles.	158
Figure VII-60 Turbulent fluctuations at 34m AGL.....	159
Figure VII-61 Turbulent fluctuations at 63m AGL.....	160
Figure VII-62 Turbulent fluctuations at 124m AGL.....	160
Figure VII-63 Turbulent fluctuations at 152m AGL.....	161
Figure VII-64 Turbulent fluctuations at 183m AGL.....	161
Figure VII-65 Turbulent fluctuations at 213m AGL.....	162
Figure VII-66 Turbulent fluctuations at 245m AGL.....	162
Figure VII-67 Turbulent fluctuations at 309m AGL.....	163
Figure VII-68 Standard deviations of the turbulent components over altitude; 7/9/2010 10:30-12:45 UTC+1.	163
Figure VII-69 Standard deviations over altitude on 11 June 1982: Run 9 up (9:00-9:44) and down (9:44-10:42); run 10 up (11:00-12:40) and down (12:40-13:20); time EDT; (Ogawa Y., 1986).	164
Figure VII-70 Vertical eddy fluxes profiles; 7/9/2010, 10:30-12:45 UTC+1.....	164
Figure VII-71 Vertical eddy fluxes measured on 11 June 1982, 14:44-16:36 EDT; Thermal internal Boundary Layer (TIBL); (Ogawa Y., 1986).....	165
Figure VII-72 Linear correlation coefficient of u' and w' ; 7/9/2010, 10:30-12:45 UTC+1.	165
Figure VII-73 TKE profile; 7/9/2010, 10:30-12:45 UTC+1.	166
Figure VII-74 Normalized power spectra density of turbulent longitudinal component (u) of wind over altitude; 7/9/2010, 10:30-12:45 UTC+1.....	166
Figure VII-75 Normalize power density spectra of turbulent vertical component (w) of wind over altitude; -2/3 power law is shown in bleu; 7/9/2010, 10:30-12:45 UTC+1.	167
Figure VII-76 Normalized power density spectra of crosswind component (v) over altitude; 7/9/2010, 10:30-12:45 UTC+1.....	167
Figure VII-77 Normalized power density spectra of sonic virtual potential temperature (θ_v^*) over altitude; 7/9/2010, 10:30-12:45 UTC+1.....	168
Figure VII-78 Normalized power density spectra of virtual potential temperature (Roth, 2000).	168

List of tables

Table II-1 Air pollutants concentrations' limits (UE directives: 1999/30/EC, 2000/69/CE and 96/62/CE).....	40
Table III-1 Review of atmospheric turbulence over cities.	45
Table III-2 Characteristics of sensors (Ogawa, 1982).....	47
Table IV-1 Ranges, Accuracy and Resolution of Sens3000 sensors.....	59
Table IV-2 <i>IG 500N</i> : used output mask (data format in appendix C).	60
Table IV-3 Power consumption table.....	62
Table IV-4 Instruments' mass budget.	64
Table IV-5 <i>Dynema Sky 75 Ultra</i> cable characteristics.	68

Table IV-6 Gross lift versus altitude and sea Level temperature; Stable free lift is 15% gross lift at S.L.	71
Table IV-7 Cable characteristics, horizontal displacement and Free Lift of the kytoon, at 300m of altitude, changing temperature.....	74
Table IV-8 Safety Factor of the DSK75-Ultra cable; worst case (Temperature, 0°C).....	74
Table IV-9 Gas cylinder specifications (per cylinder)	85
Table IV-10 Gas cylinder cage specifications.....	86
Table IV-11 Winch motor and speed reducer specifications.	89
Table IV-12 SKYDOC™ Winch specifications	89
Table IV-13 Specifications of the <i>Honda EU30is</i> power generator.....	90
Table V-1 Caserta experimental campaign at S.V.G.'s training camp (September 2010).....	102
Table V-2 Mean weather conditions at sea level at the launch site on 26/2/2010.	104
Table VI-1 Anemometer raw data; sampling frequency: 32 Hz.	106
Table VI-2 Air pollution sensor and thermo-hygrometer probe raw data; sampling frequency: 0.2 Hz.	106
Table VI-3 <i>IG 500N</i> data; sampling frequency: 50 Hz.	106
Table VI-4 <i>UniTech Sens3000</i> , calibration curves.....	109
Table VI-5 Calibration range of the pollutants' concentration.	110
Table VII-1 Averaged stop altitude and pause; 7/9/2010, 10:30-12:45 UTC+1.....	159

I

Boundary Layer Meteorology

Since the dispersion mechanisms depend on the circulation of air masses in the Planetary Boundary Layer (PBL), an understanding of the basic characteristics of the PBL is strictly due.

The chapter follows mainly the order as by R.B. Stull's "Introduction to Boundary Layer Meteorology" book (Stull, 1988); it describes wind characteristics, transport mechanism (turbulence and buoyancy), structure and evolution of the PBL; particular attention is made on the description of the local microclimatic phenomena (as Urban Heat Island, sea breeze, and valley flows), underlining how the latter affect the dispersion of pollution.

I.1. Boundary Layer Definition

The troposphere extends from the ground up to an average altitude of 11 km. So, the Earth's Planetary Boundary Layer (PBL) can be defined as “that part of the troposphere that is directly influenced by the presence of the earth's surface, and responds to surface forcings with a timescale of about an hour or less” (Stull, 1988). The boundary layer thickness is quite variable in time and space, ranging from hundreds of meters to a few kilometers. The remainder of the atmosphere is loosely called the free atmosphere. Indirectly, the whole troposphere can change in response to surface characteristics, but this response is relatively slow outside of the boundary layer.

I.2. Wind and flow

Air flow, or wind, can be divided into three broad categories: mean wind, turbulence, and waves. Each can exist independently from the others in the boundary layer, where transport of quantities as moisture, heat, momentum and pollutants is dominated in the horizontal by the mean wind and in the vertical by turbulence.

A common approach for studying either turbulence or waves is to split the variables into a mean part and a perturbation part. The mean part represents the effects of the mean temperature and wind, while the perturbation part can represent either the wave effect or the turbulence effect that is superimposed on the mean wind (Fig. I-1).

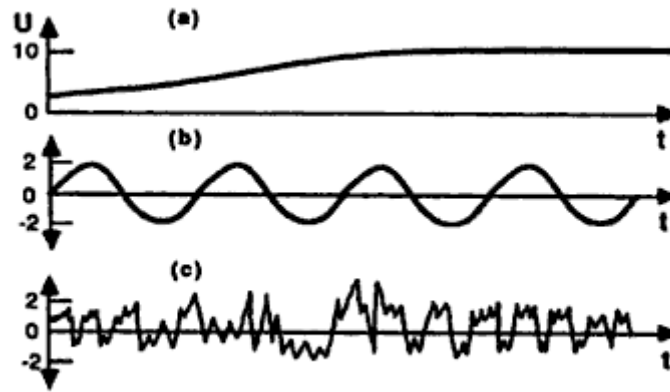


Figure I-1 Idealization of (a) Mean Wind alone, (b) waves alone, (c) turbulence alone. In reality waves or turbulence are superimposed on a mean wind (Stull, 1988). U is the component of wind along the dominant direction.

I.3. Virtual Potential Temperature

Buoyancy is one of the driving forces for turbulence in the PBL, causing thermals¹ of warm air to rise due to the difference in density with the surrounding air. Virtual temperature is an important variable for the study of these phenomena because it is the temperature that dry air must have to equal the density of moist air at the same pressure. Virtual potential temperature is

¹Thermal: a column of rising hot air in the lower altitudes of the Earth's atmosphere. It is generated by the uneven solar heating of the ground.

analogous to potential temperature in that it is independent from the changes in pressure altitude. It is defined as:

$$\theta_v = \theta(1 + 0.61r_{sat} - r_L) \quad (1.1)$$

where $\theta = T(\frac{P_0}{P})^{0.286}$ ($p_0 = 100\text{kPa}$) is the potential temperature, r_{sat} is the water-vapor saturation mixing ratio of the air parcel, and r_L is the liquid-water mixing ratio.

1.4. Turbulent Transport

The turbulent flow is considered a condition of irregular flux in which the thermo-fluid variables show a random variation in both time and space. The relative high frequency of occurrence of turbulence near the ground is one of the characteristics that makes the PBL different from the rest of the atmosphere. The turbulence is the main mechanism of the dispersion of pollutants in the atmosphere produced by anthropogenic activities.

It is generated by nonlinear effects superimposed on the mean wind and can be visualized as consisting of irregular swirls of motion called eddies. Usually turbulence consists of many different size eddies superimposed on each other. The relative strengths of these different scale eddies define the turbulence spectrum.

Much of the boundary layer turbulence is generated by forcing from the ground. For example, solar heating of the ground during sunny days causes thermals of warmer air to rise. These thermals are just large eddies (between 100 and 3000 m in diameter, by covering all PBL depth). Frictional drag on the air flowing over the ground cause wind shears to develop, which frequently become turbulent. Obstacles like trees and building deflect the flow, causing turbulent wakes adjacent to, and downwind of the obstacle.

Turbulence is several orders of magnitude more effective at transporting quantities than is molecular diffusivity. It is turbulence that allows the boundary layer to respond to changing surface forcings. The frequent lack of turbulence above the boundary layer means that the rest of the free atmosphere cannot respond to surface changes. The free atmosphere behaves as if there were no boundary to contend with, except in sense of mean wind flowing over the boundary-layer top height contours.

A common approach for studying turbulence is to split variables such as virtual potential temperature (\mathcal{G}_v) and wind (U, V, W) into a mean part ($\overline{\mathcal{G}_v}, \overline{U}, \overline{V}, \overline{W}$) and a perturbation part ($\mathcal{G}'_v, u', v', w'$)

$$\begin{aligned} \mathcal{G}'_v &= \mathcal{G}_v - \overline{\mathcal{G}_v} \\ u' &= U - \overline{U} \\ v' &= V - \overline{V} \\ w' &= W - \overline{W} \end{aligned} \quad (1.2)$$

The mean part represents the effects of the mean virtual potential temperature and mean wind, while the perturbation part can represent the turbulence effect that is superimposed on the mean wind.

Note that for any variable $A(t,s)$, function of time (t) and space (s) we can define two averages:

$$\text{Time average: } \overline{A(t,s)}^t = \frac{1}{N} \sum_{i=1}^N A(i,s) \quad (1.3)$$

$$\text{Space average: } \overline{A(t,s)}^s = \frac{1}{M} \sum_{j=1}^M A(t,j) \quad (1.4)$$

The turbulence analysis requires the first definition.

In agreement with scientific literature (Roth, 2000) we define:

- U : “longitudinal”, that is the component of wind along the dominant direction; it is in the local horizontal plane;
- V : “transverse” or “crosswind”, that is the component perpendicular to the longitudinal one; it is in the local horizontal plane too;
- W : “vertical” or “down”, that is the component along the local vertical direction.

The following subsections will introduce the variables that characterize the turbulence.

1.5. Kinematic Flux

Flux is the transfer of a quantity per unit area per unit time. In PBL meteorology, we are often concerned with mass, heat, moisture, momentum and pollutant fluxes. The turbulent kinematic flux is represented by following matrix:

$$\begin{bmatrix} \overline{u'u'} & \overline{u'v'} & \overline{u'w'} \\ \overline{v'u'} & \overline{v'v'} & \overline{v'w'} \\ \overline{w'u'} & \overline{w'v'} & \overline{w'w'} \end{bmatrix} \quad (1.5)$$

The elements of the principal diagonal can be interpreted as variances (whose root square is the standard deviation):

$$\sigma_A^2 = \frac{1}{N-1} \sum_{i=0}^{N-1} (A_i - \bar{A})^2 \quad (1.6)$$

$$\sigma_A^2 = \frac{1}{N} \sum_{i=0}^{N-1} (a'_i)^2 = \bar{a'^2}, \quad a' = (A - \bar{A}) \quad (1.7)$$

while the others as covariances:

$$\text{covar}(A, B) = \frac{1}{N} \sum_{i=0}^{N-1} (A_i - \bar{A})(B_i - \bar{B}) = \frac{1}{N} \sum_{i=0}^{N-1} (a'_i)(b'_i) = \overline{a'b'} \quad (1.8)$$

These quantities are presented purely as vertical profile in the PBL [e.g. (Ogawa Y., 1986) and (Ogawa Y., 1986)] or normalized [e.g. (Roth, 2000), (Hongstrom U., 2002) and (Zhang H., 2001)].

I.5.1. Vertical Eddy Heat Flux

The vertical eddy heat flux is represented from term $\overline{w'\theta'}$ which is similar to the kinematic flux terms of the previous paragraph, except that the perturbation values are instead of the mean values of W and θ .

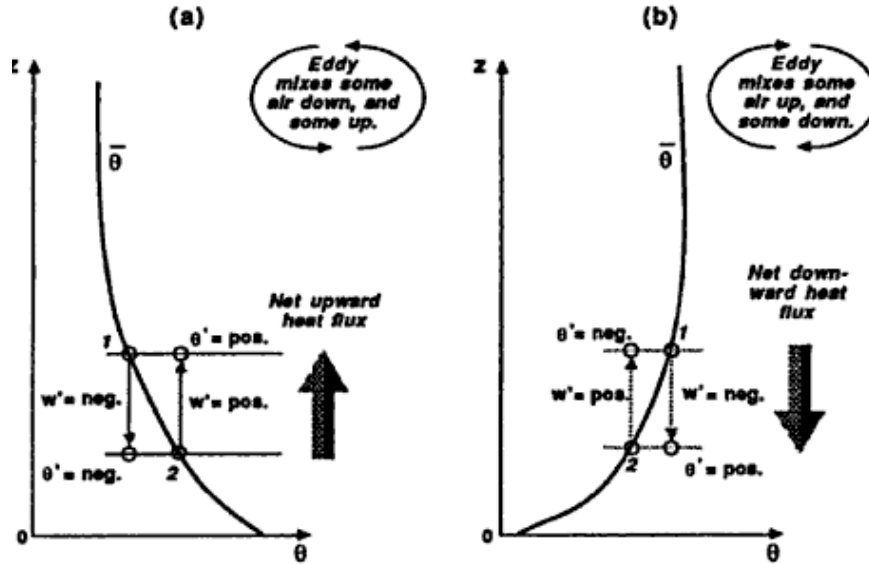


Figure I-2 Idealization of the small eddy mixing process, showing (a) net upward turbulent heat flux in a statically unstable environment and (b) net downward turbulent heat flux in a stable environment (Stull, 1988).

Up/downward heat transport (Fig. I-2) is possible even if $\overline{w'} = 0$ (no net transport of mass) with $\overline{w'\theta'} \neq 0$: turbulent eddies transport the heat up/downward to make the lapse rate more/less adiabatic when $\overline{w'\theta'} > 0$ / $\overline{w'\theta'} < 0$.

Consequently, it is interesting to evaluate the vertical profile of this quantity [as made by (Ohara T., 1989)] , and to compare it with the turbulent kinematic flux components [e.g. (MacCready Paul B., 1953), (Ohara T., 1989), (Zhang H., 2001)]

I.5.2. Turbulent Kinetic Energy and Energy spectra of atmospheric Turbulence

The usual definition of turbulent kinetic energy (TKE) is the following:

$$TKE = \frac{1}{2}(\overline{u'^2} + \overline{v'^2} + \overline{w'^2}) \quad (I.9)$$

TKE is one of the most important quantities used to study the turbulent boundary layer. It is a measure of the turbulence.

The Energy spectrum of atmospheric turbulence allows to learn about the contribution of each different size eddy to the total turbulence kinetic energy. Peaks in the spectrum show which size eddies contribute the most of the turbulence kinetic energy [(Met Office, 2008), (Lovejoy, 2010)].

I.6. Boundary Layer Structure and Evolution

Over both land and oceans, the general nature of the boundary layer is to be thinner in high-pressure regions than in low-pressure regions. The effect of synoptic² high pressure is to move boundary layer air out of the high towards lower pressure regions.

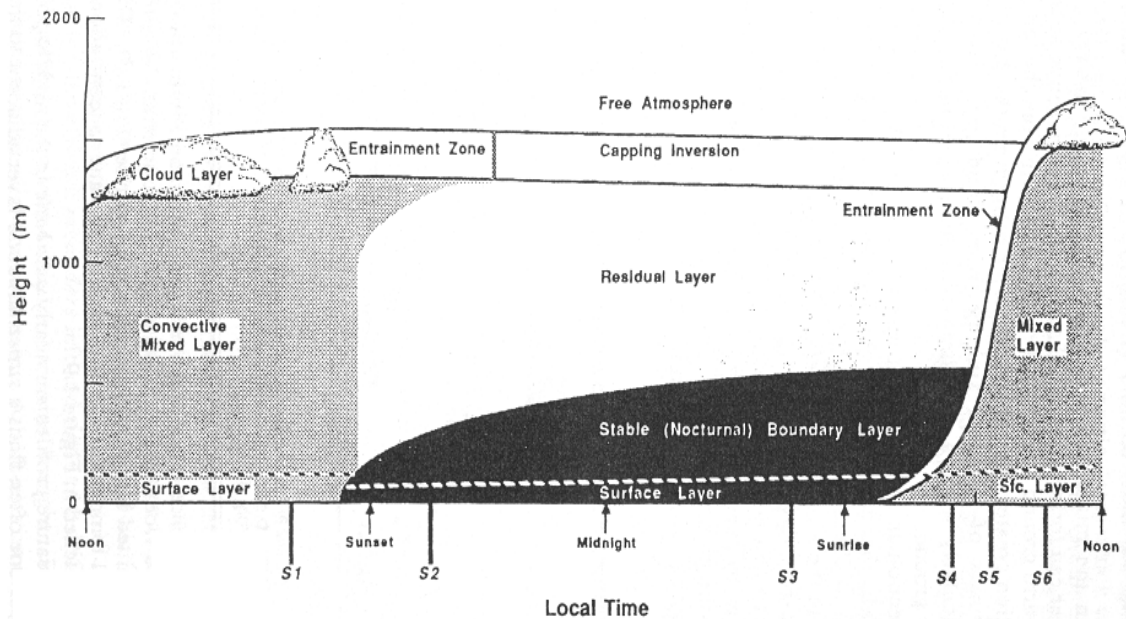


Figure I-3 Evolution of the Boundary Layer during the day.

Over land surfaces in high pressure regions the boundary layer has a well defined structure that evolves with the diurnal cycle, shown in figure I-3.

The three major components of this structure are the Mixed Layer (ML), the Residual Layer (RL) and the Stable Boundary Layer (SBL). The Surface Layer is the region at the bottom of the boundary layer where turbulent fluxes and stresses vary by less than 10% of their magnitude.

The Mixed Layer is present during the daytime hours, in which the ground is exposed to the solar heating. The ML is convectively driven by sources like heat transfer from a warm ground surface and radiative cooling from the top of the cloud layer. Starting from dawn and during the daytime, the ML depth continuously increases, and reaches its maximum in the late afternoon.

The ML grows by entraining (mixing down into it) the less turbulent air from the free atmosphere. The resulting turbulence tends to mix heat, moisture, momentum and pollutants uniformly in the vertical direction. Virtual potential temperature profiles are nearly adiabatic³ in the middle portion of the ML, and often superadiabatic³ in the surface layer. Most pollutant sources are near the earth's surface, thus, pollutant concentrations can build up in the ML while concentrations in the free atmosphere remain relatively low. The inability of the thermals to

²Synoptic: relative to a scale corresponding to horizontal lengths of 1000 km or more.

³A temperature profile is superadiabatic when the temperature lapse rate is greater than $-10\text{ }^{\circ}\text{C/km}$.

I. Boundary Layer Meteorology

penetrate very far into the free atmosphere also means that pollutants cannot easily disperse into the free atmosphere.

About half an hour before sunset the thermals cease to form, allowing turbulence to decay in the formerly well-mixed layer.

The resulting layer is sometimes called the Residual Layer (RL) because its initial mean-state variables and concentration variables are the same as those of the recently decayed mixed layer. The turbulence in the RL is of nearly equal intensity in all directions.

Non passive pollutants may react with other constituents during the night to create compounds that were not originally emitted from the ground.

Variables such as virtual potential temperature usually decrease slowly during the night because of radiation divergence, with a cooling rate in the order of 1 °C/d. The cooling rate is more or less uniform throughout the depth of the RL, so the potential temperature profile remains nearly adiabatic.

The RL does not have direct contact with the ground, because a nocturnal stable layer develops during the night and modifies the RL's bottom, increasing in thickness. Thus, the remainder of the RL is not affected by turbulent transport of surface-related properties.

The RL can exist for the while in the mornings before being entrained in the new ML. As the night progresses, a stable boundary layer, characterized by statically stable air with weaker and sporadic turbulence, forms at the basis of the Residual Layer.

Although the wind at ground level frequently becomes lighter at night, the winds aloft may accelerate in a phenomenon that is called the nocturnal jet. Turbulence can occur in short bursts in the layer due to the wind shear caused by this phenomenon.

Pollutants emitted into the stable boundary layer disperse relatively little vertically, but they do it more rapidly in the horizontal direction (fanning).

Knowledge of the virtual potential temperature profile is usually sufficient to identify the parts of the boundary layer, as shown in figure I-4.

As the virtual potential temperature profile evolves with time, so must the behavior of smoke plumes: for example, smoke emitted into the top of the stable boundary layer rarely is dispersed to the ground because of the limited turbulence. Smoke plumes in the RL may disperse to the point where the bottom of the plume hits the top of the stable boundary layer. The strong static stability and reduction of the turbulence reduces the downward mixing into the stable boundary layer, and the top of the plume can sometimes continue to rise into the neutral air (*lofting*).

After sunrise a new ML begins to grow, eventually reaching the height of the elevated smoke plume from the previous night. At this time, the elevated pollutants are mixed down to the ground by ML entrainment, in a process that is called *fumigation*.

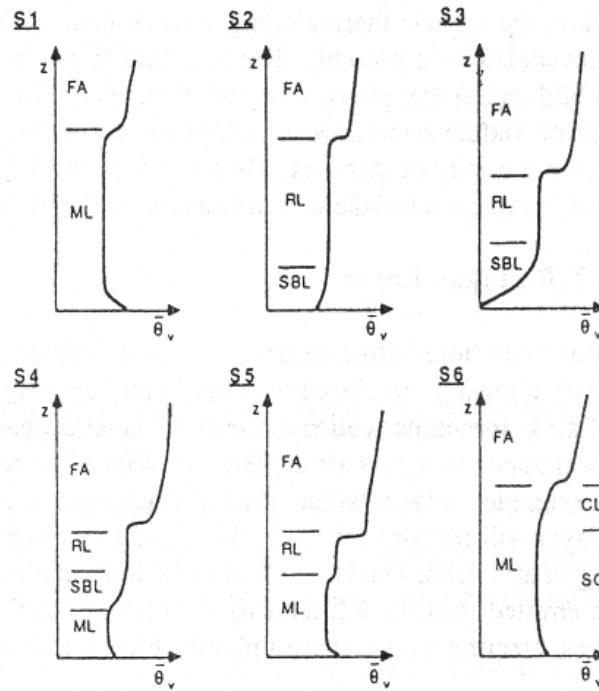


Figure I-4 Virtual potential temperature vertical profiles taken at different instants during the day, identified by S1-S6 in figure I-3.

I.7. Urban Heat Island

The particular terrain of an urban zone, in which concrete buildings and asphalted roads are present, usually has a greater heat capacity than its rural surroundings.

This means that the urban area is capable of storing more efficiently the heat accumulated during the day, and of releasing it at night, together with the heat generated by human activities. Consequently, the air temperature during the night increases near an urban area and reaches a maximum on it (Fig. I-6). This profile is similar to the one generated by a warm island surrounded by colder sea: hence the “Urban Heat Island” definition.

The final configuration is a closed air circulation (Fig. I-5) between the urban area and surrounding areas. This phenomenon can radically modify temperature and speed in the flow field but can also modify the pollutants dispersion and production mechanism (O_3 production increases with temperature!).

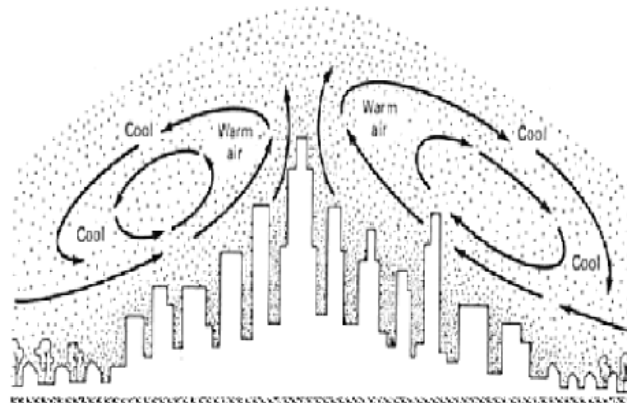


Figure I-5 UHI: air circulation.

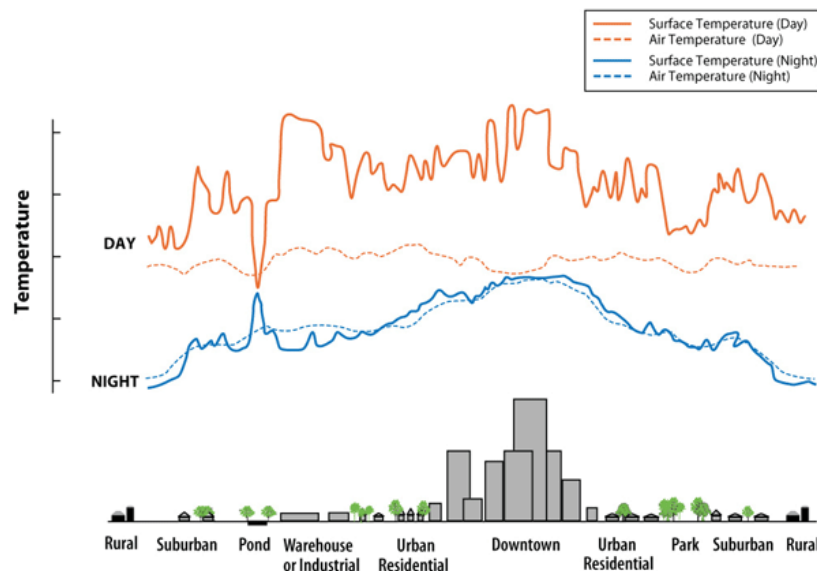


Figure I-6 Urban Heat Island: profile of air/soil temperature during daytime and nighttime.

Studies on the existence of the Urban Heat Island started in the 1970's and 80's, due to the increasing problem of the creation of clouds of pollutants during the nighttime. The main characteristics of the BL overlying the UHI were discovered by Oke (Oke, 1971): the circulation is the same as rural areas, but the humidity decreases and the turbulence increases. The maximum temperature difference in relation to rural areas was measured to be about 2-3 °C (cities of a million or more inhabitants have been known to generate excesses of 8-12°C!), while the BL depth has been valued to be about 150-450 m.

The alteration brought by the Urban Heat Island, however, remains still partially unknown due to the fact that cities at the same latitude often have very different systems of air circulation. Besides, human activities can strongly influence the air circulation (particularly in the urban canyon: space between buildings).

The review about two decades of urban climate research (Arnfield, 2003) shows how “Mediterranean climates seem to have been particularly well served by heat island studies ...” due probably to the not well known interaction phenomena with sea breezes and valley flows.

The studies concentrated on the night and first morning hours: it is in these hours that the ML grows to the disadvantage of the SBL and hazardous mixing of pollutants can happen.

Studies conducted with wind tunnels or tank simulations have brought good results on the comprehension of the behavior of heat islands. In this case a tank is realized where heated side panels simulate land and sea breezes and UHI are simulated through electrical resistances. However, the roughness of the urban terrain desired to obtain values of the dimensionless numbers similar to those experienced in the environment is not achievable: this gives a lower limit on the scales that can be simulated with this method.

CFD simulations have been also used to simulate UHI, but an adequate comprehension of the BL behavior and its interaction with urban canyons still lacks at the time, so the predictions obtainable by means of computer simulations are limited (Fig. I-7).

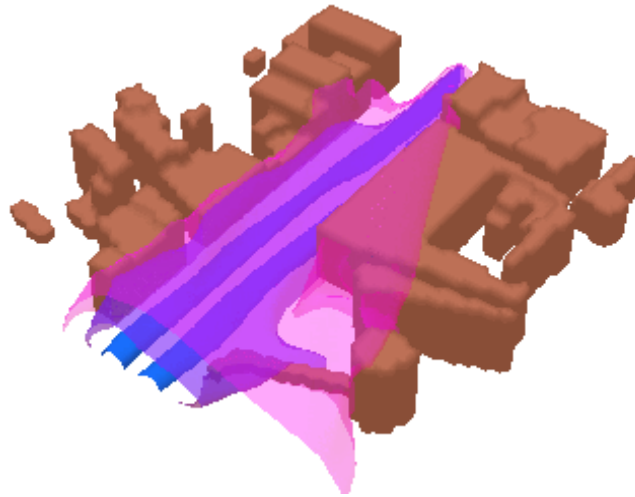


Figure I-7 CFD simulation of an urban canyon.

The various difficulties in simulating the environment underline the importance of conducting field studies to enhance the comprehension of the Urban Heat Island. Usually, field studies on UHIs are conducted with a series of observation campaigns in the interested zone which have the purpose of collecting a great deal of atmospheric data which have to be processed and validated with statistical instruments. In particular, the measurements of vertical profiles of wind, pressure, humidity, and aerosol composition are of crucial importance in these studies, since they are direct information on the structure of the boundary layer. In addition, the data collected during the experiment campaigns can be used as validation tools for the CFD codes that are currently used to predict pollutants' dispersion.

I.8. Land and Sea Breeze

The influence of geographical characteristics on the behavior of the boundary layer is particularly evident in the case of the land and sea breezes.

The breeze is a particular phenomenon which happens in coastal zones. In these zones, the different values of the heat capacity between the land and the sea create a circulation system of horizontal winds (breezes) and series of sub-phenomena (convective cells, front generation).

During daytime, both the land and the sea are subject to the same amount of solar radiation. However, since the sea has a greater heat capacity than the one of the land, its temperature is lower than the land's. Convective cells form over the land, and the generated turbulence recalls fresh air from the sea at ground level, which is then warmed on the ground and rises in the convection cells. The cycle is closed by a return current, directed towards the sea, in the higher level of the boundary layer (Fig. I-8).

This first phenomenon is called sea breeze, because the wind keeps blowing from the sea during the whole day. Sea breeze progresses horizontally and is eased in its advance by the turbulence generated by the convective cells.

The typical intensity of sea breezes ranges between 1-8 m/s [e.g. (Ogawa Y., 1986), (Winston Jeeva, 1992)] and its front can progress far inland (30 to 100km, if background synoptic flow is in the same direction as low-level sea breezes and no major barriers to the flow). Pollutants emitted into the sea breeze can thus be recirculated back further up the coastline.

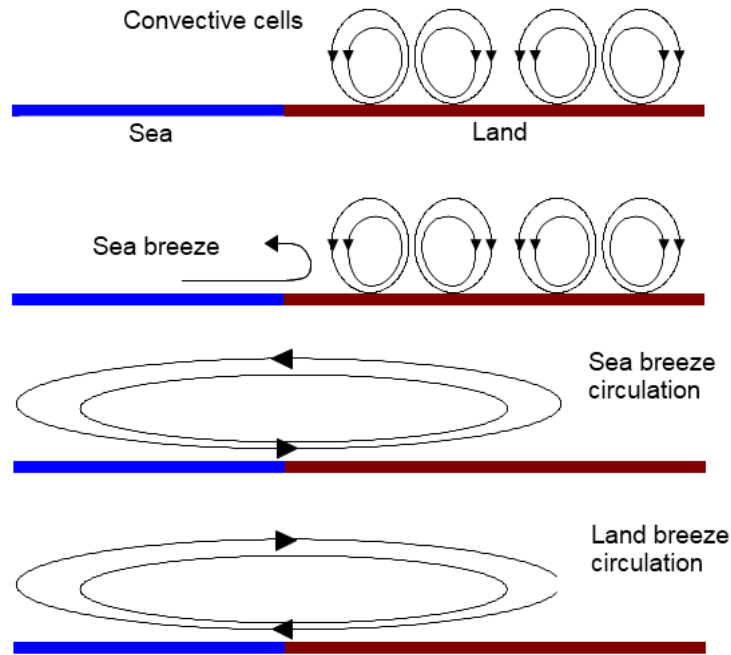


Figure I-8 Land and Sea breezes circulations scheme.

During nighttime, the land cools more quickly than the sea, owing to the difference in heat capacities. Consequently, the temperature of the ground is lower than the sea's. A circulation pattern is generated with the same mechanism of the sea breeze, but in the opposite direction, and it is called land breeze.

However, this breeze is hindered in its advance by the presence of the nocturnal stable boundary layer (SBL), in which there is no turbulence. Consequently, land breeze does not penetrate as much as the sea breeze. Typically, the land breezes velocity is 1-3m/s, but it is also measured 5-6 m/s of maximum wind speed in the middle of Tokyo metropolitan area due to the presence of the Sagami's and Tokyo's bays (Ohara T., 1989).

Both of the breezes have some phenomena in common. Weak return currents form in the upper levels of the BL, which closes the circulation pattern. An inversion of the wind speed exists where these return currents are generated, and the Kelvin Helmholtz wave perturbations are produced by this wind gradient. The presence of such perturbations identifies the breeze front, which is the maximum penetration distance (Fig. I-9). The depth of the sea/land breezes has been observed to be an order of 100-500m, and the total circulation depth, including the return circulation, can range from 500-2000m.

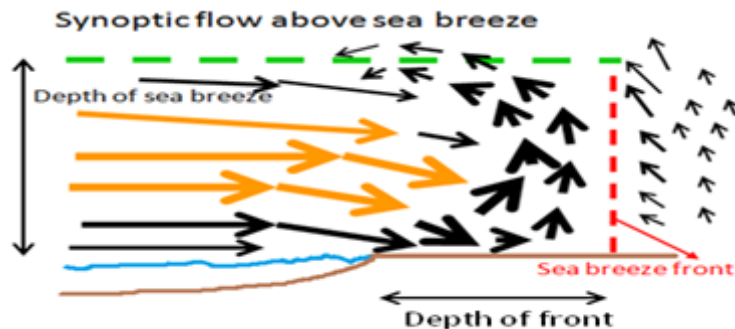


Figure I-9 Scheme of the sea breeze circulations.

Extensive studies have been conducted on land and sea breezes, mainly for the influence that they have on coastal urban areas such as the Mediterranean ones. Mostly, field research campaigns have been conducted, due to the difficulties of obtaining adequate dimensionless numbers in simulating the environment in tanks or wind tunnels.

Some information has been discovered by Yoshikaido (Crosman, 2010), who executed numerical simulations based on the city of Tokyo, from which emerged that, a coastal urban area delays in time the formation of the different breezes. In addition, the breezes are displaced towards higher levels of the boundary layer, creating a downwind, low-level zone where the pollutants' dispersion is compromised. In the review of numerical studies about lake and sea breeze a scheme of the phenomenon is shown (Fig. I-10).

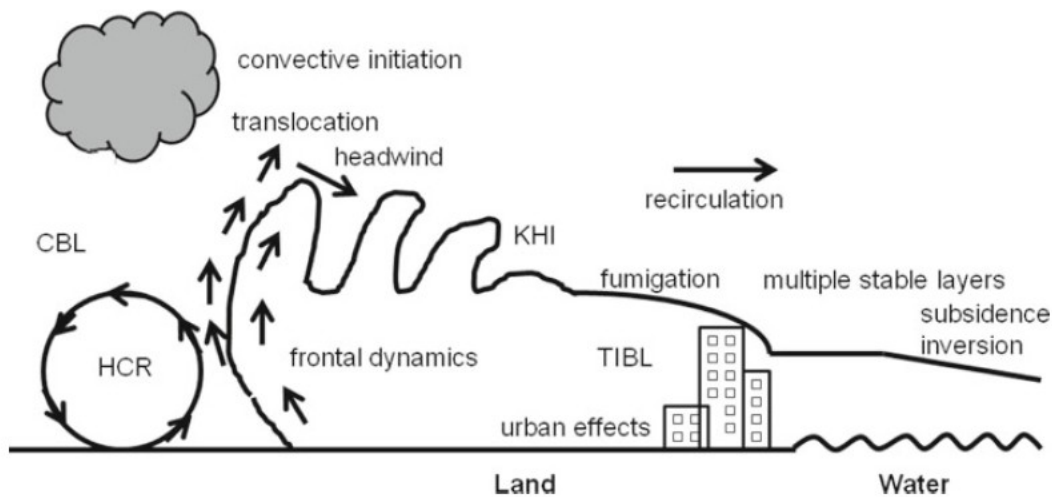


Figure I-10 recent topics of interest in high-resolution numerical modeling studies of sea breezes including: horizontal convective roll (HCR), convective boundary layer (CBL), Kelvin–Helmholtz instability (KHI), and the thermal internal boundary layer (TIBL).

I.9. Valley, Katabatic and anabatic winds

Valley, katabatic, and anabatic winds are particular wind currents that form in mountain zones. They are caused by several factors, among which there are the orography of valleys and slopes, and the different solar exposure of the mountainsides.

The phenomenon is three-dimensional, but a decomposition in the transverse (katabatic and anabatic winds) and in the longitudinal (valley winds) direction is useful.

Katabatic winds are generated just after sunset (Fig. I-11a). During the day, the ML grows until it usually reaches depths higher than the mountains themselves: a more or less constant temperature in the valley is then achieved (Fig. I-11f). At sunset, the reduction in solar heating causes the ground to cool. The difference in temperature between the ground and the air produces cold winds that descend in the valley, driven by gravity.

In the valley the cold winds create a cool “pool”, which expands during the night (Fig. I-11b,c). The expansion continues, driven by the katabatic winds, until the temperature of the pool reaches the one of the surrounding air. When this happens, the pool remains stable for the rest of the night.

Katabatic winds usually range between 1 and 5 m/s and are contained in the first 2 to 10 m of the surface layer.

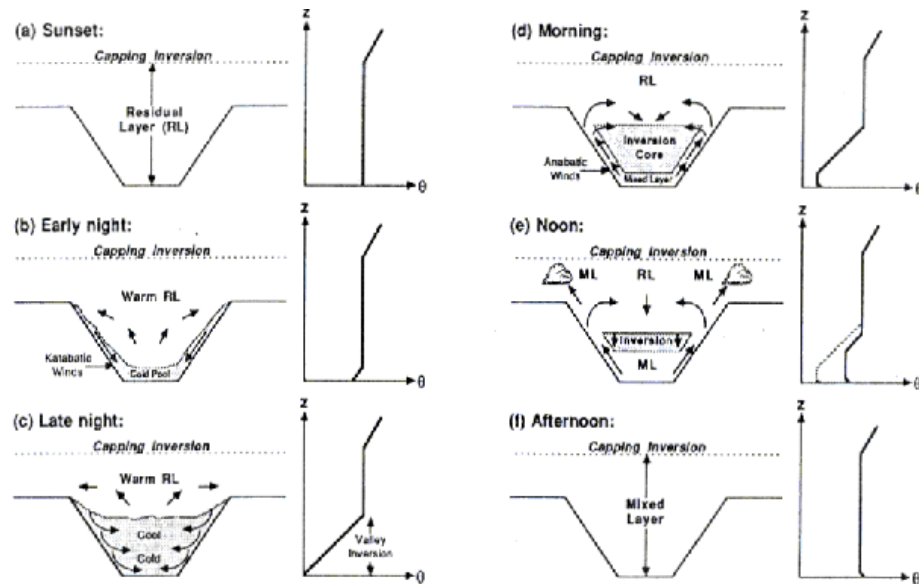


Figure I-11 Katabatic and anabatic winds scheme with virtual potential temperature profiles.

The layering of cold air in the valley “pool” can generate a high concentration of pollutants, possibly creating a pollution hazard for inhabitants in the valleys. At dawn, the circulation pattern changes directions: the mountain slopes get warmer due to solar exposure, and anabatic winds, directed uphill, are generated.

The anabatic circulation pattern is not symmetrical due to the different solar exposures of the mountain slopes (Fig. I-11d). In the first hours of the morning, the anabatic winds recall fresh air from the cold pool left by the katabatic winds of the night before to a warmer top layer. On the valley floor, the solar heating generates a ML which increases in depth to the disadvantage of the top layers. However, the ML expansion is hindered by the anabatic winds, which expands the top layers by bringing fresh air from the valley floor. Different situations will be possible depending on the prevalence of the anabatic winds or the ML expansion. In most cases, a dynamic equilibrium is established in the morning hours.

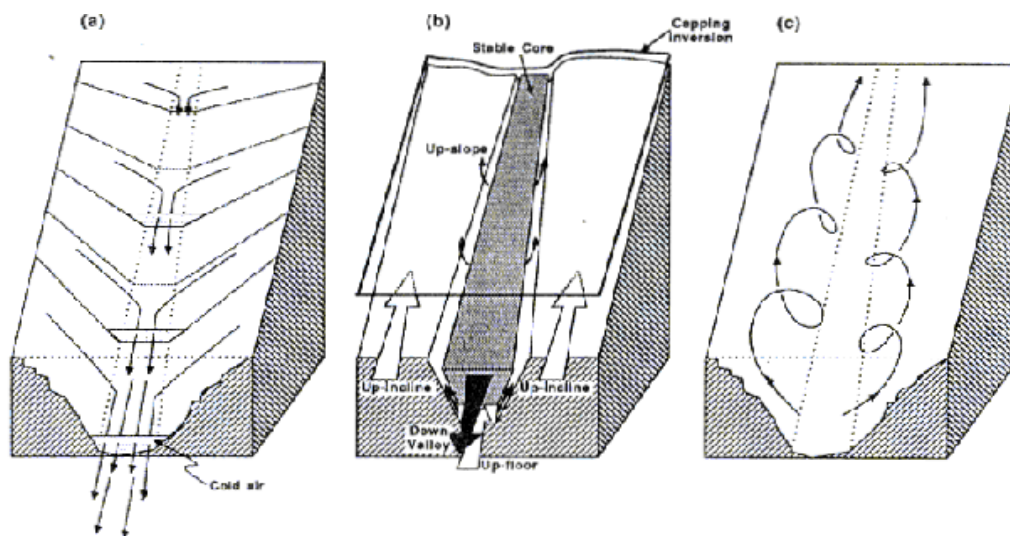


Figure I-12 3D circulation pattern of winds in a valley during the night (a), morning (b), and afternoon (c).

I. Boundary Layer Meteorology

In the longitudinal direction of the valley, a different phenomenon will happen. During the night (Fig. I-13b), a valley wind transports fresh air from the top of the mountains to the plains. A warm return current, flowing in the opposite direction and at a higher level, closes the circulation.

During the day, a mountain wind flows from the plains to the mountains (Fig. I-13a), while a cold return current is present at a higher level, which closes the circulation.

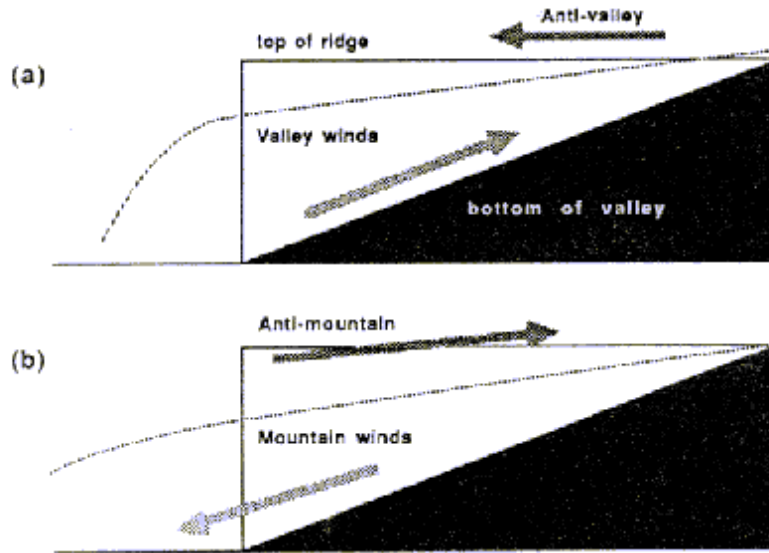


Figure I-13 Valley winds scheme; (a) day; (b) night.

The three-dimensional wind flow which results from the superposition of valley winds with anabatic and katabatic winds, can easily be described during the night (Fig. I-12a): katabatic and valley winds converge at the valley floor and flow downhill, while weak return currents are present.

During the day (Fig. I-12b), the anabatic and mountain winds interact and form a wind shear above the valley floor, while they are involved in a helix circulation pattern later on in the afternoon (Fig. I-12c).

II ***Air Pollution***

Every day, the average person inhales about 20,000 liters of air. Every time we breathe, we risk inhaling dangerous chemicals that have found their way into the air. Air pollution includes all contaminants found in the atmosphere.

This chapter deals about four dangerous substances (ozone, carbon monoxide, nitrogen dioxide and benzene) focusing on their production, dispersion, and showing the limits imposed by rules on their concentrations.

II.1. Air pollutants

With reference to the Italian law (Legislative Decree no. 152 04/03/2006) for air pollution means "Any change of atmospheric air, the same due to the introduction of one or more substance in quantities and characteristics that affect or endanger human health or the environment or quality of such material property damage or compromise the legitimate uses of the environment.". Since atmospheric phenomena occur which alter the natural composition, the term normal has margins of ambiguity.

To avoid this incident, refers to the composition of dry air at sea level, consists mainly of nitrogen and oxygen, other gases are present in insignificant quantities. Alterations the composition of reference may be caused by:

- Natural sources (volcanoes, forest fires, decomposition of organic matter ...)
- Anthropogenic sources (burning hydrocarbons, traffic, etc.); in the last century, due to human activities, was undoubtedly prevailing over the natural one.

Pollutants can be also distinguished according to their origin:

- primary are produced in the combustion process,
- while other pollutants (secondary), produced directly into the BL by the reactions between primary pollutants and air.

The more present and more harmful substances (those on which it is then focused the attention of the legislature to set limits, see table II-1) are:

- CO
- NO₂(gas)
- O₃(ozone)
- Sulfate (particulate)
- Nitrate (particulate)
- Volatile organic compounds

Carbon dioxide, CO₂, while the greenhouse produces no direct damage on living organisms and is not considered among the pollutants.

The choice of the measured parameters was then made by considering two criterias: the first, based on the danger, and the second about the nature of the pollutants. According to these fees, the preference has fallen on the following: carbon monoxide (CO), ozone (O₃), nitrogen dioxide (NO₂), benzene (C₆H₆) as volatile organic compounds.

Carbon monoxide is produced during the incomplete combustion of materials staff. It is a gas poisonous to humans and easily able to infiltrate inside homes and through walls.

II. Air Pollution

Ozone is an extremely reactive gas instead. Also is poisonous and oxidizing for living beings. It is produced mainly during the time when his presence can be felt even with its pungent odor.

Nitrogen dioxide is rather irritating to the airways. May cause cough, but especially when taken for a long time, can cause serious lung damage. It is carcinogen, and is mainly produced by diesel engines.

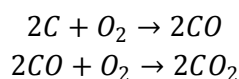
Finally, benzene, founder of aromatic compounds, is in the oil and its derivatives. The atmosphere as a volatile liquid, it is deemed dangerous it facilitates the emergence of some diseases including cancer.

A more detailed description of the main characteristics of the selected pollutants follows.

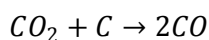
II.1.1. Carbon monoxide

Carbon monoxide is a colorless, odorless and tasteless compound, which is in a gaseous state for temperatures above -192 ° C. The main processes of formation are:

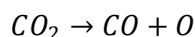
- lack of oxygen in the combustion of carbon-containing compounds



- high-temperature reaction between CO₂ and carbon-containing compounds



- dissociation of CO₂ at high temperature

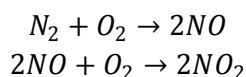


The most important source of CO is motor vehicles powered by gasoline. The removal of the carbon monoxide occurs through the microorganisms present in soil. This mechanism is very limited, due to the presence of surfaces in urban areas, where you have the highest concentrations.

Carbon monoxide interacts with hemoglobin in blood, reducing its oxygen-carrying capacity, thanks to a greater affinity with the organic molecule, producing effects on the central nervous system, heart and lung when its concentration is greater than 100 ppm (parts per million, measured usually in mg/kg).

II.1.2. Nitrogen oxides

Nitrogen oxides (indicated by NO_x) are of biological origin and produced by reactions between nitrogen and oxygen in the air, at high temperatures (above 1210 °C)



The amount of NO produced depends on:

- Combustion temperature, increases of which there was an increase in production and a reduction in training time;
- Duration of the gas in the combustion chamber;
- The amount of oxygen; by decreasing the amount decreases NO production but increases CO production.

During cooling, a portion of the nitrogen oxide (about 10%) interacts with oxygen, giving rise to the nitrogen dioxide which is an active part in photochemical reactions leading to ozone production.

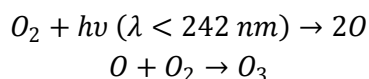
The most significant production of the nitrogen oxides is that even if the bacterial anthropogenic emissions (cars, combustion plants) in limited areas result in high concentrations. The residence time of the nitrogen oxides in the air is because a few days turn into nitric acid (HNO_3) and then into nitrates.

Concentrations of nitrogen oxides, exceeding 13 ppm, can cause irritation of the mucous membranes of the eyes and nose.

II.1.3. Ozone

Ozone is a colorless gas that plays a positive role when it is in the stratosphere by absorbing a large proportion of ultraviolet radiation present in sunlight. Instead, his presence at the ground level has an adverse effect on human health.

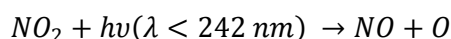
In the stratosphere, ozone is formed as a result of a photochemical reaction in the presence of solar radiation:



A small part of the product penetrates the ozone in the troposphere and is due to the level of background concentration.

Tropospheric ozone is a secondary pollutant produced by photochemical reactions involving the following hydrocarbons and nitrogen oxides emitted mainly by the vehicular traffic. The concentration is not so much in the concentrations of the primary pollutants as weather conditions (solar radiation, temperature, etc.).

The oxygen released by the photochemical reaction



gives rise to a series of reactions involving VOCs producing ozone as well as a number of the compounds (smog).

Ozone is irritating to mucous membranes (eyes, nose, throat and respiratory system) with varying degrees of severity depending on the levels of concentration and exposure time.

II. Air Pollution

Because of its high toxicity may cause adverse effects on the ecosystem is that the historical and artistic heritage.

II.1.4. Benzene and volatile organic compounds

Volatile organic compounds means the set of organic substances in the atmosphere in a gaseous state (acetone, ethyl alcohol, methyl alcohol, benzene, hydrocarbons, etc.).

There are hundreds of compounds that are grouped into families having the same chemical and physical properties.

The negative effects on human health and the concentrations at which these effects occur differ from family to family:

- Aromatic hydrocarbons (e.g. Benzene) irritate the mucous membranes of the airways from a concentration of 25 ppm; a prolonged appearance has a carcinogenic effect;
- Methane and acetylene have suffocating effects;
- Phenols cause digestive problems and nervous system;
- polycyclic have impact on lung cancer.

II.2. Air quality

Pollution linked to anthropogenic effects has experienced a rapid growth since the nineteenth century following the industrial revolution and the exponential population. However, only from the past half century have been introduced rules to limit the adverse effects of pollution on humans, animals, plants and things.

As often happens, the rules were subsequently adopted to catastrophic events that have caused the deaths of many people. All these events have occurred regardless of weather conditions: high pressure, very little wind, height of temperature inversion near the ground. In these situations all the pollutants trapped in very limited areas resulting in high concentrations.

For the assessment of the air quality, the directive⁴, in particular, provides the opportunity to appeal, according to the levels of pollution, not only directly, but also in modeling techniques and objective estimates.

The rules identified (in different ways for different pollutants) different values characteristic:

- (L.P.H.H.) limit values for the protection of human health (or ecosystems or vegetation) level of concentration that should never be exceeded or not exceeded for more than N times in a given period of time (usually one year);

⁴ Ministerial Decree No. 60 of 02/04/2002 , *Transposition of Directive 1999/30/EC of 22 April 1999 relating to limit values for ambient air quality for sulfur dioxide, nitrogen dioxide, nitrogen oxides, particulate matter and lead, and the Directive 2000 / 69/CE on ambient air quality limit values for benzene and carbon monoxide. Remember also the UE directive 96/62/CE for ozone limits.*

II. Air Pollution

- (I.R.) information threshold: a level beyond which there is a risk to human health in case of brief exposure for particularly sensitive sections of the population and at which information must be updated;
- (T.A.) threshold alarm: level above which there is risk to human health from brief exposure of the general population, and at which immediate intervention is necessary;
- (M.T.V.) target values for the protection of human health and the protection of vegetation: limit to be achieved in the medium term (by 2010);
- (L.T.V.) values long-term objective for the protection of human health and the protection of vegetation limit to be reached in the long term (by 2020);

Table II-1 shows the limits, the alarm thresholds and the period within which limit values are to be achieved for different pollutants.

<i>air pollutant</i>	<i>classes</i>	<i>average time</i>	<i>value ($\mu\text{g}/\text{m}^3$)</i>
<i>Nitrogen Oxides</i>	L.P.H.H.	hour	200 (Max 18 exceedings allowed)
	L.P.H.H.	year	40
	T.A.	3 consecutive hours (on 100 km ²)	400
<i>Carbon Monoxide</i>	L.P.H.H.	mobile window 8 hours	10000
<i>Benzene</i>	L.P.H.H.	year	5
<i>Ozone</i>	L.P.H.H.	Moving average over 8 hours on hourly measurements	120 (Max 25 exceedings allowed)
	I.R.	1 hour	180
	T.A.	1 hour	240

Table II-1 Air pollutants concentrations' limits (UE directives: 1999/30/EC, 2000/69/CE and 96/62/CE)

II.3. Dispersion of pollutants

It is very important to underline that the dispersion of pollutants strictly depends by the meteorological conditions; particularly:

- wind speed influences the processes of dry deposition, resuspension, transport to distance of pollutants and the level of turbulence;
- Cloud cover and humidity affects the amount of precipitation and solar radiation reaching the soil;
- Rainfall determines the process of wet deposition;

- The radiation that reaches the ground, as well as the cloud cover, is linked to the presence of aerosols and photochemical reactions and affects the temperature in the atmospheric boundary layer;
- The temperature trend in the atmospheric boundary layer determines the degree of stability, then the height of temperature inversion;
- The level of turbulence is related to wind speed, atmospheric stability, the Site topography and roughness of the soil and affects the transport processes and dispersion.

Using a mathematical model for the dispersion of pollutants (Leuzzi, et al.) is possible to:

- Assess concentrations even in areas where there are no monitoring stations
- Evaluate the impact of a single source to obtain the relationship between emissions and concentrations in defined points
- Designing a rational monitoring network
- Predict the effects of different issues from those in place

The evaluation of the average concentration or probability that the concentration exceeds a certain threshold is related to the climatic characterization of the site in question or the knowledge of the probability that a given weather conditions. So the use of dispersion models requires a priori knowledge of the meteorology of the study area in terms of temperature, humidity, average speed and intensity of turbulent wind.

This scenario shows how it is important to collect meteorological data; the review of published literature of the next chapter will show how this is critical in to Mediterranean Cities.

III Bibliographic Review

Several field studies on boundary layer meteorology have been published in the scientific literature in the past fifty years, and the whole field of micrometeorology itself relies heavily on field data to validate proposed theories and computer codes. It is important to remark the dominance of boundary layer phenomena on the dispersion of pollutants: achieving a good knowledge of these phenomena is critical to understand the dispersion mechanisms.

Even if land/sea breezes, Urban Heat Islands and valley and slope winds have been extensively studied one by one, their interaction has not been fully understood and described, standing to current literature.

This gives further motivation to an experiment campaign to be organized in a Mediterranean urban area, intrinsically characterized by the presence of all together phenomena.

As reported by the field study, aerostats have demonstrated their validity in providing accurate measurements of atmospheric quantities over vertical profiles; in spite of the importance they play, no author has been founded publishing vertical profiles of air pollution and simultaneously complete turbulence characterization (Energy spectra and statistics), useful to study pollution dispersion, especially during nighttime.

The chapter is divided in three parts:

- *A brief overview of the micrometeorological research about UHI, sea/land breeze and valley flows;*
- *Articles about the characterization of atmospheric turbulence, particularly over cities;*
- *Experiments using kytoon station to collect vertical profile data.*

III.1. Micrometeorology research (UHI, sea breeze, valley flows)

There are a lot of study about micrometeorology effects, particularly about UHI, breezes [e.g. (Finkele, 1998), (Hinkel, 2003), (Winston Jeeva, 1992), (Edmilson, et al., 2007), (Shafran, 2000), (Weber, et al., 2010), (Roulet, 2004), (Sailor, 2007)]. Here we remember those cited in chapter I: Oke, the discoverer of the BL overlaying the UHI (Oke, 1971), and the review work by Arnfield, that focalizes the attention on urban climatology as published on *International Journal of Climatology* from 1980 to 2000 year, emphasizing the aspect about UHI, turbulence and exchanges of energy and water in city (Arnfield, 2003).

As said by Arnfield: “Mediterranean climates seem to have been particularly well served by heat island studies during the period...” of analysis but the cited authors, to reinforced this sentence, deal about only the effects of UHI, without no implication of sea breeze or slope winds.

The flow structure on a gentle slope at Vallon d’Ol in the northern suburbs of Marseille in southern France has been documented by means of surface wind and temperature measurements collected from 7 June to 14 July 2001 during the ESCOMPTE experiment (Bastin, 2005). The author tries to foresee numerically the combine effect of UHI, slope wind and sea breeze but she doesn’t validate the results with any profile measurement of meteorological quantities and neither considers the air pollutions dispersion mechanism.

This work, in spite of its limitation, is a good first attempt because the most of the authors focused only on one of the aspect of the micrometeorological phenomena as Tijn, who used wind profiler to investigate the vertical structure of the sea breeze with the accompanying return current at the North Sea coast in the Netherlands (Tijn, 1999). “The coastline of the Netherlands is nearly straight and orography is almost absent...Therefore the sea breeze can be studied almost in a pure form, undisturbed by orography and inhomogeneous vegetation cover”.

The last review (Crosman, 2010) about sea and land breezes, numerically studied, by Crosman, joint with the review work of Salmond (Salmond, 2005), about turbulence in the very stable nocturnal boundary layer and its implications on air quality, show that the attempts to integrate in a single model all the micrometeorological effect are increasing; the will to validate the numerical results led to the necessity of more and more experiments, particularly modeling turbulence over cities.

The following section makes a brief overview of the state of art about atmospheric turbulence researches.

III.2. Overview of atmospheric turbulence studies over cities

A good review of atmospheric turbulence over cities is provided by Roth (Roth, 2000). More than fifty studies are analyzed; no author has been founded studying completely turbulence statistics profiles with high accuracy and frequency (more than 20Hz) using kytoon station. As we will see in the following section only Ogawa (Ogawa Y., 1986) and Ohara (Ohara T., 1989) publish eddy fluxes and standard deviations of turbulent components (u' , v' , w' , θ'), but no

III. Bibliographic Review

spectra are reported in their respective works. In table III-1 are reviewed some authors, not cited by Roth, that have studied some atmospheric turbulence characteristics.

<i>References</i>	<i>City-Site</i>	<i>z [m]</i>	<i>Statistics reported</i>	<i>Sensors & frequency</i>
Rudolf (1999)	-	25	u_* (definition)	Sonic anemometer 20Hz
Van der Hoven (1957)	USA	91-108-125	fS_u (plot semilog)	Sonic anemometer 0.25Hz
Burns (1964)	U.K. and N. Africa	30-490	$fS_{u,v,w}$ (plot loglog)	Airplane
Busch (1968)	Vancouver, Hanford	Tower 15-320	$fS_{u,v,w}/u_*^2$ (plot loglog)	Sonic, hot-wire, thrust, thermistor anemometer; heated thermocouples wires.
Kaimal (1972)	Kansas	Tower (32m): 5.66-11.3-22.6 (T); 2-32 (8 level mean wind)	Non dim Spectra, cross spectra: u', v', w', T'	Sonic, cup and hot-wire anemometers, platinum wire thermometers
Grachev (1993)	Coastal zone of Black Sea	Tower (12m above s.l.)	$fS_{u,v,w,T,Hu}$ (loglog also non dim.)	0.01-10Hz
Kaiser (1997)	Karlsruhe university	Wind tunnel	Turbulence spectra: u', v', w', T'	Laser Doppler
Hogstrom (2001)	Lövsta (Sweden) et alii.9 sites.	1.5-30	Theory for turbulence spectra	
Jiboori (2001)			$fS_{u,v}/u_*^2$ (over different ground)	
Zhang (2001)	Gobi Desert Grassland Suburban urban	4.90 3.45 43-75 47	$\sigma_{u,v,w}/u_*$ function	Sonic anemometer, platinum wire thermometer
Hiyama (2005)	Loess plateau	2-12-32	$fS_{u,v,w}/u_*^2$	Ultra-sonic anemometer, gas analyzers, 10Hz

Table III-1 Review of atmospheric turbulence over cities.

Some authors focus the attention on friction velocity: this parameter, used by numerical modeler to characterize the small scales near the ground, is very variable with surface roughness, changing deeply over cities (Zhang H., 2001).

Except for Burns (Burns, 1964), using measurements of turbulence by an airplane, no authors make vertical representation of turbulent statistics and spectra at high altitude or with more

vertical measurements. Moreover the maximum sampling frequency detected is about 20Hz (Weber, 1999) limiting the study of the smaller scales of motion.

III.2. Experiments using kytoon station

Follows the description of the founded research project using a kytoon station as atmospheric characteristics profiler. It can be noted that authors don't publish turbulent spectra and vertical profile of any air pollutant.

III.2.1. Wallops "Aeropalynologic Survey Project"

In 1966 the "Aeropalynologic Survey Project" (Silbert, 1967) was conducted at the Wallops Flight Center by NASA. The project had the purpose to monitor the presence of pollutants at various heights above the ground. This was one of the first field experiments using kytoons in micrometeorology.

In the summer of 1966, three helium-filled kytoons were used to lift various pollution sensors. The sensors were adhesive slides fixed to Teflon tubes, which in turn were positioned on the tether lines at several heights.

Single braid nylon tether lines were used because of their good elastic response, and the connection system between the tethers and the kytoons consisted in swiveling joints and simple knots.

Three small kytoons, instead of a bigger single one, were used to reduce the loss of lift due to the permeability of the kytoons' envelopes to helium. A check on the state of the kytoons was necessary every 12 hours.

The experiment was successful in collecting the required measurements and demonstrated the viability of the kytoon as a pollution sensor station, even if it presented some management issues.

III.2.2. Boulder Observatory Experiments

Situated near the city of Denver, Colorado; the atmospheric observatory of Boulder greatly increased the comprehension of several pollutants dispersion mechanisms since its opening in 1978 (Schotz, 1980).

The main sensor platform was a tower 300 m high, on which a complete sensor array was placed. Aircraft and kytoons were used occasionally.

The data harvested by the observatory was used to develop the first mathematical-statistical models of the dispersion of pollutants, which brought to partially correct predictions.

III.2.3. Observation of land sea breeze in Tokyo, Japan

The penetration of land sea breeze front and its turbulence structure was good observed at the center of the Tokyo metropolitan area on 27-28 January 1983 by (Ohara T., 1989). The meteorological data were obtained by three independent instruments: a big kytoon, a small tether-sonde and an acoustic sounder. (Ogawa, 1982) The first was about 70m³, has an available lift of approximately 20 to 30kg and lifted instrumentations up to 1000m height. The sensor package (10kg heavy) could measure instantaneous velocity (u, v, w), instantaneous temperature, wind direction, mean potential temperature, humidity, pressure, and temperature

III. Bibliographic Review

gradient, see table III-2. The sampling frequency was 10Hz and all data, included that of inclination (pitch, yaw), useful to correct wind data, were transmitted via an optical fiber cable system (1500m long) and then recorded by digital magnetic tape recorder. In addition, a Teflon pipe, attached to tethering wire, sampled ambient air, to measure vertical profile of NO and NO_x. The small tether-sonde instead measured the vertical profiles of wind speed and direction, temperature, relative humidity, and oxidant concentration (O_x) from the ground to 600m height.

During this experiment land breeze velocity have been measured end their relative inversions; the results show that the penetration of the front is strongly correlated with the appearance of severe air pollution in urban area during nighttime. However, Ohara writes: “[...] to clarify the formation mechanism of such high air pollution phenomena, more extensive field studies including turbulence measurements must be conducted”. The influence of valley winds in these phenomena has not been clarified.

Item	Method	Range	Sensitivity	Accuracy
Longitudinal Velocity	Ultrasonic anemometer	+/- 20 m/s	0.005 m/s	0.01 m/s
Lateral velocity	Ultrasonic anemometer	+/- 20 m/s	0.005 m/s	0.01 m/s
Vertical velocity	Ultrasonic anemometer	+/- 20 m/s	0.005 m/s	0.01 m/s
Temperature	Ultrasonic anemometer	-10 / +40°C	0.025°C	0.05 °C
Wind direction	Magnetic-photo encoder	0 /360 °	360°/256	5°
Mean temperature	Transistor Thermometer	+/- 50°C	0.05°C	0.3 °C
Humidity	High polymer sensor	30/90 % RH	0.1% RH	4% RH
Inclination (Yaw)	Pendulum inclinometer	+/- 5°	0.1°	0.5°
(Pitch)	Pendulum inclinometer	+/- 5°	0.1°	0.5°
Pressure	Dual-chamber barometer	650/1050Mb	0.5mb	1.2 mb
Velocity Gradient	Photo pulse cup anemometer	+/- 2.5 1/s	0.0025 1/s	0.005 1/s
Temperature Gradient	Thermocouples	+/- 2.5 °C/m	0.0025 °C /m	0.005°C/m

Table III-2 Characteristics of sensors (Ogawa, 1982).

During the *Nanticoke II shoreline diffusion experiment* the turbulence kytoon described above was used by the same team research (Ogawa Y., 1986) to observe the lake breeze penetration and subsequent development of the thermal internal boundary layer .The study were carried out in Canada near lake Eire, during the first two weeks in June, 1982.

III.2.4. ASCOT Field Study

During September and October of 1984 W.E.Clements et al., under ASCOT (Atmospheric Studies in Complex Terrain) program (Clements, et al., 1989), conducted an intensive field study in the Brush Creek Valley (western Colorado) to enhance the understanding of pollution dispersion transport and diffusion associated with valley flows. Data collections were designed to investigate nocturnal and morning transition wind, turbulence, and temperature fields in the valley, in its tributaries, and on its side-slope, and how these were affected by the free stream condition above valley. A tethered balloon was used to collect wind velocity and direction, using a small lightweight ultrasonic anemometer, temperature, wet-bulb temperature, and pressure altitude from the ground up to 800m of altitude. All data were acquired with a sampling rate of 18Hz and transmitted to a ground receiving station by an optical fiber cable. An on board AHRS corrected data for pitch and yaw.

III.2.5. Polar Experiments

In the Weddell Sea region of coastal Antarctica, during January and early February of 2000, A.M.Rankin and W.Wolf showed the difference in aerosol composition with height using, for first time, only a kytoon station (Rankin, 2002). A 11.32m³ blimp, 7m long supplied by Cameroon Balloons hoisted lightweight sampling system until 300m of altitude, with raising and lowering speeds of little over 1m/s. A spectra line, 3mm in diameter, was used as the tether because it has a good strength-to-weight ratio. The lightweight (2274g) meteorological sonde included pressure sensor, a small platinum resistance thermometer element, a cup anemometer and a compass sensor to give wind direction. Data were telemetered back by a VHF radio link to a laptop computer on the ground. The power was supplied by a PP3 battery (9V, 45g) and four Lithium ion batteries (10.8V, 439g). The number of flights (12) was restricted by the suitable weather windows; the blimp manufacturer recommended a maximum wind speed of 12 m/s, although in practice it was not flown in ground-level winds of greater than 8 m/s. The duration of each flight was of 4 h.

This study has highlighted that air masses in Antarctic have very different aerosol composition compared to those sampled at ground level; in fact aerosol is not well mixed in troposphere.

Between 29 June and 26 August 2001 an other polar experiment (in high Arctic) with tethered balloon were deployed (Tjernstorm, 2001). Alongside a Sodar system, a meteorological tower and other instrumentations, a kytoon was used to lift up to 200m three type of payload: a basic one for mean profiles of temperature, humidity and wind, a second for turbulence and finally a simplified aerosol package. The experiment was motivated by the need for a better understanding of the effects boundary-layer processes on atmospheric chemistry and aerosol processes relevant for the formation of low-level Arctic clouds but also provided new data to validate numerical simulations in that area.

The polar experiments have been a good guide line to the design of the kytoon.

III.2.6. Lower Fraser Valley Experiment

During summer of 2001 A.Maletto et al. tested a commercial miniature particle mass spectrometer against standard gravimetric and optical instruments studying profile of particulate matter (Maletto, 2003). A 5m³ helium kytoon hoisted night/daytime to 1000m the instrumentation. The mini-aerosol-spectrometer, suspended approximately 1m below balloon, recorded data in on board memory card every 2 minutes and a tether-sonde, slug immediately

III. Bibliographic Review

below, acquired and transmitted to a ground station, every 10s, the standard meteorological parameters (wind speed and direction, temperature, humidity and pressure). The two experiment sites were both located in the Lower Fraser Valley, in British Columbia (Canada), where pollutants' dispersion were conditioned by land–sea breeze and valley/slope winds.

In this scenario fine material tends to be well mixed vertically during daytime whereas coarse material tends to be found close to ground; instead the night-time case is more complex. In the stable nocturnal boundary layer all size classes tend to be trapped near ground.

However Maletto says: “Further research is required to investigate the role played by such layers and the extent to which they may be mixed to the ground”.

IV Kytoon Station Description

The development of a kytoon station depends mainly from the selection of the sensors (section IV.3) that must satisfy such experimental requirements (as the measurement of wind speed vector, its turbulent spectrum and statistics, the virtual potential temperature, the concentration of the selected pollutants, all in their typical ranges, with some accuracy and with suitable sampling frequency and resolution; section IV.2).

Size, weight and the functional mechanisms of the sensors are like a guide line to design the gondola (that integrates and hosts all the sensors and subsystems; section IV.4.2), consequently and parallel they help to choose the aerostat (section IV.4.1) and the ground trailer (that allows the transportability of all the kytoon station; section IV.4.3).

IV.1. Selection of Sensor Station

The characteristics and the evolution (in time and space) of BL in presence of UHI, of sea breeze and valley flows, and the pollutions can be well monitored by the vertical profiles of:

- direction and intensity of wind velocity vector;
- static pressure;
- static temperature;
- relative humidity;
- concentration of CO, O₃, NO₂, C₆H₆.

In atmospheric measurements mainly two kinds of sensor platform exist: **direct** and **remote**. Direct sensor platforms make in situ measurements at a given location, whereas remote sensors measure wave signals that are generated or modified by atmospheric phenomena at some distance away (Tropea, 2007).

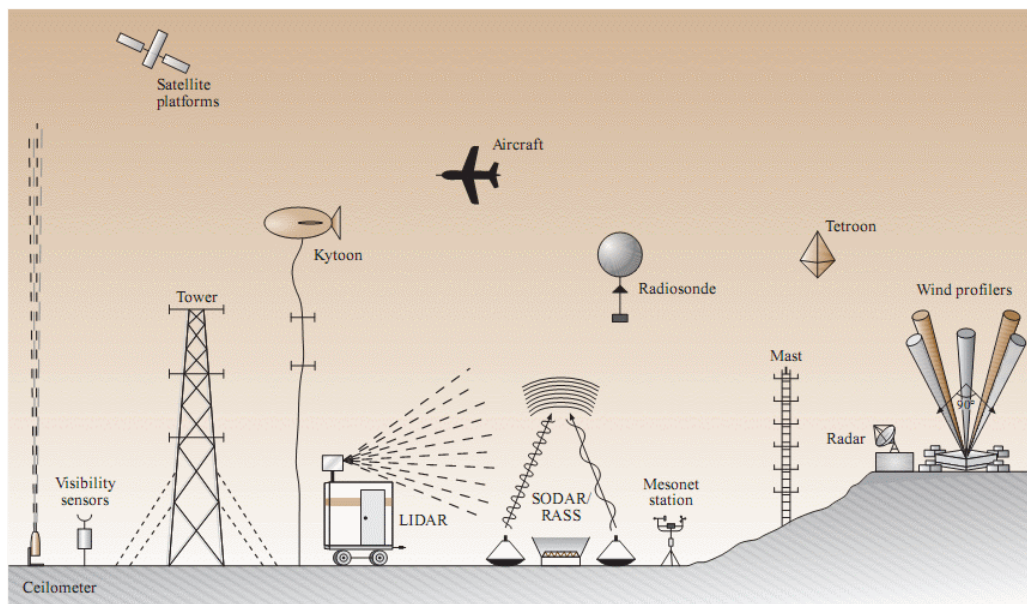


Figure IV-1 Typical atmospheric flow sensor deployment in a field campaign.

Both types have different advantages and disadvantages:

- Direct sensings have high space-time resolution, but they also modify local wind fields to yield potentially unrepresentative point values.
- Remote sensing offers wide-area coverage and physically nonintrusive measurements which are often more cost-effective than the direct ones, but usually their spatial resolution is limited and they may require convoluted calibration techniques.

IV. Kytoon Station Description

Since the research project on the dispersion of atmospheric pollutants needs accurate measurements, especially of vertical profiles of atmospheric quantities, it is evident from the beginning that remote sensors cannot be used in the planned experiment campaign. This because, while they offer the possibility of acquiring data over a large area, the accuracy of the measurements is not sufficient for the data to be used. In addition, many remote sensors encounter difficulties in detecting micro scale weather structures generated by the peculiar characteristics of the Urban Heat Islands.

The choice then relapses on direct sensor platforms. It is then appropriate to review the main direct sensor platforms (Fig. IV-1):

- **Masts and towers:** they are used to place point instruments at various heights. There are different types of sensors associated with masts and towers, of which the most interesting ones for the aim of the project are: anemometers (sonic, cup, hot-wire and vane), thermometers, barometers, hygrometers, and pollutant sensors. However, this kind of sensor array is permanently fixed at one location, and so it only returns point measurements at various heights. In addition, the flow around the mast/tower can be disturbed by the building itself, and obtaining vertical profiles of atmospheric quantities is difficult due to the large number of instruments that would have to be placed on the tower. The height of the measurements is also limited by the height of the structure, and building even a relatively simple meteorological mast can be quite expensive.
- **Mesonet stations:** they are portable stations which can measure multiple variables such temperature, humidity, rain, pressure, radiation and turbulent flux at 2 m and 10 m height.
Being portable, their measurements can cover a large area, even if not at the same time. However, they are confined to ground measurements.
- **Kytoons:** they are a particular kind of tethered aerostat which has hybrid characteristics between those of a kite and of a tethered balloon; The configuration “kite + balloon” is simply called “kytoon”: a kytoon stays in flight by using the Archimedean lift generated by the lifting gas, but can soar in wind currents like a kite thanks to control surfaces joined to the envelope, while staying in position thanks to its tethering. A wide choice of sensors can be suspended under the kytoon at an appropriate height, or various sensor packs can be fixed to the kytoon tether line at intervals. A kytoon offers the possibility to acquire continuous vertical profiles (Profile mode) of data during the ascent/descent due to its very nature or operate also as tower, acquiring data at fixed altitude intervals. In addition, a kytoon can flight up to a height of 1000 m, it is relatively cheap and it can be launched from a mobile launch platform, permitting to acquire data over an area large.

The good characteristics, demonstrated also in field experiments (see chapter III) , jointly with the development of newest and most performing sensors, determined the choice of Kytoon station for the research target.

IV.2. Sensor Requirements

The development of a kytoon station starts from the selection of a suitable sensor, which depends strictly by four factors:

- ranges of the measurements;
- resolution;
- accuracy;
- sampling frequency.

The typical range of wind velocity's intensity can be fixed by:

- the knowing of the more general PBL's characteristics, particularly in presence of only one local effect (sea breeze [1-7] m/s, valley flows [1-5] m/s);
- analyzing (if available) the meteorological data provided by ground stations near launch site;
- analyzing the experimental data recorded in similar conditions, such as Ohara (Ohara T., 1989) and Ogawa (Ogawa Y., 1986)[1-6] m/s.

A good range of analysis for the present study would be [1-10] m/s but a more preferable is [0 20] m/s, in order to foresee the possibility of gusts and nocturnal jet, eventually occurring during night flight. A three dimensional measurements of wind speed is necessary to know its horizontal and vertical components. High frequency of time sampling (10Hz or higher) and 0.001m/s of resolution allows to capture the turbulent fluctuation velocities and the calculation of their turbulent spectra and statistics, as the standard deviations, cross-correlations, Turbulent Kinetic Energy (TKE). An accuracy of 0.01m/s is enough to estimate the module of mean wind.

Variations of the temperature between 0 and 40°C are expected in a typical Mediterranean city while the humidity can reach in particular case 98%. A sampling frequency close to that of wind measurements would be preferable since the will to calculate particularly temperature's spectra, co-spectra between wind and temperature, and also the cross-correlations of their fluctuation components (resolution of 0.01°). Accuracy of 0.5°C would be preferable in temperature measurements, in order to evidence the thermal excursion of UHI.

Static pressure measurements can be used both to calculate potential temperature (the sampling rate must be the same with which you acquired the temperature) and to good provide altitude (precise altitude can be obtained with high accuracy and resolution) even if is subjected to weather change.

The measuring range of air pollutants is only lower constrained (absence of pollutant) since the upper limit can change deeply because of the time and the monitoring location. However, you can steer using, as appropriate, the values set by the UE directives 1999/30/EC, 2000/69/CE and 96/62/CE (see table II-1, section II.2): these values in fact are averaged on such period as year or hours and they can't be directly used, because they don't consider any possible oscillation over the top. Consequently it have been fixed enhance factors to all them so that the measuring ranges are [0-100] mg/m³ (CO), [0-500] $\mu\text{g}/\text{m}^3$ (O₃ and NO₂) and [0-100] $\mu\text{g}/\text{m}^3$ (C₆H₆). Desirable resolutions would be 0.1 $\mu\text{g}/\text{m}^3$ (O₃, NO₂, C₆H₆) and 0.1 mg/m³ (CO).

IV. Kytoon Station Description

In order to calculate good vertical profiles, all the sensors' measurements must be collocated in time and space. If they are placed close, the instantaneous position (Latitude Longitude and Altitude) of them can be fixed respect to the World Geodetic System 84 (WGS-84) using a Global Positioning System (GPS). More than an accurate spatial (vertical and horizontal) resolution (estimated for the best devices in the order of less than one meter), a good measurement of the speed in the WGS-84 is very useful to carefully calculate the wind vector in the Nord-East-Down (NED) reference system: in fact we must observe that a 3D anemometer measures three velocities' components in its own reference system that, subjected to the kytoon movement, can rigidly translate but also rotate respect to the NED one.

NED reference and the attitude of anemometer's reference system can be obtained via an Attitude and Heading Reference System (AHRS) platform, using three magnetometers (fixing magnetic Nord), three gyroscopes (accurate measure of angular position and velocity) and three accelerometers (identifying local vertical).

Finally, together with the requirement defined below, there are two other very important ones in the design of any aircraft:

- weight
- size

Small and light sensors are obviously preferable.

IV.3. Sensors and Subsystems

The sensors that best has fitted the requirements are:

- ✓ *Gill-Windmaster*, 3D sonic anemometer;
- ✓ *Vaisala-HMP50*, thermo-hygrometric probe;
- ✓ *UniTec-Sens3000*, thick film solid state sensors for environment;
- ✓ *Sbg systems-IG 500N*, miniature Inertial Navigation System (INS) with integrated barometer.

These instruments must be aided by the following support systems:

- ✓ *Vortex86*, on board *XLinux* computer;
- ✓ *Datex-MUX 3017*, multiplexer;
- ✓ *ACCULi-Ion* battery
- ✓ *BeeLine-APRS* (Automatic Reporting Position System).

IV.3.1. Gill Windmaster – 3D Sonic Anemometer

The *Gill WindMaster* anemometer is an ultrasonic anemometer which senses the speed of the flow from the difference in the times of flight of ultrasonic pulses which are generated by the transducers (Fig. IV-2).

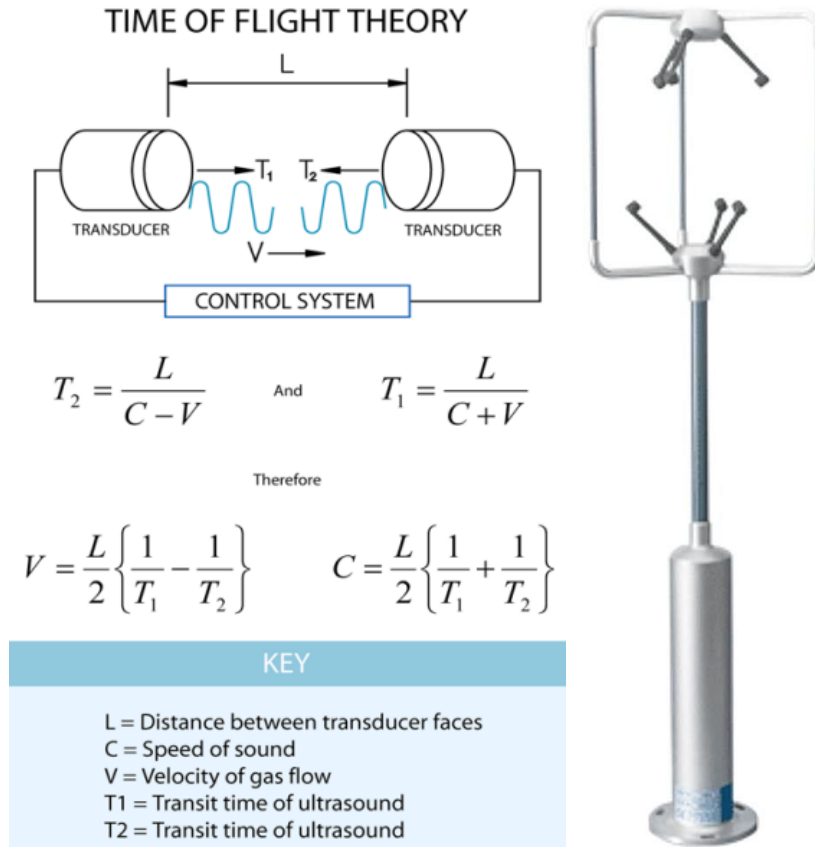


Figure IV-2 Scheme of operation (left) of the *Gill WindMaster* anemometer (Right).

At the same instant, the two transducers emit an ultrasonic pulse each. If a wind speed component on the line of flight is present, the two pulses will cover the flight path in different times of flight. By comparing these times of flight, the on-board systems of the anemometer can extract both the speed of the flow and the speed of sound of the gas. The last one allows the calculation of the sonic temperature (the formula does not account for the Humidity):

$$T^* = C_1^2 \cdot 403 \quad (\text{IV.1})$$

The anemometer does not need a calibration before being used, since it is already executed by the supplier. It has a top operating wind speed of 45m/s. The declared resolutions regarding velocity |direction (see appendix A) are: 0.001m/s | 0.1° with an accuracy of less than 1.5% RMS|2°. The velocity components are respect to the Cartesian reference system of figure IV-3; a reference spar on the mounting flanges identifies U^+ direction (Fig. IV-4).

The selected data output rate is 32Hz.

The body of the anemometer is of aluminum/carbon fiber construction, which guarantees a low overall weight of 1kg; the dimensions are 750 mm (height) x 240mm (max diameter) and the power absorbed is low with 55mA required at 12Vcc.

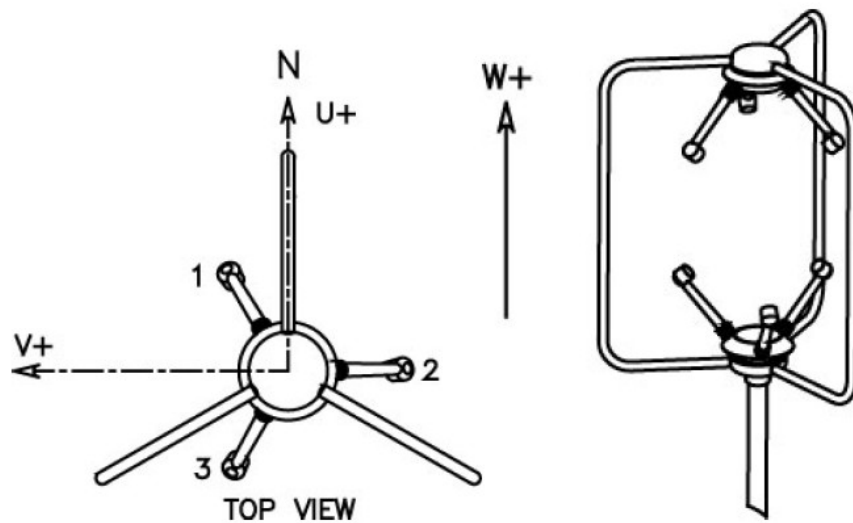


Figure IV-3 Cartesian *WindMaster* reference system of velocities.

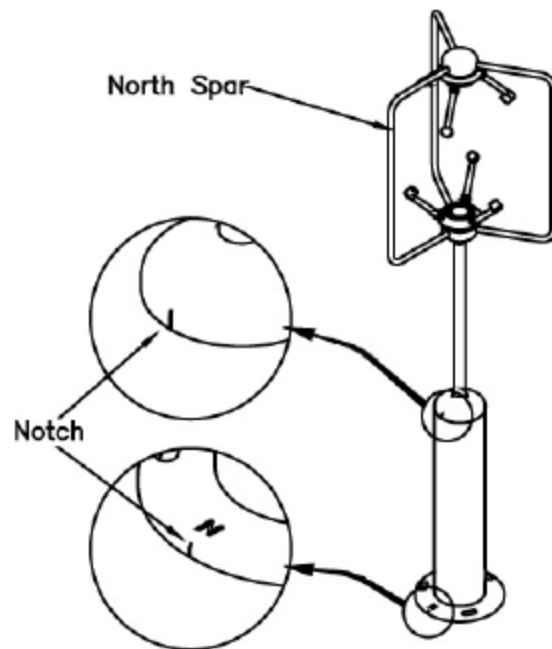


Figure IV-4 Notches identifies the North Spar (U^+ direction of the cartesian *WindMaster* reference system).

IV.3.2. Vaisala HMP50 – ThermoHygrometer

The HMP50 is a small, lightweight, and low-power absorbent temperature and humidity probe, which makes it suitable for integration in the payload.

The probe is capable of measuring relative humidity (RH) in the 0-98% range, and air temperature in the -10°C - $+60^{\circ}\text{C}$ with a resolution of 0.01° (see appendix A). The Accuracies are 0.6° (at 20°C) and 3-5% (in the ranges 0-90% and 90-98%).



Figure IV-5 Vaisala HMP50 temperature and humidity probe.

Its body is in chrome coated aluminum (Fig. IV-5), and the sensor is protected by a membrane filter and plastic grid. Its total weight is 25g, including the 0.3 m cable. It absorbs 2mA in the 7 to 28Vcc range. Its overall dimensions are 71 mm (length) x 12 mm (diameter).

The sampling rate is 0.2Hz.

IV.3.3. UniTech-Sens3000 – Air pollution sensor

The SENS3000 sensors consist in a series of solid state, thick film, sensor cells, each capable of measuring the atmospheric concentration of one of the following gases: CO, NO₂, O₃, C₆H₆.



Figure IV-6 UniTec SENS3000 pollutants sensor.

The sensible surface of the sensor is a semiconductor oxide made of nano-particles of the size of 200 μm . The first reaction which happens on the surface of the sensor is the absorption of the atmospheric oxygen and the consequent charge transfer from the semiconductor to the oxygen molecule. The second reaction is related to the specific gas to be measured, which while linking to the oxygen molecule allows the electrons to be released in the conduction band of the semiconductor. Taking the current signals from the sensor, the direct concentration of the specific gas in atmosphere can be measured. Selectivity and precision are reached using special semiconductor oxides with appropriate filters.

The output analog signal from the sensor needs to be converted into concentration using a known function.

Each sensor cell measures the concentration with a precision of less than 2% of the full scale, with the operational range varying for the various gases (see Tab. IV-1).

IV. Kytoon Station Description

<i>Mixture</i>	<i>Range (at 0°C ,1 atm)</i>	<i>Accuracy</i>	<i>Resoluti on</i>
Carbon monoxide (CO)	0-100 mg/m ³ 0-80 ppm	+/- 0.5 mg/m ³	0.1 mg/m ³
Nitrogen dioxide (NO ₂)	0-500 µg/m ³ 0-400 ppb	+/- 10 µg/m ³	0.1 µg/m ³
Ozone (O ₃)	20- 500 µg/m ³ 10- 200 ppb	+/- 10 µg/m ³	1.0 µg/m ³
Benzene (C ₆ H ₆)	0-100 µg/m ³ 0-30 ppb	+/- 1 µg/m ³	0.1 µg/m ³

Table IV-1 Ranges, Accuracy and Resolution of Sens3000 sensors.

The input of the sensor cell is 150 mA at 12Vcc, while the output ranges from 0 to 5 Vcc. Each sensor cell weighs 220 g, and the sensor pack is contained inside an anodized aluminum cylindrical enclosure. Each cell measures 55 x 94 mm (more details in appendix A).

IV.3.4. *Sbg Systems IG 500N – Navigation System/Barometer*

The IG-500N is the world smallest GPS enhanced Attitude and Heading Reference System (AHRS). It includes a MEMS based Inertial Measurement Unit (IMU), a GPS receiver and a pressure sensor, providing precise drift-free attitude and position (Fig. IV-7 left).

This miniature (36x49x22mm, only 46g heavy) Inertial Navigation System (INS) runs a real time Extended Kalman Filter (Fig. IV-7 right) that computes orientation, position and velocity data at high update rates, up to 100 Hz.

The attitude accuracy is also improved, compared to traditional AHRS, by removing transient accelerations measured with the GPS receiver.

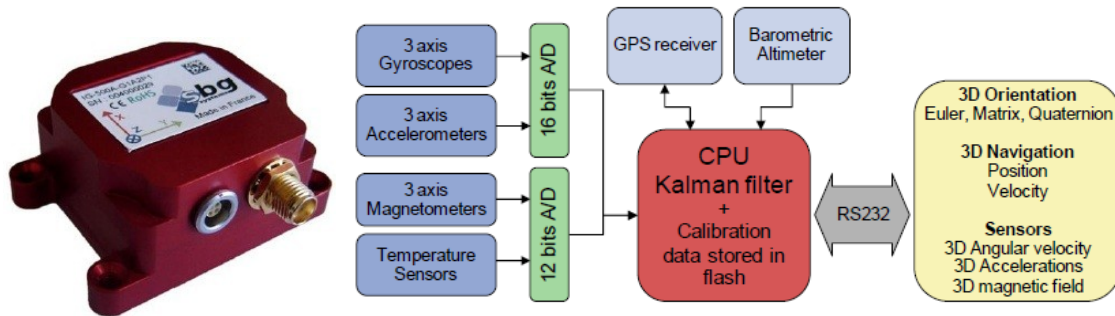


Figure IV-7 Sbg IG 500N INU (left); Block diagram of the Kalman filter integration (right).

A lot of data can be get connecting, via an USB interface, the device to a PC and installing the *SbgCenter* software, or using the low level protocol communication (Embedded CPU board application).

Table IV-2 shows the selected data (output mask, see appendix C): the first column is the name used by the low level protocol to identify a specific output data; the second gives its brief description.

Details (measurement resolutions, accuracies and other information) about the device are in appendix A and in the user manual.

<i>Low level protocol Item</i>	<i>Description</i>
SBG_OUTPUT_GPS_POSITION	Raw GPS position (WGS84): latitude [10^{-7}°], longitude [10^{-7}°], and altitude [mm above ellipsoid].
SBG_OUTPUT_GPS_INFO	UTC timer [ms], number of satellites.
SBG_OUTPUT_GPS_NAVIGATION	Raw GPS 3D velocities [cm/s] (local NED reference).
SBG_OUTPUT_GPS_ACCURACY	Raw GPS Position accuracy (horizontal e vertical) [mm]; velocity accuracy [cm/s]; heading accuracy [$^\circ$].
SBG_OUTPUT_EULER	Euler angle [rad] between device and local NED references (roll, pitch, e yaw).
SBG_OUTPUT_GYROSCOPES	Gyroscopes calibrated (Kalman, no BIAS errors) values [rad/s] around device reference.
SBG_OUTPUT_TIME_SINCE_RESET	Time since last reset of the device [ms].
SBG_OUTPUT_BARO_PRESSURE	Absolute pressure [Pa].
SBG_OUTPUT_POSITION	Calibrated (Kalman) position (WGS84): latitude [$^\circ$], longitude [$^\circ$], and altitude [m above ellipsoid] .
SBG_OUTPUT_VELOCITY	Calibrated (Kalman) 3D velocities (device reference system) [m/s].
SBG_OUTPUT_NAV_ACCURACY	Position [m] and velocity [m/s] accuracies (Kalman filter).
SBG_OUTPUT_TEMPERATURES	Internal and external device's temperature [$^\circ\text{C}$].

Table IV-2 IG 500N : used output mask (data format in appendix C).

The output data are classified as:

- **Control parameters**; they are used to verify acquisition operation:
 - SBG_OUTPUT_GPS_POSITION
 - SBG_OUTPUT_GPS_INFO
 - SBG_OUTPUT_GPS_ACCURACY
 - SBG_OUTPUT_GYROSCOPES
 - SBG_OUTPUT_VELOCITY
 - SBG_OUTPUT_NAV_ACCURACY
 - SBG_OUTPUT_TEMPERATURES
- **Navigation parameters**; they are used to localize in space and time the measurements of the other kytoon sensors and to correct anemometer's data:
 - SBG_OUTPUT_GPS_NAVIGATION
 - SBG_OUTPUT_EULER
 - SBG_OUTPUT_TIME_SINCE_RESET
 - SBG_OUTPUT_BARO_PRESSURE
 - SBG_OUTPUT_POSITION

The device coordinate system is shown in figure IV-8. Note that the Euler angles are between this reference and the local NED one, which X axis is aligned with magnetic North (Fig. IV-9).

IV. Kytoon Station Description

True Nord can be obtained setting the value of the magnetic declination (function of date and location), is calculated via external software (we used *GeoMag* www.resurgentsoftware.com/geomag.html).

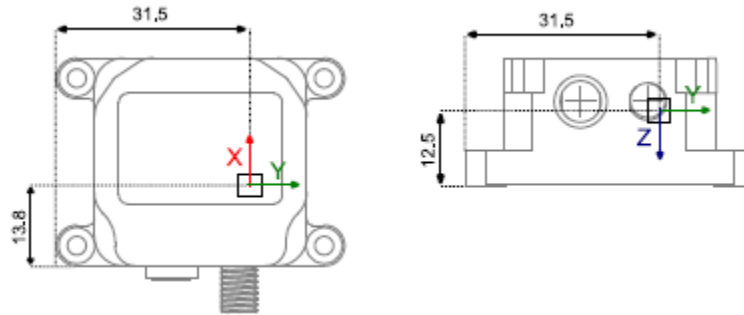


Figure IV-8 IG 500N : Physical location of the 3D accelerometer (device coordinate system); dimension are in mm.

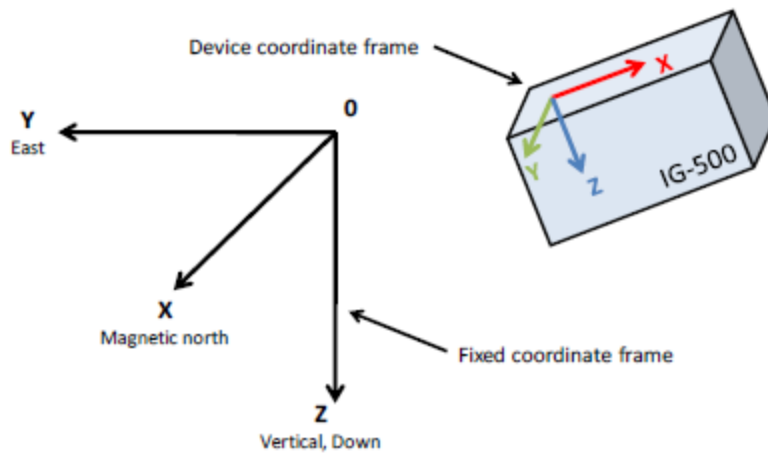


Figure IV-9 IG 500N: Representation of the sensor in the fixed coordinate system (NED).

Other configuration parameters of the INU are:

- The gravity constant;
- The lever arm: the raw GPS position and velocities are that of the GPS antenna; it is possible to set the distance between the device coordinate origin and the antenna;
- The output frequency (set to 50Hz);
- The kalman filter frequency: used the default settings (100Hz);
- The dynamic platform model: the GPS receiver has a built in filter which is able to get a very good precision by taking into account some dynamic constraints; we found appropriate for our application the “Airborne <1g” model (higher dynamic range than a car and higher vertical accelerations; assuming intermediate process noise).

IV.3.5. *Vortex86* – On board computer

The single chipset, Vortex86 family (see appendix A), provides a high performance/low cost SoC (System on Chip) solution to acquire sensors' data. It is small (180x122x135 mm), light (195g) and has low power consumption (360mA at 12Vcc). Embedded XLinux Operative System was installed.

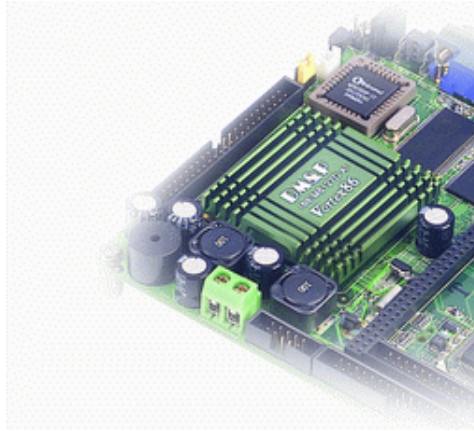


Figure IV-10 *Vortex86*.

IV.3.6. *Datex MUX 3017 V* – Multiplexer

The device converts analogical to digital signal (appendix A). We need it mainly to convert the air pollution sensor output signal and use the analogical input port of the anemometer.

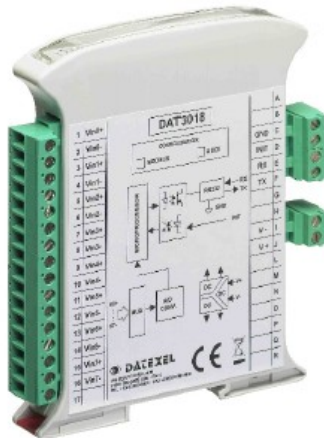


Figure IV-11 *Datex MUX 3017 V*.

Table IV-3 shows the power consumption budget of the station.

<i>Item</i>	<i>Model</i>	<i>N</i>	<i>Tension [V]</i>	<i>Consumption [mA]</i>	<i>Performance DC/DC %</i>	<i>Total [mA]</i>
Temp. e Humid.	HMP-50	1	12	2	0,82	2,44
Data Acq.	Vortex86	1	12	360	0,8	450,00
Anemometer	Windmaster	1	12	102	0,82	124,39
MUX	3017	1	12	47	1	47,00
AHRS-GPS	IG-500N	1	5	105	0,62	70,56
Air pollutant	Sens3000	4	12	174	0,88	790,91
Total consumption						1.485,30

Table IV-3 Power consumption table.

IV.3.7. *ACCU Li Ion battery*

The *ACCU* Li-Ion battery (8Ah, 600g heavy; 135x80x45mm) has been selected to power all the instruments, considering the will to obtain at less 4^h,30' of endurance.



Figure IV-12 *ACCU* Li-Ion battery.

IV.3.8. *BeeLine APRS – Automatic Reporting Position System*

Since it was not possible to transmit the real-time position using the tools described, a telemetry independent system (self powered) was adopted. The need for the information about the height reached is twofold: on one hand it allows a consistency check with the data acquired, on the other hand it's essential for safety reasons.

The BeeLine GPS Telemetry transmitter integrates a microcontroller, an FM radio transmitter, a GPS module and an active GPS receiver antenna onto a single, small, low power board (Fig. IV-13 right). An on-board microcontroller converts the latitude, longitude and altitude from the GPS module into an AX.25 data packet. This AX.25 data packet is then modulated and transmitted at 1200 baud over a radio link. A suitable receiver and packet decoder (TNC) are required on the receiving end (Fig. IV-13 left). The Software decoder used is *MIXW* (<http://mixw.net>).

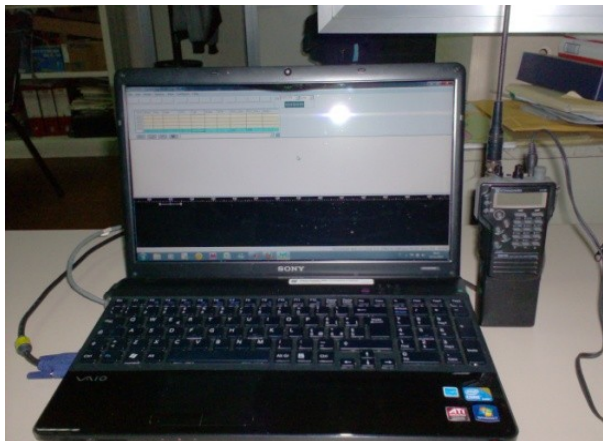


Figure IV-13 Altitude monitoring system: land receiver (left) and APRS transmitter (right).

The *BeeLine APRS* is a small (20x60x150mm) and light (220g) device, able to transmit the position data packets to 36km of distance (at clear view). The endurance declared is 10 hours.

IV.3.9. Mass budget Table

The following table lists the weight of all sensor and subsystems.

<i>Item</i>	<i>Description</i>	<i>Model</i>	<i>Units</i>	<i>weight (g)</i>
Wind	Ultrasonic 3D Anemometer	<i>GILL WINDMASTER</i>	1	1000
Sonic temperature				
Temperature	Thermo-Hygrometer	<i>Vaisala HMP50</i>	1	25
Relative Humidity				
Concentration of: CO	Thick film solid state sensor	<i>UniTech-SENS3000</i>	4	220
NO ₂				
O ₃				
C ₆ H ₆				
Position/Velocity	GPS	<i>SBG-IG500N</i>	1	45
Pressure	Barometer			
Attitude				
Heading	AHRS			
Local vertical				
-	GPS antenna + cable	<i>SBG</i>	1	120
Acquisition System	-	<i>Vortex86 + Datex MUX</i>	1	195
Power supply	Battery (12V)	<i>ACCU</i>	1	600
Lights ⁵	Led+Battery	<i>NAViled</i>	1	300
<i>Varii</i>	Connections, Cable etc..	-	1	165
Payload		Total weight		3330

Table IV-4 Instruments' mass budget.

⁵ *Hella Marine Naviled 360* (www.hellamarine.com) was selected as possible led light for nocturnal flight; it is taken in to account in the mass budget since it was installed on the kytoon station even if no nocturnal launch was performed.

IV.4. Kytoon station

A kytoon station is mainly composed by three elements:

- The Kytoon;
- The Gondola;
- The Trailer.

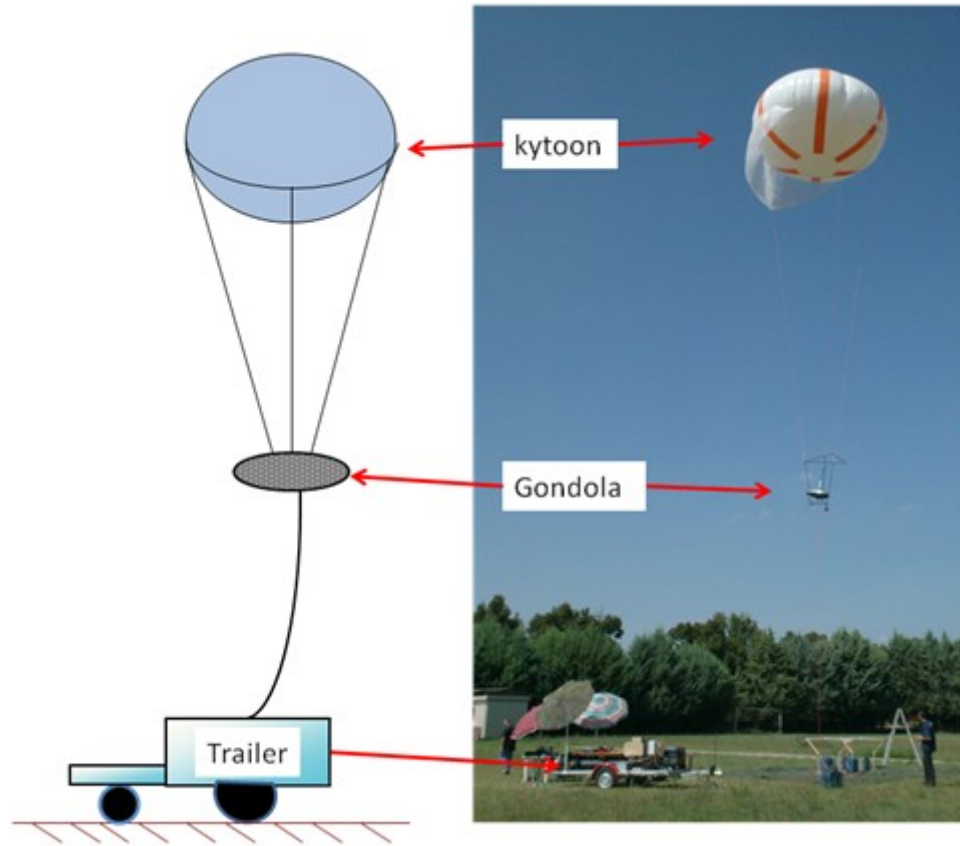


Figure IV-14 Kytoon Station: Kytoon blimp, gondola and trailer in a schematic representation (left) and in a photo (right).

A schematic representation of the station comparing to a photo is shown in Fig. IV-14. More details about design process and details of the three elements are given in the following subsections.

IV.4.1. Floatograph SkyDoc#18 - Kytoon

The selection of balloon is bound by the weight of payload, by the maximum altitude, and by the site of experiment (Urban), that led to prefer small balloons, because of the little launch areas.

After the preliminary selection of *Cameroon Helium blimp AB2000 lightweight* (Panelli, 2009) able to lift up the payload to the prescribed maximum altitude, the smaller *Floatograph Skydoc #18* has been selected.

It is a helium blimp, made of aromatic thermoplastic polyurethane, having a maximum diameter of 4.33 m, and an height of 2.81 m (its shape is an ellipsoid of revolution around its vertical

IV. Kytoon Station Description

axis); a volume of 27.44 m³ results. The six orange aviation stripes (0.30m wide; Fig. IV-15) satisfy the FAA OBSTRUCTION MARKING AND LIGHTING (AC No.: 70/7460-1K) rules, as required by ENAV (Ente Nazionale di Assistenza al Volo).

A particular characteristic of this balloon is that it can generate dynamic lift by using a sail, made of porous material, which is sewn along half of its maximum circumference. This greatly increases both the total lift generated flying in wind conditions and the stability of balloon, due to the “kite” effect.

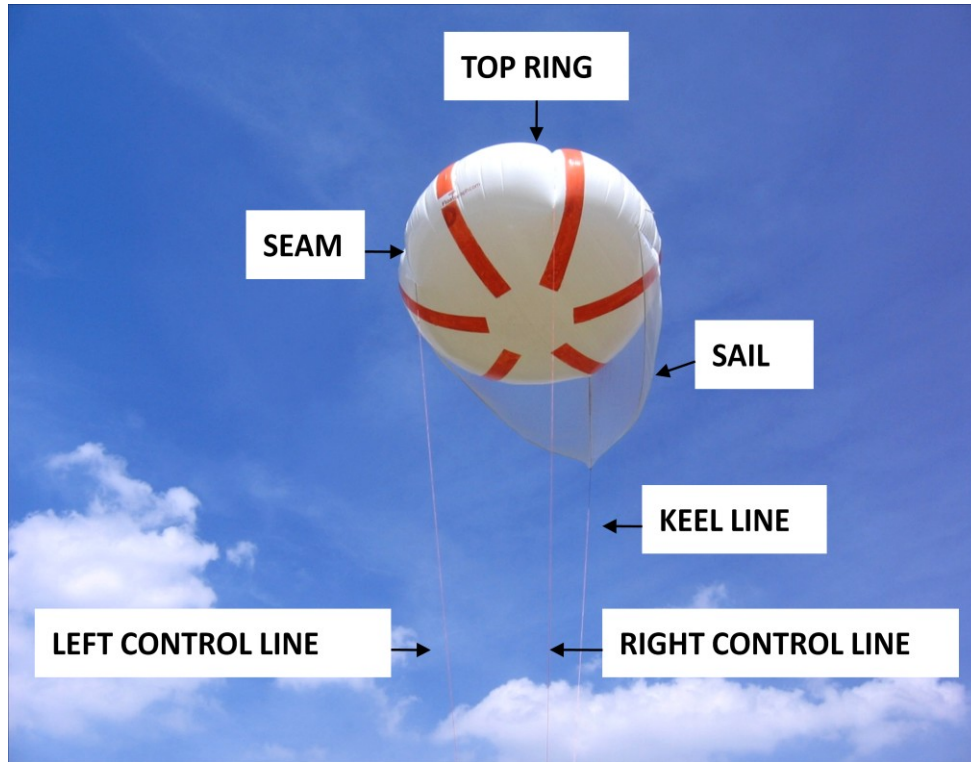


Figure IV-15 Photo of *Floatograph Skydoc #18*.

The kytoon envelope is contained in a harness which consists of three webbed straps made of polyester placed at about 120° from each other (Fig. IV-16). The straps extend from the "top ring" placed in the centered upward part of the kytoon, and terminate in rings on the centerline seam of the kytoon.

Also, three sewn handles are located in correspondence of the end of the straps on the centerline of the kytoon, to help the operators in keeping the kytoon stable while it is on the ground (inflation/deflation phase).

On the back of the kytoon envelope, in correspondence of the end of the back harness strap, a filling sleeve and three helium release valves are present. They are used in the inflation and deflation of the kytoon, respectively (Fig. IV-16).

IV. Kytoon Station Description



Figure IV-16 Front view of the upper surface of the kytoon. The direction of harness straps are put in evidence. The helium valves can be seen.

The kytoon is connected to the payload via three control lines (Right Control Line, Left Control Line, Keel Line) which are 10.9m long (Fig. IV-15). They are connected to the metal rings at the end of the harness straps of the kytoon via a self-stringent knot on the free end. The left and right control lines influence the lateral-directional attitude of the kytoon. Since a slight variation in their relative lengths can heavily influence the kytoon's lateral-directional stability, their length is accurately trimmed to 10.9m.



Figure IV-17 Loops at the ends of the control line, which are connected to the payload (left). Detail of the keel line and its knots. Notice that the line is set on the 3rd knot, which gives an AoA of 0° (right).

In addition, the keel line controls the pitch attitude of the kytoon (Fig. IV-17). By lengthening or shortening the keel line, the angle of attack of the kytoon respectively decreases or increases. The keel line has 9 pre-measured knots at a pitch of 8cm. Since an AoA (Angle of Attack) variation of 1° is caused by a variation of 4cm of the keel line's length, changing the keel line's length by one knot corresponds to a variation of $\pm 2^\circ$ of AoA. Using the middle (5^{th}) knot of the keel line gives the kytoon an AoA of -4° , which corresponds to the most stable flight behavior of the kytoon (as said by the sellers).

All the control lines are made of Dynema Sky 75 Ultra by Gottifredi-Maffioli (DSK75 Ultra, see appendix A). Table IV-5 lists the main characteristics of the only two cables used for each line.

IV. Kytoon Station Description

	<i>Diameter (mm)</i>	<i>Tensile strength (kN)</i>	<i>Linear weight (g/m)</i>
Right/Left control line	3	9	4.7
Keel line	5	27.9	14.1

Table IV-5 Dynema Sky 75 Ultra cable characteristics.

The kytoon possesses an Emergency Deflating Device, which has the purpose of rapidly deflating the kytoon in case of failure of the main components of the system.

The device consists of two units:

- EDD land unit (Fig. IV-18 right)
- EDD kytoon unit (Fig. IV-18 left)

The land unit is composed by a battery housing and a single channel Linear XT-1 FM transmitter. It has a POWER and a BURN switch, of which the last one is protected by a cap which prevents accidental activation of the device: turning on the BURN switch sends an FM signal to the kytoon unit which activates the device.

The kytoon unit is composed by a circuit and battery housing, a Linear XR-1 FM receiver, an electric actuator, and an arm on which end an electrical resistance is located. If both the POWER and ARM switches on the casing are turned on, on receiving the activating signal from the transmitter the resistance heats itself and the actuator lowers the arm to place the resistance against the kytoon's surface, in order to burn a hole through it and cause a major loss of helium, besides irreparable damage to the kytoon envelope.



Figure IV-18 (Left) EDD kytoon unit. The actuated arm with the circular electrical resistance is shown on the left. EDD land unit (Right).

The kytoon unit is fixed at the center of the top ring of the kytoon through a Velcro pad and a harness linked to the kytoon through three plastic clips.

The land transmitter broadcasts a 10W, 27.255MHz, digital encoded, signal modulated FM signal to the kytoon receiver. The antenna used on the transmitter is a Linear ANT-2 model, while the one used on the receiver is a Linear “rubber duck” ANT-1. The antennas are

IV. Kytoon Station Description

connected on the units through SO-239 connectors. The batteries of both units can be charged with the 12V DC charger.

To evaluate the safety of the kytoon system before flying (for example having an idea of the flight envelope) and as tool design, the report “Equilibrium Configurations of Flying Cables of Captive Balloons, and Cable Derivatives for Stability Calculations” (Neumark S., 1963) has been used.

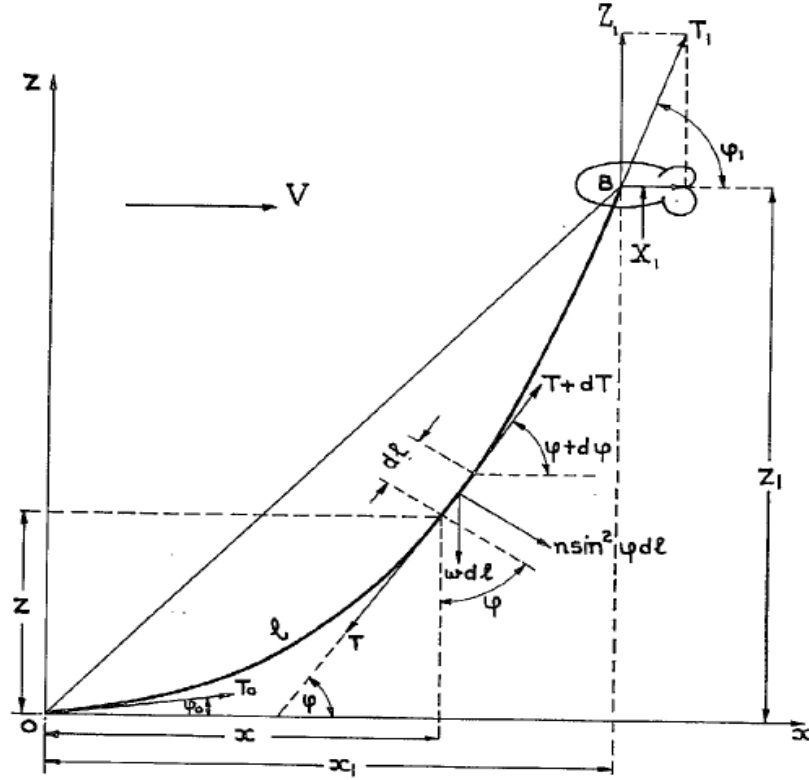


Figure IV-19 Typical two-dimensional cable configuration and forces acting on cable.

The equilibrium of cable of a captive balloon is uniquely determined by (Fig. IV-19):

- x_1 : horizontal displacement of the balloon
- l_1 : main tether line length
- ϕ_0 : inclination of main cable with the ground near latter
- ϕ_1 : inclination of main cable with ground at the maximum altitude

The parameters can be calculated using some formulas obtained by solving the equilibrium equation of infinitesimal cable length dl :

$$\text{tangential direction: } dT = wdl \sin \phi \quad (\text{negligible}) \quad (\text{IV.2})$$

$$\text{normal direction : } Td\phi = (n \sin^2 \phi + w \cos \phi) dl \quad (\text{IV.3})$$

and considering the McCloud equation:

$$(C_{dc} 1 / 2 \rho V^2 d_c) \sin^2 \phi d\phi = n \sin^2 \phi \quad (\text{IV.4})$$

IV. Kytoon Station Description

where C_{Dc} and d_c are respectively the drag coefficient and the diameter of main tether line ; w is the weight-to-length ratio; n is main cable's drag-to-length ratio; T is tether tension.

A step procedures can be used to solve the problem.

- a) Fix the maximum altitude (z_I).
- b) Calculate the areas of frontal impact of balloon (S_k); for the SkyDoc's kytoon $S_k = 9.55\text{m}^2$.
- c) Evaluation of balloon's drag coefficient (C_D); see step (f).
- d) Fix wind velocity (V); the present study would measure wind speed between 3 and 10m/s.
- e) Fix the type of main tether line (w , d_c , C_{Dc}); the DSK75 Ultra cable of 5mm diameter is used. $C_{Dc}=1.025$ (cylinder). Orange flags (0.3x0.6 m) stands along the main cable at 15 m intervals beginning at 60m above the surface of earth, as required by the FAA OBSTRUCTION MARKING AND LIGHTING (AC No.: 70/7460-1K) rules. 18 flags assure the visibility at 300m of altitude. An additional weight of 0.37kg results.



Figure IV-20 Obstruction Marking flags and stripes.

- f) Assess the value of balloon's reserve buoyancy and aerodynamic lift (Z_I); Reserve buoyancy (or net lift) is defined as the excess of total buoyancy over the entire weight of balloon (including its envelope, gas and air contents, rigging, and payload but

IV. Kytoon Station Description

excluding the cable weight). If the excess buoyancy is considerably greater than the cable weight, then T_0 will be large (though always less than T_1), and the difference ($\varphi_1 - \varphi_0$) small under all conditions, the cable will then be 'highly tensioned'. In the opposite case T_0 may be small, and $(T_1 - T_0)$ may become quite large.

The SkyDoc blimp, EDD valve, keel line and right/left control line weighs 11.84 kg. The gross lift, or total buoyancy, can be evaluated applying the Archimedes' principle, being known the weight of fluid displaced (air) and considering that gases' density (helium and air) changes because the altitude and the temperature.

Altitude (m)	0°C S.L.		15°C S.L.		35°C S.L.	
	Gross lift (kg)	Stable Free Lift (kg)	Gross lift (kg)	Stable Free Lift (kg)	Gross lift (kg)	Stable Free Lift (kg)
0	35.46	5.31	33.61	5.04	31.43	4.71
300	34.41		32.62		30.5	
500	33.73		31.98		29.90	

Table IV-6 Gross lift versus altitude and sea Level temperature; Stable free lift is 15% gross lift at S.L. .

Balloon sellers recommend for stable flight to leave always a “free lift” measured as a percentage of the “standard gross lift” i.e. the gross lift at Sea Level (S.L.): 10% is the bare minimum required for stable flight. 15% is a much more comfortable level at which to fly, especially if the air is turbulent (thermals etc).

The aerodynamic lift can be computed using the measured tether strain wind tunnel tests on SkyDoc model #18 (Fig. IV-21) and the graphic of SkyDoc Height vs. wind speed (Fig. IV-22). Subtracting to all values of table the value of tether strain in calm air condition (gross lift), the aerodynamic lifts follows; the latter can be compared to that obtained with the formula:

$$(C_T 1/2 \rho V^2 S_k) = T \quad (IV.5)$$

Where C_F is an unknown total force coefficient: 0.83 is the value that minimizes the difference of the wind tunnel's measurements and that given by the formula (IV.5). This assumption is true only with big φ_1 .

The graphic of the figure IV-22 allows to calculate the angle ($90 - \varphi_1$) between the aerodynamic lift and the local vertical; the decomposition of C_F gives a C_D (0.35) and C_L (0.74), with 5m/s of wind speed. Note that the total force coefficient has been used also at 7 m/s (at which would correspond different AoA of the kytoon), because a very small difference has been find.

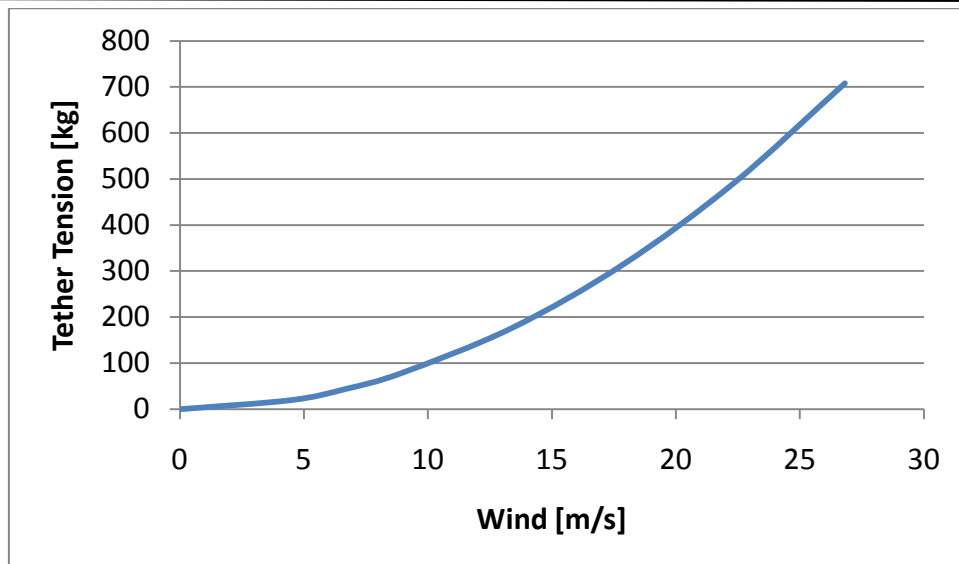


Figure IV-21 Tether strain resulting by *SkyDoc* wind tunnel tests.

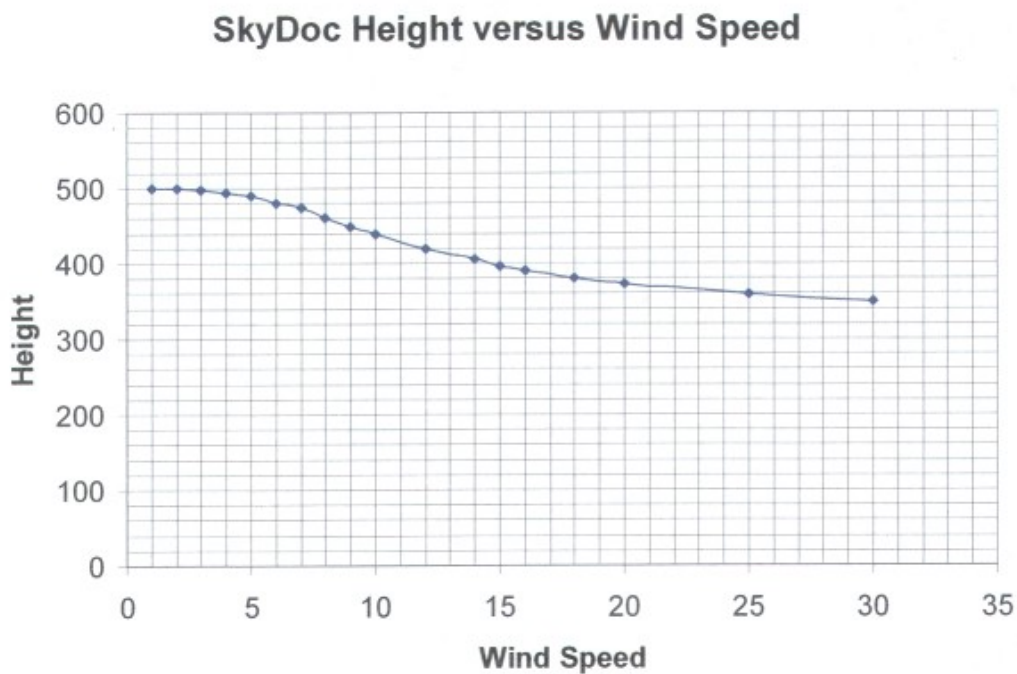


Figure IV-22 SkyDoc Height (ft) vs. wind speed (mph) considering a fix cable length of 500ft.

A brief summary about given definitions follows.

GROSS LIFT (or TOTAL BUOYANCY) + AERODYNAMIC LIFT = PAYLOAD + RIGGING LINES + FLAGS + EDD + CABLE + FREE LIFT

RESIDUAL LIFT (or NET LIFT) = GROSS LIFT – (RIGGING LINES + FLAGS + EDD + PAYLOAD)

FREE LIFT = RESIDUAL LIFT – CABLE + AERODYNAMIC LIFT

IV. Kytoon Station Description

- g) Calculate $n = (C_{dc} 1/2 \rho V^2 d_c)$ and $X_1 = (C_d 1/2 \rho V^2 S_k)$;
- h) Calculate $T_1 = \sqrt{X_1^2 + Z_1^2}$ and then $\varphi_1 = \arctan(Z_1 / X_1)$;
- i) Calculate $\psi = 0.5 \arccot \cot \alpha (w/2n)$;
- j) Calculate $\tau_1 = \tau(\varphi_1)$, where $\tau(\varphi) = \left(\frac{\cot \psi - \cos \varphi}{\tan \psi + \cos \varphi} \right)^{\cos 2\psi}$;
- k) Calculate τ_0 from $wz_1 \tau_1 = T_1 (\tau_1 - \tau_0)$ and φ_0 (step j);
- l) Calculate $\lambda_1 = \lambda(\varphi_1)$ and $\lambda_0 = \lambda(\varphi_0)$ from $\lambda(\varphi) = \int_0^\varphi \frac{n \tau d\phi}{n s e n^2 \phi + w \cos \phi}$ and so l_1 from $nl_1 \tau_1 = T_1 (\lambda_1 - \lambda_0)$
- m) Calculate $\sigma_0 = \sigma(\varphi_0)$ and $\sigma_1 = \sigma(\varphi_1)$ from $\sigma(\varphi) = \int_0^\varphi \frac{n \tau \cos \phi d\phi}{n s e n^2 \phi + w \cos \phi}$ and so x_1 from $nx_1 \tau_1 = T_1 (\sigma_1 - \sigma_0)$

The results of the calculation (Tab. IV-7) show that:

- All the parameters grow with the air temperature (obviously except the free lift) but there is little difference between the data at 0 and 15°C;
- The Free lifts are 3-3.5 times the stable free lift (Tab. IV-6);
- Increasing in wind led to growing of all the parameters, except free lift that decreases;
- The computed values of main cable's strain are very close to the experimental measurements of *SkyDoc* #15; the dimension of the model #18 differs little from #15.

Consequently, in order to estimate the Safety Factor (S.F.) of tether line, defined as max load line to tether tension ratio (Tab IV-8), the results of calculation have been used.

0°C					
<i>Wind (m/s)</i>	<i>Cable length (m)</i>	<i>weight (kg)</i>	<i>strain (kg)</i>	<i>x1 (m)</i>	<i>Free lift (kg)</i>
5	323.26	4.56	19.98	105.38	18.93
7	372.86	5.26	21.92	211.84	18.23

15°C					
<i>Wind (m/s)</i>	<i>Cable length (m)</i>	<i>weight (kg)</i>	<i>strain (kg)</i>	<i>x1 (m)</i>	<i>Free lift (kg)</i>
5	324.63	4.58	18.17	109.33	17.12
7	378.16	5.33	20.05	220.63	16.36

35°C					
<i>Wind (m/s)</i>	<i>Cable length (m)</i>	<i>weight (kg)</i>	<i>strain (kg)</i>	<i>x1 (m)</i>	<i>Free lift (kg)</i>
5	326.74	4,61	16.03	115.10	14.97
7	386.38	5,45	17.84	233.81	14.13

Table IV-7 Cable characteristics, horizontal displacement and Free Lift of the kytoon, at 300m of altitude, changing temperature.

<i>Wind (m/s)</i>	<i>Tether tension (kg)</i>	<i>S.F.</i>
5	19.98	142
7	21.92	130

Table IV-8 Safety Factor of the DSK75-Ultra cable; worst case (Temperature, 0°C).

Note that the nomenclature used in this paragraph is exclusive and it isn't used in the rest of thesis.

IV.4.2. CATFISH gondola

All the selected sensors, to be lifted up by the kytoon, are placed in the so called “gondola”, which satisfies the following requirements:

- Compactness, in order to have all the measurements in the same point in the space and to help the portability of the system;
- Lightness, to have the most free lift as possible (stable flight);
- Minimal interference on the measurements; big attention has been done in the design of gondola's shape, in the positioning of the sensors respect to each other and to the kytoon.

The “gondola” is composed by two part (Fig. IV-23), each one made of Carbon Fiber Reinforced Polymer (CFRP), with fibers woven in the 0° , $+45^\circ$ and -45° to assure isotropic resistance, and epoxy matrix:

- The CATFISH⁶ nacelle;
- The cage.

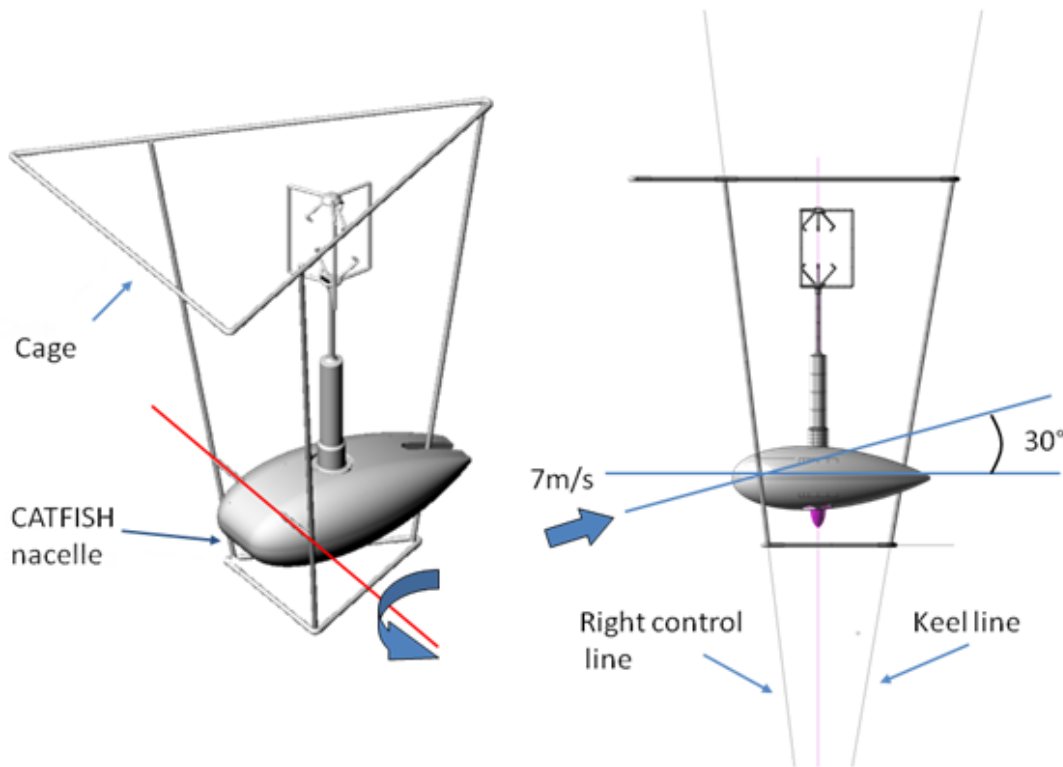


Figure IV-23 3D CAD model of the CATFISH gondola; Maximum allowed rotation (30°) of CATFISH nacelle at 7 m/s of wind speed.

The nacelle hosts all the atmospheric sensors, the AHRS-GPS, the data acquiring system and the battery to power the whole system. The body has a shape similar to an hull of Americans Cup with NACA 0032 airfoil cross-section: main chord is about 0.71 while the maximum width is 0.32m.

The CATFISH nacelle is joined to the cage by means of an hollow tube (Nacelle support tube) which passes through a support near its the nose. The nacelle is virtually free to rotate around the nacelle support tube, but its dynamic of pitch is blocked by a regulating cable, which links the back end of the nacelle to the upper part of the chassis. A maximum angle of rotation of 30° degrees has been calculated for the equilibrium configuration of the balloon at 7 m/s of wind speed (Fig. IV-23). Prerotation is essential to avoid that the anemometer is in the CATFISH-box's wake (inclination is the angle of attach of CATFISH!).

⁶ The name “catfish” belong from the shape of the box; the two protuberances on its the nose seem like fish's mustache while the intake in the trailing its tail.



Figure IV-24 CATFISH gondola: they are visible the Gill Windmaster anemometer and the GPS's antenna (black rhomboid object); silver tape cover the CATFISH's body to surely avoid over heating due to the sun light. It can be seen the cable to regulate AoA of the nacelle.

The cage has the purpose to join the CATFISH payload to the riggings' lines of the kytoon and to protect it in the hypothesis of any ground impact.

Consequently, it is made of CFRP hollow tubes, and consists of:

- 2 front tubes (Fig. IV-25);
- 1 back tube (Fig. IV-25);
- The nacelle support tube (Fig. IV-25);
- Lower triangular chassis (Fig. IV-26);
- Upper triangular chassis (Fig. IV-27).



Figure IV-25 From the top: left front tube, back tube, front tube. The nacelle support tube spans between the others.



Figure IV-27 Upper triangular chassis.



Figure IV-26 Lower triangular chassis. The elastic cable which is normally linked to the nacelle's back, can be seen.

The vertical tubes are engaged in three dedicated slots of the triangular chassises. The two front tubes have two tubular protrusions in which nacelle support tube is inserted.

The payload is attached to the control lines and the main tether line by means of holding bridles, which are passed through each hollow vertical tube. On the end of these there are two loops: one is knotted to a snap hook with a self-tightening knot, and allows to connect control lines to payload (Fig. IV-28); the other one is linked to the main snap hook, which connect them with tether line (Fig. IV-29).

Aluminum stoppers are placed under the upper loop of the bridles to block them in position respect to the vertical tubes.

The payload rests on three knots at fixed and equal distance from the bottom end of the holding bridles. Six circular plastic sleeves, put inside the end parts of vertical tubes, prevent cutting of the holding bridles due to the carbon fiber shards.

Notice that the housings of the front tubes are placed in a rear position on the upper triangular chassis. This feature is designed on the purpose of protecting the nacelle in the hypothesis of a ground impact by making the upper chassis impact on the ground before the nacelle itself. The distance of projection has been calculated with a 30° degrees rotation of gondola (Fig. IV-23,24).



Figure IV-28 (Right) Holding bridle in position: the stopper blocks the bridle, while the snap hook links the bridle to the control lines (bottom left); circular plastic sleeves (top left).

The structure has a height of 1.27 m and a lateral overall dimension of 0.96 m (details in appendix B); its total weight (without any sensors mounted) is 4.09kg. The snap and the main hooks have respectively a maximum load of 1100 and 3000 kg.

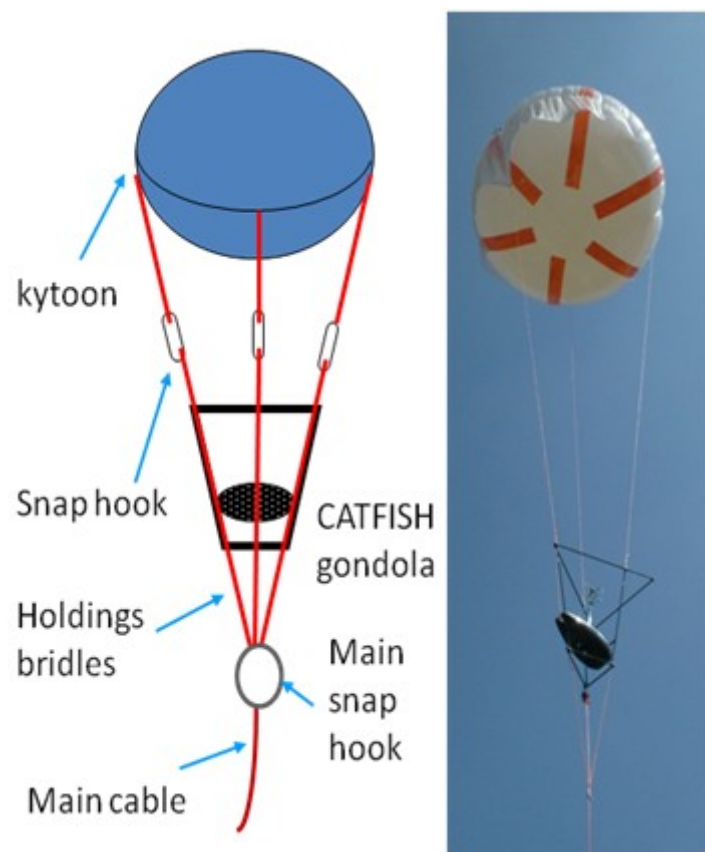


Figure IV-29 CATFISH gondola connections: scheme (left) and photo (right).

IV. Kytoon Station Description

All the sensors are placed inside or outside the CATFISH nacelle despite of the APRS, which has its own box, connected to the cage via a snap hook and to the keel line via adhesive tape.

Watching the upper part of CATFISH nacelle, it can be seen:

- the anemometer (the most evident sensor) placed on it (Fig. IV-24);
- the GPS antenna (Fig. IV-30);
- the location of battery (Fig. IV-30);
- the Ethernet port⁷, to configure (see section V.2.4) on board computer (Fig. IV-30);
- the ON/OFF switch (Fig. IV-31);
- the fuse (Fig. IV-31);
- the APRS-GPS external data input port, to configure and calibrate (see section VI.4) the device (Fig. IV-31);
- six warning leds (Fig. IV-31).

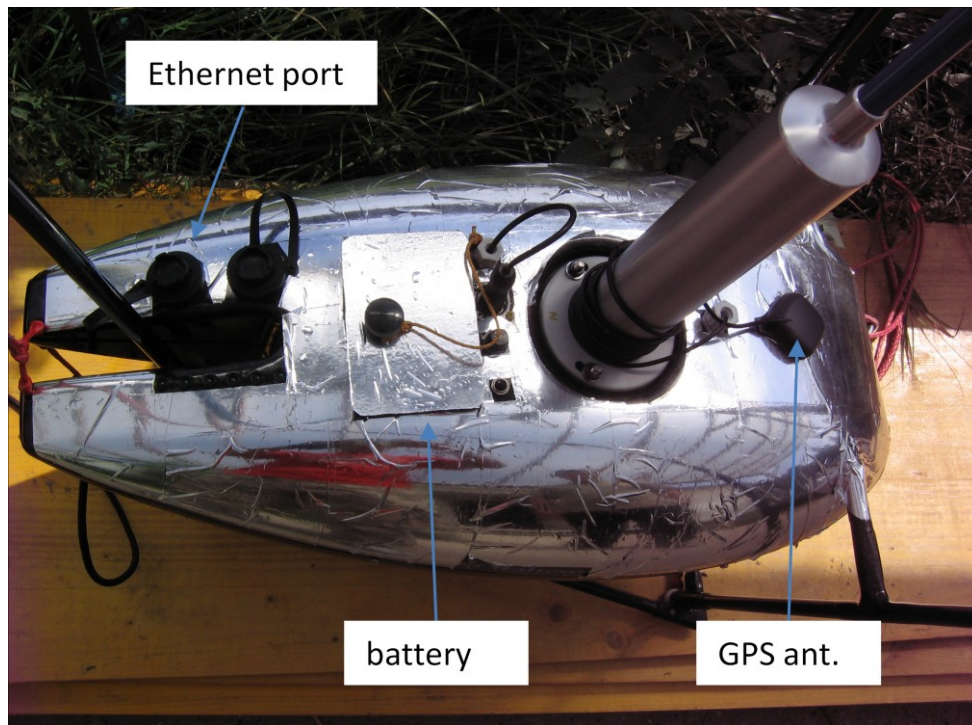


Figure IV-30 Top part of CATFISH gondola: Battery, Ethernet port (set/warm-up phase), GPS antenna.

⁷ Two Ethernet ports are easily visible in fig. #F; only one is connected to on board computer; originally there were two different data acquisition cards.

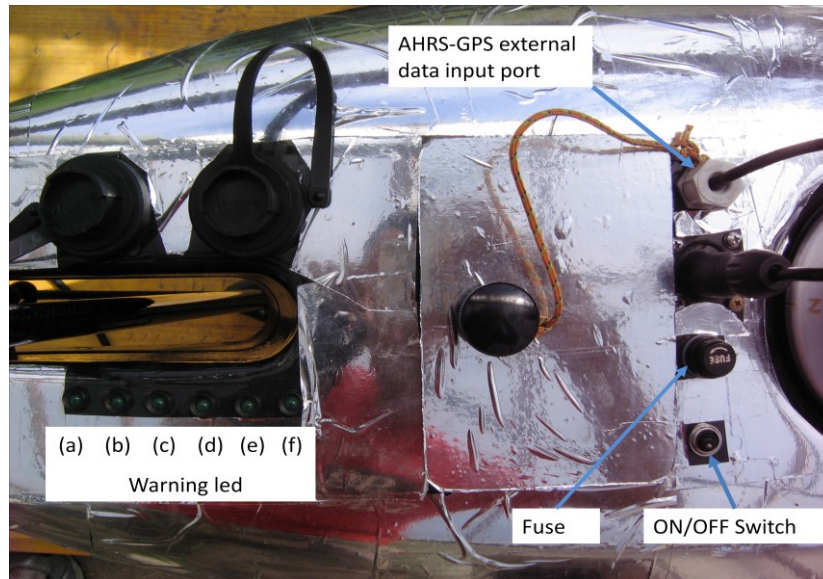


Figure IV-31 Top part of CATFISH nacelle: warning led, fuse, ON/OFF switch and AHRs-GPS external data input port (calibration phase).

The meanings of the leds follow:

- (a) Anemometer diagnostic;
- (b) Power status alarm of the GPS;
- (c) Power status alarm of the air pollution sensors (CO , O_3);
- (d) Power status alarm of the air pollution sensors (C_6H_6 , NO_2);
- (e) Power status alarm of the Anemometer;
- (f) Power status alarm of the acquisition system.

Watching the lower part (belly) of the CATFISH nacelle are visible (Fig. IV-32):

- The Vaisala thermo-hygrometric probe;
- A led light (according to FAA OBSTRUCTION MARKING AND LIGHTING ,AC No.: 70/7460-1K): actually no permission of nocturnal flight was given but in the future it should be; night dispersion of pollutions is the most critical!
- Six straight air intakes to cool on board computer (partially visible in the figure);
- Four circular air intakes to allow the suction of air on the thick solid state sensors.

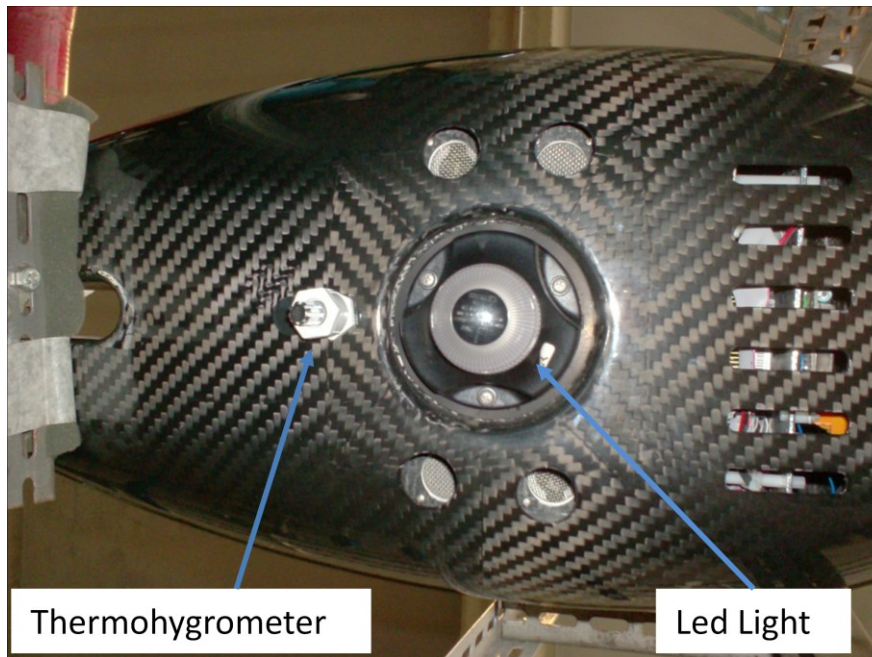


Figure IV-32 Belly of the CATFISH nacelle; the thermo-hygrometer probe , the led light, the four circular air intakes of the chemical sensors and the six straight intakes for the inside cooling are visible.

The AHRS-GPS (*IG500 N*) and the four chemical sensors are fully inside the CATFISH nacelle; particularly the *IG500 N* device is linked to a circular plate just under the base of the anemometer; three screws allow the connection between the two sensors and the carbon surface of the nacelle (Fig. IV-33).

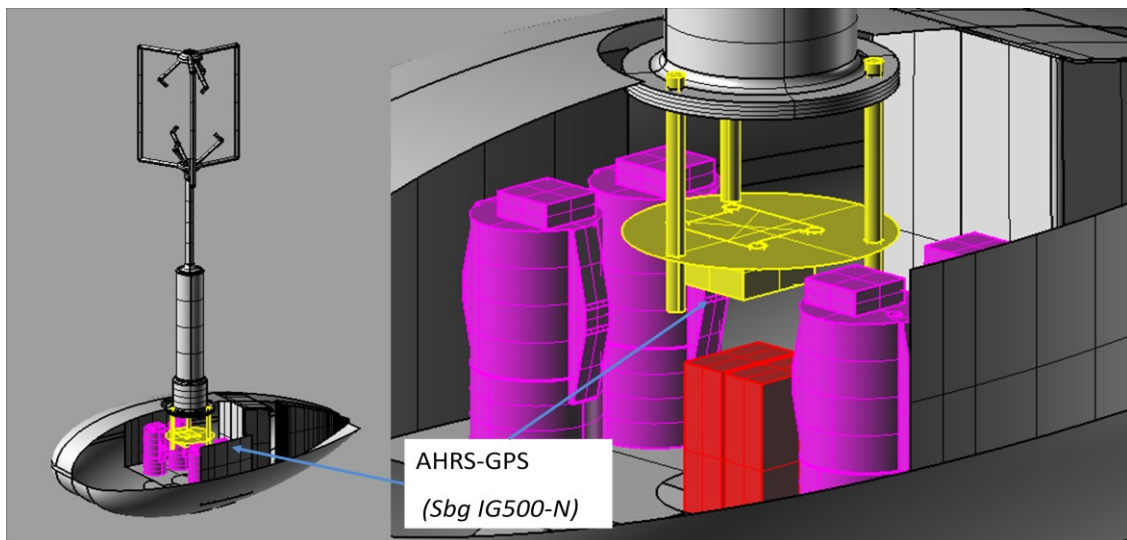


Figure IV-33 Position of the *Sbg IG500-N*, AHRS-GPS (yellow parallelepiped), device and its support structure inside the cover of the CATFISH gondola; they are also visible: the chemical sensors (violet), and the led light's battery.

All the sensors and subsystems are placed around the vertical axis of the anemometer so that the center of gravity of the CATFISH gondola is near the origin of AHRS's reference system.

Finally note that silver tape (Fig. IV-24,30) covers the upper hemisphere of the nacelle: during a static laboratory set-up test very high temperature (65°) were reached on its nose despite of the

IV. Kytoon Station Description

low emissivity of the covering paint; the system, inclined of 30° around the support tube, lied on the sun at 35°C of air temperature. Even if the extreme no flight conditions, with no cooling wind coming inside air intakes, it has been preferred to protect the instrumentation.

The distance between balloon and nacelle is a compromise between the desire to maintain the rigging lines short (for stability reason) and to reduce the influence of balloon on the anemometer's measurements. The result of a RANS (Reynolds Average Navier Stokes) CFD simulation of flow field around the balloon (without the sail) has shown that a distance of about 10m (considering the length of the inclined control lines: 10.9m) between the belly of the balloon and the anemometer head gives an error of less than -1% on the wind measurements (Fig. IV-34).

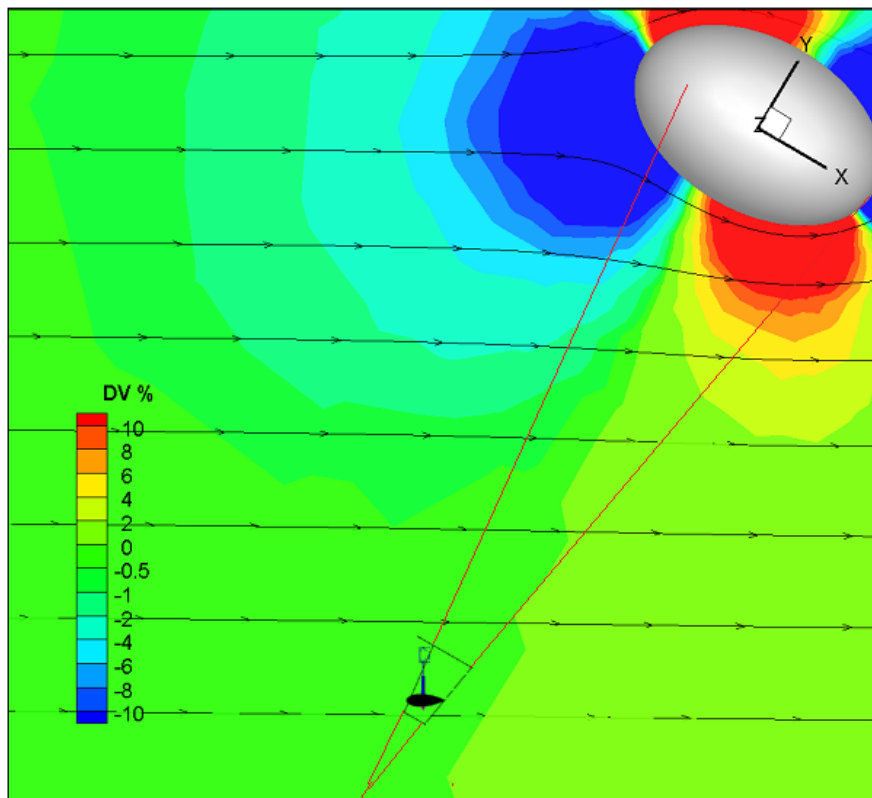


Figure IV-34 Aerodynamic interference of the balloon on the anemometer's measurements. DV is the difference between the velocity module, calculated with RANS simulation, and the value of free wind stream (7m/s). The stream lines are shown, too.

The NACA 4-digit series provides itself negligibly influencing the readings of the anemometer : 3D RANS simulations has stated that the measurement o the anemometer, acquired 0.60 m far from the body of CATFISH, are overestimated of less than 1%.

In conclusion the resulting aerodynamic effect (CATFISH plus balloon) doesn't affect the readings of the anemometer.

IV.4.3. Trailer

The trailer used as the mobile launch platform is the *Umbra Rimorchi TM100B/D*. It acts as the base for the inflating and power plants, and there is also free space on which other systems can be fixed and transported.

The trailer dimensions are 1460 x 3055 x 350 mm and the maximum fully charge weight is 750 kg.



Figure IV-35 *Umbra Rimorchi TM100B/D*. Front connection trunk is on the right.

The trailer is mechanically and electrically (due to the position lights) joined to the towing vehicle via the front connection trunk (Fig. IV-35), on which both the towing hook and the electrical plug are present.

The front connection trunk also hosts the emergency brake and supports the front wheel leg, which can be used in moving the trailer by hand. The height of the wheel leg can be adjusted by using the crank on the front connection trunk.

The trailer is equipped with a safety braking system which brakes the trailer in case of disconnection from the towing vehicle while in travel. The trailer's weight when stationary is distributed by three (2 lateral and 1 frontal; Fig. IV-36) removable supports.

The front support is placed under the front connection trunk, at the front end of the trailer, while the lateral ones are placed just before the position lights.



Figure IV-36 Front support of the trailer.

IV. Kytoon Station Description

The lateral supports' height is adjustable via a clamp, while the front supports' height is adjustable by inserting a bar into a hole on the supports' moving part.

A spare tire is provided with the trailer, which is mounted on its left side in a dedicated housing. Both the inflating and the power plant are supported on the trailer.

To better distribute their weight, the trailer has been reinforced during the setup phase by fixing two crossbars, which span through the whole planking width, at the lateral chassis.



Figure IV-37 View of the ensemble trailer.

The trailer transports five principal objects:

- The inflating plant;
- The winch plus the tension inverter;
- The power plant;
- The collapsible balloon cradle.

The inflating plant consists in:

- 4 compressed helium gas cylinders,
- the gas cylinder cage,
- the pressure regulator,
- the inflating hose fixed to the inflating wand.

The helium cylinders contain the helium used to inflate the kytoon. They are blocked in the gas cylinder cage during transport and operation to increase safety.

IV. Kytoon Station Description

Each cylinder has a threaded cap on its top which has the function of protecting the cylinder valve. The caps are always screwed on the cylinders, apart when the cylinder is being used. The cylinder specifications are listed in table IV-9.

Diameter	230 mm
Height	1620 mm (with cap)
Weight	80 kg (filled)
Helium type	4.6
Cylinder volume	50 L
Gas pressure	200 bar
Gas volume	9.384 m ³

Table IV-9 Gas cylinder specifications (per cylinder)

The cage houses the four gas cylinders which are needed for inflation, and occupies the rear portion of the trailer, as shown in figure IV-38; it assures safe way to transport the gas cylinders.



Figure IV-38 Gas cylinder cage after welding of the bars. The support platforms and the gas cylinders supports are still missing at this stage of setup.

The cage is made of welded 40 x 40 mm section bars made of iron and it is permanently bolted on the trailer through 4 support platforms. The gas cylinders are housed in suitably dimensioned “C” supports, which are welded on the central cross bars of the cage base. When the cylinders have been inserted, they can be permanently blocked by bolting on them the upper blocking bars (Fig. IV-39).



Figure IV-39 Loaded gas cylinder cage. The upper blocking bars are visible.

IV. Kytoon Station Description

“C” supports are also welded on these bars, and, together with the lower “C” supports, completely constrain the cylinders in place for safe transport and usage. A back stopper bar is then bolted at the back end of the cage to constrain the horizontal movement of the cylinders (Fig. IV-41).

A support planking (Fig. IV-41) is screwed on the top of the cage, both to provide a usable surface and as an additional protection for the cylinders. The back end of the planking can swivel around a hinge to permit access to the cylinders during inflation. The swiveling end of the planking is secured against accidental openings by two butterfly screws (Fig. IV-40).



Figure IV-40 Detail of the closing butterfly screw.



Figure IV-41 Open back end of the gas cylinder cage. The stopper bar is visible and the cylinder caps are pushing against it. The swiveling back end of the planking is open to permit access to the cylinders.

The gas cylinder cage dimensions and weight are listed in table IV-10.

Length	1690 mm
Width	1148 mm
Height	380 mm
Weight	77 kg

Table IV-10 Gas cylinder cage specifications

IV. Kytoon Station Description

Since an excessive pressure surge in the inflation can damage the kytoon fabric, a pressure regulator is used to decrease and control the output pressure of the helium cylinders.

The ID pressure regulator (Fig. IV-42) presents 2 high and low output pressure manometers (one with 300 bar and the other with 25 bar F.S.). A crank permits to adjust the pressure output. The regulator has two connections on its side, of which one is screwed on the cylinder valve and the other one is joined to the inflating hose (Fig. IV-43).



Figure IV-42 Pressure regulator mounted on the cylinder valve during inflation.

The hose conveys the helium from the pressure regulator to the wand, which brings it into the kytoon envelope.



Figure IV-43 Inflating wand and hose.

IV. Kytoon Station Description

The hose-pressure regulator joint and the hose-wand connections are by means of metal clips suited for gas use. In particular, the clip connecting the hose to the wand has been covered with duct tape to avoid damage to the kytoon fabric when inflating.

The hose has a diameter of 20 mm and has a length of 15 m, which is enough to inflate the kytoon at a safe distance from the launch platform.

The wand is plugged at its end and has several holes along its length to reduce the pressure output, in order to avoid fabric damage.

Operators can control the launch, retrieval and flight height of the kytoon by activating the winch (Fig. IV-44) and releasing or withdrawing the tether line.



Figure IV-44 SKYDOC winch.

Using a control pendant connected to electrical inverter (*Toshiba VF-S11*), it is possible to operate at three-speed winding: 2 (slow), 20 (fast) and 40 (emergency recover) m/min (Fig. IV-45).



Figure IV-45 Toshiba inverter.

The tether line is wound on the drum of the winch and has one end which is fixed in the tether line junction box. When the winch is activated through the control pendant, the tether line

IV. Kytoon Station Description

comes off the bottom part of the drum and passes through the roller fair lead, which moves along the upper shaft to keep the tether line uniformly wound on the drum (Fig. IV-46).



Figure IV-46 Winch in operation during a test flight. The roller fairlead is in the center.

The specifications of the electrical winch motor, the speed reducer and the winch are listed in tables IV-11 and IV-12.

Motor model	<i>Neri-Motors</i>
Horsepower	2 HP
Full load RPM	3396 RPM
Full load torque	4.22 Nm
Full load frequency	60Hz
Speed reducer model	<i>Dayton 4Z730</i>
Nominal output RPM	29
Nominal gear ratio	60

Table IV-11 Winch motor and speed reducer specifications.

Length	530 mm
Width	1175 mm
Height	546 mm
Body	Aluminum
Weight	165 kg
Drum shaft torque	200 Nm (nominal load)
Line pull speed	17 m/min

Table IV-12 SKYDOC™ Winch specifications

The motor and speed reducer are housed in the casing on the right side of the winch, as shown in figure IV-44, and the electrical power is supplied by the generator through the 220 V plug (Fig. IV-47).

IV. Kytoon Station Description



Figure IV-47 220 V motor plug.

The winch is permanently fixed on the trailer with 4 bolts placed on the mounting flanges.

The power plant for the station consists in a *Honda EU30is* portable gasoline generator; it supplies electrical 12Vcc and 220V power for every other electrical appliance on the field.

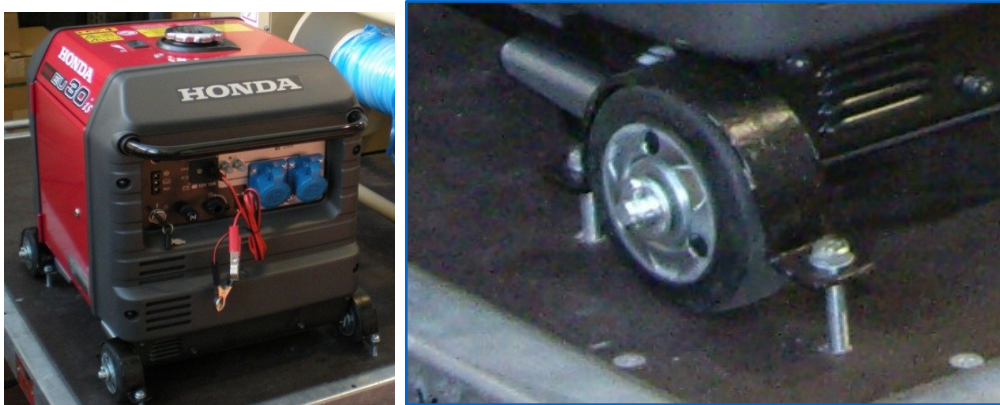


Figure IV-48 *Honda EU30is* power generator. The control panel with the DC cable is clearly visible (Left). (Right) fixing bracket (connection with trailer).

The generator runs on automotive unleaded gasoline fuel with Research Octane Number of 91 or higher, and it uses SAE 10W-30 oil. The specifications of the generator are listed in table IV-13.

Model	<i>Honda EU30is</i>
Length	658 mm
Width	482 mm
Height	570 mm
Dry weight	61.2 kg
Engine model	GX200
Displacement	196 cm ³
Fuel tank capacity	13.3 L
Battery	12V, 8.6 Ah
AC rated output	230 V, 50 Hz, 12.2 A
AC rated output power	2.8 kVA
AC max output power	3.0 kVA
DC rated output	12 V, 12 A

Table IV-13 Specifications of the *Honda EU30is* power generator

The generator is placed on the left front side of the trailer platform, and it is fixed to the planking with four removable brackets, shown in figure IV-48. When the generator is operated,

IV. Kytoon Station Description

it has to be detached from the trailer by unbolting the brackets and placed on a flat and level ground.

The collapsible cradle (Fig. IV-49) allows the garaging of the balloon to the ground when unused. This occurs, for example, during the nighttime between two days of the field experiment.



Figure IV-49 Garaging of the balloon (left) on the collapsible cradle (Right).

IV.5. Flight requirements

The authorities E.N.A.C and E.N.A.V issued the NOTAM⁸ (flight permission, Fig. IV-50) after:

- Respecting the the FAA OBSTRUCTION MARKING AND LIGHTING (AC No.: 70/7460-1K) rules;
- Writing an operative manual of the kytoon system (Panelli, 2009);
- Make a FUNCTIONAL HAZARD ASSESSMENT ANALYSIS: (see appendix E) in it is a failure analysis that establish a class of risk to all critical part of the kytoon system; particularly all the ground connections (main cable, control lines, snap hooks and winch) was analyzed.

⁸ NOTAM: *quasi-acronym of “NOTice To AirMen”*. They are short communications issued by national aviation authorities to alert aircraft pilots of any hazards en route at a specific location.

IV. Kytoon Station Description

```
17 08 10 10:54      CAAV NAPOLI - Uff. OPERAT      0817070036      p.1
                    *** ENAV S.p.A. ***              PAGE 1 OF 1
*** AERONAUTICAL INFORMATION SERVICE AUTOMATED SYSTEM ***
*** SINGLE NOTAM INQUIRY ***      17/08/10 10:15:57
OPTIONS USED FOR NOTAM SEARCH:
SERV. LOC.:LIXX CLASS:1 SERIES:W
YEAR:2010 NUM:3212
=====

LIXX 1W3212/2010 12/08/2010 22:50
RACR A)ROMA FIR-CASERTA
COO B)06 SEP 2010 HR 00:00 C)10 SEP 2010 HR 23:59 EST
D)SR MINUS30-SS PLUS30
E)TEMPORARY RESERVED AREA WI AREA 0.07NM RADIUS CENTRED ON
410352.72N0141938.38E (WGS-84) /CASERTA/ DUE TO CAPTIVE BALLOON
(DUE TO NATICKAL CAMPAIGN FOR POLLUTANTS ANALYSIS IN THE ATMOSPHERE)
CHARACTERISTICS:
1. COLOUR: WHITE WITH ORANGE AVIATION STRIPES
2. DIAMETER: 4.33M
3. CABLE WITH FLAGS
4. MAXIMUM ELEVATION RAISED 1148FT AMSL
F)GND G)1148FT AMSL
Q)LIRX/QRACA/IV/NBO/W /000/012/4103N01419E/001

***** END TEXT *****
```

Figure IV-50 Information extracted from NOTAM.

V Launch site and procedures

The kytoon station, described in the previous chapter, needs safety and functional tests. On 26th February 2010 a flight with strong wind conditions, was conducted. On 6th, 7th 13th, 15th, 16th and 17th September 2010 there was the first collecting field of data.

The description of the main launch procedures, occurring in a typical measurement with kytoon, is also described.

V.1. Selection of launch site

The experiment campaign has the purpose of collecting field data, in form of vertical profiles of relevant atmospheric quantities, in the context of a Mediterranean metropolitan area, where complex interactions between a variety of micro scale meteorological phenomena act (chapter I).

A part the presence of these phenomena, a number of factors must be carefully considered by choosing the launch site:

- Proximity to airports, airport runways and/or other air operations;
- Avoidance of obstacles which could interfere with or could be damaged by the kytoon including:
 - Electrical lines: the tether line could conduct electrical current down to the operator if in contact with a power source, in addition to cause blackouts and hazardous situations in case of damage to the electrical lines;
 - Trees and towers: these obstructions tend to act as a vortex for wind currents and could cause the kytoon to be drawn to the obstruction. Besides, the tether line could become stuck into these structure even if the kytoon is still high;
 - Buildings: wind vary around buildings and wind shear may be a possibility;
 - Highways: do not fly low and close to a busy highway. Vehicles can create a vortex system and cause the system to crash into the highway. The tether line could get in the way of vehicular traffic and cause damage to passing vehicles and their passengers. In addition, One must be aware, when flying the system very near a busy street or highway, that the distraction of observing the kytoon may cause an accident;
- Accessibility of the location in order to deploy the launch platform;
- A clearance of 30 meters from any ground obstacles is required (Fig. V-1);
- Relatively flat, level, firm ground position for the launch platform and for the inflation and the deflation of the kytoon;
- Ability to secure optional ground anchors.

Naples' city area wasn't taken in to account because the restrictions on the use of the kytoon station (presence of elevated obstacles, wind shear in urban canyons), particularly the air traffic due to the Capodichino Naples City Airport.

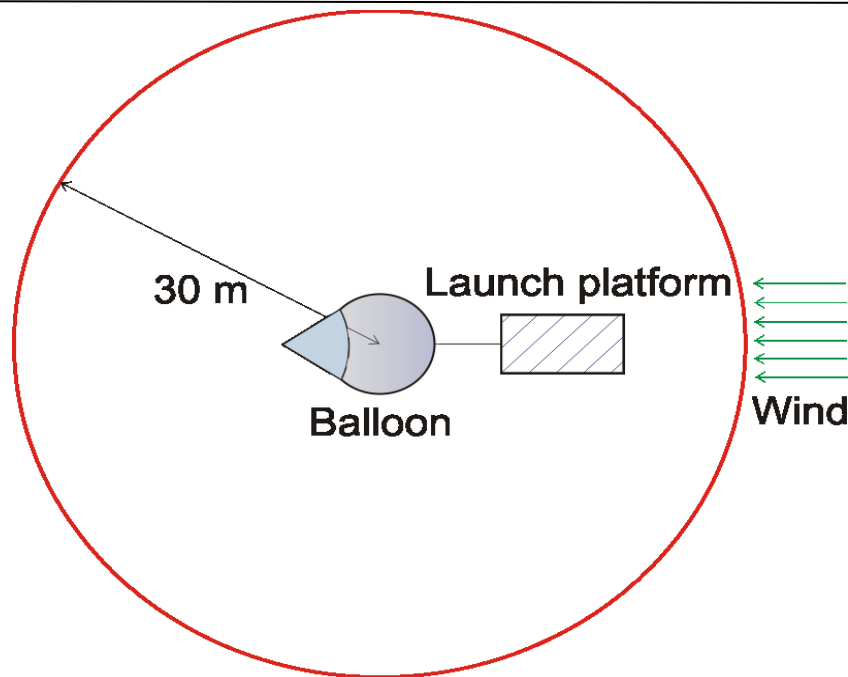


Figure V-1 Kytoon clearance and orientation – top view.

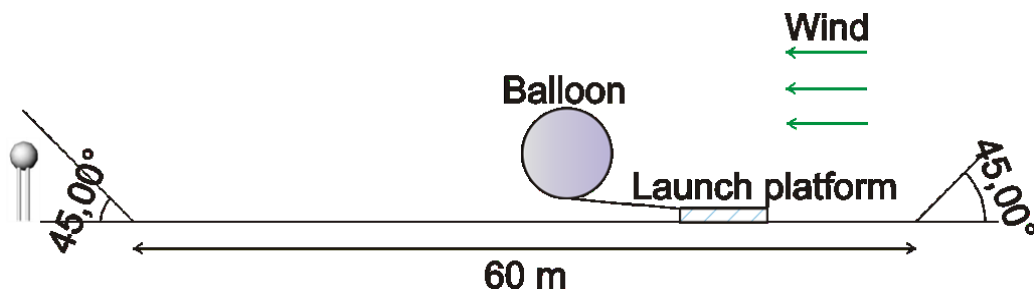


Figure V-2 Kytoon clearance and orientation – side view.

Caserta metropolitan area was a good site of the experiments in fact there are all the typical micro scale phenomena:

- **Urban Heat Island:** as it can be seen in figure V-5,6, the area is densely populated, even if in concentrated town centers;
- **Anabatic / katabatic winds and valley winds:** the urban area is situated inside a plain which is delimited by a chain of several hills, spanning from Monte Tifata on the North to Monte Longano on the East (Fig. V-5). The presence of katabatic and anabatic winds, together with valley currents (especially in the Maddaloni valley) can be easily expected;
- **Land and sea breezes:** Caserta is situated at 30 km from the Tyrrhenian sea (Fig. V-3); western fronts of sea and land breezes can be expected (as verified by ground station measurements).

Moreover Caserta is far from the Grazzanise and Capodichino's flight area (Fig. V-4).

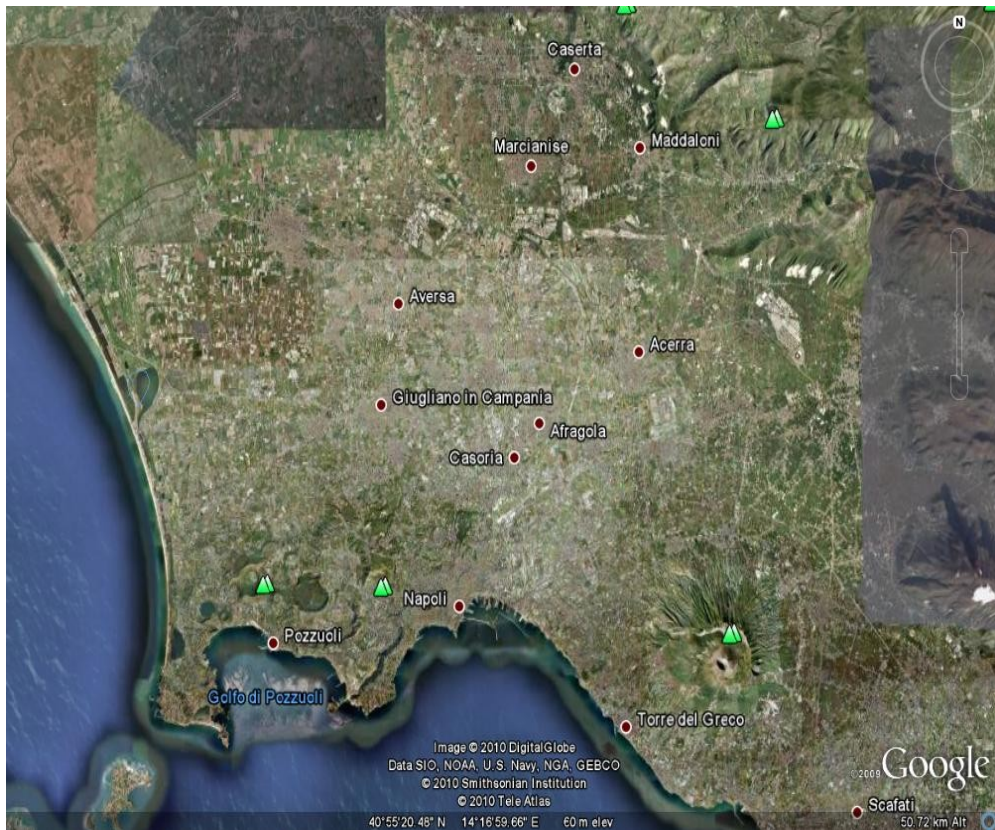


Figure V-3 Overview of the Caserta (Italy) metropolitan area at 20 km of altitude (Google image).

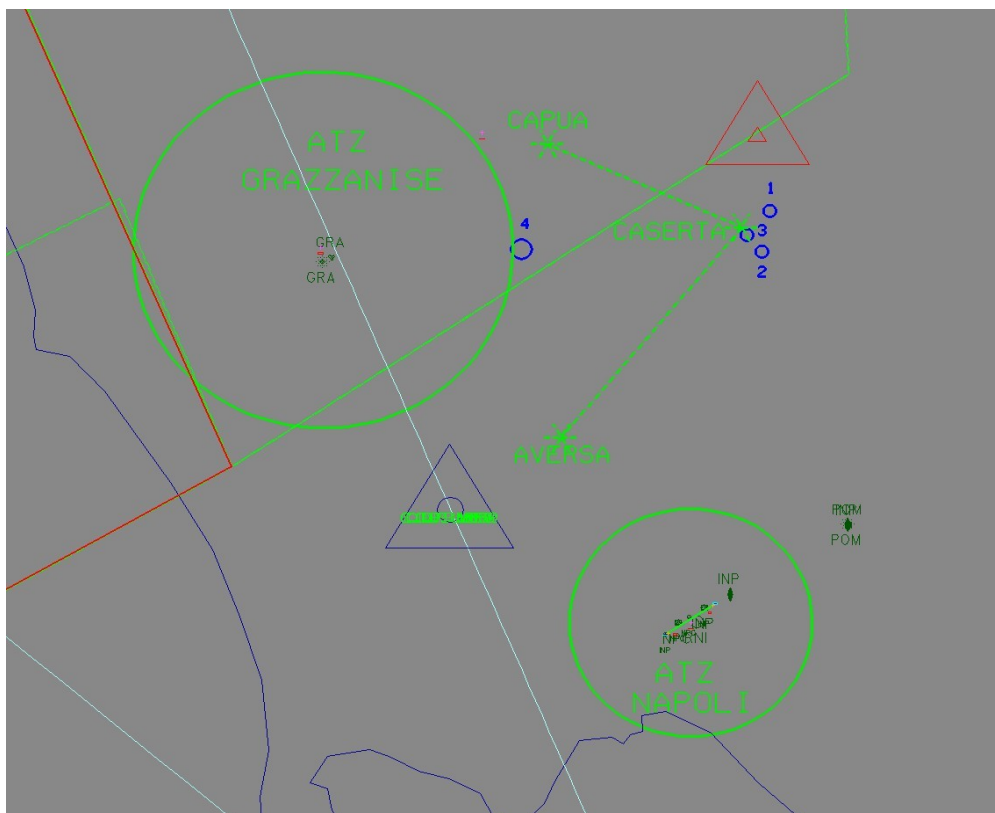


Figure V-4 Airport no flight zone (green circle); potential points of analysis (blue circle).

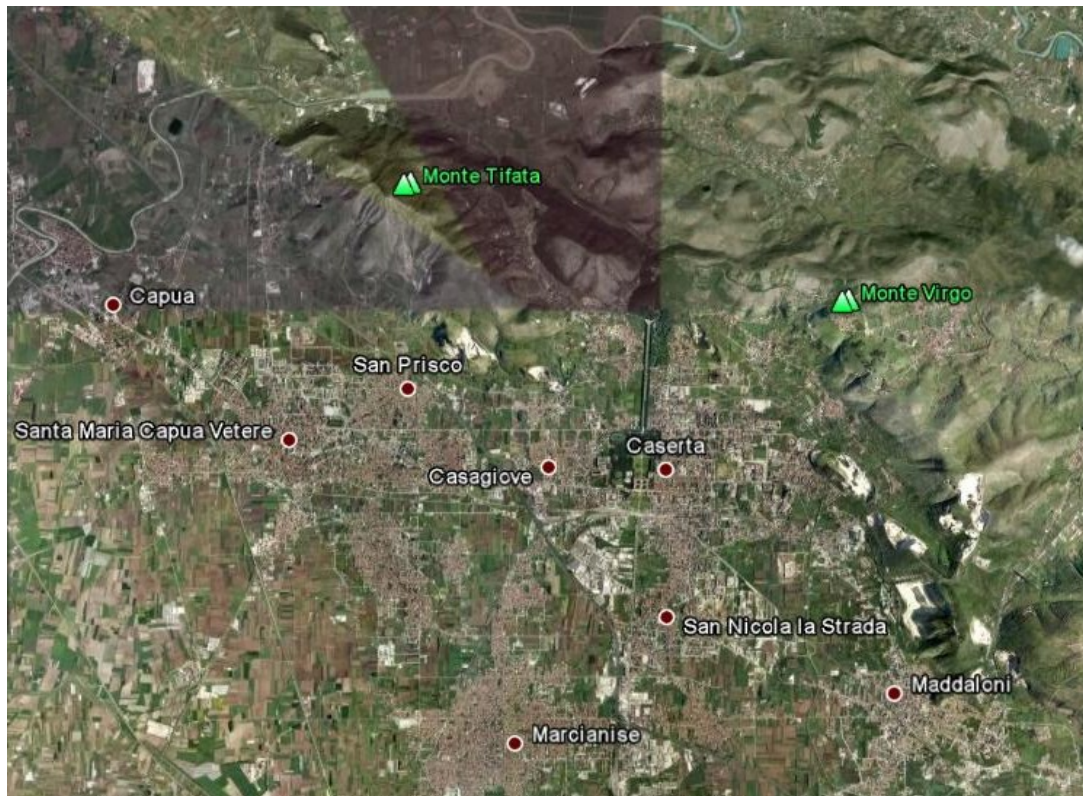


Figure V-5 the topography near Caserta city (Italy)



Figure V-6 Location of the selected launch site (B point); note the proximity to city center.

The training camp of the S.V.G. (Servizio Volontario Giovanile) good satisfy all the launch and safety requirements: it is very close to the town and it is away from airports; there is also enough space to operate in safety (Fig V-7) and no tall obstacles to the flight.

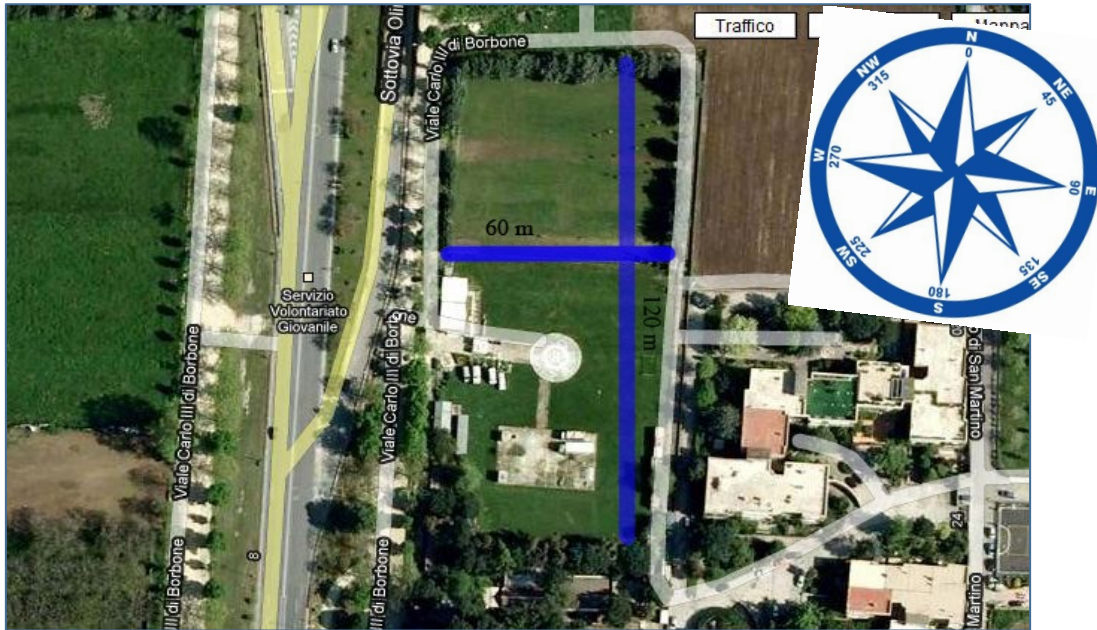


Figure V-7 Training Camp, Servizio Volontario Giovanile (SVG)
(410352.72'N, 141938.38'E WGS-84; 60 m above sea level, Caserta, Italy)

V.2. Launch operations

The section, summarized from the operational manual of the kytoon station (strictly required by ENAC and ENAV to obtain the NOTAM), describes the main sequences of the launch operations.

V.2.1. Weather forecast

Checking weather forecasts a suitable time period before the flight is mandatory for the safe operation of the system, as well as getting a good understanding of the usual weather conditions in the area of the flight and constantly observing real-time weather conditions.

The station should not be operated when thunderstorms or potential lightning conditions are observed in the area of flight, due to the potential of very high or gusty wind conditions, heavy precipitation and lightning. Any of these conditions may cause serious injury or death to the operators and damage to the equipment or surrounding property.

Flying during precipitations is not considered in the study for which this station is designed.

V.2.2. Inflation of kytoon

The inflation process requires that the kytoon is lying on a tarp to protect it from any possible damage.

If the operating area has a prevailing wind direction the launch platform should be positioned so that the rear end of the trailer is downwind of the prevailing wind direction (to minimize the probability of the kytoon impacting on the launch platform). If there is no prevailing wind direction, the orientation of the platform should be determined by the forecast wind direction during inflate (Fig. #F). The kytoon is to be deployed with the sail upwind and on the farther side of the tarp in respect to the launch platform.



Figure V-8 Tarp positioning.



Figure V-9 Blimp deployed on the tarp.

During the inflation and deflation operations there is a much higher risk of damage to the kytoon envelope than during normal flight operations. During these operations the kytoon envelope will be in various stages of partial inflation and much more susceptible to high wind or gusty conditions.



Figure V-10 Sail effect during inflating phase.

V. Launch site and procedures

In this partially inflated state, wind can create the potential for a sail effect (Fig. V-10), which could make the kytoon handling difficult. When fully inflated, the kytoon will be in its most aerodynamic shape and will be less susceptible to the sail effect.

Before the inflating phase (it takes about 40'), the EDD unit must be positioned while the blimp lies on the tarp (V-9).

Finally (Fig. V-11), the fully inflated kytoon is tethered to the ground through its three control lines, linked to four iron ballasts (80 Kg heavy).



Figure V-11 Fully inflated kytoon linked to the ground.

V.2.3. Preparation for mounting of payload.

While three operators control the inflating phase other two members of the crew will mount the CATFISH gondola (section IV.4.2).

The catfish is secured to the winch through the main tether line, while the kytoon is bound to the ground with a pulley (Fig. V-12) connected to ballasts and three safety lines, which are secured to the trailer.



Figure V-12 Pulley.



Figure V-13 Kytoon bounded trough the pulley (Red circle).

It is possible to use a pulley fixed to ballasts (Fig. V-13), firstly linked to the control line and subsequently to the main tether line; this configuration is useful during release and recovery phases. In fact, releasing the kytoon from safety lines and disengaging the pulley from the ballasts you can pick up the equipment slowly to avoid strains that can damage the structure of the catfish.

V.2.4. Preparation of the acquisition

with the gondola at 2 meters from ground an operator can shut on instruments and link the acquisition board to computer trough LAN cable (Fig. V-13). Thanks to this network operators can:

- Configure trough remote control AHRS-GPS dispositive fixing magnetic declination (calculable using *GeoMag* free software), calibrating the gyroscopes, setting the gravity constant and the dynamic filter of the inertial platform;
- Check the correct running of devices, displaying instantaneous data;
- Launch AHRS-GPS warm up that needs of 15', during which, also takes place the cleaning of chemical sensors;
- the APRS must be set and turned on;
- Launch acquisition.

Now is possible pick up the equipment for measurements.

V.2.5. Garaging or deflating balloon

Between two field days, if it isn't possible or set nocturnal flight, the balloon can be garaged on the collapsible cradle (Fig. IV-49, section IV.4). The only recommendation is to remove EDD unit from the top of the balloon to avoid accidental puncture and to recharge it.

V.3. Description of the Caserta Experimental Field tests

Table V-1 summarizes the Caserta experimental field during September 2010 at S.V.G.'s training camp. The kytoon were used both (separately or conjunctly) in tower mode (T) and profile mode (P); the winding speed of the ascending (↑) and descending phase (↓), the Stop Altitude (SA) and Averaging Time (AT), was selected in agreement with Ohara [(Ogawa Y., 1986), (Ohara T., 1989)] values, in order to well calculate turbulence statistics and altitude average values.

<i>Day</i>	<i>Time</i> [start-stop]	<i>Duration</i> [hours:min]	<i>Winding Speed</i> [m/min] ↑/↓	↑ <i>SA/AT</i> [m]-[min]	↓ <i>SA/AT</i> [m]-[min]
7	09:10-11:40	2:30	(2.5&5)/15	P	T (300/245/215/ 180/150/125/ 60/30)-10
7	13:20-16:20	3:00	15 /3.3	P	P
7	16:35-18:55	2:20	3.3/30	P	P
15	09:30-12:20	2:50	1.5/30	P	P
15	14:05-18:08	4:00	1.5/30	P	P
13	10:20-13:30	3:10	5/15	P	T (271/215/190/ 150/135/70/40)-(5-10)
13	14:00-17:30	3:30	5/15	P	T (100/80/50/30)-10
16	09:40-11:50	2:10	5/15	P	T (300/200/ 100/75/30) -10
16	12:00-14:25	2:25	5/15	P	T (220/175/125/ 100/75/50/30)-10
17	9:30-12:15	2:45	5/15	P	(270/150/125/ 100/75/45)-10
17	12:20-15:20	3:00	5/15	P	(275/200/ 100/75/45)-10

Table V-1 Caserta experimental campaign at S.V.G.'s training camp (September 2010).

V.4. Safety test

A flight test was necessary for various reasons:

- Validation of the operations manual;
- Estimation of the influence of the test site on the management of the system, both in the pre-flight and flight stages;
- Estimation of the correct team size and teamwork necessary to safely get the system airborne;
- Estimation of the flight dynamics of the system in the various phases of the flight.

The test was scheduled to take place at Capua City Airport on 24th of February 2010, but weather conditions delayed it until 26th.

The weather forecasts were checked since three days before flight. Once it was considered that the forecast weather conditions would permit the flight, a NOTAM was issued by ENAC spanning from 11:00 to 16:00 local time notifying the presence of a kytoon on the site.

The kytoon flight level was chosen to be, at most, 60 meters above ground level. It was not chosen to lift the system to a higher flight level because the height was considered sufficient to make the system stay out of the ground air turbulence, and also because additional flight authorizations from ENAC would have been needed if the kytoon flight level was to be increased.

According to the criteria listed in section V.1, Capua City Airport was chosen as the site for the flight test (Fig. V-14).

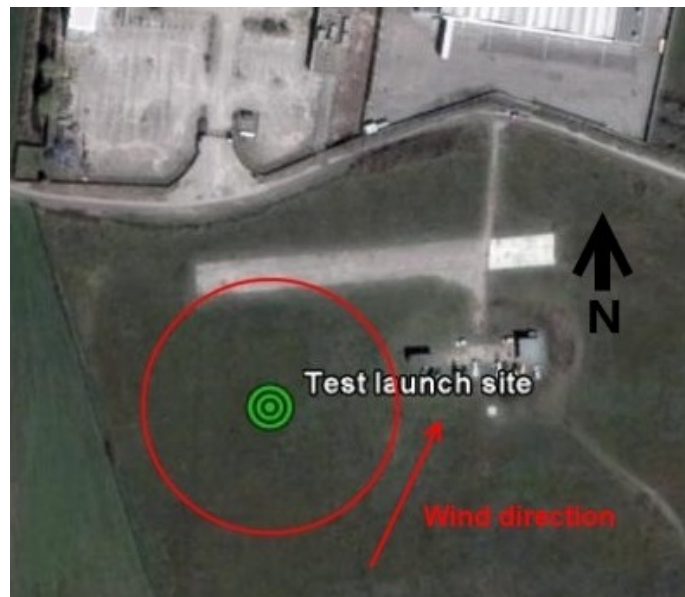


Figure V-14 Test launch site location at Capua City Airport (41° 7'3.88"N, 14°11'1.12"E). The red circle outlines a clear area 40 meters wide.

V. Launch site and procedures

This site guaranteed optimal conditions for the launch and the flight:

- Easily reachable zone nearby (5 km) Capua highway exit.
- Clear, flat area to deploy the launcher and kytoon unit.
- Airport area completely devoid of high obstacles, such as poles or high buildings.
- Ideal ground conditions (soft earth and grass) to anchor the launcher. trailer.

The operations on site spanned from 10.30 to 14.30, respecting the NOTAM requirements, and they involved six people. Since the scope of the test flight did not include gathering data, and to increase the safety of the project, the payload flown was a dummy derived from the one planned to fly in the scientific campaign, with the same dimensions and weight distribution (Fig. V-15).



Figure V-15 CATFISH gondola: dummy version used during Capua (CE, Italy) safety flight test (26th February 2010).

The weather conditions on site on the day of the test are described in table V-2.

<i>Temperature</i>	<i>Humidity</i>	<i>Pressure</i>	<i>Wind Velocity</i>	<i>Wind direction</i>
13°C	88%	1007 mb	15.1 m/s	SE – ESE

Table V-2 Mean weather conditions at sea level at the launch site on 26/2/2010.

VI *Data Reduction*

The developed kytoon station provides a lot of raw informations (well 38 variables!) that can be properly treated.

First, the chapter explains the strategy to synchronize the three set of data acquired, at three different sampling frequencies, by the gondola CPU board.

Second, it was shown how the heading measurement, given by the magnetometer, was compensated by the fixed external magnetic source.

Third, the anemometers' measurements are transported to NED reference and depurated by the relative motions, to calculate the true wind speed vector.

The possible calculations using the corrected measurements and obtainable in both the profile and tower mode, are finally discussed.

VI.1. Raw parameters

The following tables list the raw variables belonged by the sensors (the INU “control” parameters, defined in section IV.3.4 are omitted because they aren’t used in the interest calculations).

<i>File Column</i>	<i>Item</i>	<i>Symbol</i>	<i>Ref. System</i>	<i>Unit</i>
2	X-Velocity	U_{anm}	Anemometer	[m/s]
3	Y-Velocity	V_{anm}	Anemometer	[m/s]
4	Z-Velocity	W_{anm}	Anemometer	[m/s]
6	Sonic temperature	T^*	-	[°C]

Table VI-1 Anemometer raw data; sampling frequency: 32 Hz.

<i>File Column</i>	<i>Item</i>	<i>Symbol</i>	<i>Unit</i>
3	Static temperature	T	[°C]
4	Relative Humidity	RH	[%]
6	Carbon monoxide	CO	[V]
7	Nitrogen dioxide	NO_2	[V]
8	Ozone	O_3	[V]
9	Benzene	C_6H_6	[V]

Table VI-2 Air pollution sensor and thermo-hygrometer probe raw data; sampling frequency: 0.2 Hz.

<i>Data file order</i>	<i>Item</i>	<i>Symbol</i>	<i>Ref. System</i>	<i>Unit</i>
1	Pitch	α	DEV-NED	[rad]
2	Roll	φ	DEV-NED	[rad]
3	Yaw	ψ	DEV-NED	[rad]
6	Latitude	Lat	WGS-84	[°]
7	Longitude	$Long$	WGS-84	[°]
8	Altitude	z	WGS-84	[m]
20	Time last reset	t	-	[ms]
21	X-Velocity	U_{GPS}	NED	[m/s]
22	Y-Velocity	V_{GPS}	NED	[m/s]
23	Z-Velocity	W_{GPS}	NED	[m/s]
28	Pressure	p	-	[Pa]

Table VI-3 IG 500N data; sampling frequency: 50 Hz.

Note that the :

- The output of air pollutant sensors are in Volt; a calibration was performed by the manufacturer;
- The North axis of NED reference would be aligned with magnetic Nord in absence of any local magnetic field; instead, the *IG 500N device* is placed in the center of the masses of the CATFISH gondola, and suffers the magnetic influence of the other sensor, distributed around it. A calibration procedure was obliged;

- There are three sets of data sampled at three different frequencies, moreover the sensor that have the most precise time reference, is the *IG 500N* device⁹; the problem of data synchronization are discussed in the following section.

VI.2. Data synchronization

The *Vortex86* embedded CPU board interfaces:

- the anemometer (32Hz);
- the *IG 500 N* device (AHRS-GPS-barometer, 50Hz);
- Thermo-hygrometric probe and air pollutant sensors; these can be named “slow”, according to their sampling frequencies (0.2Hz).

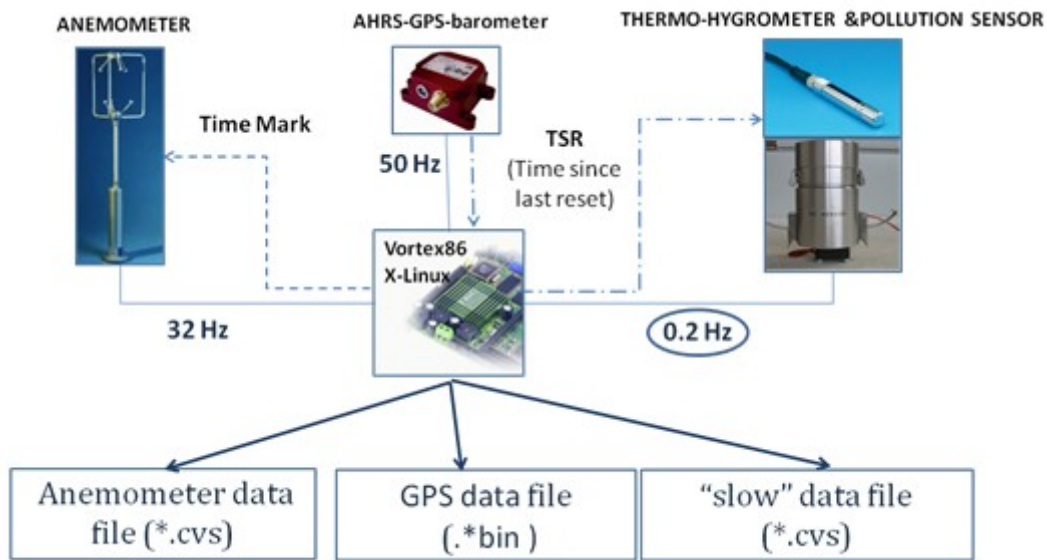


Figure VI-1 Scheme of the synchronization way.

After the CPU board has been connected via Ethernet port (section V.2.4), to external PC, it is possible to launch the acquire routine, using X-Linux terminal console. Three different file are written for the anemometer (Fig. VI-2), the *IG 500 N* (for simplicity we call it GPS), and the “slow” data (Fig. VI-3).

```

00Q,+000.004,-000.013,-000.007,M,+025.71,00,+0.0831,+2.4294,+0.0050,+0.0031,004
00Q,+000.004,-000.014,-000.007,M,+025.74,00,+0.0831,+2.4294,+0.0050,+0.0031,006
00Q,+000.001,-000.014,-000.008,M,+025.62,00,+0.0831,+2.4244,+0.0050,+0.0031,006
00Q,+000.001,-000.008,-000.006,M,+025.69,00,+0.0831,+2.4244,+0.0050,+0.0031,00E
00Q,+000.001,-000.009,-000.006,M,+025.67,00,+0.0831,+2.4156,+0.0050,+0.0031,001
00Q,+000.002,-000.011,-000.005,M,+025.66,00,+0.0831,+2.4156,+0.0050,+0.0031,007
00Q,+000.005,-000.010,-000.007,M,+025.69,00,+0.0843,+2.4037,+0.0050,+0.0031,001
00Q,+000.006,-000.013,-000.006,M,+025.74,00,+0.0831,+2.4037,+0.0050,+0.0031,009
  
```

Figure VI-2 Structure of the Anemometer data file; Time mark in evidence (black circle)

⁹ The *IG-500N* outputs a UTC time reference derived from the internal GPS receiver. This time references the sample time, with an accuracy better than 1 μ s. This output contains the full date information: Year, Month, Day, Hour, Minutes, Seconds, and Nano-Seconds.

VI. Data reduction

1	2	3	4	5	6	7	8	9	10
12/05/2010 09:49	0.020	0.020	23.7	55	1.318	2.561.000	3.299	0.658	11310420
12/05/2010 09:49	0.000	0.020	23.7	55	1.331	2.519.000	3.314	0.660	11315560
12/05/2010 09:49	-0.180	0.160	23.7	55	1.377	2.442.000	3.314	0.647	11320440
12/05/2010 09:49	-0.100	-0.020	23.7	55	1.396	2.586.000	3.299	0.670	11325400
12/05/2010 09:49	-0.080	0.180	23.7	55	1.397	2.474.000	3.315	0.653	11330440

Figure VI-3 Structure of the “slow” data file; 10th column reports the TSR.

Tables VI-2,3 allow to indentify the variables directly in to *.cvs file of the anemometer and “slow” sensors; table VI-3 show the writing sequence of the variables to the GPS binary file.

The synchronization is possible thanks to the combined use of the GPS’s time since last reset (TSR) and the “time mark”. Every 5s (or with frequency of 0.2Hz) the Vortex86 board writes the TSR, reads from the GPS device, to the “slow” data file and simultaneously sends to the anemometer, via one of the two analogical input ports which it is equipped with, an input signal in volts (time mark). This one appears in the Anemometer file (Fig. VI-1) and can be univocally distinguished since it ranges between 0.1-5 V (lower/upper values are not considered). So the record in correspondence of the first time mark can be directly related to that of the “slow” data file, and thanks to the TSR, to the GPS one, too. Between two consecutive time marks the anemometer would have performed about 160 sampling while, between the two correspondents TSR, about 250 records to the GPS file results. Consequently a “spline” interpolation has been used to reduce GPS data.

To verify the procedures, a synchronization test has been performed.

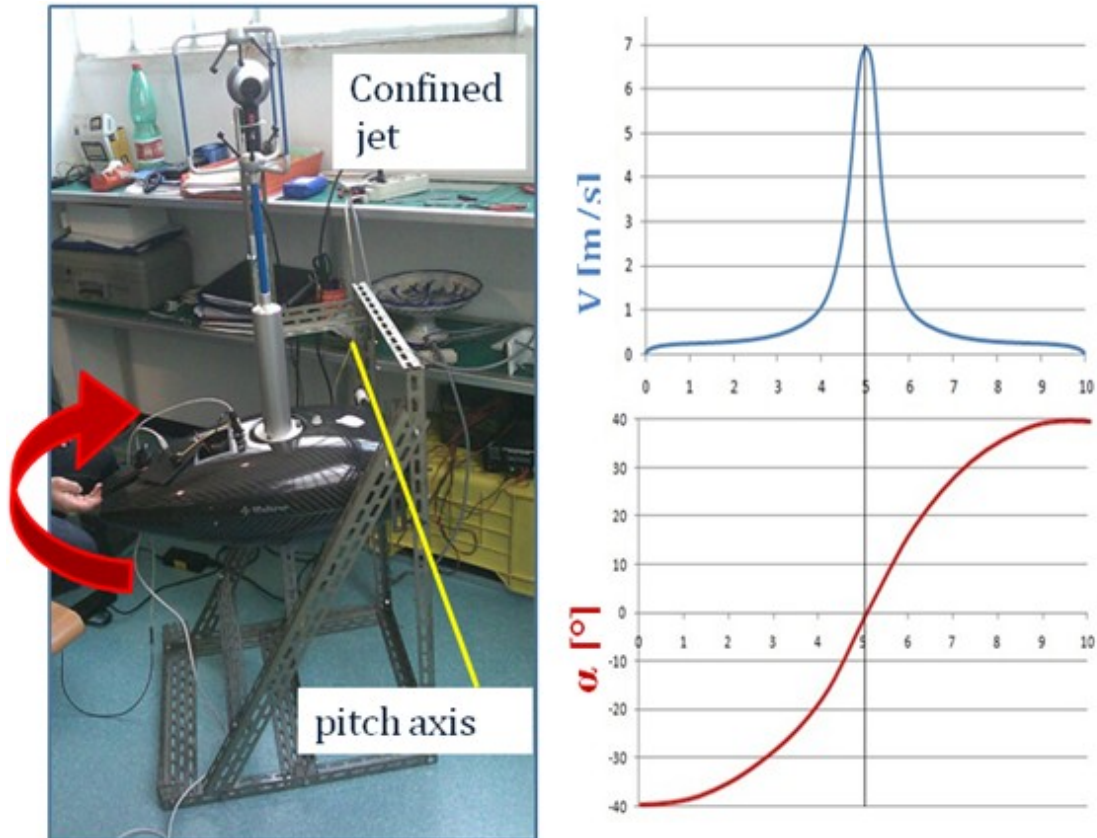


Figure VI-4 Synchronization test: experimental apparatus (left) and expected results (Right).

VI. Data reduction

The CATFISH nacelle was bound by an iron structure so that can only rotate about its axis of pitch (Fig. VI-4 left). A confined jet, generated by a phone (other solutions were tested too), was directed along Y-direction of the anemometer's coordinate system (aligned to pitch axis one), so that at the same fixed angle of pitch the anemometer could register non-zero speed (Fig. VI-4 right). The gondola was made to oscillate up and down manually in the range about $[-40, +40]^\circ$, growing the angular speed.

A lot of tests were performed to make sure its repeatability. One of these is shown (Fig. VI-5).

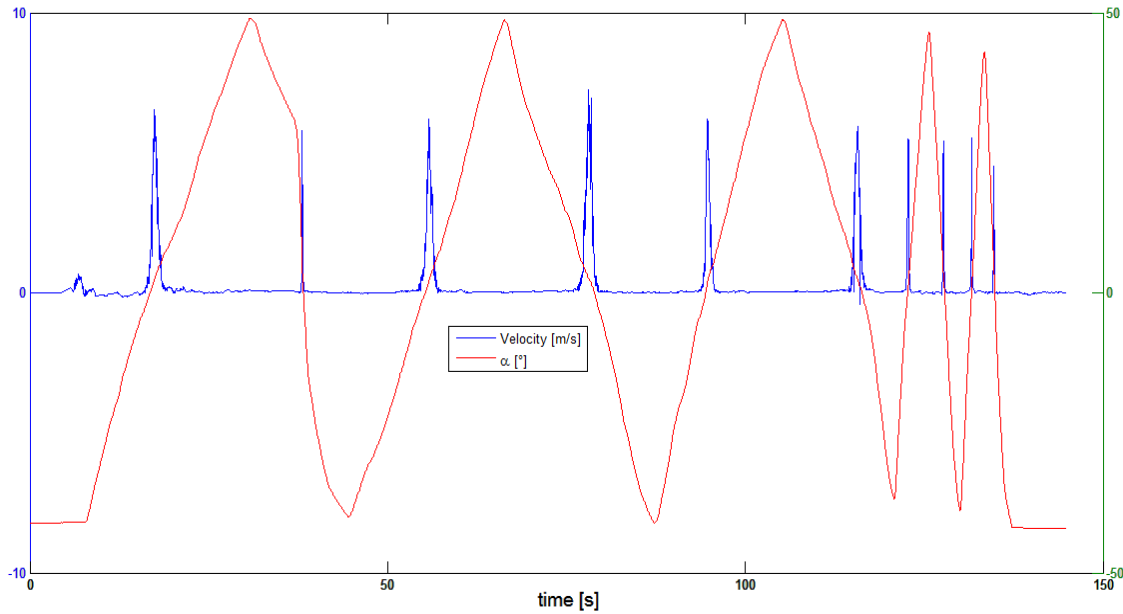


Figure VI-5 Synchronization test result.

VI.3. Air pollution sensors calibration

UniTech provided the calibration curve of table VI-4, tested in the ranges of table VI-5.

<i>Pollutant</i>	<i>A</i>	<i>B</i>	<i>C</i>	<i>Calibration Curve</i>
<i>CO</i> (440< <i>X</i> <5074.223)	0.279	3.873e-6	2	$Y = A + B X^C$
<i>CO</i> (296< <i>X</i> <440)	0.1	0.00625	296	$Y = A + B \cdot (X - C)$
<i>O₃</i> (47.23604< <i>X</i> <5299.92)	-31.6	5330.9	-0.598	$Y = A + B X^C$
<i>NO₂</i> (235.15< <i>X</i> <4921.1849)	1397.742	-164.415	-	$Y = A + B \ln(X)$
<i>C₆H₆</i> (372< <i>X</i> <1928)	-2.0003	0.0062238	-	$Y = B^2 X^2 + 2 A B X + A^2$

Table VI-4 UniTech Sens3000, calibration curves.

Y is the concentration of the pollutant ($[\mu\text{g}/\text{m}^3]$, except *CO* curves that are expressed in mg/m^3) while *X* is the tension from the sensors $[\text{mV}]$. Negative values of concentration can be treated as under the scale and must be fixed to zero while those out of scale can be fixed to maximum ranges of table VI-5.

<i>Pollutant</i>	<i>Minimum concentration</i> <i>($\mu\text{g}/\text{m}^3$)</i>	<i>Maximum concentration</i> <i>($\mu\text{g}/\text{m}^3$)</i>
CO	100	100000
O ₃	0	800
NO ₂	0	500
C ₆ H ₆	0.1	100

Table VI-5 Calibration range of the pollutants' concentration.

The thick film solid state sensors are very sensible. A warm up of about 5-10 min is required, particularly if the sensors has been in closed ambient, as room too (e.g. in a closed room, wall paint compromise deeply measurements!)

VI.4. Magnetometer calibration

IG 500N device is fully calibrated in factory. As for other sensors a full temperature compensation is performed on magnetometers, as well as cross-axis and misalignment correction. However, magnetic sensors are very sensitive to their close environment (mainly the object on which they are strapped) : Some materials can generate magnetic fields that will be summed with Earth magnetic field, and some other can distort the existing magnetic field. These effects will be measured by magnetometers and will not be distinguished from the Earth magnetic field, and therefore error will occur in heading estimation. The amount of error can be really significant in some cases.

There are two kinds of distortions:

- Hard Iron distortions: This kind of distortion is caused by magnets, or anything that act as a magnet. It is very easy to magnetize objects like screws or nuts. Hard irons generate magnetic fields that are summed with the Earth magnetic field. Hard Iron effect shifts the magnetic field measured by magnetometers by a constant offset, whatever the device orientation is. Power supplies, which generate high current (several amperes) and their associated wires, may generate magnetic fields.
- Soft Iron distortions: These kinds of distortions are caused by ferromagnetic objects that are placed in the vicinity of the device. Iron, and some steels for example are ferromagnetic materials, but more generally, anything that sticks to a magnet is ferromagnetic. Ferromagnetic materials do not generate their own magnetic field. Instead of that, they react to existing magnetic field (in our case Earth magnetic field). So, Soft Irons can distort the local magnetic field in a different way at each orientation. This is why soft Irons are much more difficult to compensate for.

It is important to differentiate two origins of distortion:

- Distortions that come from materials which are fixed with respect to the device coordinate frame (can be compensated).
- Distortions that are not fixed with the device, and move independently with respect to the device, or distortions that change over time (can't be compensated).

VI. Data reduction

The *IG 500 N* device in our case is placed in the center of the CATFISH nacelle's masses, so that all the other sensor are around it at fixed distance, as all the ferromagnetic elements. Consequently there are both Hard and Soft iron effects but, because they are fixed respect to the magnetometers, fortunately they can be compensated by using the following calibration procedure.

- 1) Fixing Magnetic Nord direction via external source; the x-axis of DEV coordinate system (line between the Nord spar on anemometer's mounting flange and the yellow screw's head Fig. VI-6) is aligned with the Nord fixed by compass.



Figure VI-6 Magnetometer Calibration: x-axis of DEV coordinate system (line between the Nord spar on anemometer's mounting flange and the yellow screw's head) is aligned with magnetic Nord fixed by compass; *IG 500N* device connected to external PC via USB connection cable (white).

- 2) Connecting the INU device to a PC via USB connection cable; the *SbgCenter* interface software, installed on the PC, provide the power to the device and allows to monitor the heading angle (yaw angle); when the other instrumentation is OFF it has been possible to evaluate the soft iron effects: no deviation on the heading angle results.
- 3) Gondola ON a with INU disconnected; in this way, using *SbgCenter* software, a deviation of heading has been verify (Fig. VI-7) due to Hard iron effects (magnetic fields induced by other instruments).
- 4) Gondola ON with INU connected; Here the yaw angle is sampled via standard acquisition method (embedded); Hard iron effects affect in a different way heading measurement, generating oscillation bigger in amplitude and in period (Fig. VI-8); using a bigger temporal observation window (400s), very close value of mean has been calculated (-6.1°) .

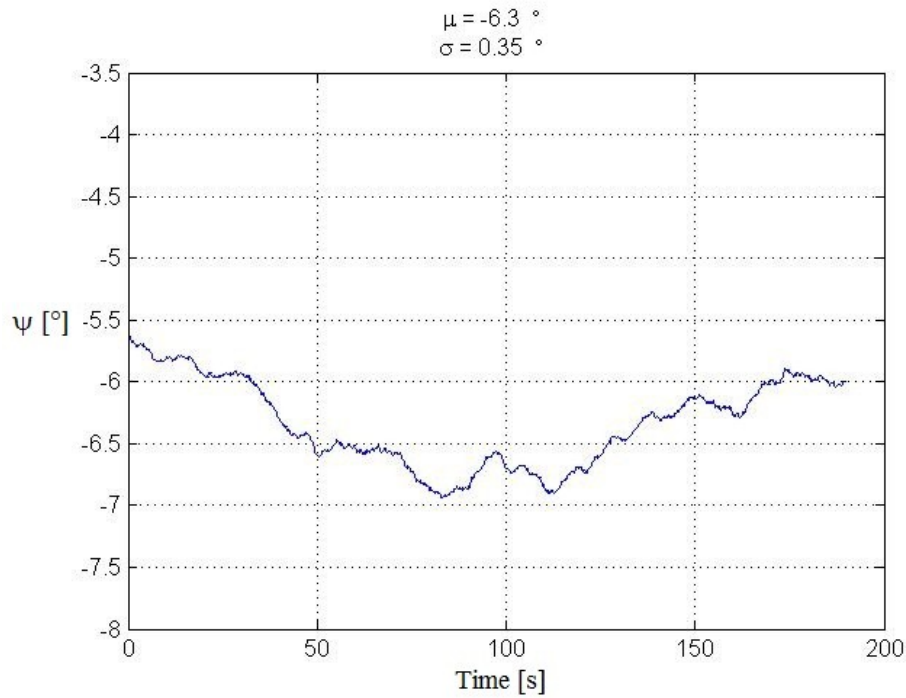


Figure VI-7 Magnetometer calibration; INU disconnected: Hard Iron effects' heading deviation; average (μ) and standard deviation (σ) are shown.

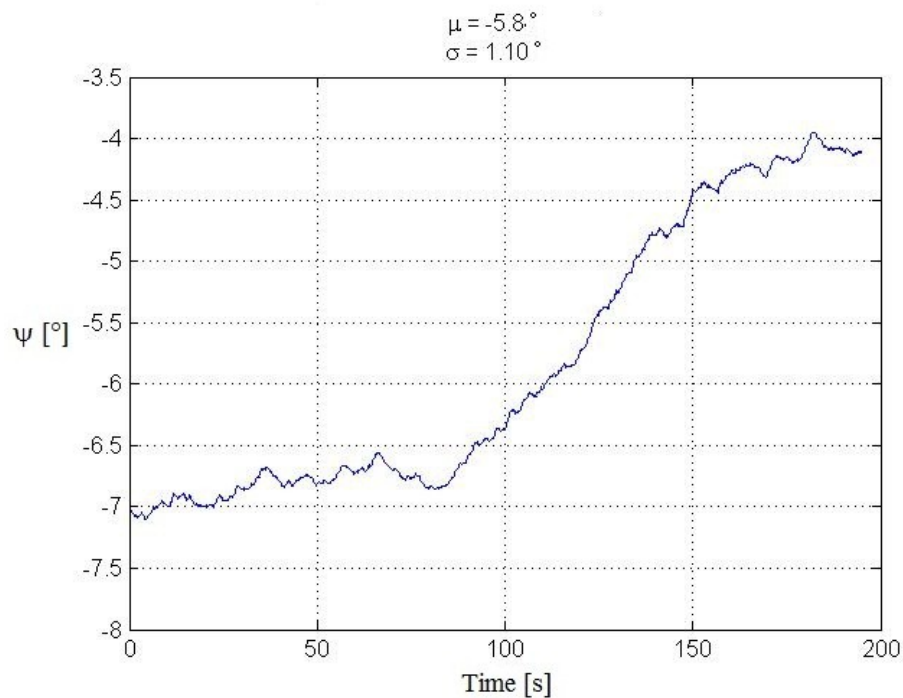


Figure VI-8 Magnetometer calibration; INU connected: Hard Iron effects' heading deviation; average (μ) and standard deviation (σ) are shown.

- 5) Sbg calibration procedures: it is obtained with the magnetometer calibration tool of the *SbgCenter* software (INU is again connected via USB connection cable to external PC).

The main goal of the procedure is to rotate at slow rate (300°/s) the device in different orientations to measure the magnetic field (gondola ON). SBG Systems' algorithms are able to map the magnetic distortions in each orientation and compensate for them. The

more orientations will be passed through, the best will be the results; a minimum of 9 significantly different orientations is required to perform a good calibration.

The CATFISH gondola has been kept away from at least 3 meters all external sources of magnetic disturbances (as well as computers, chairs, desks, etc.).

The calibration procedure has been repeated outdoors until the yaw angle, displayed by *SbgCenter*, was about 0° .

- 6) Calibration verification: finally a set of repeated tests was conducted with standard acquisition method. The result of one of these test are plotted in figure VI-9.

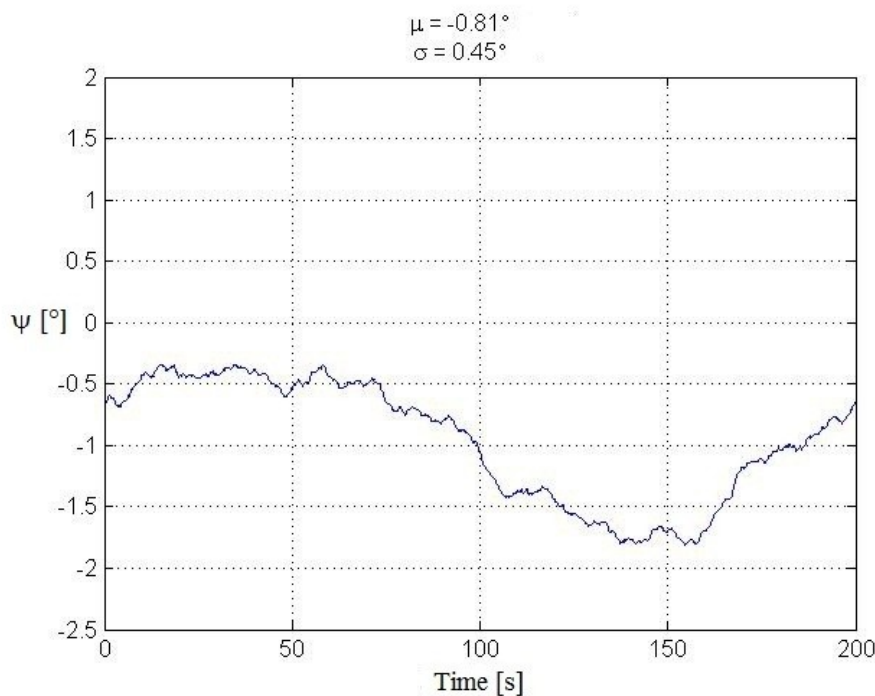


Figure VI-9 Magnetometer calibration verification; average (μ) and standard deviation (σ) are shown.

In spite of the big care in calibration procedure, not very easy because of the anemometer dimension, there is a residual value of the heading deviation of about -0.5° , for the first 60s, that begin to oscillate around -0.8° value after 100s. This mean value has been taken in to account especially considering that the magnetic declination (angle between local magnetic and Geographic Nord directions) calculated (by *GeoMag* software) at experiment site and dates ranges 2.3 - 2.5° .

VI.5. Wind calculation

Wind, as explained in section I.4, is commonly measured in to NED coordinate system; particularly it can be decomposed in to three components: two on the local horizontal plane (U , V) and one on the local vertical direction (W). These are quite different from the raw ones measured by the anemometer (Tab. VI-1), which moves in to NED reference, measuring apparent wind speeds.

VI. Data reduction

The INU helps us in this calculation: the *IG 500N* is rigidly mounted respect to the anemometer so that their coordinate reference systems coincide, except for the origin (Fig. VI-10).

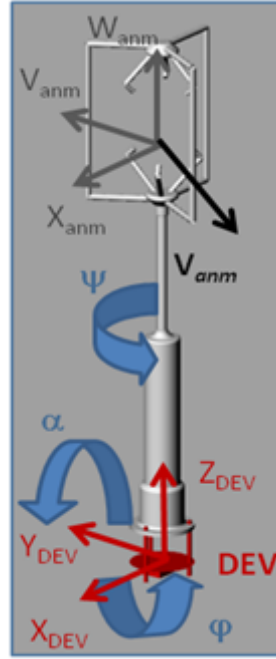


Figure VI-10 Relative motions correction.

Hence, they will be known the position ($s(t) = [Lat(t), Long(t), z(t)]$, in WGS-84 system) and all the movements of the anemometer, which can be more in general three translations and three rotations (six d.o.f. in the space) respect to NED coordinate frame¹⁰. Because the CATFISH gondola oscillates little respect to the balloon, which is suspended below, all the corrections using the angular speeds are negligibly. In fact has been observed that movements are limited to only rigid translations in to NED during all flight tests, except the start and end phase of the launch, where ground operation took place.

Using the Direct Cosine Matrix (*DCM*), build up by the knowledge of the instantaneous Euler angles (α , φ , ψ), it is possible to transport the anemometer speed vector to NED reference as follows:

$$\mathbf{V}_{anm} \equiv (U_{anm}, V_{anm}, W_{anm}) \quad (VI.1)$$

$$\mathbf{V}_{anm_{NED}} = DCM \cdot \mathbf{V}_{anm} \quad (VI.2)$$

$$DCM = \begin{pmatrix} \cos \alpha \cos \psi & \sin \varphi \sin \alpha \cos \psi - \cos \varphi \sin \psi & \cos \varphi \sin \alpha \sin \psi + \sin \varphi \sin \psi \\ \cos \alpha \sin \psi & \sin \varphi \sin \alpha \sin \psi + \cos \varphi \cos \psi & \cos \varphi \sin \alpha \cos \psi - \sin \varphi \sin \psi \\ -\sin \alpha & \sin \varphi \cos \alpha & \cos \alpha \cos \varphi \end{pmatrix} \quad (VI.3)$$

Subtracting the velocity vector of the device measured by the GPS in to NED reference,

$$\mathbf{V}_{GPS} \equiv (U_{GPS}, V_{GPS}, W_{GPS}) \quad (VI.4)$$

¹⁰ Tilt correction: see (Wilczak, 2001).

VI. Data reduction

finally we obtain that:

$$(V_{wind})_{NED} = V_{anm_{NED}} - V_{GPS} \quad (VI.5)$$

Figures VI-11,12 show $(V_{anm})_{NED}$ and V_{GPS} and their means (μ) and standard deviations (σ) and the typical position (horizontal and vertical) and speed (GPS) accuracies.

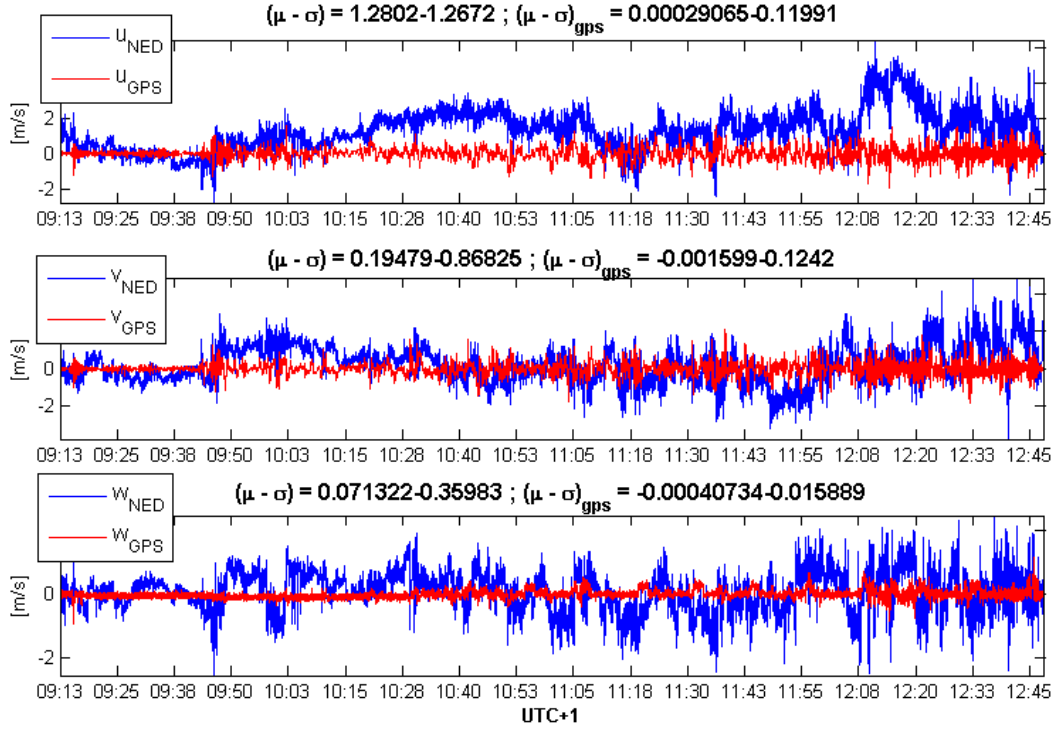


Figure VI-11 Wind velocity correction (7/9/2010): Anemometer's ($U_{NED}, V_{NED}, W_{NED}$) and GPS's ($U_{GPS}, V_{GPS}, W_{GPS}$) measurements; average (μ) and standard deviation (σ) are shown.

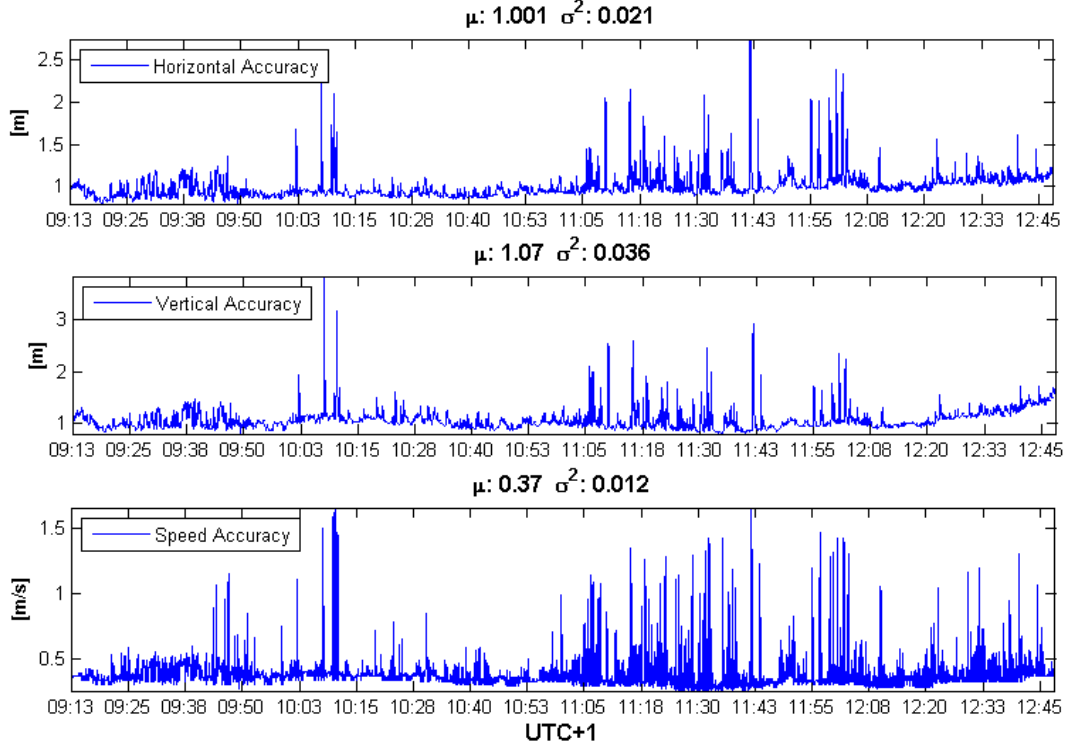


Figure VI-12 Accuracies of the speed (GPS) and position measurements; average (μ) and variance (σ^2) are shown.

VI.6. Profile mode calculations

When the kytoon station continuously rises (falls) up (down) to (from) top altitude, it says that you are working in the *profile mode*.

The measurements, function of time and space, are altitude averaged, since the high number of the sampling [e.g. (Ogawa Y., 1986), (Ohara T., 1989)]. The variables that can be represented are:

- Wind speed module and direction: according to literature we focus on longitudinal, vertical and cross wind component (U, V, W); these are simply obtainable rotating the horizontal component of $(V_{wind})_{NED}$ (calculated in previous section) on the mean (it has the major occurrences) direction of the wind (U direction);
- Static temperature (T), potential temperature (θ), virtual potential temperature (θ_v) and Specific Humidity (q); not that the measurements of thermo-hygrometric probe has been used (no high sampling frequency was required); the calculation procedures are shown in chapter I;
- The calibrated air pollutants' concentrations of O_3 , CO , NO_2 , C_6H_6 ;
- The Bulk Richardson Number (Ri_B).

It is important to note that:

- according to literature [e.g. (Ogawa Y., 1986), (Ohara T., 1989)] the ascending (descending) rate range between 3-30 m/min;
- all the variables are averaged on 10m of altitude, using an average moving filter.

In the following section are given the definitions of Richardson Number.

VI.6.1. Richardson Number

By comparing the relative magnitudes of the shear production and buoyancy consumption terms of TKE equation (Stull, 1988) [see also (Jerevic, 2006), (Launiainen, 1995), (Sharan, 2003), (Zoumakis, 1991)] we can hope to estimate when the flow might become dynamically unstable. The resulting ratio is called Flux Richardson Number is given by:

$$R_f = \frac{\left(\frac{g}{\vartheta_v} \right) (\overline{w' \vartheta_v'})}{\overline{(u_i' u_j')} \frac{\partial \overline{U_i}}{\partial x_j}} \quad (VI.6)$$

The denominator consists of 9 terms (there are the kinematic flux components).

For statically unstable flows (turbulent), R_f is usually negative; for neutral flows, it is zero; for dynamically stable flows (that become laminar), it is positive.

VI. Data reduction

This occurs because in a statically stable environment turbulent vertical motion are acting against the restoring force of gravity (buoyancy suppress turbulence while wind shears tend to generate it).

In the hypothesis of horizontal homogeneity and neglecting subsidence; assuming that the value of $\overline{w'\vartheta_v'}$ might be proportional to the lapse rate $\partial\overline{\vartheta_v}/\partial z$, that the value of $\overline{u'w'}$ is proportional to $\partial\overline{U}/\partial z$ and that the value $\overline{v'w'}$ is proportional to $\partial\overline{V}/\partial z$, is possible define a new ratio called the gradient Richardson number:

$$Ri = \frac{\left(\frac{g}{\overline{\vartheta_v}}\right) \frac{\partial\overline{\vartheta_v}}{\partial z}}{\left[\left(\frac{\partial\overline{U}}{\partial z}\right)^2 + \left(\frac{\partial\overline{V}}{\partial z}\right)^2\right]} \quad (VI.7)$$

If we approximate $\partial\overline{\vartheta_v}/\partial z$ by $\Delta\overline{\vartheta_v}/\Delta z$, and approximate $\partial\overline{U}/\partial z$ and $\partial\overline{V}/\partial z$ by $\Delta\overline{U}/\Delta z$ and $\Delta\overline{V}/\Delta z$ respectively, we can define a new ratio known as the bulk Richardson number:

$$Ri_B = \frac{g\Delta\overline{\vartheta_v}\Delta z}{\overline{\vartheta_v}[(\Delta\overline{U})^2 + (\Delta\overline{V})^2]} \quad (VI.8)$$

This is the most frequently used definition in meteorology, because experimental measurements are supplied at discrete points in the space. The Richardson number, as well defined, says only about the probability of turbulence's presence (Fig. VI-13).

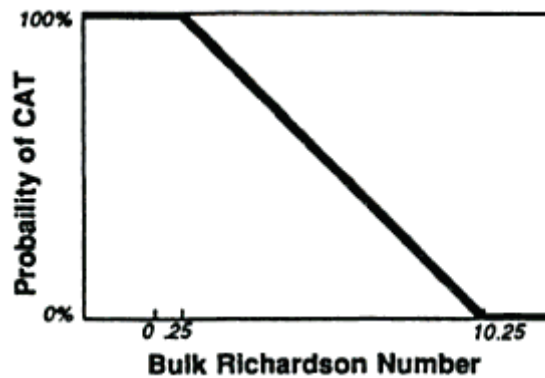


Figure VI-13 Relationship between the bulk Richardson number, over a layer and the probability of turbulence within that layer.

VI.7. Tower mode calculations

If during the kytoon station's ascending (descending) phase there are fixed pauses on the tether cable release (withdrawal), it says that you are working in the *tower mode* (this is because, presumably, the balloon stays at fixed altitude during the stop phases, as a tower).

This way allows to calculate the vertical profiles of the following turbulent characteristics:

VI. Data reduction

- Turbulent fluctuation signals ($u'(t)$, $v'(t)$, $w'(t)$ and $\theta_v^{*'}(t)$ (or $\theta^{*'}(t)$, or else $T^{*'}(t)$);
- Their variances, standard deviations, and turbulent spectra;
- The TKE;
- Fluxes (or covariances), particularly those between $u'(t)$ and $w'(t)$, $w'(t)$ and $\theta_v^{*'}(t)$;

The typical time period (correspondent to stop phase) used for a good calculation ranges between 5-10 min [e.g. (Ogawa Y., 1986), (Ohara T., 1989)]. The fluctuations are computed as shown in section I.4, subtracting to the signal the time average value, computed during the stop period.

It is important to note that the kytoon has been observed to oscillate around an equilibrium altitude, to which the turbulent characteristics were referenced to; only variation over the average altitude less than 20% had been accepted.

In addition to turbulent profiles, mean profiles can be extracted, too.

In the following sections are described:

- how to calculate and to show a turbulent energy spectra;
- the methods of calculation of vertical kinematic eddy heat flux ($\overline{w'\theta_v'}$);
- the linear correlation coefficient between two variables.

The calculation of variances and fluxes more in general had been already shown in section I.5.

VI.7.1. Turbulent energy spectra

As said in section I.5.2, the energy spectrum of atmospheric turbulence allows to learn about the contribution of each different size eddy to the total turbulence kinetic energy.

To calculate the spectrum of a generic signal is necessary to define the Fourier transform of which there are two several formulations. The first is related to continue signals

$$A(f) = \int_{-\infty}^{+\infty} A(t)e^{-j2\pi ft} dt \quad (VI.9)$$

where $A(t)$ is a generic continue signal, j is the imaginary unity, f is the frequency.

The second is related to discrete signals

$$A(k) = \sum_{n=0}^{N-1} A(n)e^{-\frac{2\pi j}{N}kn} \quad k = 0,1,2,\dots,N-1 \quad (VI.10)$$

where $A(n)$ is a generic discrete signal, N is the numbers of samples.

VI. Data reduction

In our case, having worked with discrete signals, we referred to the second formulation; in particular, we used the FFT (Fast Fourier Transform) algorithm to reduce the computational cost.

A generic discrete signal $A(n)$ is represented by a sequence of N samples referred to a sampling frequency F

$$F = \frac{1}{P} \quad (\text{VI.11})$$

where P is the sampling period.

The estimate of the spectrum was obtained using the *periodogram* method that consists of the following operations:

- It is calculated the Fourier transform $A(k)$ with the FFT algorithm obtaining N samples related to N equally spaced frequencies between 0 e F ($0, F/N, 2F/N, \dots, (N-1)F/N$)
- We consider the first $N/2$ samples of the FFT (Shannon's theorem) and it is calculated the sequence of samples of the estimate of the spectrum $S_A(k)$ in the following way:

$$S_A(k) = \frac{1}{N} |A(k)|^2 \quad (\text{VI.12})$$

The graphical presentation of spectra is very important: it must highlight the important peaks and other characteristics and show all portion of the wide range data.

Van Der Hoven represented (Fig. VI-14) the product fS , where S is the spectrum of wind speed near the ground and f the frequency, using a semilog plot (Van Der Hoven, 1957). It is visible the spectral gap, that is a large valley that separates the microscale from the synoptic scale peaks (at about 10^{-2} cycles/hours). The atmospheric turbulence energies peaks lie at the lowest frequency, starting at about 1 to 10 cycles per hour (Fig. VI-14). The middle frequencies are associated with the inertial subrange, which is important for estimated dissipation rates; instead the highest ones are associated with the dissipation of TKE into heat by viscous effect.

Note that the area under any portion of the curve is proportional to the variances.

When spectrum is plotted in to log-log space, a wide range of frequencies can be displayed and any power law relationship between S and f appear as straight line with $-5/3$ slope (Fig. VI-15), (Grachev, 1994). Now the area under the curve is no longer proportional to the variance.

The most used representation of the spectra uses a log-log plot of fS and f . It is possible to identify the power law of the inertial subrange ($-2/3$ power law) and a wide range of frequencies and spectral densities can be displayed. Very common is to make dimensionless both the axis.

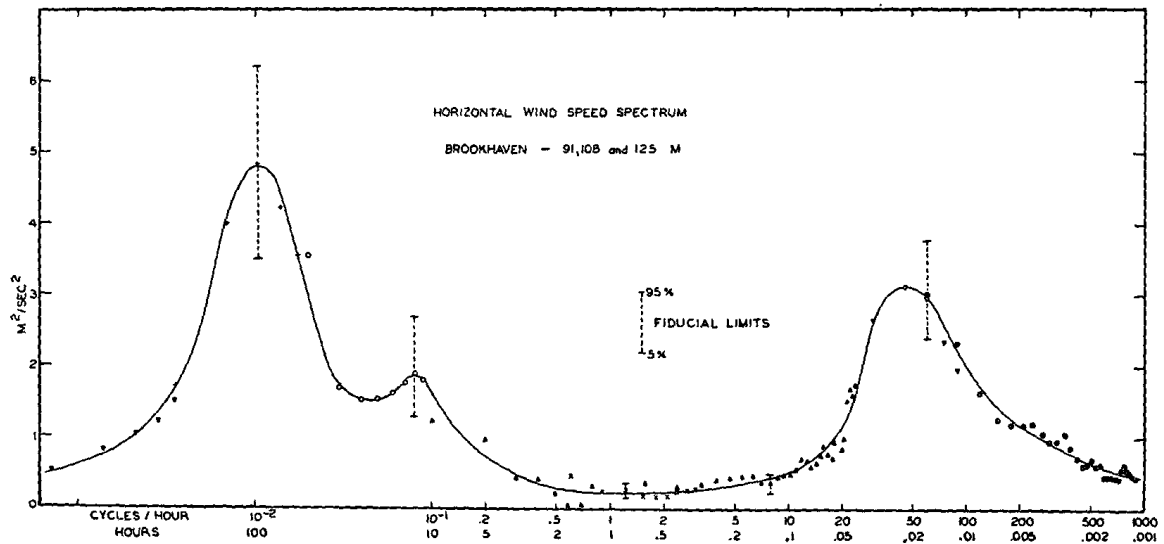


Figure VI-14 Horizontal wind-speed spectrum at Brookhaven National Laboratory at about 100m height (Van Der Hoven, 1957).

The ordinate axis has the dimension of a variances of the measurement (but the area under the curve is not proportional to it); the abscissa one has the dimension of a frequency (1/s).

A lot of scaling variables are used in literature. Friction velocities (Weber, 1999) and temperature (u_* , v_* , w_* and θ_*), mean horizontal wind component and altitude of measurement are the most used [(Busch, 1968), (Kaiser, 1999), (Li, et al., 2005), (Hongstrom U., 2002) and (Al-Jiboori, 2001)].

Roth in 2000 preferred to use variances instead friction variables in its review work (Roth, 2000) (Fig. VI-16). The use of different scaling solution is given by the same Grachev (Grachev, 1994), Kaimal (Kaimal, et al., 1972) and Zhang (Zhang H., 2001).

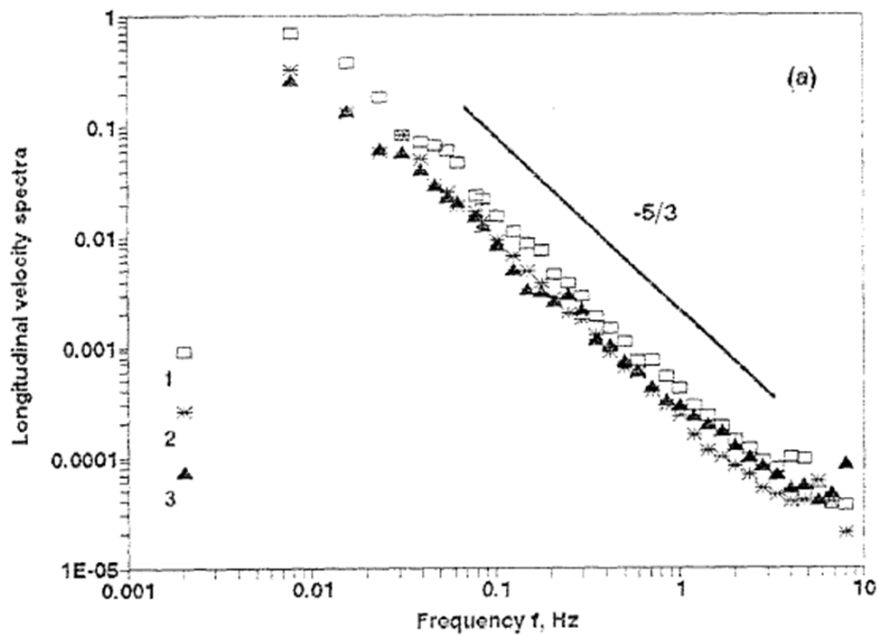


Figure VI-15 Power density spectra (m^2/s) of longitudinal velocity in log-log space (Grachev, 1994); -5/3 power law is shown.

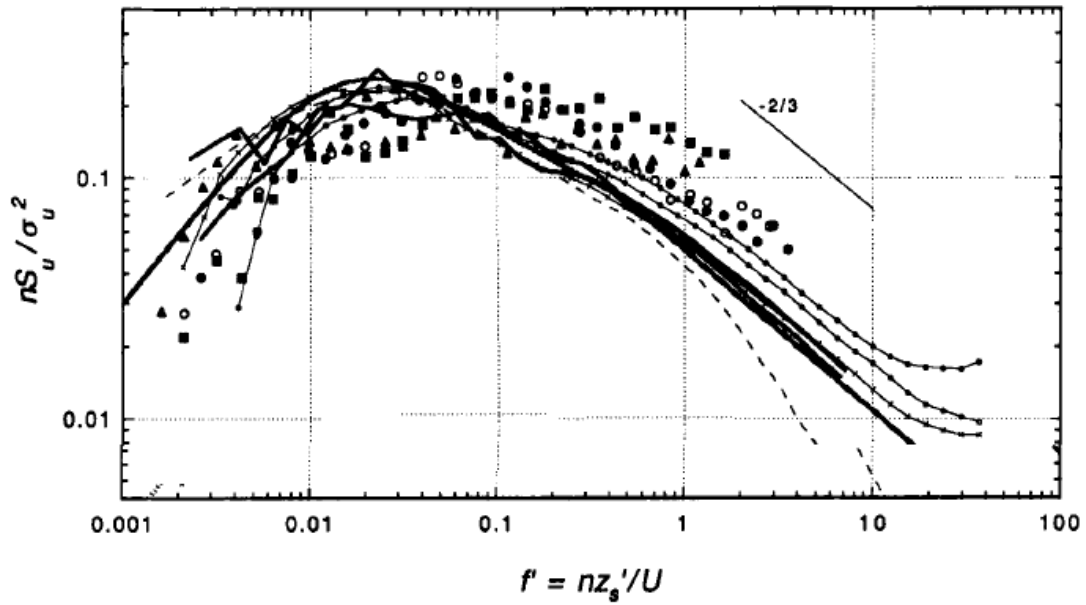


Figure VI-16 Dimensionless power density spectra of longitudinal velocity in log-log space (Roth, 2000); n is the frequency; z'_s is the altitude of the measurements; U is the mean horizontal wind; $-2/3$ power law is shown.

VI.7.2. Vertical eddy heat flux

From the signal of the sonic anemometer we can estimate the speed of sound, which is a measure for temperature. To estimate temperature from the speed of sound we have to take into account that this velocity depends both on temperature and on humidity (Van Dijk, 2004).

The relation is (in Kelvin of course):

$$T = \frac{T^*}{1 + 0.51q} \quad (\text{VI.13})$$

where T^* is the sonic temperature, q is the specific humidity.

The potential sonic temperature is given by

$$\vartheta^* = T^* + \frac{\partial T^*}{\partial z} z \quad (\text{VI.14})$$

The vapor pressure and the mixing ratio are given respectively by

$$p_v = 6.11 * 10^{\frac{7.5T^*}{237.7+T^*}} \quad (\text{VI.15})$$

$$r = \frac{622 p_v}{p - p_v}$$

where it is used the time average pressure \overline{p} and not the instantaneous pressure because, in our tests, the difference between the instantaneous values and the average value is less than 100 Pa (that is the accuracy of the barometer).

Using the values of the mixing ratio and the potential sonic temperature is possible to get the virtual potential sonic temperature by following expression:

$$\mathcal{G}_v^* = \mathcal{G}^* (1 + 0.61r) \quad (\text{VI.16})$$

Ultimately, for the covariance of temperature with vertical velocity (that represents the vertical eddy heat flux) we have:

$$\overline{\mathcal{G}_v' w'} = \overline{\mathcal{G}_v^* w'} - 0.51 \overline{q \mathcal{G}_v^* w'} - 0.51 \overline{\mathcal{G}_v^* w' q'} \quad (\text{VI.17})$$

In our tests the specific humidity can be considered constant during the observation time window (at maximum 10 min); then the last term of the second member of the (VI.14) can be neglected

$$\overline{\mathcal{G}_v' w'} \approx \overline{\mathcal{G}_v^* w'} - 0.51 \overline{q \mathcal{G}_v^* w'} \quad (\text{VI.18})$$

VI.7.3. Linear correlation coefficient

Given the definition of the standard deviation (σ_A) of a generic variable (A), defined as the root square of the variance (σ_A^2), is possible to introduce the linear correlation coefficient (r_{AB}) between two distinct variables (A, B).

$$r_{AB} = \frac{\overline{a' b'}}{\sigma_A \sigma_B} \quad (\text{VI.19})$$

This variable ranges between -1 and +1 by definition. Two variables that are perfectly correlated (i.e. vary together) yield $r = 1$. Two variables that are perfectly negatively correlated (i.e. vary oppositely) yield $r = -1$. Variables independent yield $r = 0$.

Generally, in the ML $r_{w' \theta_v'} > 0$ and $r_{u' w'} > 0$ (upward transport flux) while in the SBL $r_{w' \theta_v'} < 0$ and $r_{u' w'} < 0$ (upward transport flux).

VII *Caserta* *tests results*

The developed kytoon station was tested in an experimental campaign of measurements performed near the center of Caserta city (see chapter V) on 7th, 13th, 15th, 16th and 17th of September 2010 (see Tab. V-1).

The chapter is divided in two parts:

- (1) the first reports in order the altitude, wind (speed and direction), temperature (static potential and virtual potential), air pollution concentration profiles of each flight day; observation about the stability of virtual potential temperature profiles (Stull, 1988) are given; a comparative analysis between wind and air pollution concentration and wind and temperature profiles, is discussed; the results are also compared to that of Ogawa (Ogawa Y., 1986).*
- (2) The second part deals about turbulence characteristics calculated at several altitude between 10:30-12:44 UTC+1 on 7th September 2010; particularly they are shown over altitude: the turbulent fluctuations of U, V, W and θ^* , their standard deviations and non dimensional power density spectra; the turbulent kinetic energy and the fluxes $\overline{u'w'}$ and $\overline{w'\theta^*}$.*

VII.1. Wind profiles (7/9/2010)

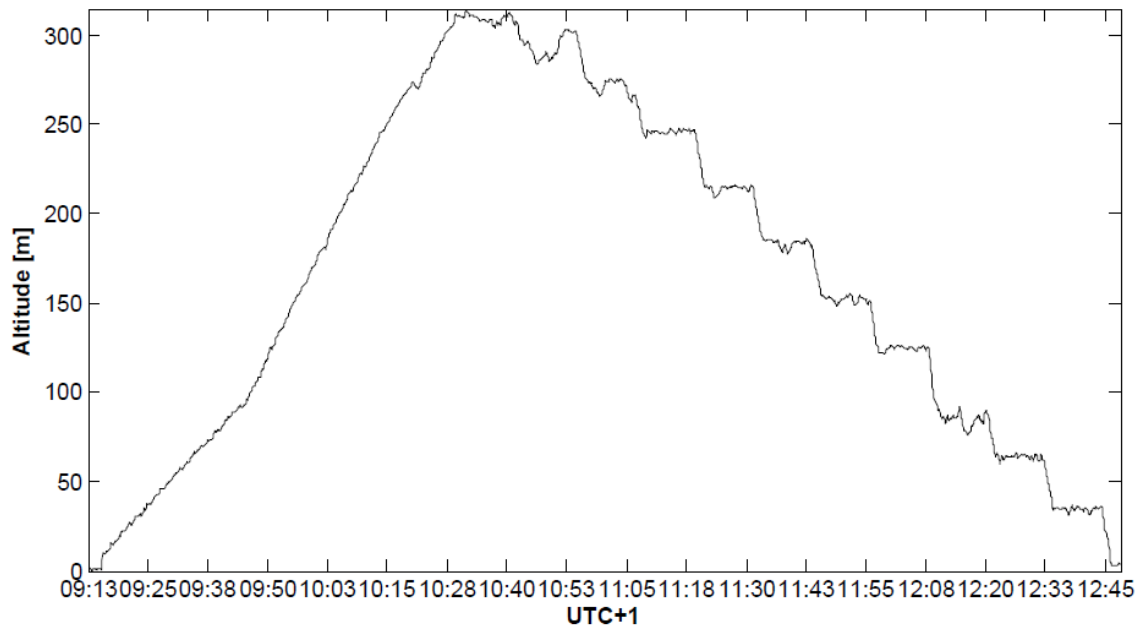


Figure VI-17 Altitude profile; 7/9/2010, 9:10-12:50 UTC+1.

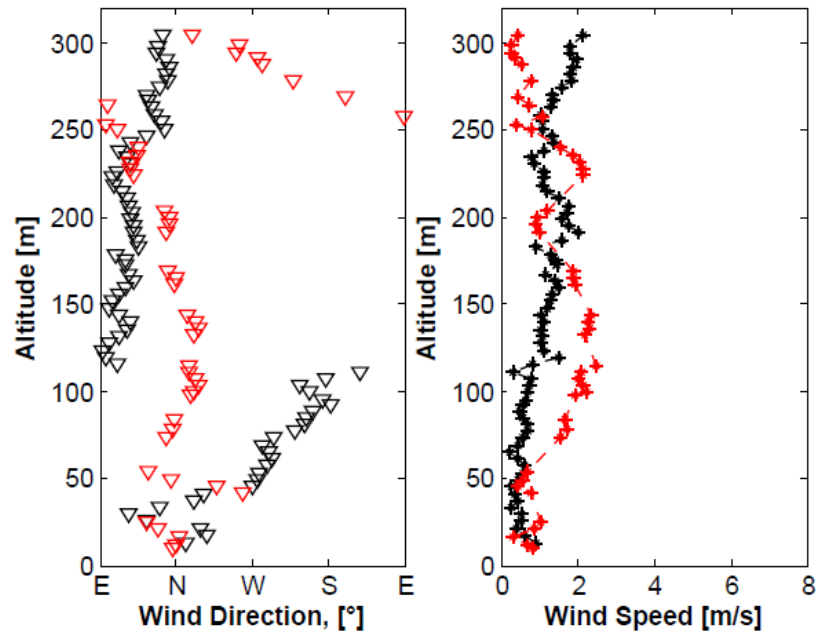


Figure VI-18 Climbing (black) and descending (red) phases: wind direction and wind speed profiles; 7/9/2010, 9:10 - 12:50 UTC+1.

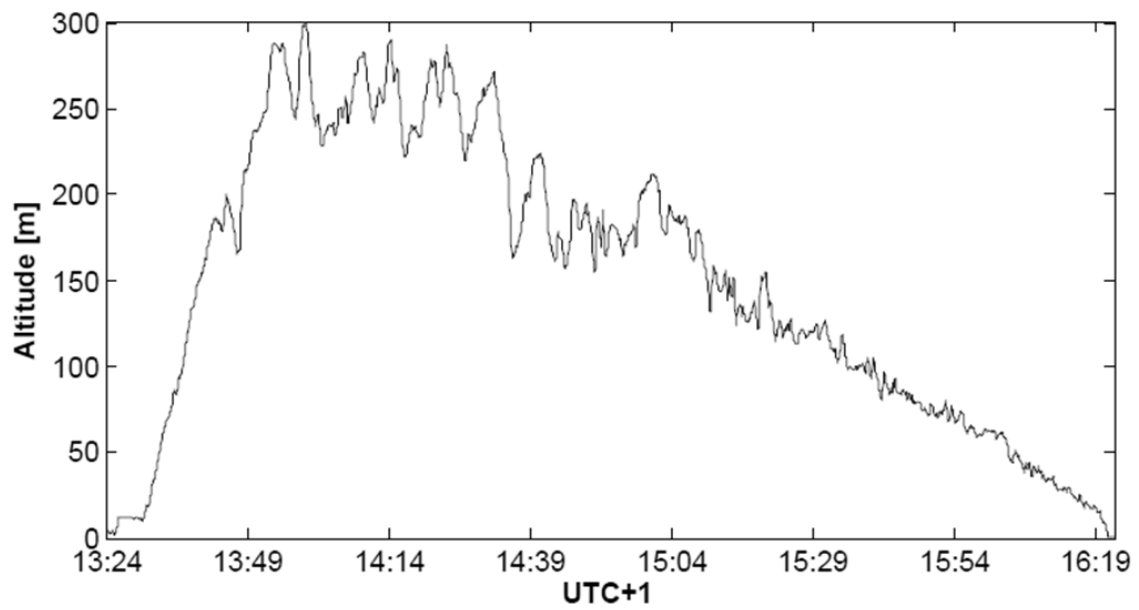


Figure VI-19 Altitude profile; 7/9/2010, 13:20-16:20 UTC+1.

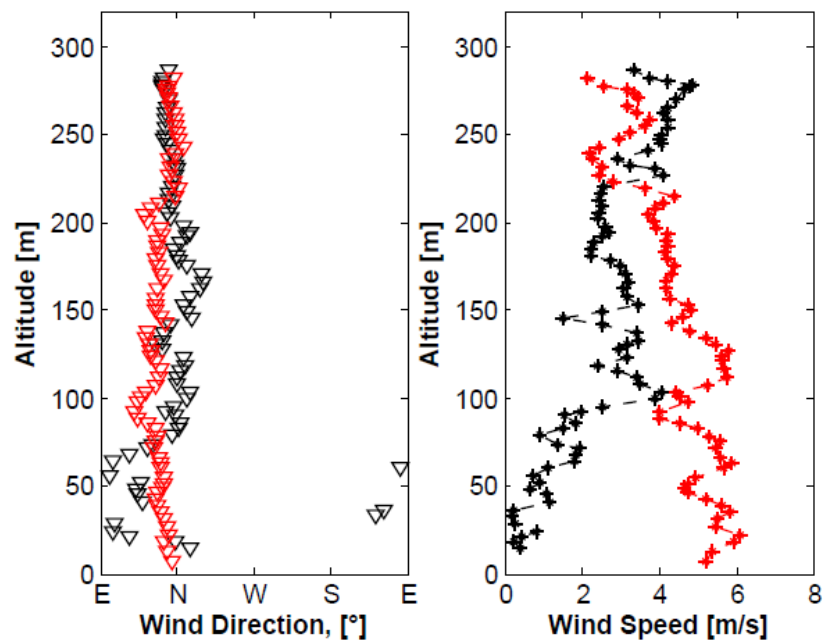


Figure VI-20 Climbing (black) and descending (red) phases: wind direction and wind speed profiles; 7/9/2010, 13:20 – 16:20 UTC+1.

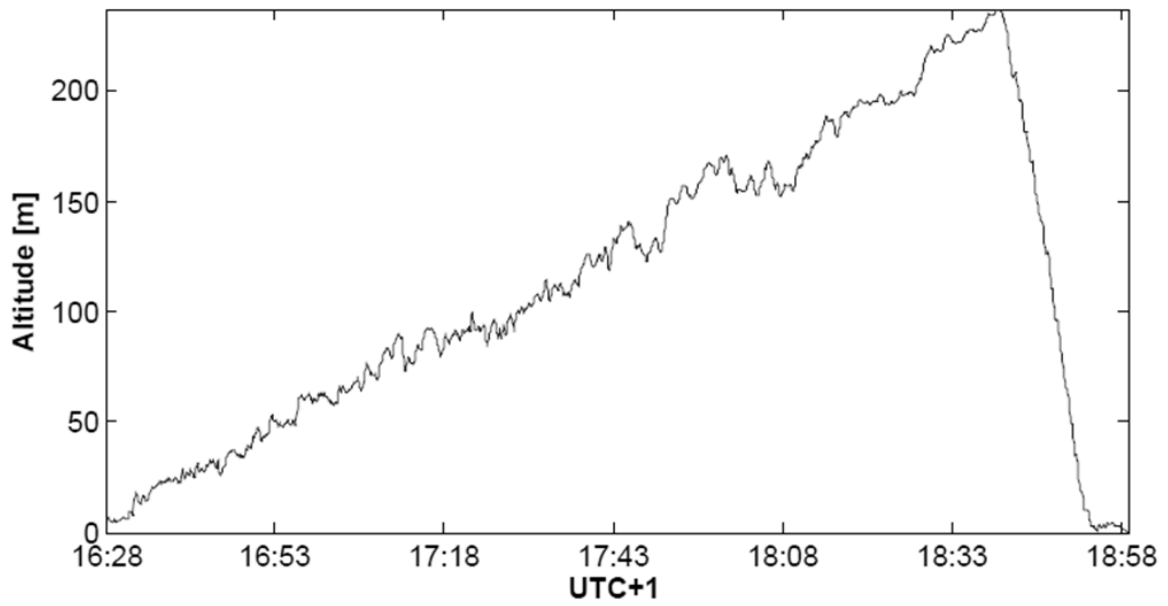


Figure VI-21 Altitude profile; 7/9/2010, 16:20-19:00 UTC+1.

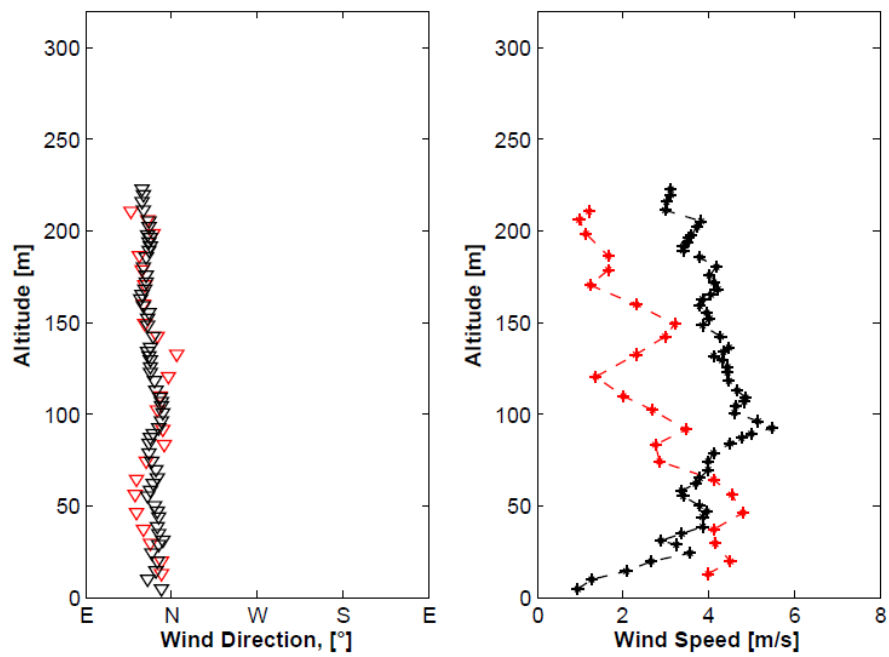


Figure VI-22 Climbing (black) and descending (red) phase: wind direction and wind speed profiles; 07/09/2010, 16:20 – 19:00 UTC+1.

VII.2. Temperature profiles (7/9/2010)

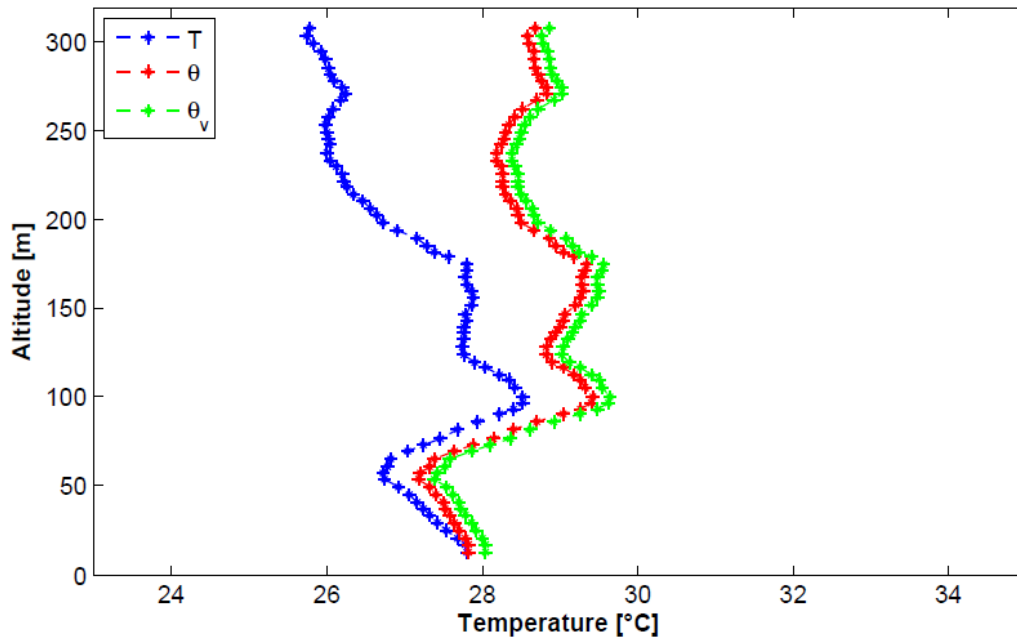


Figure VI-23 Climbing phase: static, potential and virtual potential temperature profiles;
7/9/2010, 9:10 – 10:30 UTC+1.

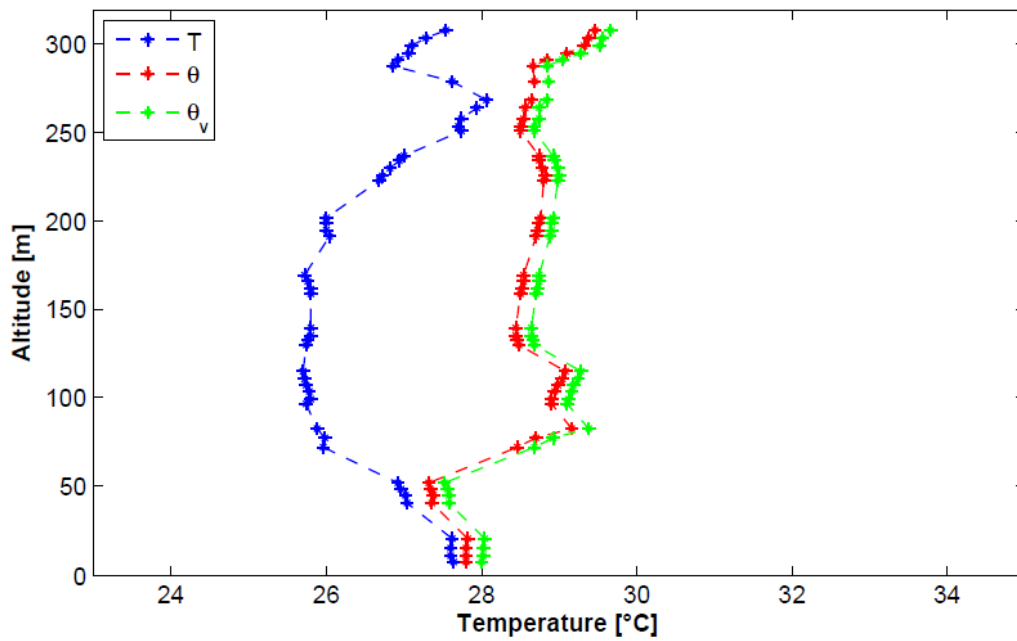


Figure VI-24 Descending phase: static, potential and virtual potential temperature profiles;
7/9/2010, 10:30 – 12:50 UTC+1.

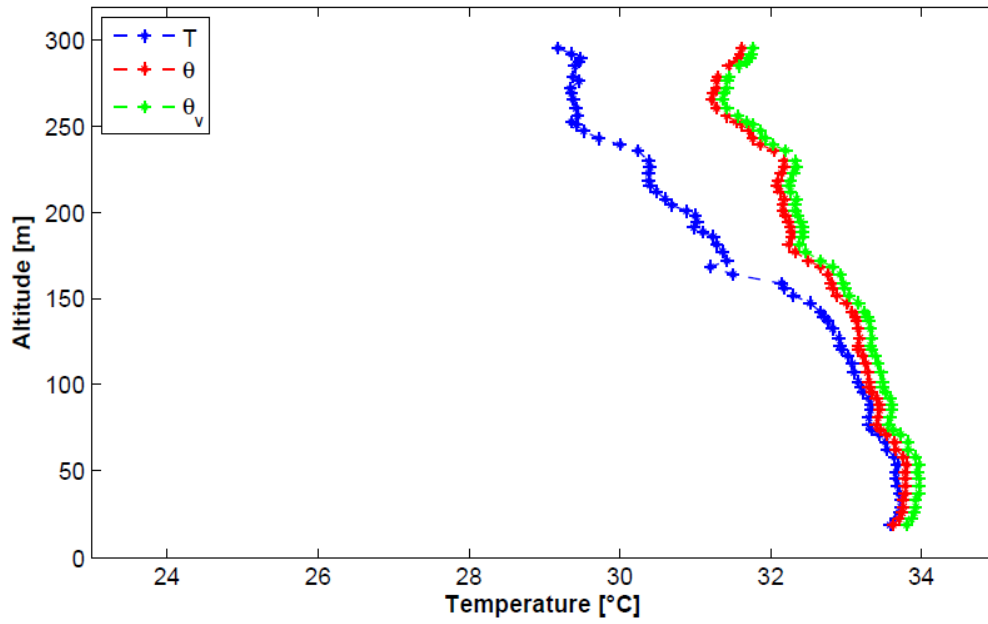


Figure VI-25 Climbing phase: static, potential and virtual potential temperature profiles;
7/9/2010, 13:20 – 13:55 UTC+1.

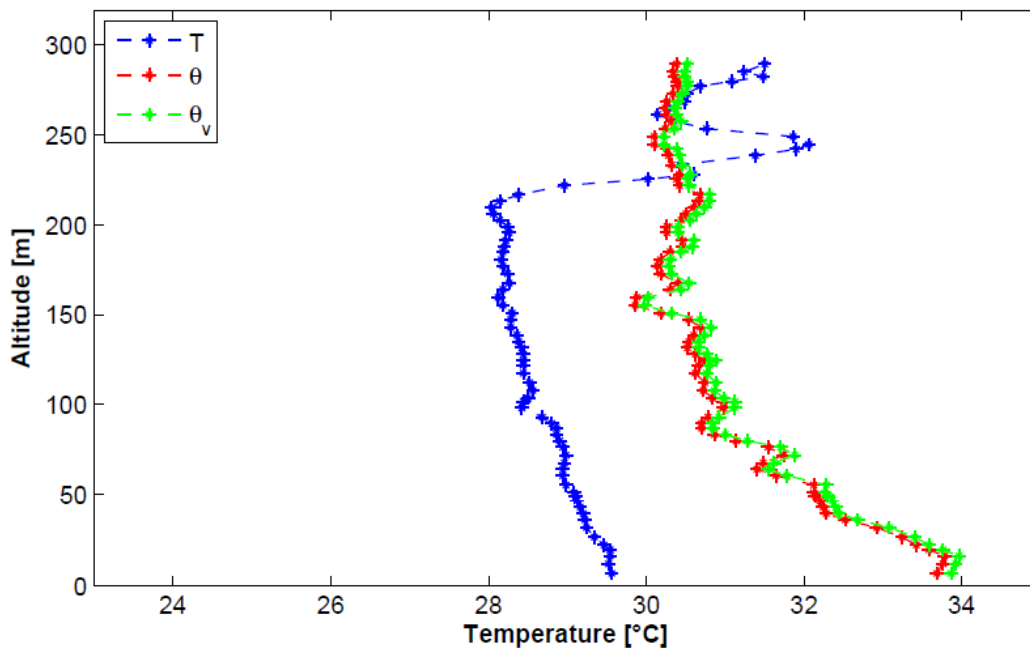


Figure VI-26 Descending phase: static, potential and virtual potential temperature profiles;
7/9/2010, 13:55 – 16:20 UTC+1.

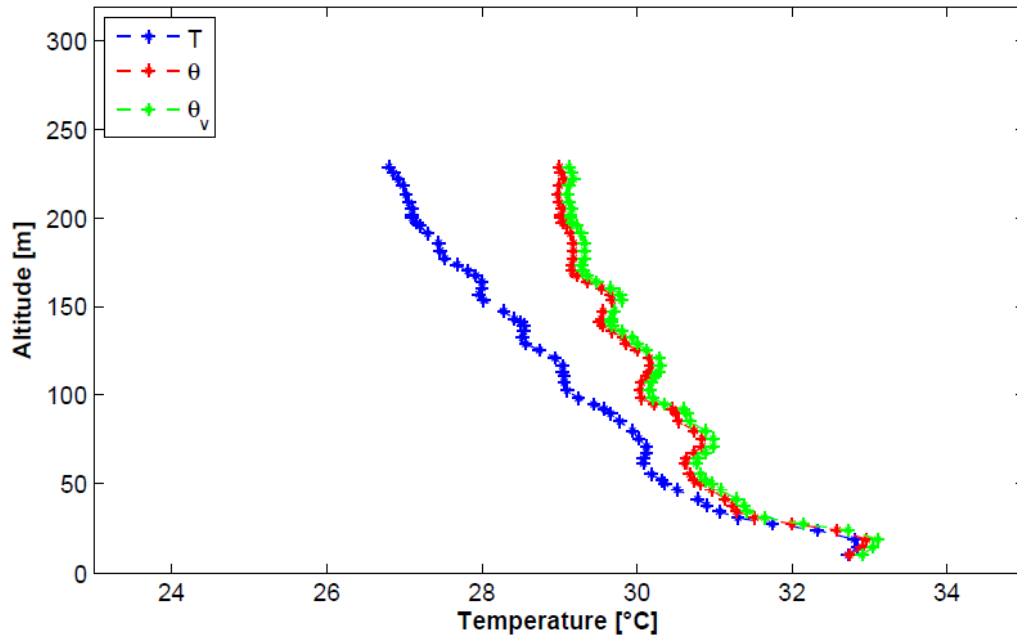


Figure VI-27 Climbing phase: static, potential and virtual potential temperature profiles;
7/9/2010, 16:20 –18:40 UTC+1.

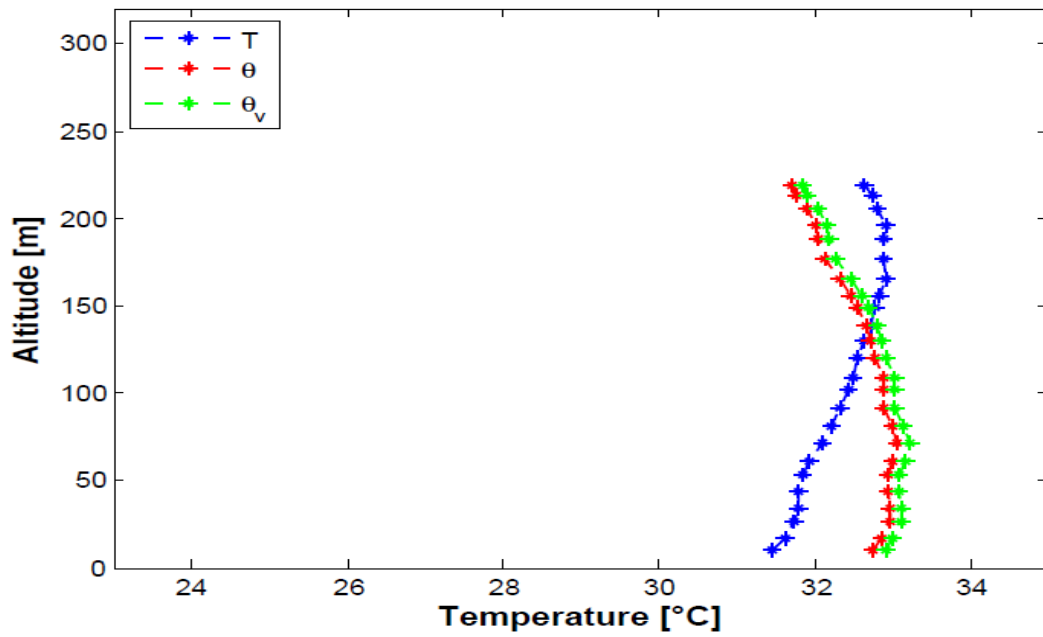


Figure VI-28 Descending phase: static, potential and virtual potential temperature profiles;
7/9/2010, – 18:40- 19:00 UTC+1.

VII. Caserta tests results

Between the 9:20-10:40 UTC+1 the profile of wind speed has low intensity (0.5 m/s) and the direction rotate of 180 deg from Nord to Sud in the first 100 m of altitude (Fig. VII-2 black). After a little increase in intensity is shown and wind is stably directed to Est. Between 10:40-12:50 UTC+1 (Fig. VII-2 red) begin to grow a sea breeze front (2 m/s of maximum intensity) toward Nord/Nord-Est (position1, Fig. VII-13).

There is a mixed stability condition, observing both climbing and descending virtual temperature profiles (Fig. VII-7,8): unstable (0-50 m), stable (50-100 m); we can identify the mixing layer height (MLH) at 270 m of altitude; this attested by the sudden change in wind direction profile and from the neutral virtual temperature one between 70-270 m (Fig. VII-8).

Between 13:20-13:55 UTC+1 the sea breeze front reaches a maximum intensity of 5 m/s at 270 m of altitude (Fig. VII-4 black); the virtual temperature profile (Fig. VII-9), superadiabatic, is the one characteristic of fully developed ML (fully unstable) and we cannot see the MLH (position 2, Fig. VII-13). During the descending phase the wind speed intensity decreases from 6 m/s, at low altitude, to about 2 m/s (Fig. VII-4 red); comparing this profile and also the correspondent temperature one to that of Ogawa (Fig. VII-13 and VII-14) it is possible to assert that we are in the middle of sea breeze structure (position 3, Fig. VII-13); it can be estimated the inversion layer of wind speed at about 300 m (Fig. VII-10).

The wind speed intensity profile between 16:20-18:40 UTC+1 has its maximum intensity (5 m/s) at 100 m of altitude and decreases both toward the ground and the higher altitude (Fig. VII-6 black); we expect the MLH to be about 300 m of altitude observing the decreasing trend of wind profile (position 4, Fig. VII-13). Between 18:40-19:00 UTC+1 (Fig. VII-6 red) the MLH height attests at about 200 m and the intensity of wind is about 4 m/s near the ground (position 5, Fig. VII-13). The virtual temperature profile reveals that it is coming the nocturnal stable layer (Fig. VII-12).

Note that the virtual potential profiles of the afternoon 13:20-18:40 UTC+1 (Fig. VII-11,12) is quite similar to that of figure VII-15 (I), where the presence of trees led to a local increase of the profile.

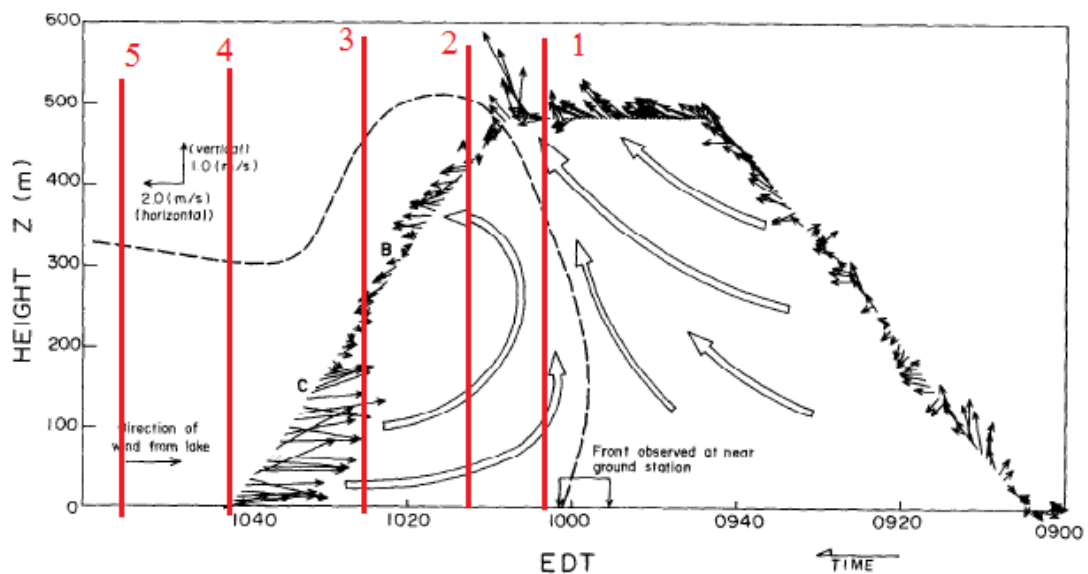


Figure VI-29 The time variation combined north-south wind component and the vertical wind profiles (Ogawa Y., 1986); dashed line denote the sea breeze front (1 m/s); red line identify the approximate location of the most particular wind and temperature vertical profiles.

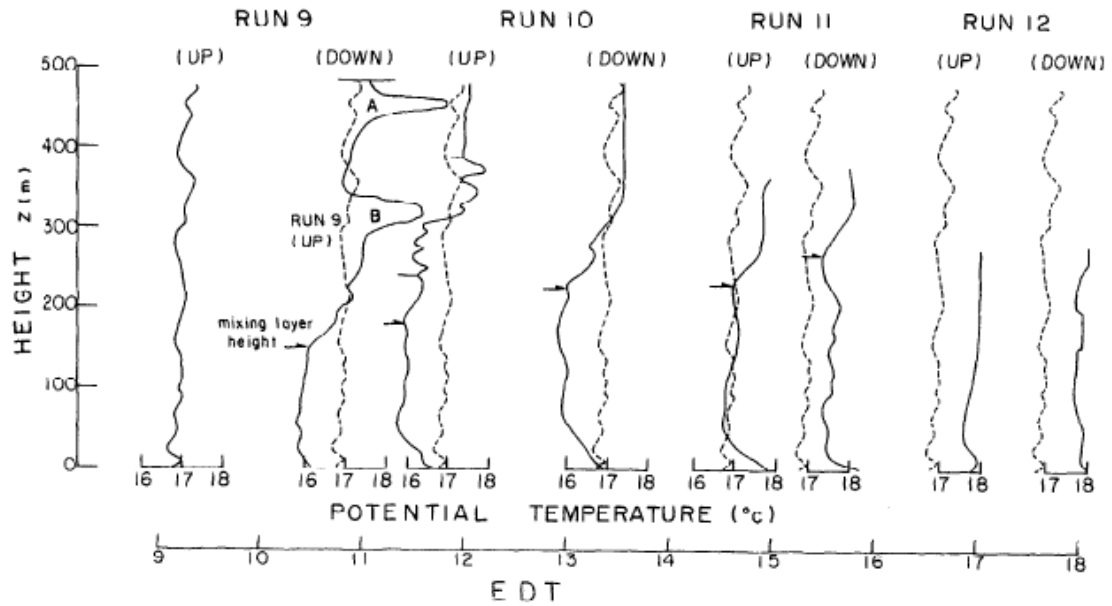


Figure VI-30 The diurnal variation of the vertical potential temperature profiles on June 11, 1982, Lake Eire, Canada. (Ogawa Y., 1986)

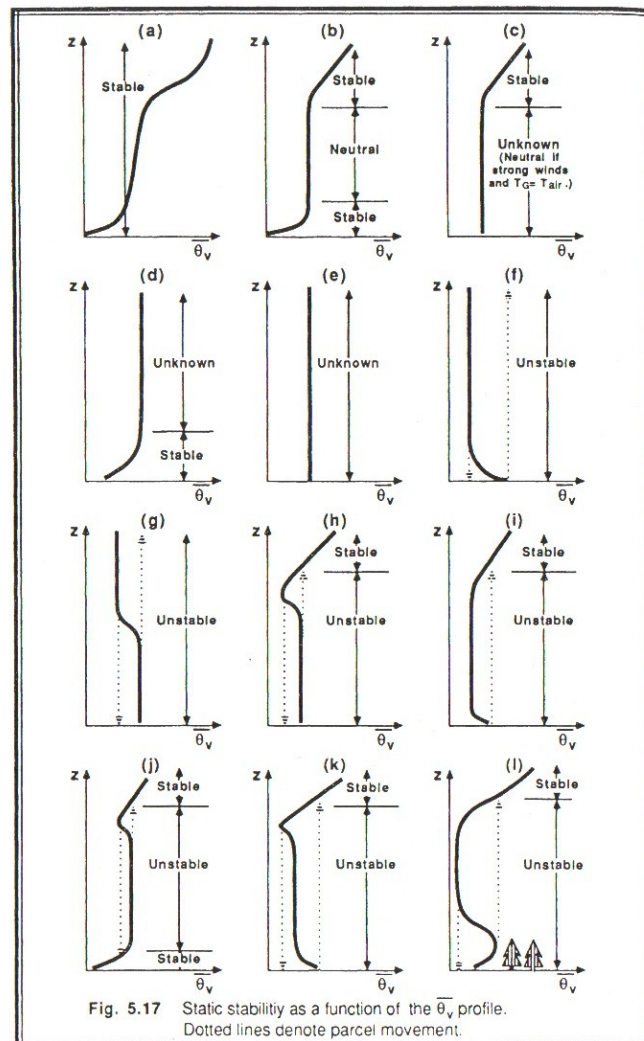


Figure VI-31 Stability of virtual potential profiles (Stull, 1988).

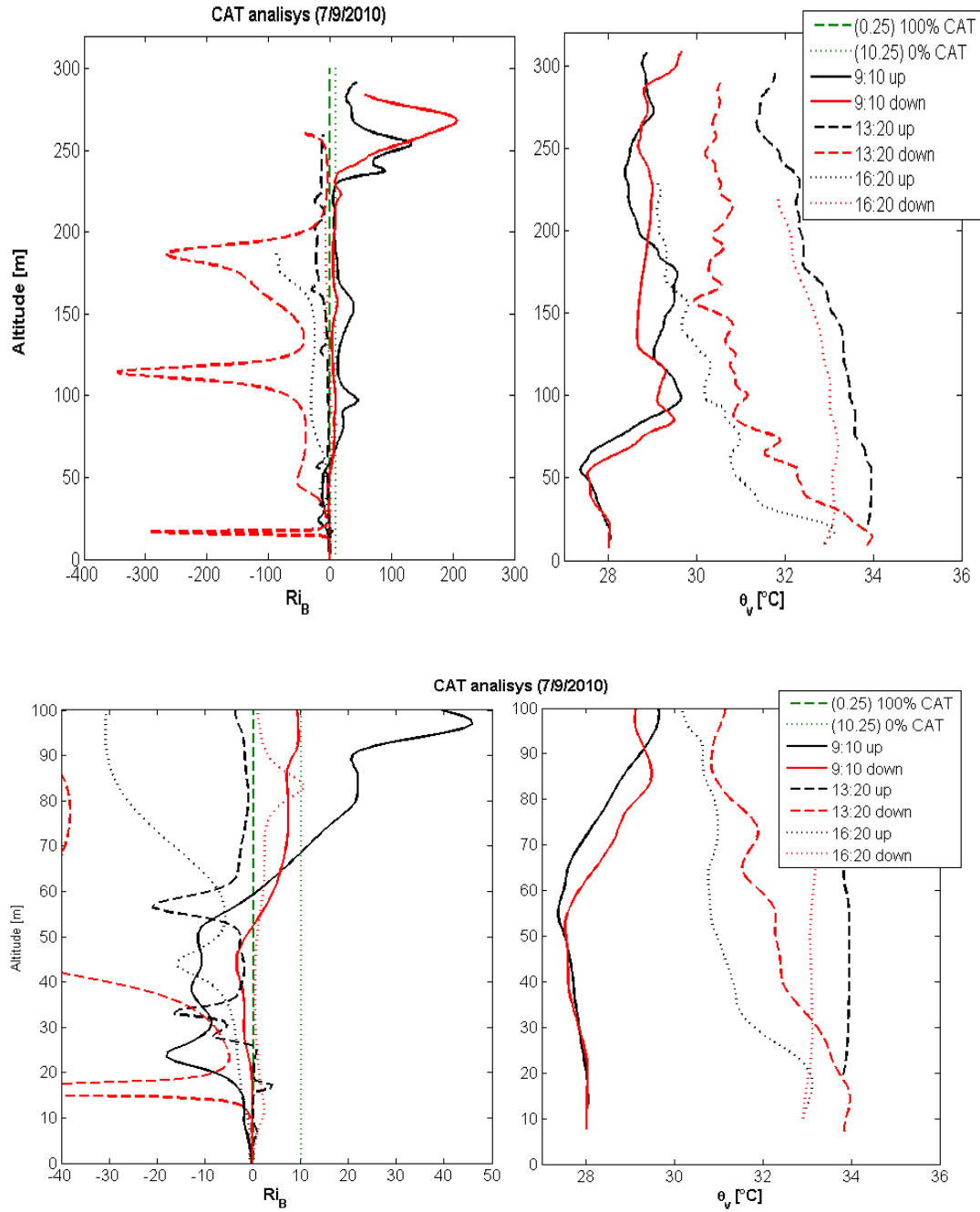


Figure VI-32 Bulk Richardson number over altitude compared to virtual potential temperature profiles; 7/9/2010 UTC+1.

Comparing the vertical profiles of bulk Richardson number and the virtual potential temperature ones (Fig. VII-16) it is possible to make a correspondence between the region of CAT with the stability as stated by the observation of the second ones.

Between 0-50m AGL the probability of CAT is always 100% ($Ri_B < 0.25$) except for the 16:20 flight, which is close to a nocturnal SBL condition : the up and down curves are near the critical Richardson number ($0.25 = 100\%$ CAT) or between it and the upper limit (10.25), which correspond to no CAT. The Richardson profiles moves toward the negative region over time between 9:10-13:20 UTC+1, that means the developed of ML. From 16:20 UTC+1 this trend reverses (as evening has coming).

VII.3. Air pollution concentrations profiles (7/9/2010)

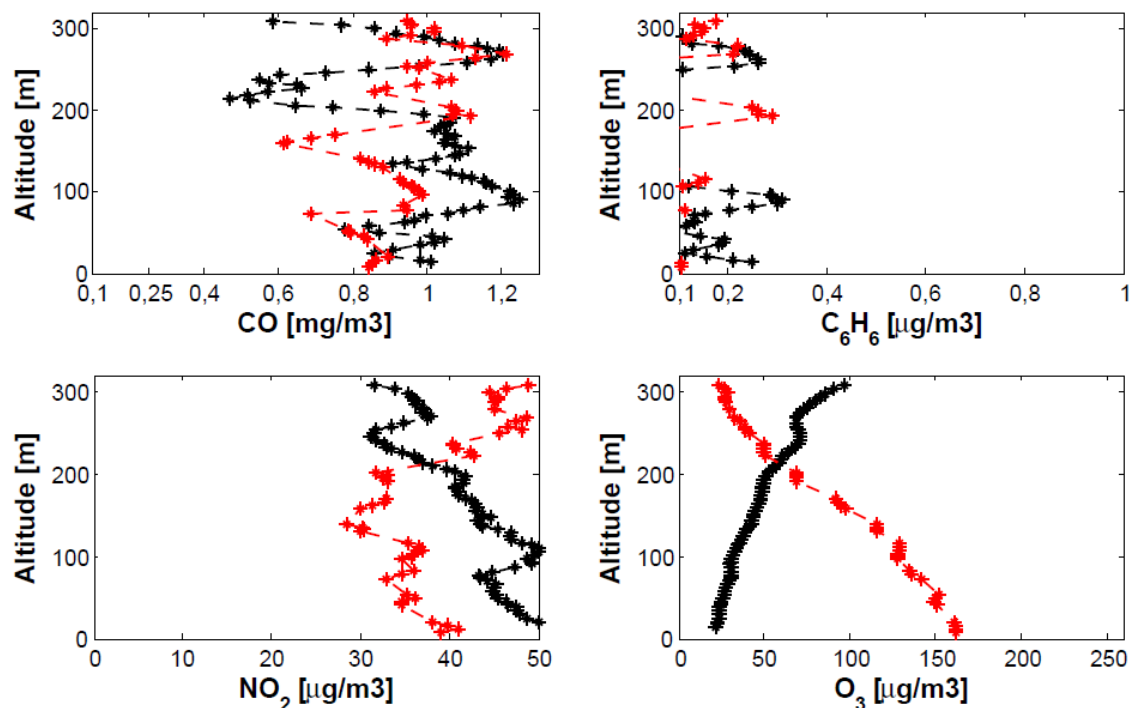


Figure VI-33 Climbing (black) and descending (red) phases: pollutants' profiles; 7/9/2010, 9:10-12:50 UTC+1.

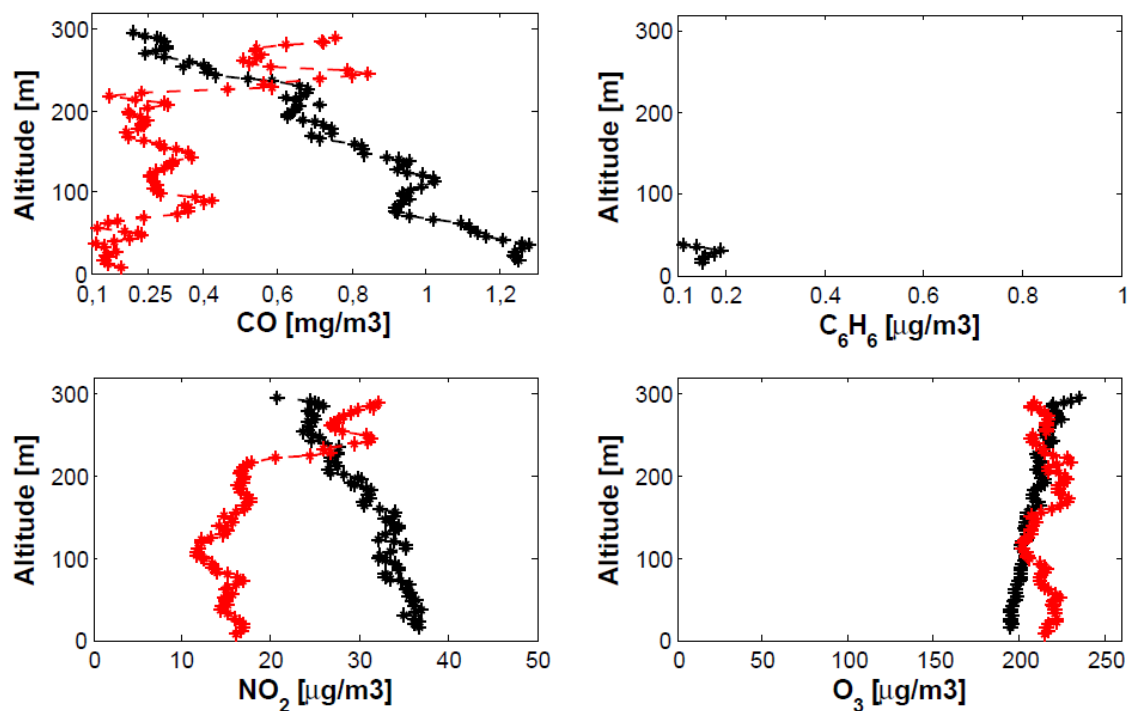


Figure VI-34 Climbing (black) and descending (red) phases: pollutants profiles; 7/9/2010, 13:20 – 16:20 UTC+1.

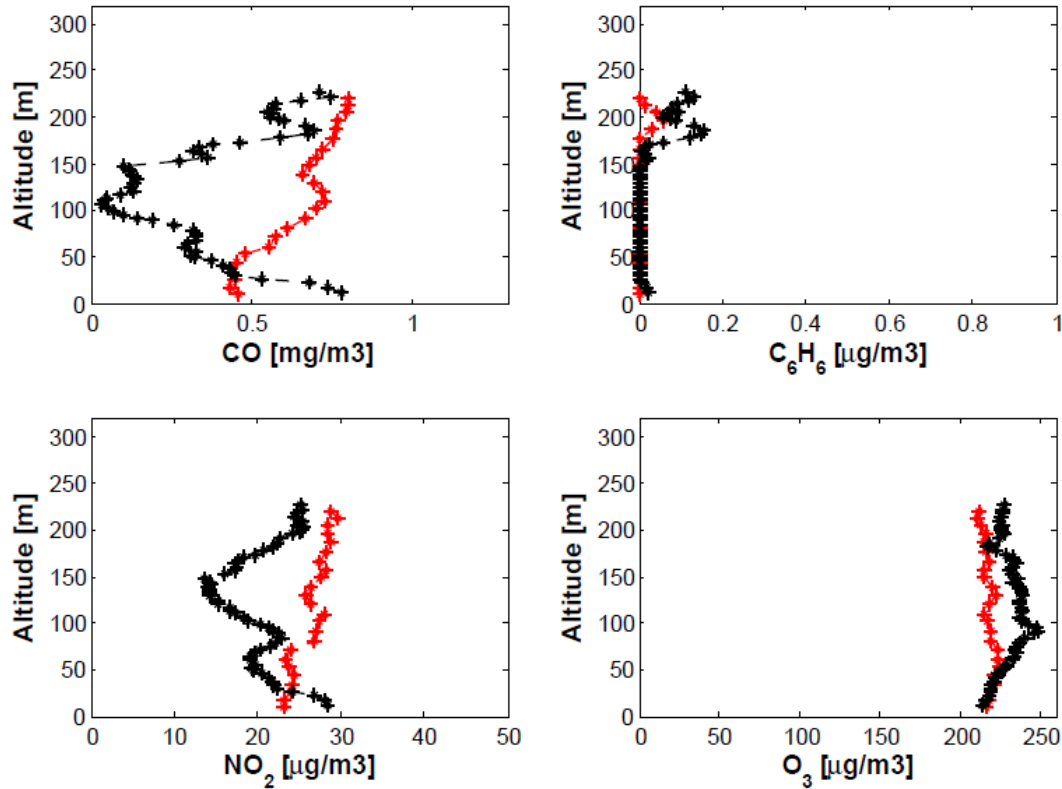


Figure VI-35 Climbing (black) and descending (red) phase: pollutants profiles; 7/9/2010, 16:20 – 19:00 UTC+1.

During the morning the maximum concentration of CO is 1.2 mg/m^3 at 100 m (9:10-10:30 UTC+1) of altitude that moves upward (thermals effect) between 10:30-12:50 UTC+1, being quite constant; the same consideration is true about C_6H_6 maximum concentration ($0.3 \mu\text{g/m}^3$).

NO_2 maximum concentration, as expected near the ground, decreases during the day because the growing of sea breeze; more in general the observation reveals that the concentration of NO_2 is inversely proportional to wind intensity.

The maximum concentrations of CO and C_6H_6 are located again near the ground (13:20-UTC+1) assuming the same values of the early morning ; this is probably due to traffic and null speed ; instead at 16:20 UTC+1 the high sea breeze near the ground wipes out part of the pollutants.

Late afternoon (19:00 UTC+1) concentrations are the same of early morning, except for the ozone that enhances during the day and is constant with altitude because it is function only with the solar irradiation.

VII.4. Wind profiles (13/9/2010)

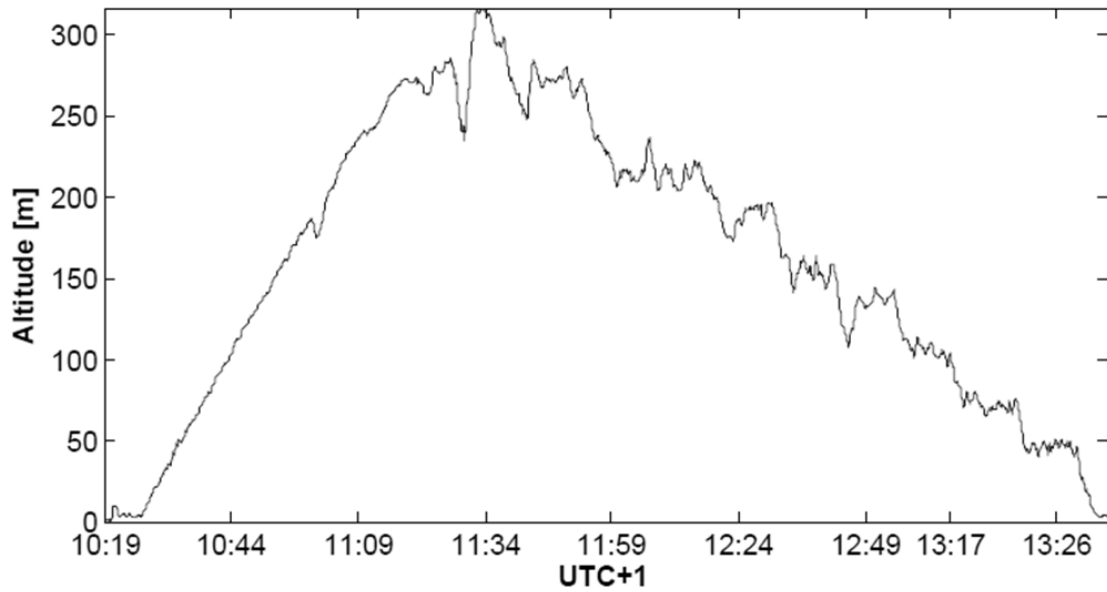


Figure VI-36 Altitude profile 13/09/2010, 10:20 – 13:30 UTC+1.

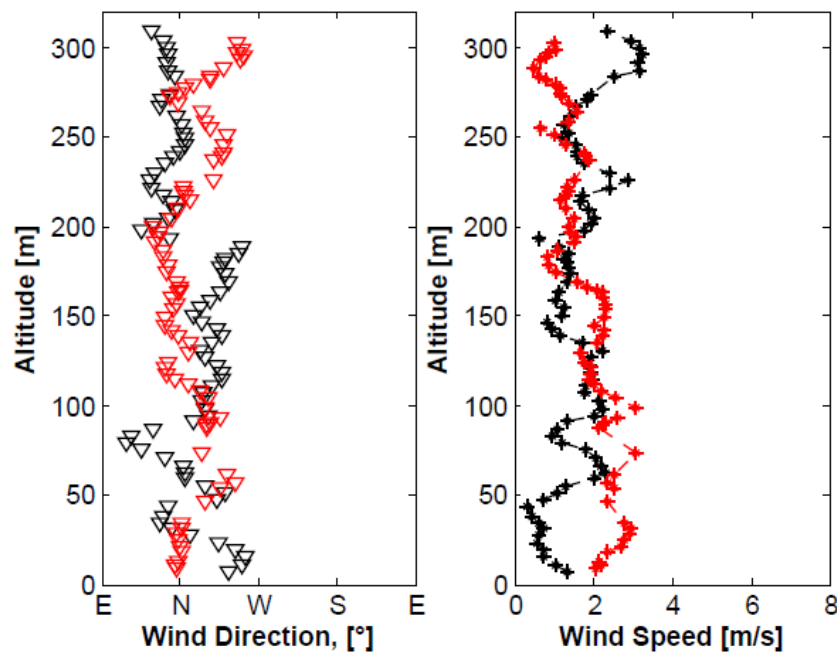


Figure VI-37 Climbing (black) and descending (red) phases: wind direction and wind speed profiles; 13/09/2010, 10:20 – 13:30 UTC+1.

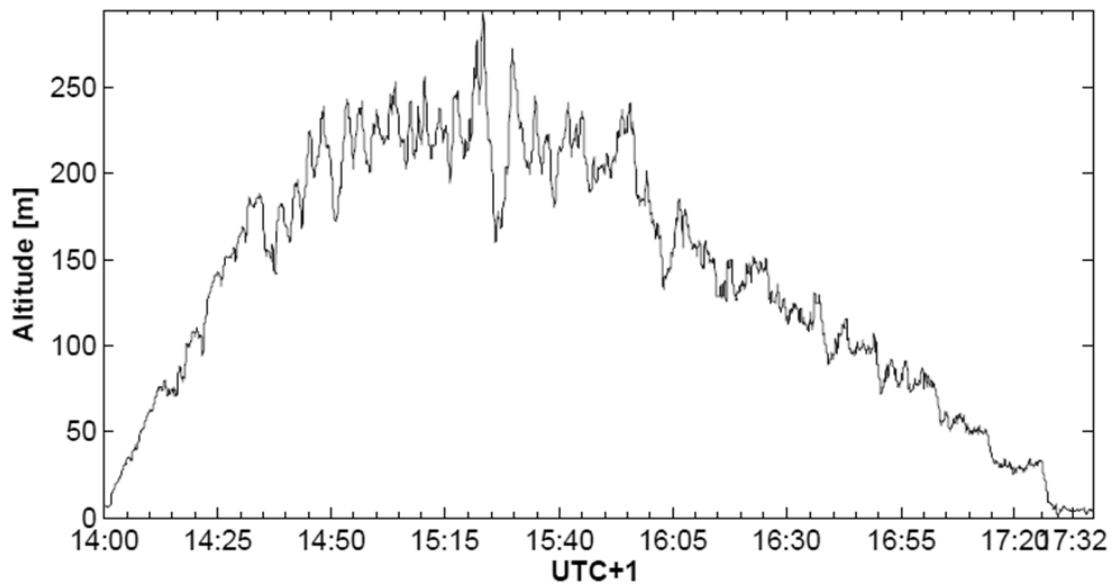


Figure VI-38 Altitude profile; 13/09/2010, 14:00 – 17:35 UTC+1 .

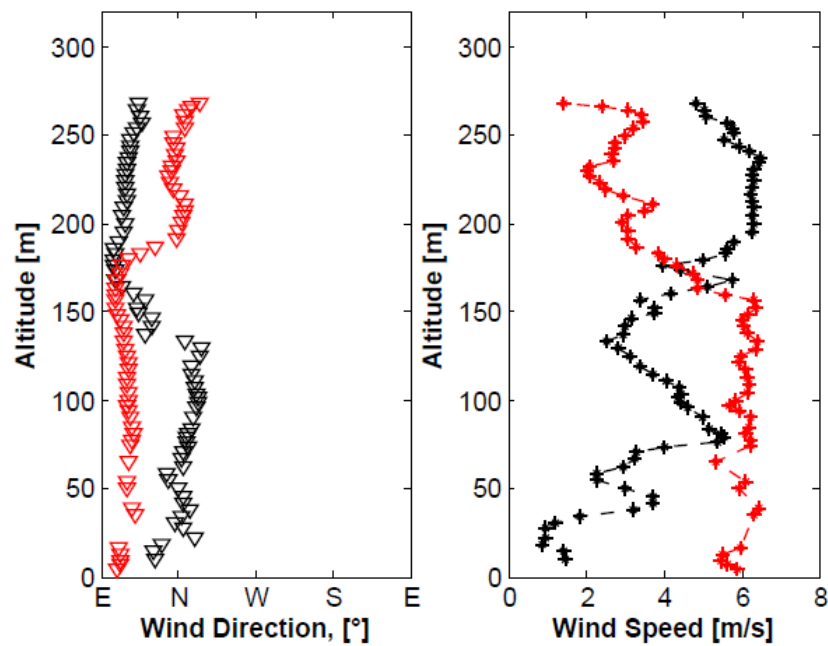


Figure VI-39 Climbing and descending phases: wind direction and wind speed profiles; 13/09/2010, 14:00 – 17:35UTC+1.

VII.5. Temperature profiles (13/9/2010)

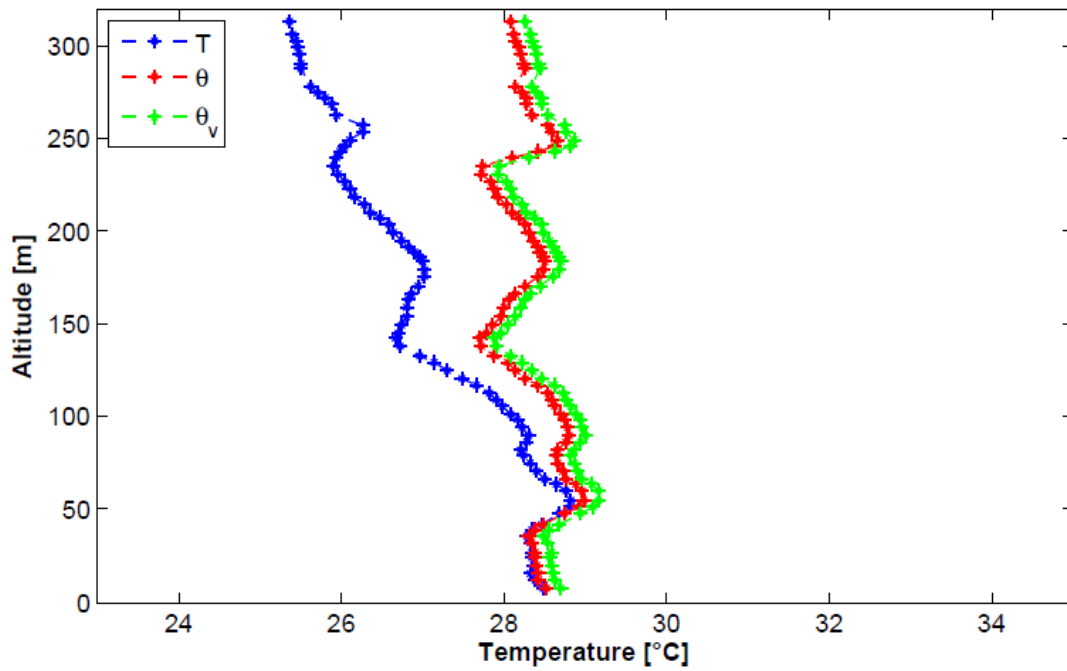


Figure VI-40 Climbing phase: static, potential and virtual potential temperature profiles;
13/09/2010, 10:20 – 11:35 UTC+1.

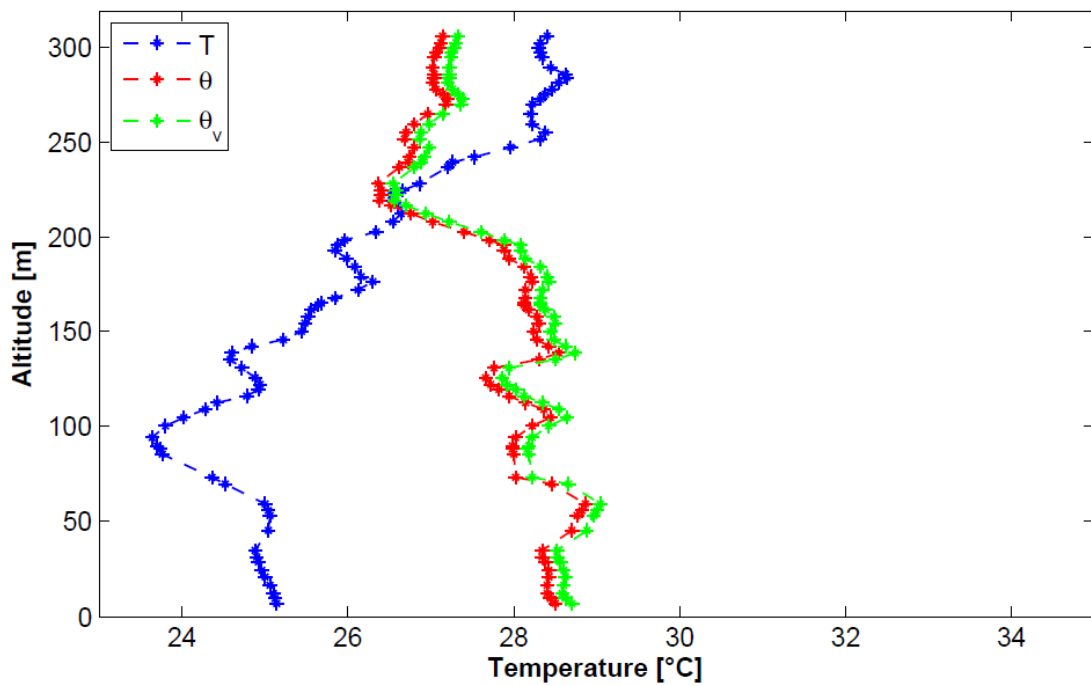


Figure VI-41 Descending phase: static, potential and virtual potential temperature profiles;
13/09/2010, 11:35 – 13:30 UTC+1.

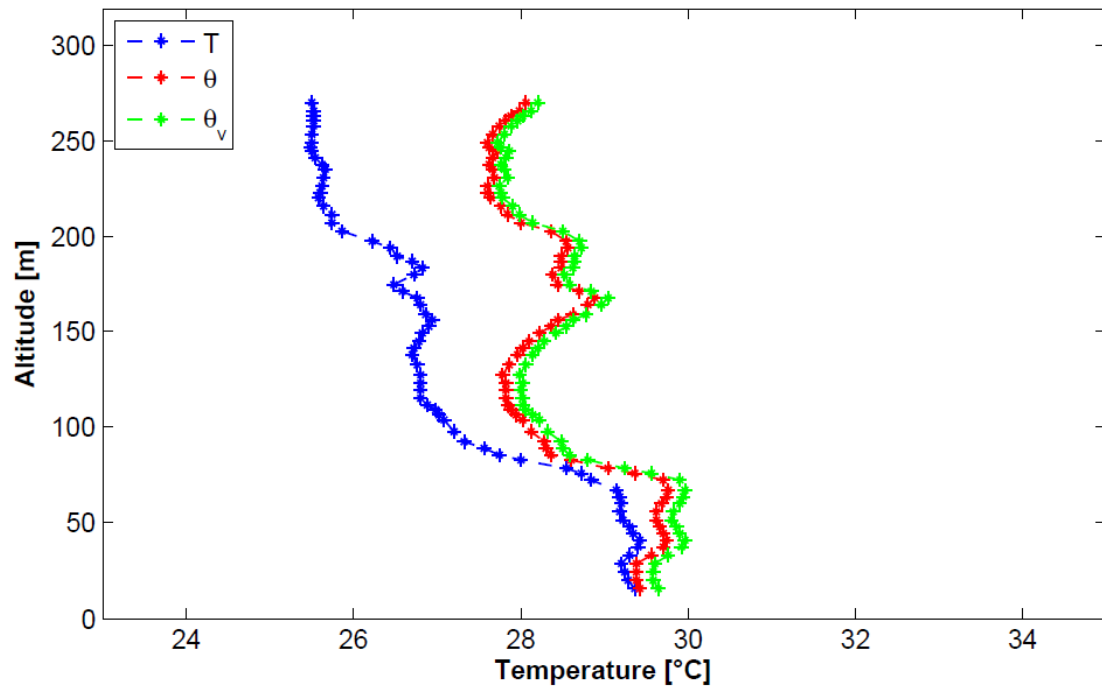


Figure VI-42 Climbing phase: static, potential and virtual potential temperature profiles; 13/09/2010, 14:00 – 15:20 UTC+1.

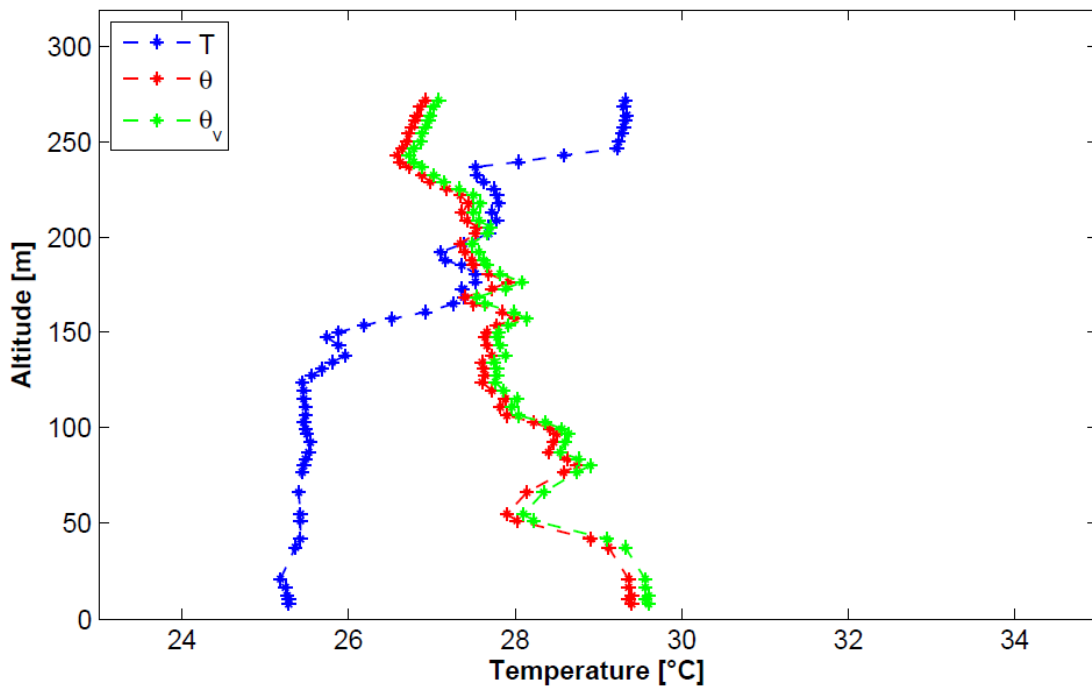


Figure VI-43 Descending phase: static, potential and virtual potential temperature profiles; 13/09/2010, 15:20 – 17:35 UTC+1.

During the ascent phase of the kytoon (10:20-11:35 UTC+1) wind direction is variable between NE and NW and its intensity ranges 0-3 m/s (Fig. VII-21 black). A light enhancing trend of wind intensity is shown from the ground; the opposite is that during the descending phase of the kytoon (11:35-13:30 UTC+1) where the wind intensity decreases from the ground (2/ms) to null value at 275m (Fig. VII-21 red). At this altitude there is a sudden change in direction (from N to W) that could reveals the MLH even if the virtual temperature profiles are of hard interoperation: the stability of the ascent profile is unknown (Fig. VII-15e), while the descent one is unstable (Fig. VII-15h).

Between 14:00 and 15:20 UTC+1 (Fig. VII-23 black) the sea breeze is well defined with intensity of 6m/s up to 200m (position 2 Fig. VII-23). A change of 90 deg is evident at 150m of altitude (E-N) in the descending profile (15:20-17:35 UTC+1) accompanied with a decrease of wind velocity, that is constant (6m/s) under this value (Fig. VII-23 red); the temperature profile become stable after 250m (Fig. VII-27) where velocity is near to zero and a little changing in wind direction profile is noted (toward W). Thus the MLH is reached (position 3 Fig. VII-13): stable condition is between about 0-200m that means a developed ML (Fig. VII-27).

VII.6. Air pollution concentration profiles (13/9/2010)

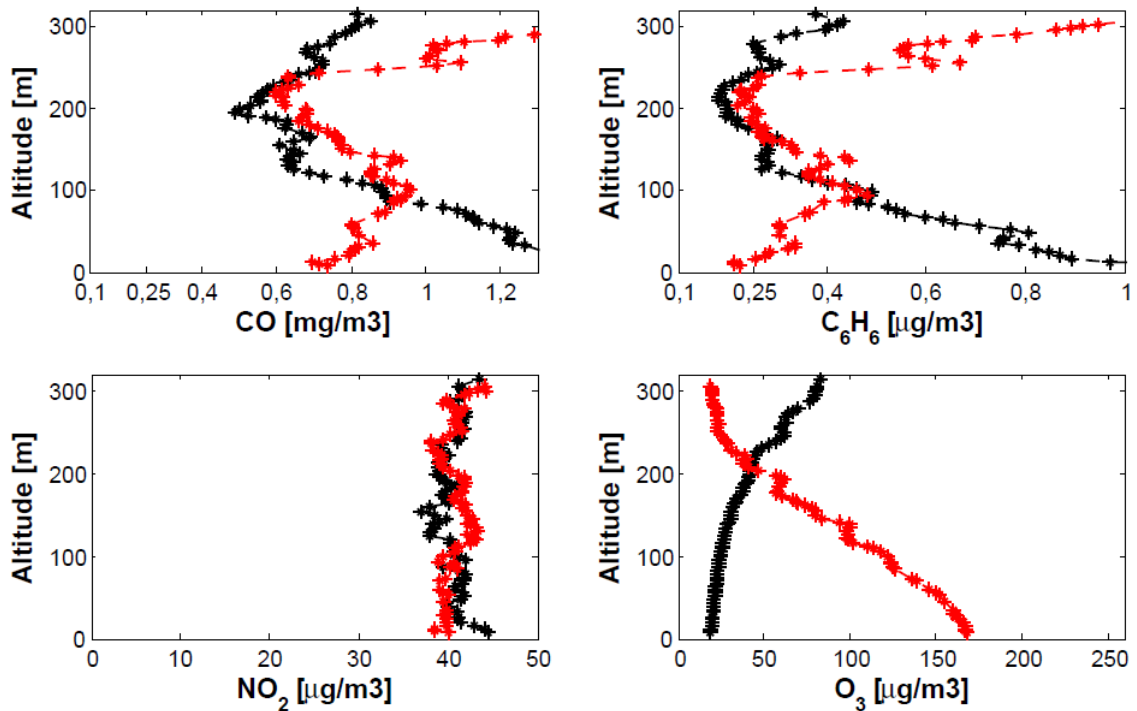


Figure VI-44 Climbing (black) and descending (red) phases: pollutants profiles; 13/09/2010, 10:20 – 13:30 UTC+1.

The maximum concentration of CO (1.2mg/m^3) and C_6H_6 ($0.8\text{ }\mu\text{g/m}^3$), near the ground at early morning (10:20 UTC+1), moves upward and decreases over time while the concentration of NO_2 is constant (about $40\text{ }\mu\text{g/m}^3$) until 13:30 UTC+1 with altitude (Fig. VII-28).

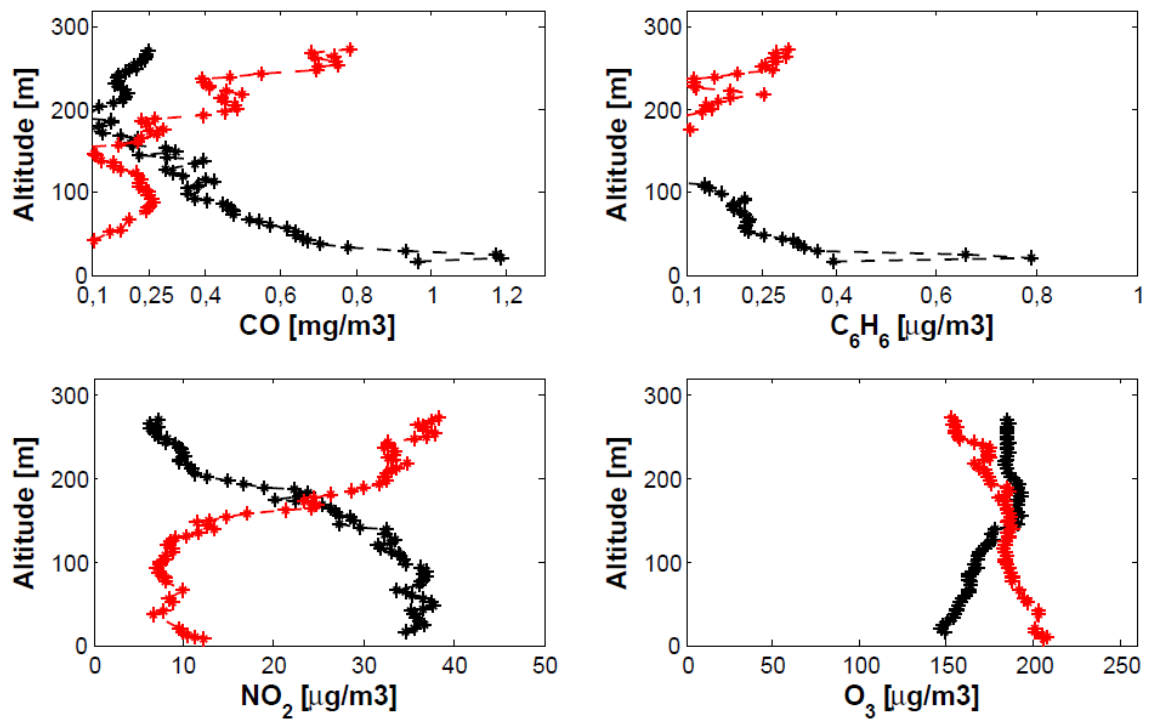


Figure VI-45 Climbing (black) and descending (red) phases: pollutants profiles; 13/09/2010, 14:00 – 17:35UTC+1.

At 14:00 UTC+1 new peaks of concentrations appears to be very close to that of early morning (the same happened on 7th September) probability due to traffic and low wind velocity (Fig. VII-29). During the afternoon the sea breeze disperses the pollutants reducing drastically the concentration in the first 150m of altitude while at higher one the concentration begin to enhance (reduction of velocity).

VII.7. Wind profiles (15/9/2010)

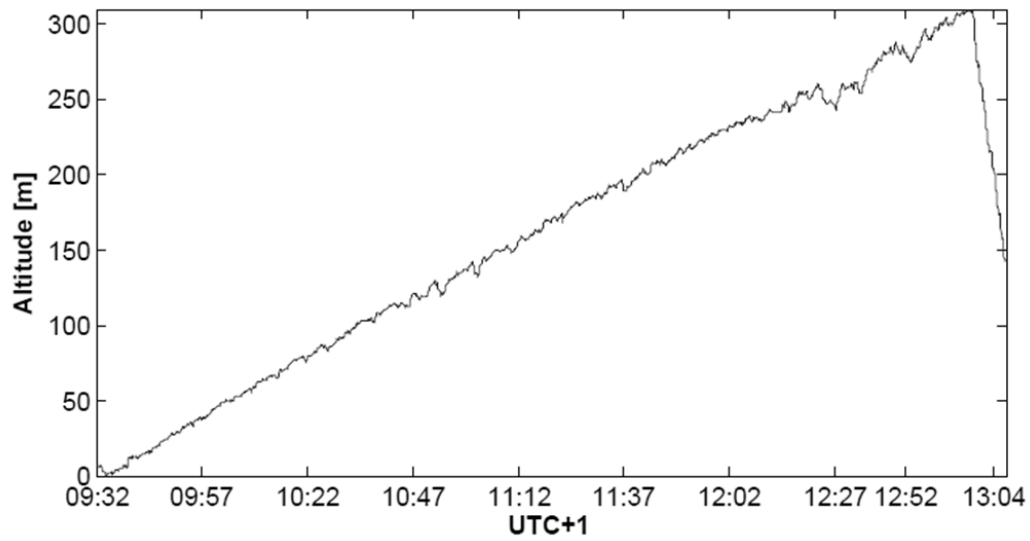


Figure VI-46 Altitude profile; 15/09/10, 9:30 - 13:10 UTC+1 .

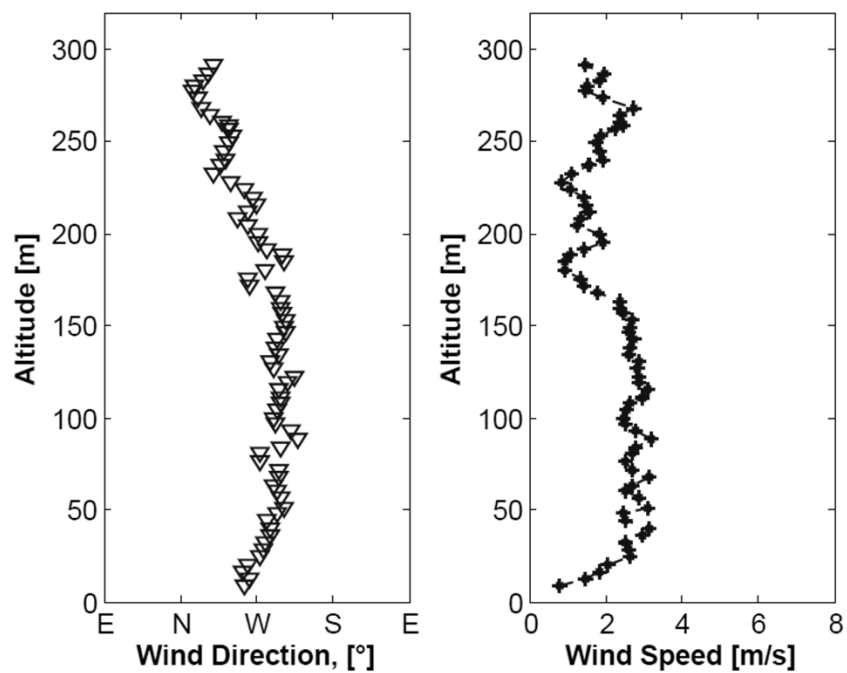


Figure VI-47 Wind direction and wind speed profiles (ascent); 15/09/2010, 9:30 - 13:10 UTC+1.

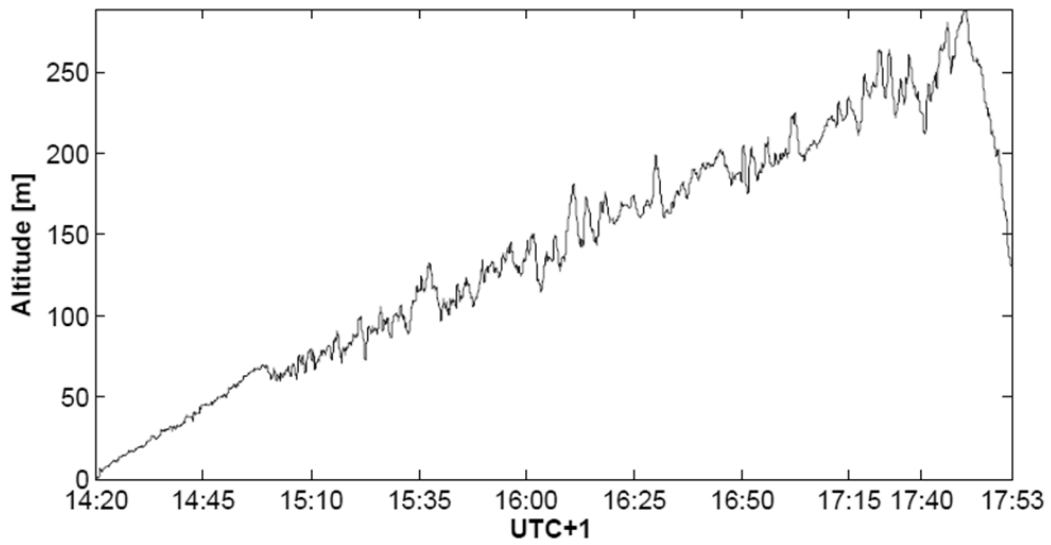


Figure VI-48 Altitude profile; 15/09/2010, 14:15 - 18:00 UTC+1.

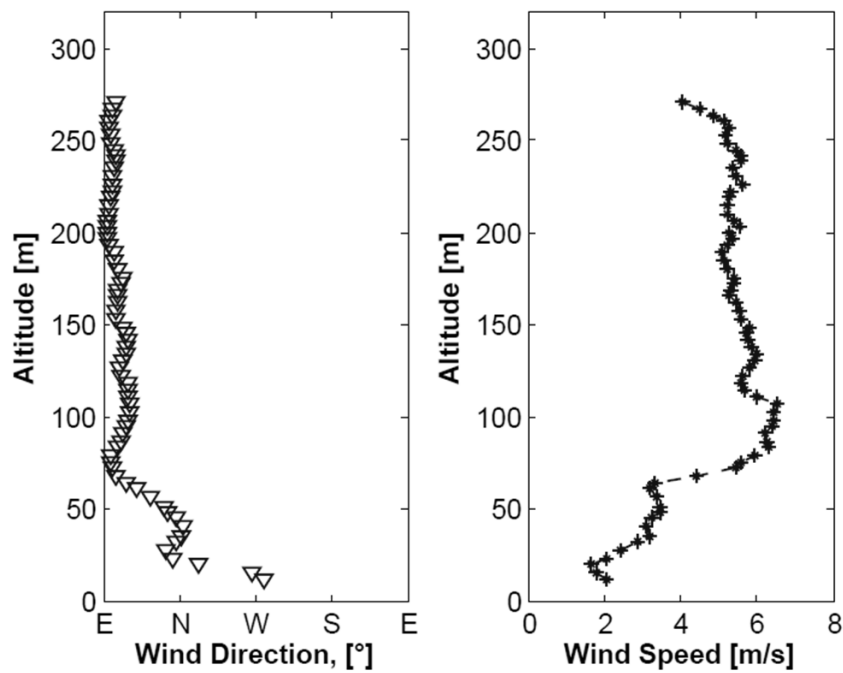


Figure VI-49 Wind direction and wind speed profiles (ascent); 15/09/2010, 14:15 - 18:00 UTC+1.

VII.8. Temperature profiles (15/9/2010)

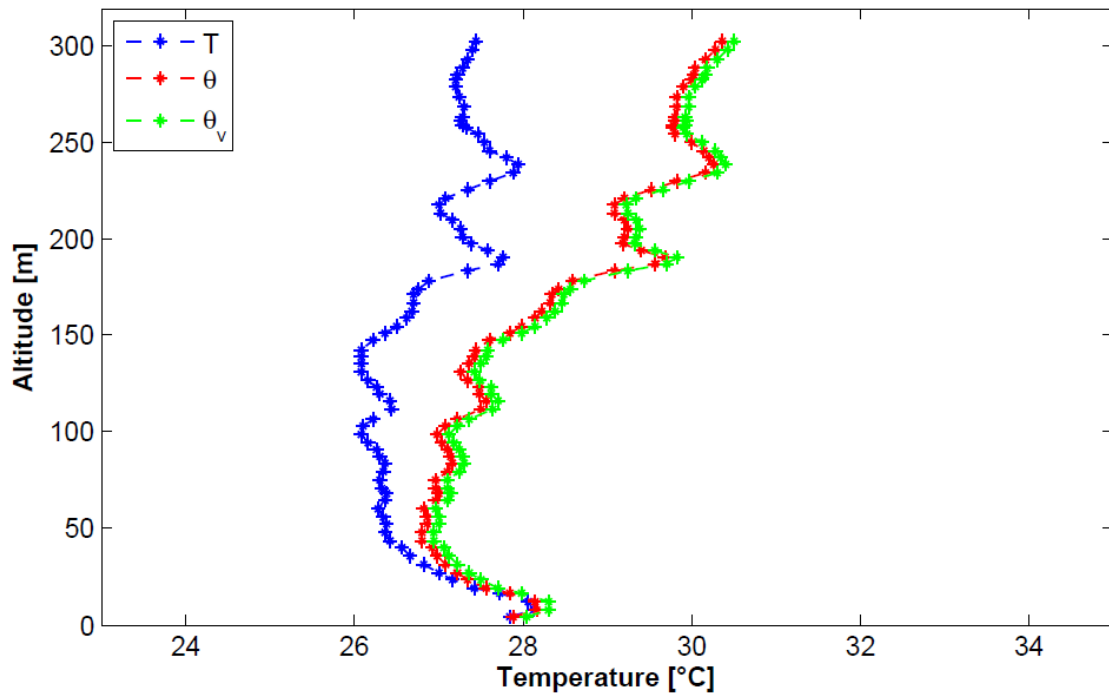


Figure VI-50 Only climbing phase: static, potential and virtual potential temperature profiles; 15/09/2010, 9:30 - 13:10 UTC+1.

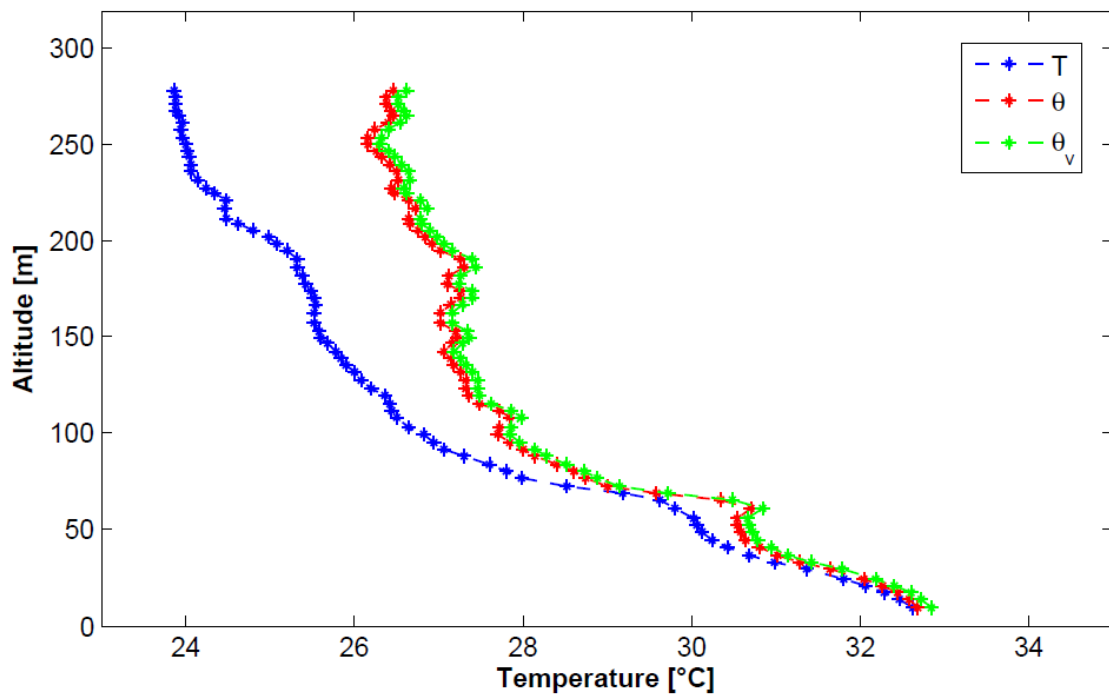


Figure VI-51 Only climbing phase: static, potential and virtual potential temperature profiles; 15/09/2010, 14:15 to 18:00 UTC+1.

VII. Caserta tests results

This flight test was programmed to be on the base of the weather forecast: an inversion on wind direction (180 deg, SW to NE) was expected between 13:00-14:00 UTC+1. Consequently two flight there had been before and after the inversion (see appendix D).

Between 9:30 and 13:10 UTC+1 a land breeze (3m/s) with MLH = 200m is toward W-SW (Fig. VII-31). The virtual potential temperature profile attests this and show the typical increase of temperature induced by trees.

During the afternoon flight there is a continuous change in wind direction (from W to E) and intensity (2-6 m/s) between 0-75m of altitude (Fig. VII-33); above this wind is directed to E-NE and a constant vertical profile (at 6 m/s of intensity) is shown, too; then a decreasing trend in wind intensity profile begins, accompanied with an initial redirection toward W. The temperature profile, superadiabatic, begins to increase just there (Fig. VII-35): we are near the MLH.

The wind roses (Fig. VII-36) show the change of direction; the kytoon, as a good kyte, moves in the direction of wind; the instantaneous position of CATFISH gondola is plotted in the 3D *GoogleEarth* map. The inclination of the trajectory is a indicator of wind intensity.

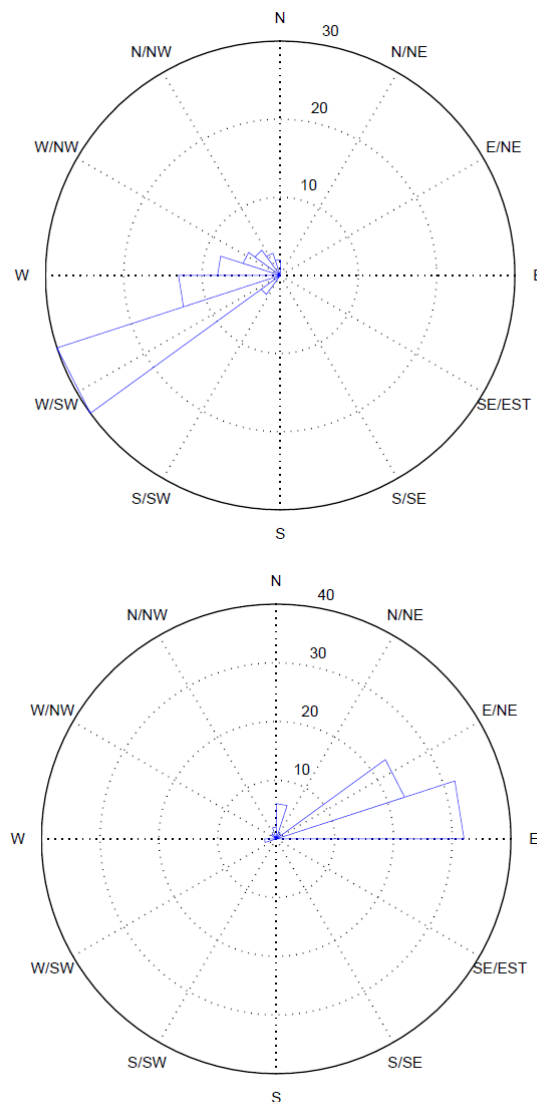


Figure VI-52 Wind roses; 9:30 - 13:10 (up) and 14:15 to 18:00 UTC+1 (down).



Figure VI-53 Trajectory of the kytoon; 9:30 - 13:10 (red) and 14:15 to 18:00 UTC+1 (black).; 15/9/2010.

VII.9. Air pollution concentration profiles (15/9/2010)

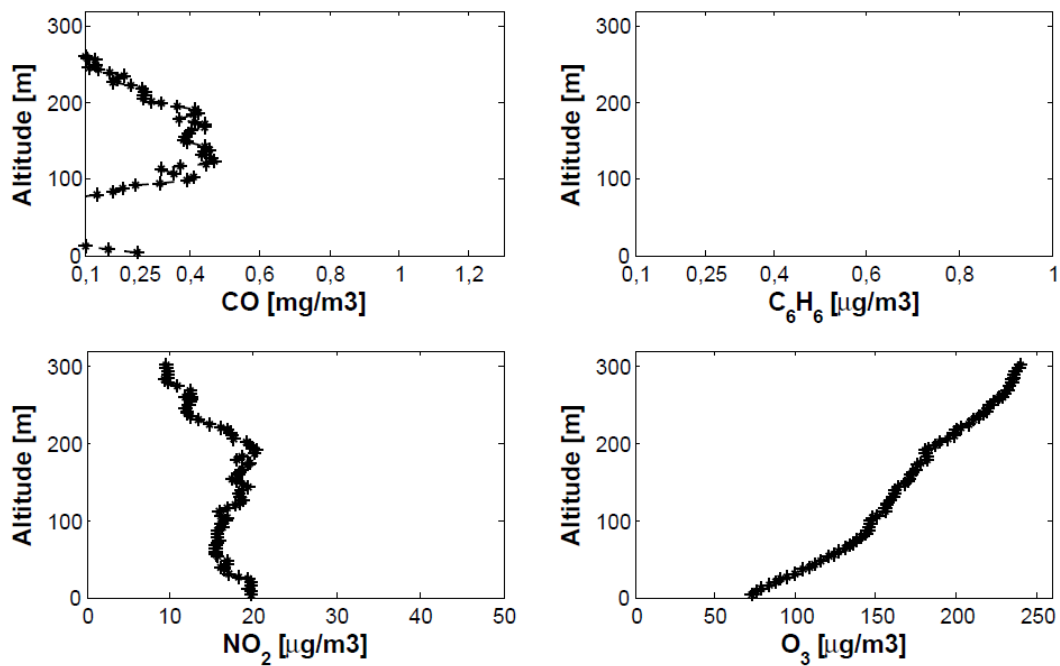


Figure VI-54 Only climbing phase: pollutants profiles; 15/09/2010, 9:30-13:10 UTC+1

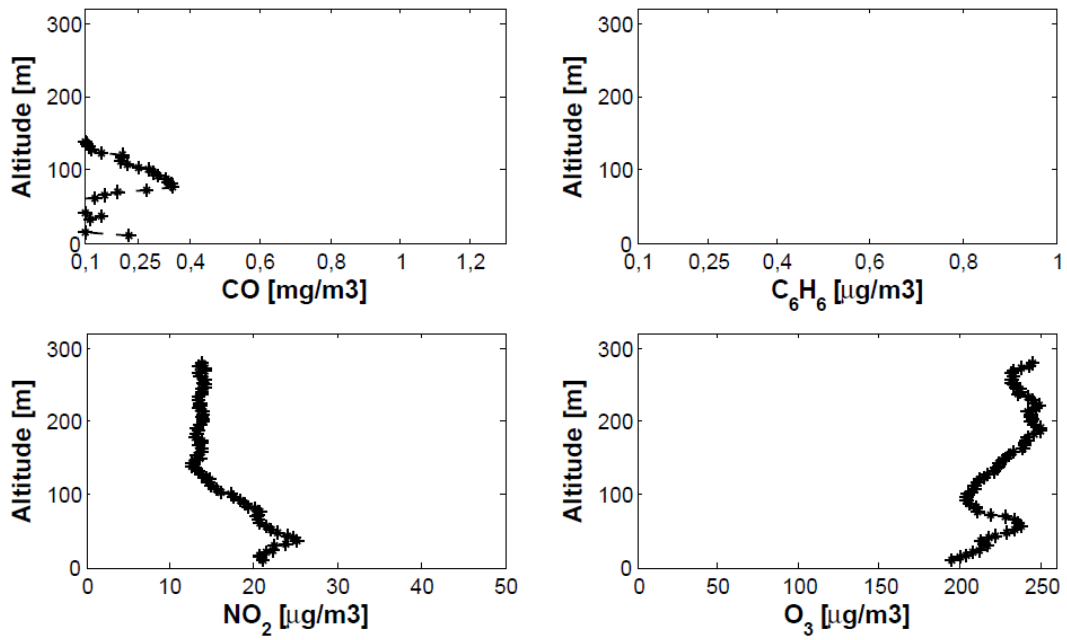


Figure VI-55 Only climbing phase: pollutants profiles; 15/09/2010, 14:15 – 18:00 UTC+1.

The concentration of CO is absolutely less than the data previously analyzed (particularly 13th september): this probably due to the light rain of the 14th September. The maximum concentration between the 9:30 and 13:10 UTC+1 is about 0.4 mg/m^3 and is constant between 100-200m of altitude; during the afternoon a peak of the same intensity is well localized at 100m.

The concentration of NO_2 decreases little from ground value (20 µg/m^3) due to the land breeze; during the afternoon a constant value (10 µg/m^3) is measured over 100m while a peak of 25 µg/m^3 is at about 50m, where sea breeze is relatively slow (2 m/s).

No concentration of C_6H_6 is measured.

VII.10. Wind profiles (16/9/2010)

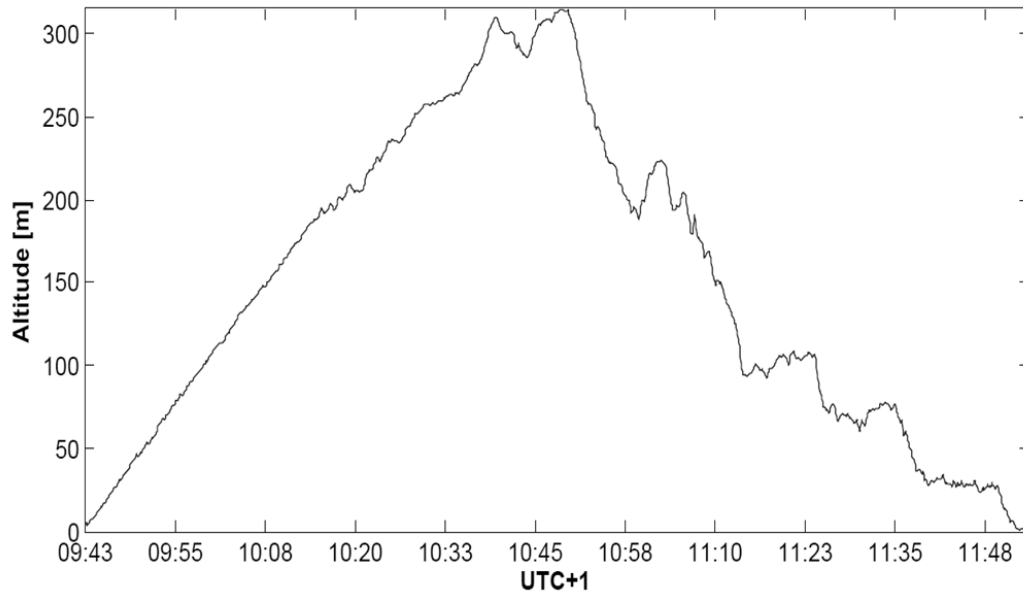


Figure VI-56 Altitude profile; 16/09/2010, 9:40 - 11:50 UTC+1.

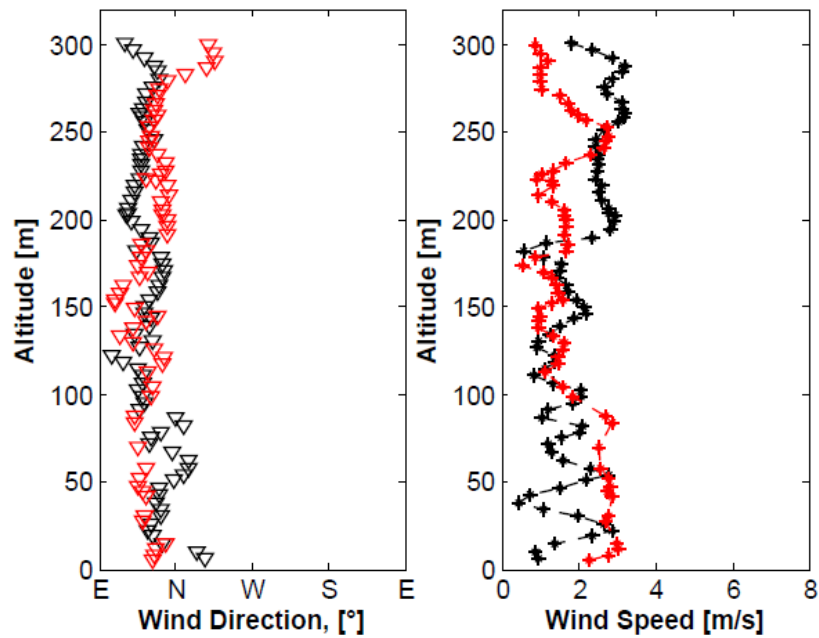


Figure VI-57 Climbing (black) and descending (red) phases: wind direction and wind speed profiles. 16/09/2010, 9:40 - 11:50 UTC+1.

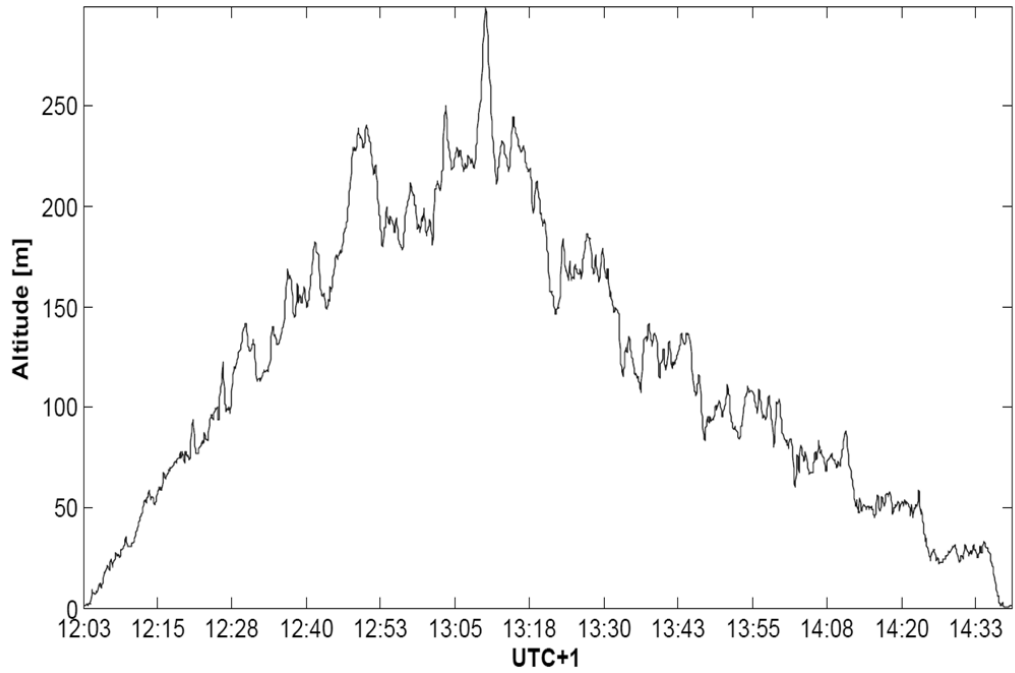


Figure VI-58 Altitude profile. 16/09/2010, 12:00 - 14:40 UTC+1.

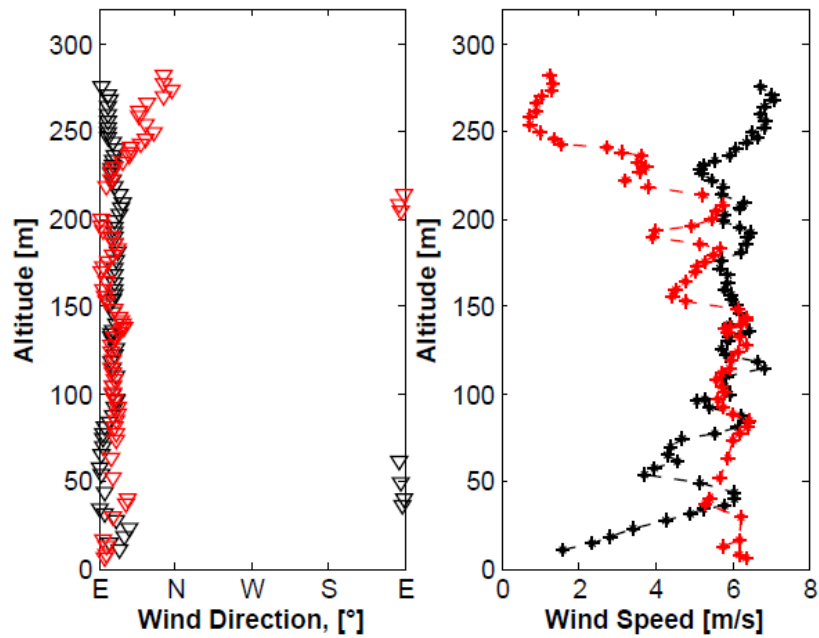


Figure VI-59 Climbing (black) and descending (red) phases: wind direction and wind speed profiles. 16/09/2010, 12:00 – 14:40 UTC+1.

VII.11. Temperature profiles (16/9/2010)

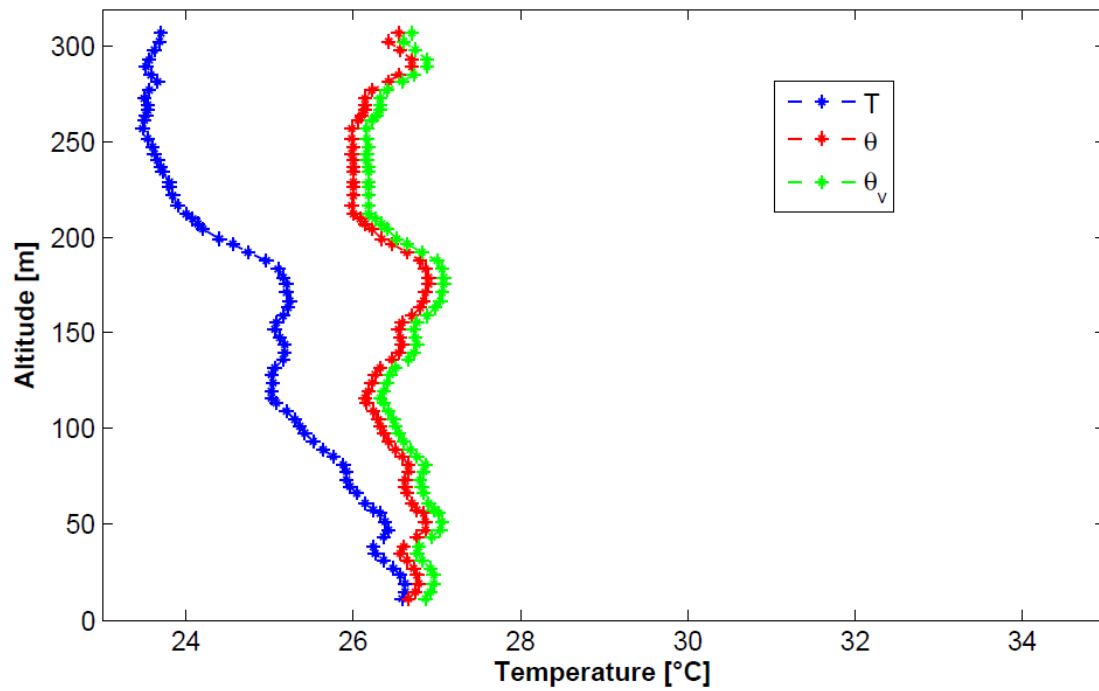


Figure VI-60 Climbing phase: static, potential and virtual potential temperature profiles.
16/09/2010, 9:40 - 10:50 UTC+1.

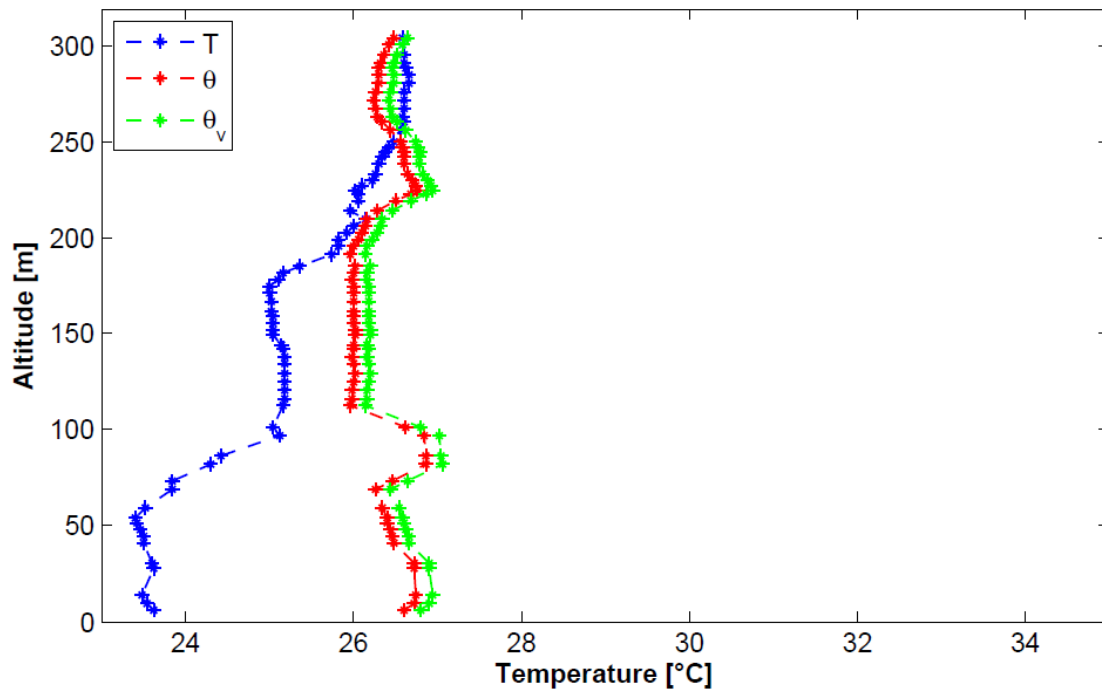


Figure VI-61 Descending phase: static, potential and virtual potential temperature profiles.
16/09/2010, 10:50 - 11:50 UTC+1.

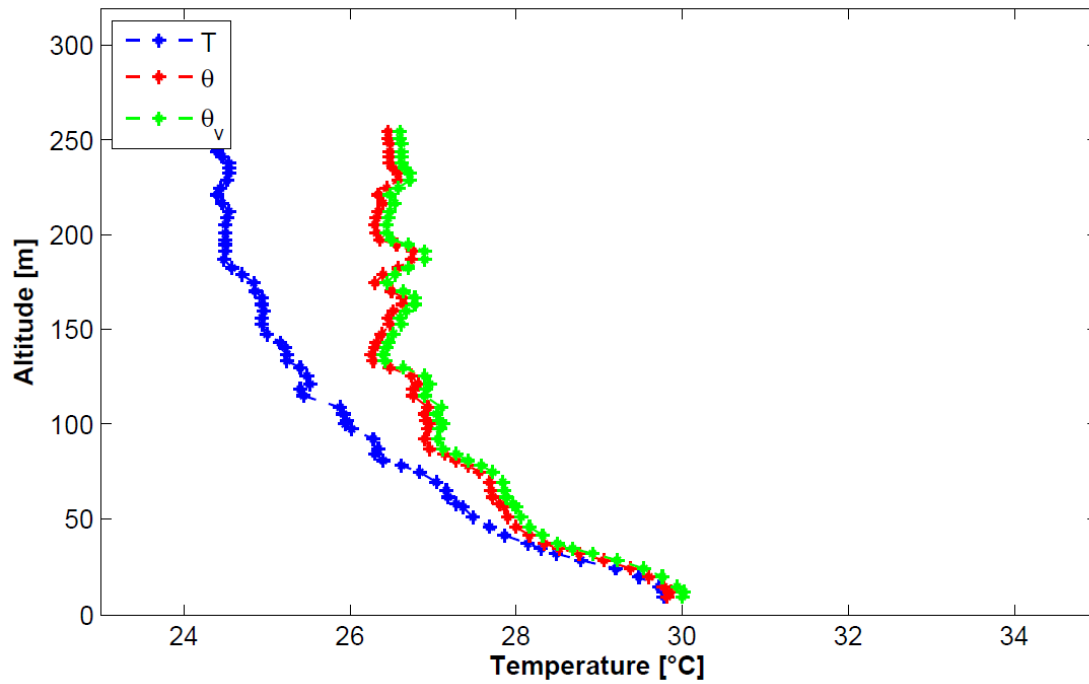


Figure VI-62 Climbing phase: static, potential and virtual potential temperature profiles.
16/09/2010, 12:00 - 13:10 UTC+1.

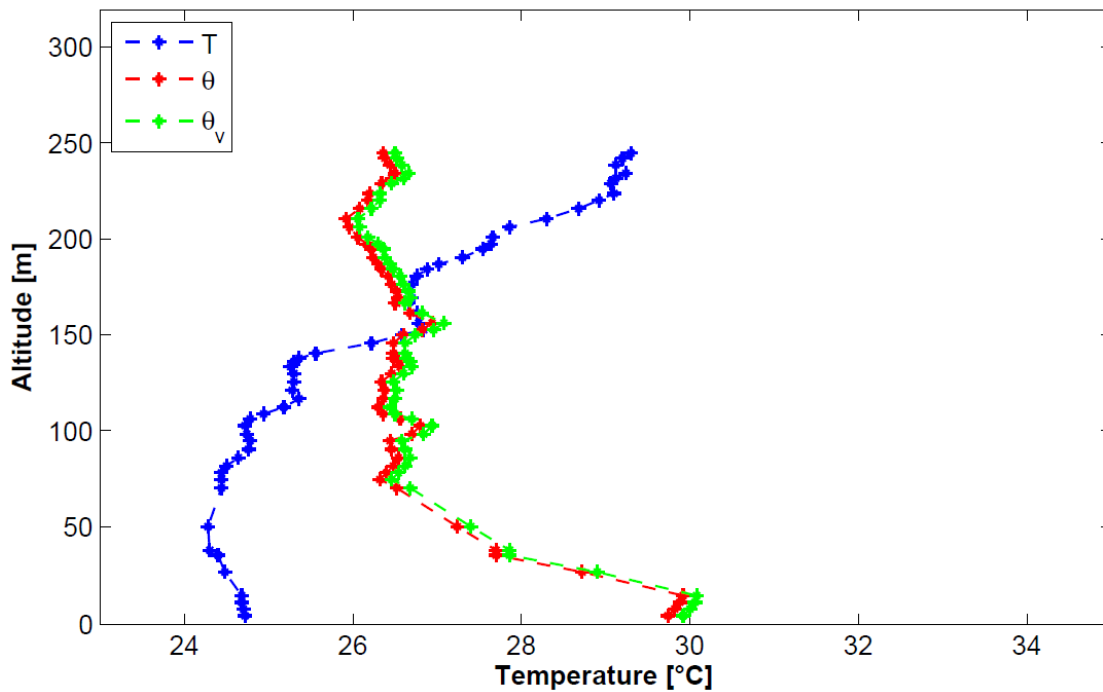


Figure VI-63 Descending phase: static, potential and virtual potential temperature profiles.
16/09/2010, 13:10 - 14:40 UTC+1.

Between 9:40 and 10:50 UTC+1 the wind blow at 1-3 m/s toward N-NE (Fig. VII-41 black). The wind intensity profile is constant (3m/s) in the range of altitude 200-300 m; analyzing virtual potential profiles (Fig. VII -44) it is possible to identify a ML region just there, but the trend below 200m of altitude is unknown (Fig. VII-44).

During the descending phase (10:30-11:50 UTC+1) wind direction is stabilized toward NE; between the ground and 80m AGL the wind intensity profile is constant (3m/s) over altitude (as can be seen from virtual potential plot), while between 100-225m AGL the wind blows at about 1m/s (a local ML develop here; Fig. VII-45).

Around noon (12:00-14:40 UTC+1) the wind intensity profile is quite similar to that of 13th September: during the ascent phase of kytoon (12:00-13:10) it increases from 2 to 6m/s and the direction is stably EST (Fig. VII-43 black).

Between 13:10 and 14:40 UTC+1 (Fig. VII-43 red). the sea breeze has an intensity of 6m/s until 200m; then it begins to decrease to zero at 250m AGL (MLH); the virtual potential temperature profile attests this (Fig. VII-47). MLH decreases over time as well as the superadiabatic region (Fig. VII-46-47).

VII.12. Air pollution concentration profiles (16/9/2010)

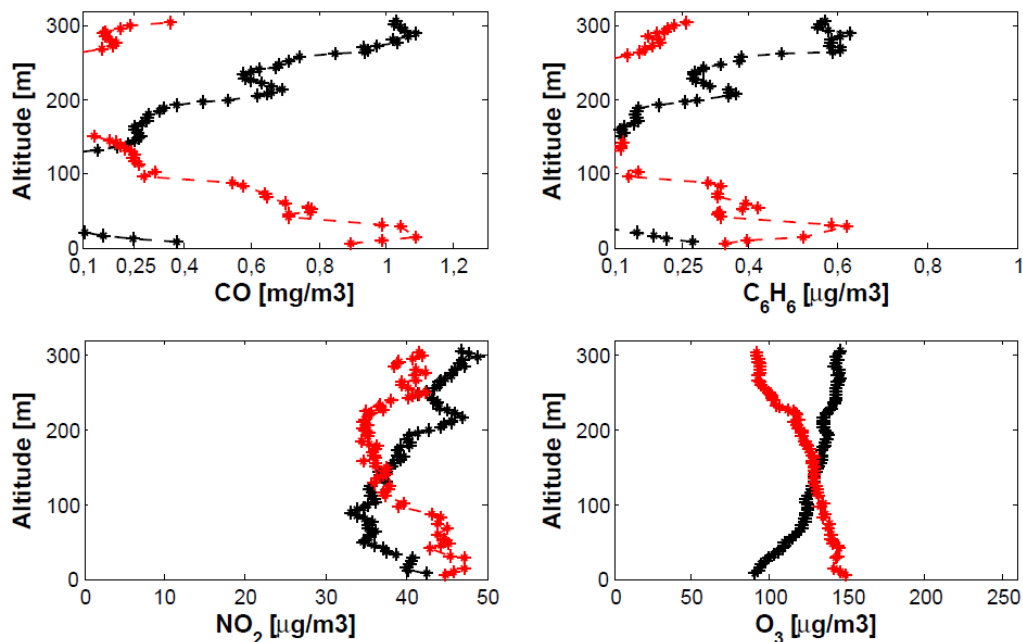


Figure VI-64 Climbing (black) and descending (red) phases: pollutants profiles.
16/09/2010, 9:40 – 11:50 UTC+1.

CO and C₆H₆ concentrations during the morning (Fig. VII-48) are quite similar to each other: the maximum values are located between 0-300m AGL (respectively 1.1 and 0.6 μg/m³); the profiles have concavity towards zero value (respectively between 50-120m in ascent phase; and 100-250m in descent phase for each pollutants); the descending concentration profiles grew over the day.

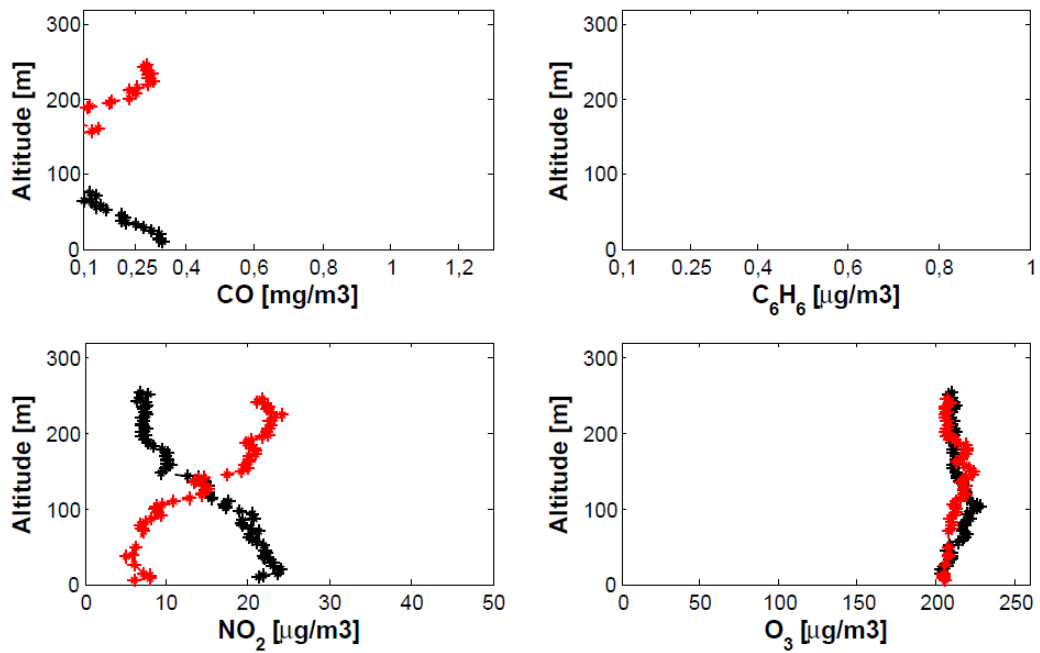


Figure VI-65 Climbing (black) and descending (red) phases: pollutants profiles.
16/09/2010, 12:00 – 14:40 UTC+1.

NO_2 concentration profile oscillates between 35 and 50 $\mu\text{g}/\text{m}^3$ following a similar trend of CO and C_6H_6 ones; the maximum concentration transforms itself from a localized peak at 200m AGL to full altitude below 100m.

In the afternoon (Fig. VII-49) the strong sea breeze (6m/s) wipes out C_6H_6 and the maximum concentration of CO (0.4 $\mu\text{g}/\text{m}^3$ that is very lower than morning value) is measured near the ground.

VII.13. Wind profiles (17/9/2010)

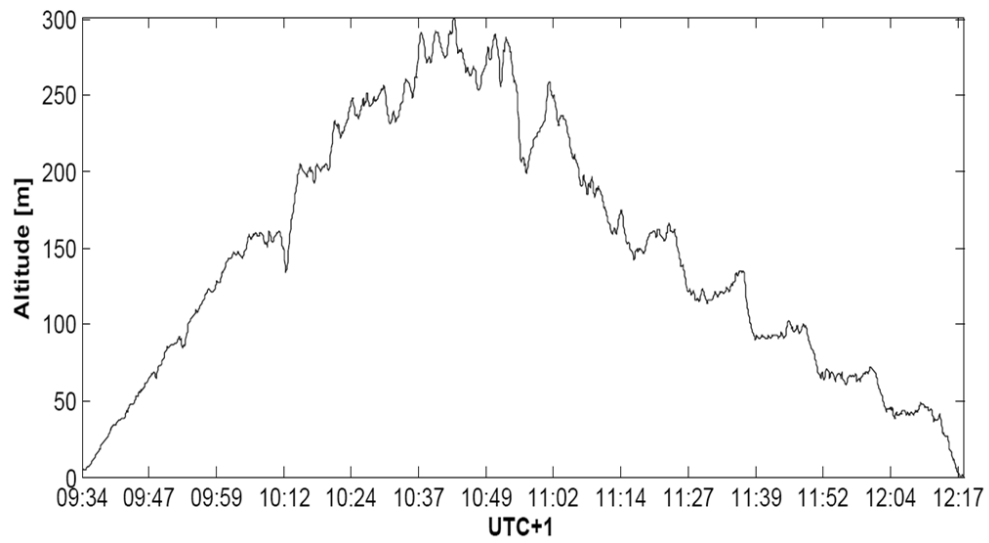


Figure VI-66 Altitude profile. 17/09/2010, 9:30 - 12:20 UTC+1.

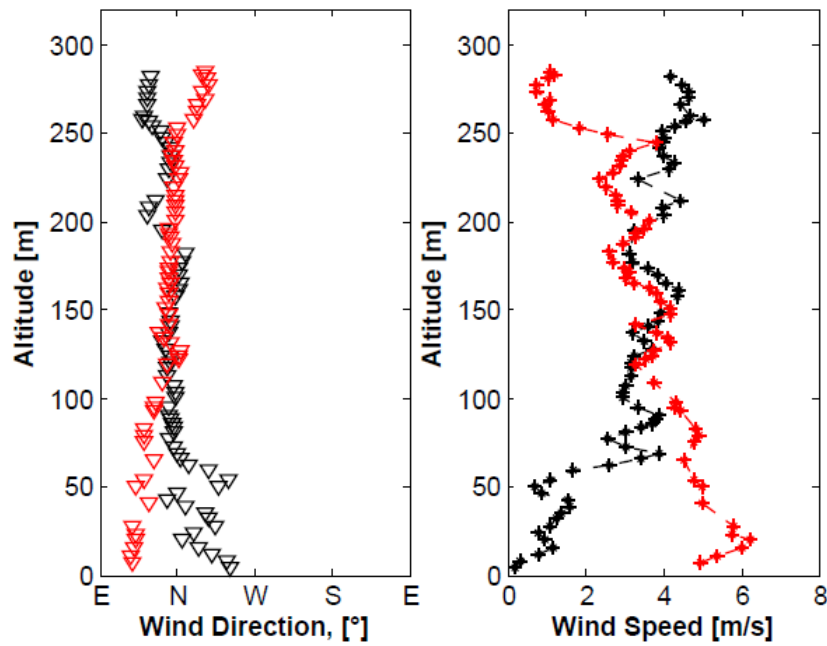


Figure VI-67 Climbing (black) and descending (red) phases: wind direction and wind speed profiles. 17/09/2010, 9:30 – 12:20 UTC+1.

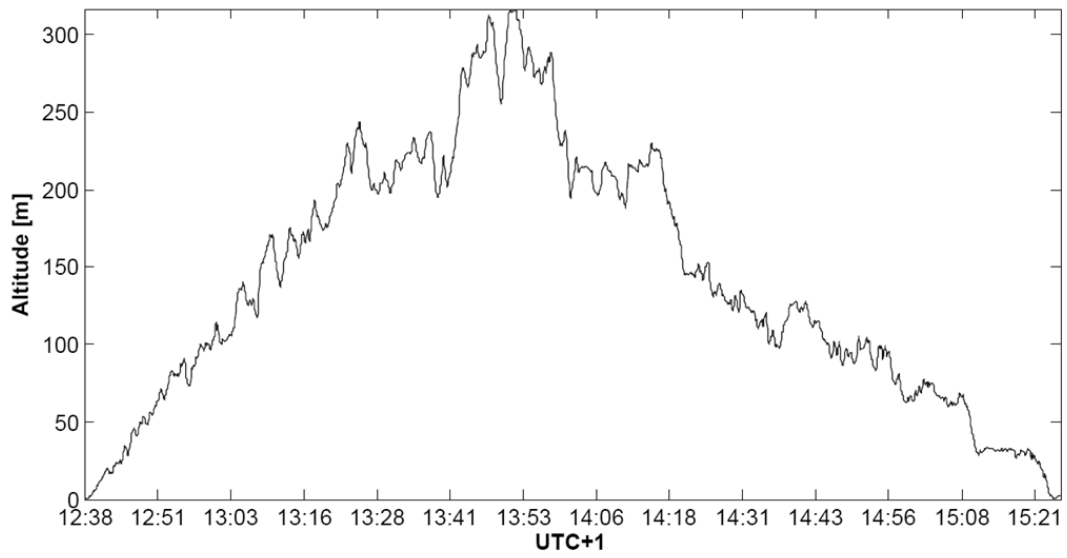


Figure VI-68 Altitude profile. 17/09/2010, 12:30 to 15:30 UTC+1.

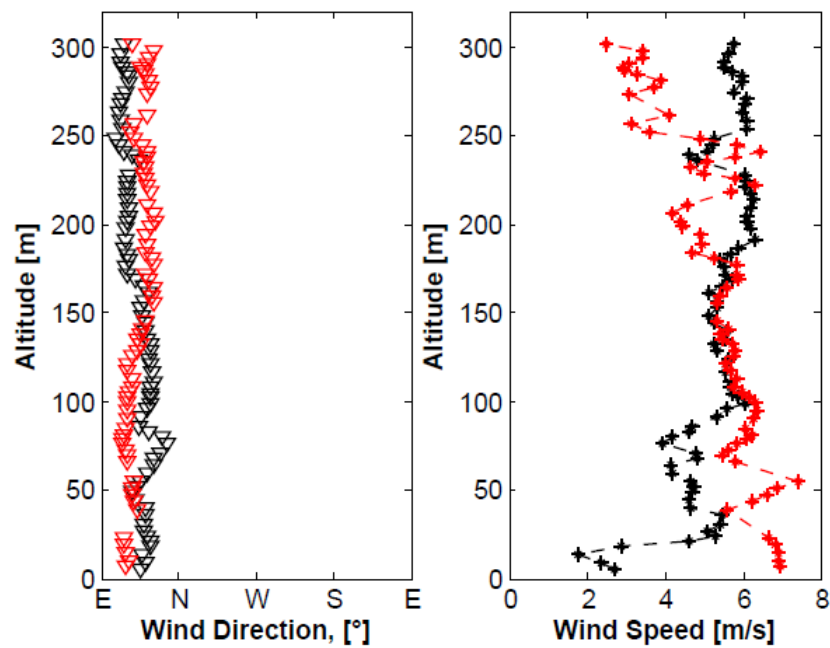


Figure VI-69 Climbing (black) and descending (red) phases: wind direction and wind speed profiles. 17/09/2010, 12:30 - 15:30 UTC+1.

VII.14. Temperature profiles (17/9/2010)

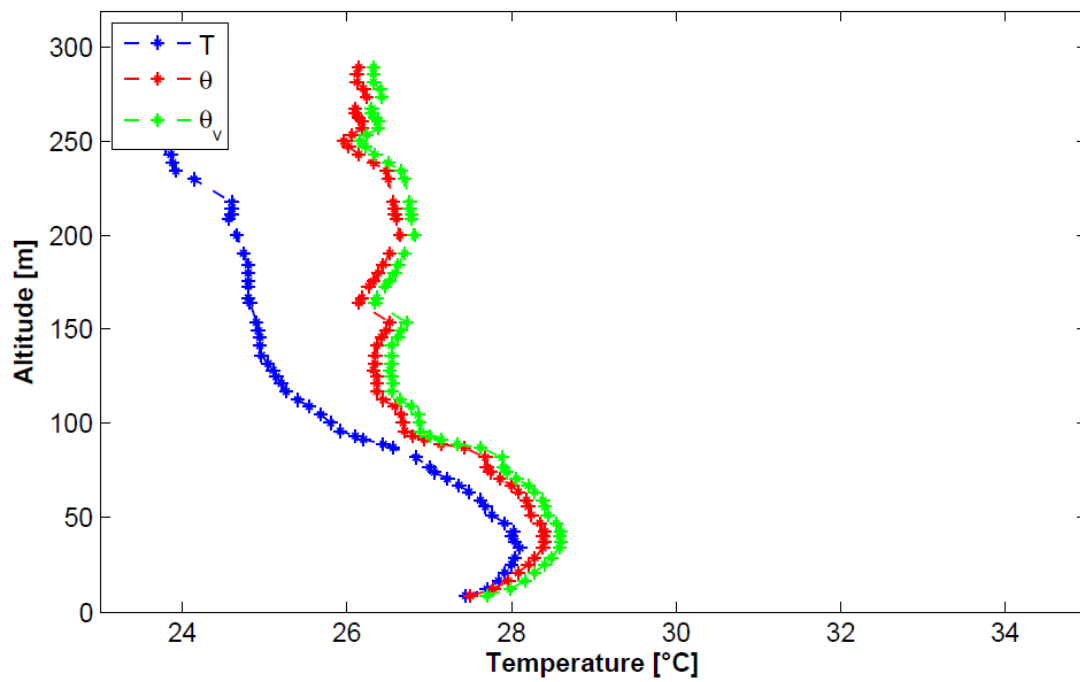


Figure VI-70 Climbing phase: static, potential and virtual potential temperature profiles.
17/09/2010, 9:30 - 10:40 UTC+1.

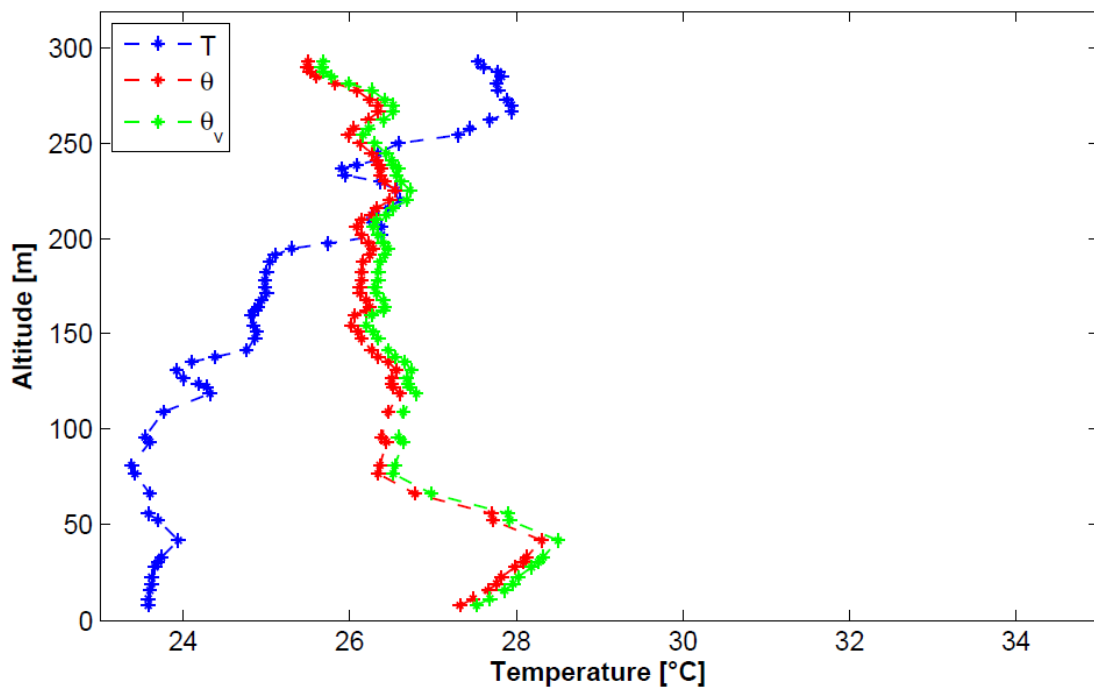


Figure VI-71 Descending phase: static, potential and virtual potential temperature profiles.
17/09/2010, 10:40 - 12:20 UTC+1.

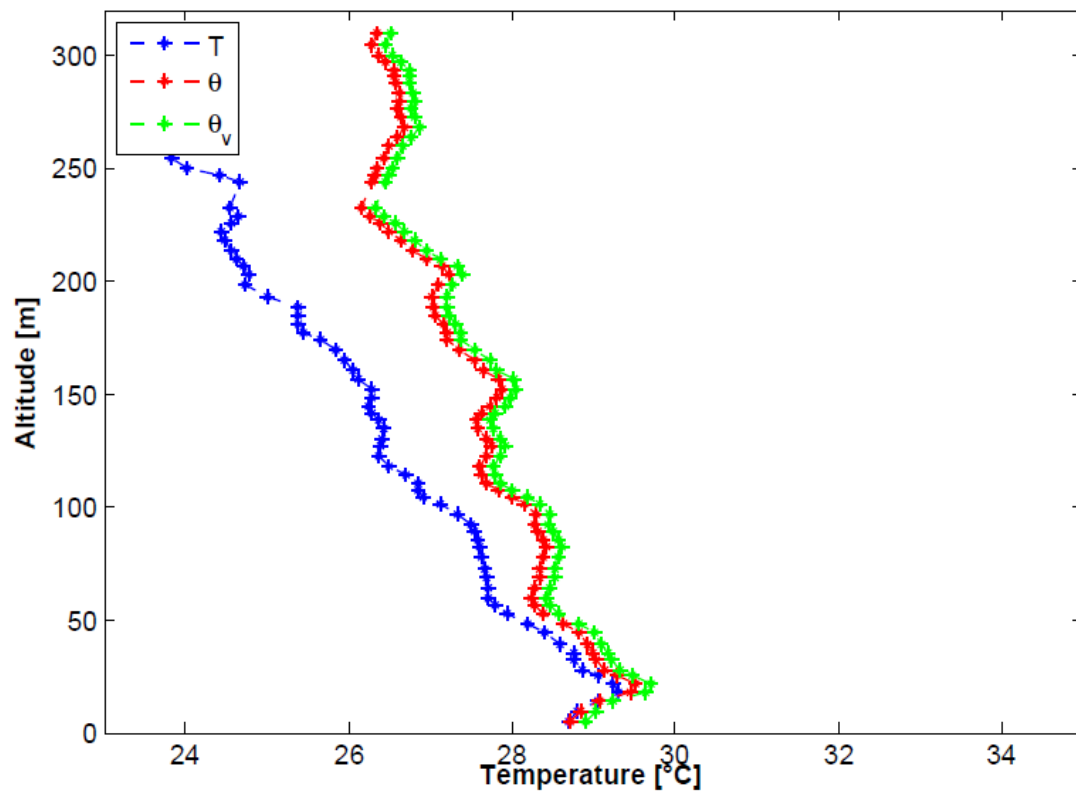


Figure VI-72 Climbing phase: static, potential and virtual potential temperature profiles.
17/09/2010, 12:30 - 13:50 UTC+1.

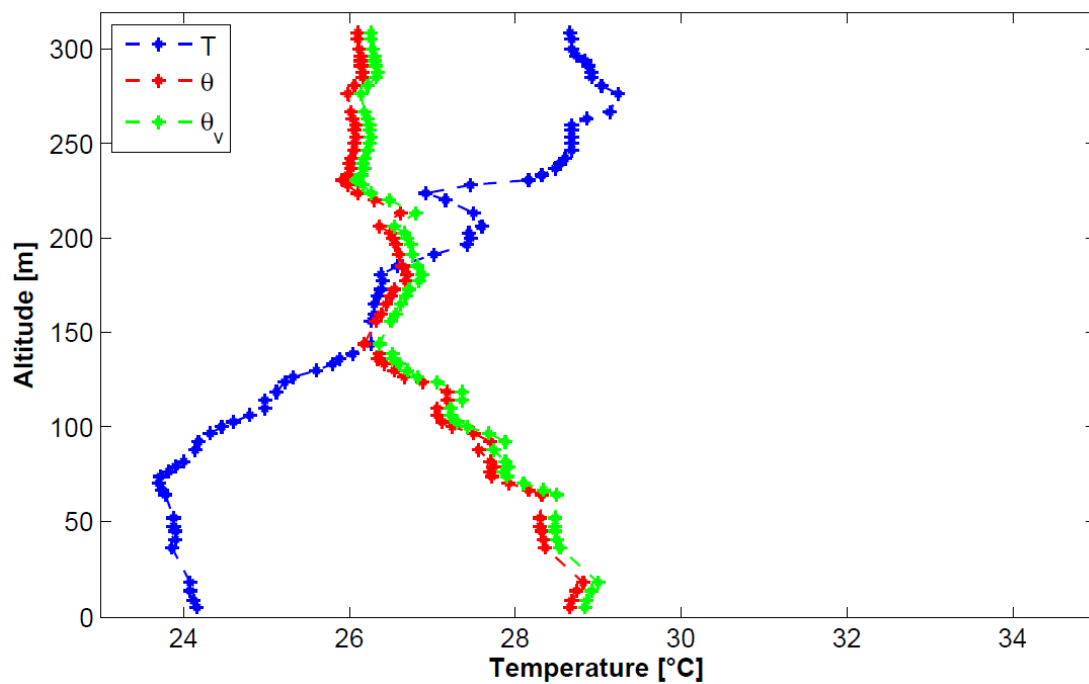


Figure VI-73 Descending phase: static, potential and virtual potential temperature profiles.
17/09/2010, 13:50 - 15:30 UTC+1.

Between the 9:30-10:40 UTC+1 (Fig. VII-51 black) the wind intensity profile grows continuously from 0 to 4m/s at 280m AGL (that is the maximum altitude); near the ground the wind blows toward W; then, in the first 75m AGL it rotates to N and changes only above 250m AGL (toward NE). The initial changes of direction above 250m (respectively from NE to N and NW to W) identify a condition near the MLH (see also Fig. VII-54,55).

Between the 10:40 and 12:20 UTC+1 (Fig. VII-51 red) the wind intensity profile has maximum value near the ground and reaches zero at 250m (MLH); the direction changes from N to NE; this conditions are verified by the virtual temperature plots.

After 12:30 UTC+1 (Fig. VII-53) the direction of wind is well stabilized to NE and the trends are quite similar to that of the 16th September, even if the intensity of sea breezes are higher (2m/s the minimum value and 7m/s the maximum one).

A particular characteristic of the virtual potential profiles is an increase near the ground, which vertical depths and intensities decrease over time; trees effect cannot be, because the high altitude (also 100m); it is possible that is SBL of night (Fig. VII-54 to 57).

VII.15. Air pollution concentration profile (17/9/2010)

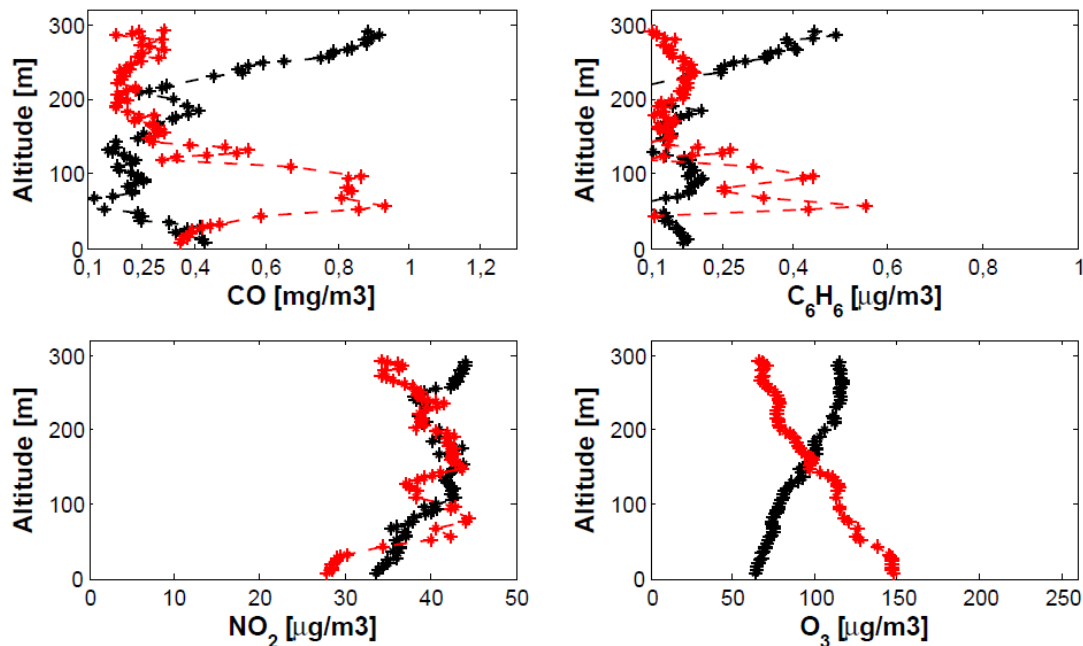


Figure VI-74 Climbing (black) and descending (red) phases: pollutants profiles. 17/09/2010, 9:30 – 12:20 UTC+1.

From the early morning to noon the *CO* and *C₆H₆* concentration profiles are quite similar to each other (except for the value): the maximum concentrations move from 300m AGL (9:30UTC+1) downward at about 12:00UTC+1, covering the range of altitude 50-100m; the ground levels of pollutants near the ground is the same at early morning and at noon, probably because wind blows at high speed (6m/s) between 0-50m AGL.

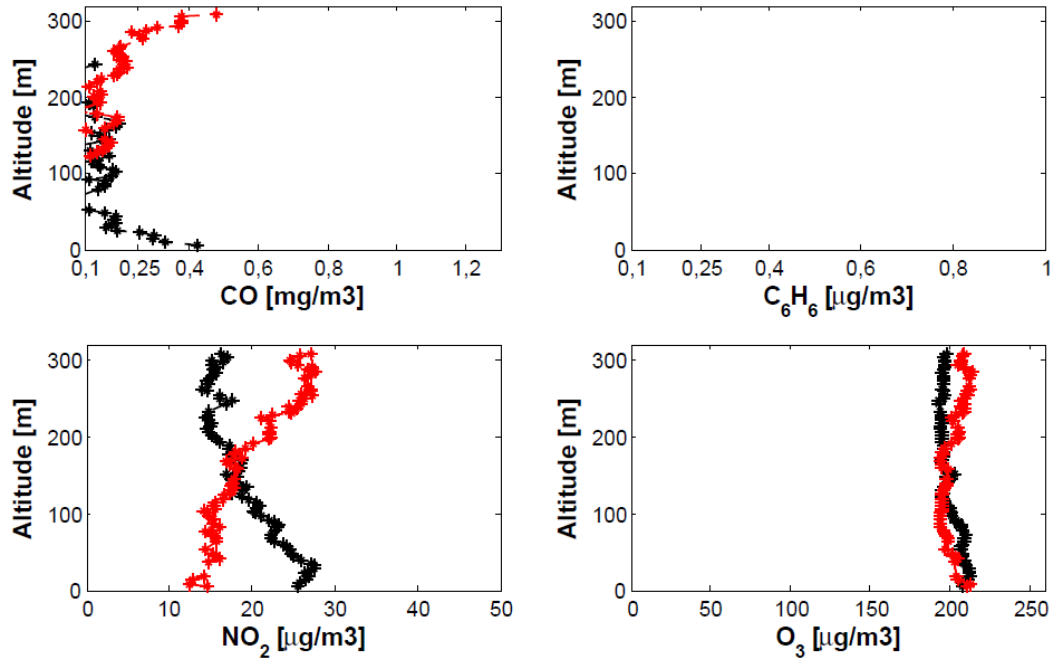


Figure VI-75 Climbing (black) and descending (red) phases: pollutants profiles.
17/09/2010, 12:30 – 15:30 UTC+1.

During the afternoon (12:30-15:30 UTC+1), as on 13th and 16th September, the sea breeze disperses the C₆H₆ at every altitude and, comparing the concentration at launch and landing phase, we note that there is only a low concentration of NO₂ (10 μg/m³).

In general the same trend of NO₂ concentration with altitude is observed, comparing with the 16th September test.

VII.16. Analysis of atmospheric turbulence (7/9/2010)

As example of possible calculation follows the turbulent calculations performed on the test on 7th September 2010. Table VII-1 shows the averaged altitudes to which the measurements were made and the corresponding temporal range of observation.

z (m)	Δt (mm:ss)
309	10:30/10:41
245	11:09/11:19
213	11:22/11:31
183	11:34/11:43
152	11:46/11:56
124	12:00/12:08
63	12:23/12:32
34	12:34/12:44

Table VI-6 Averaged stop altitude and pause; 7/9/2010, 10:30-12:45 UTC+1.

VII.16.1. Turbulent fluctuations

The temporal trend of the turbulent components follows (Fig. VII-60 to 67). Note that the mean value of all the fluctuations is zero.

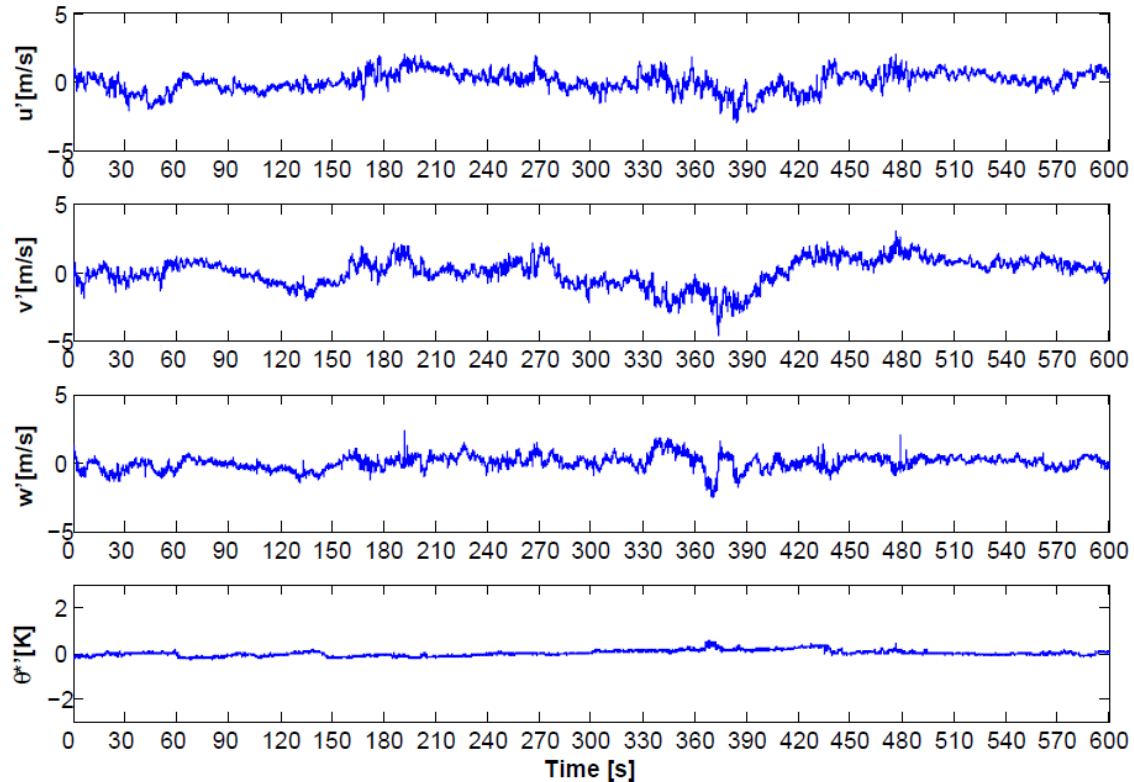


Figure VI-76 Turbulent fluctuations at 34m AGL.

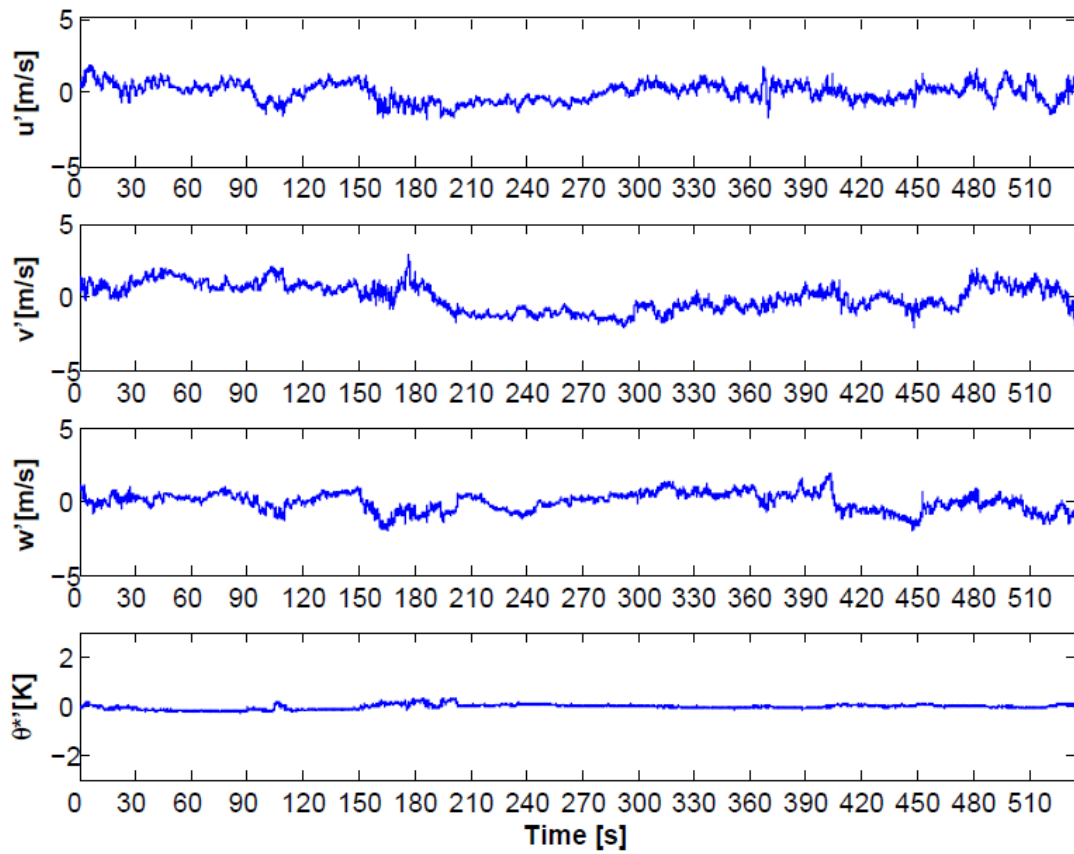


Figure VI-77 Turbulent fluctuations at 63m AGL.

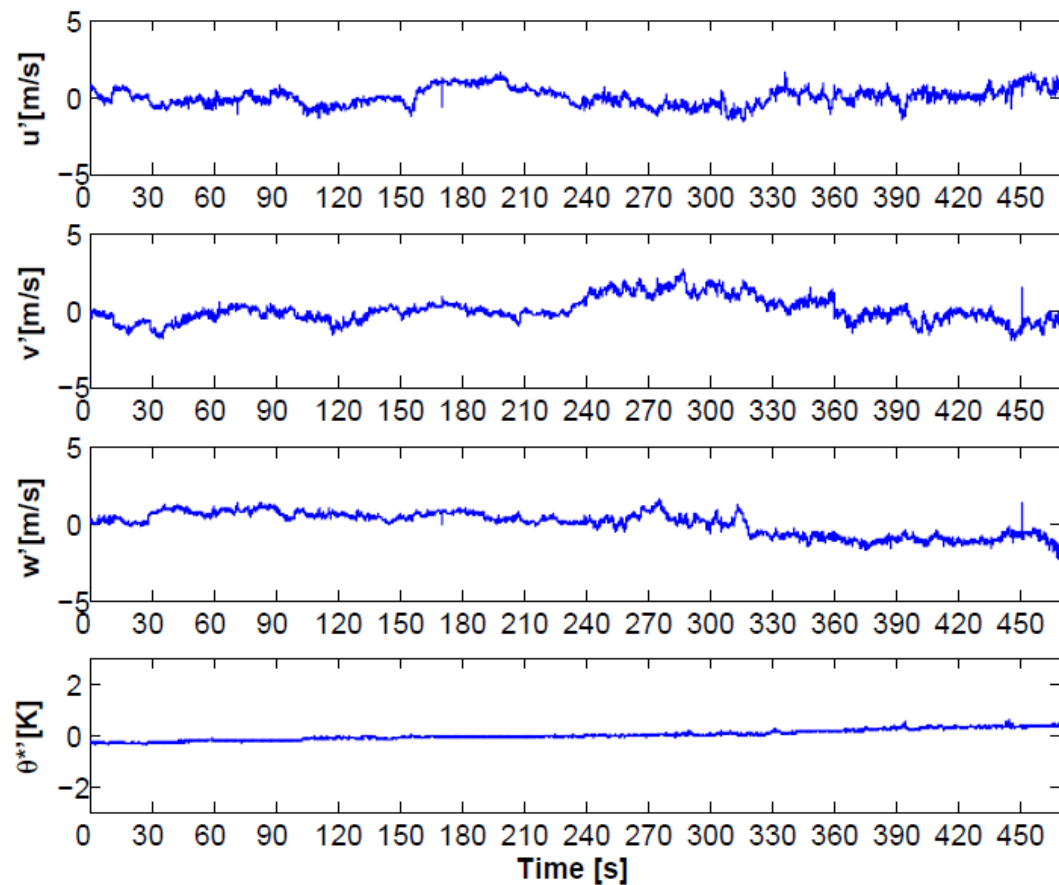


Figure VI-78 Turbulent fluctuations at 124m AGL.

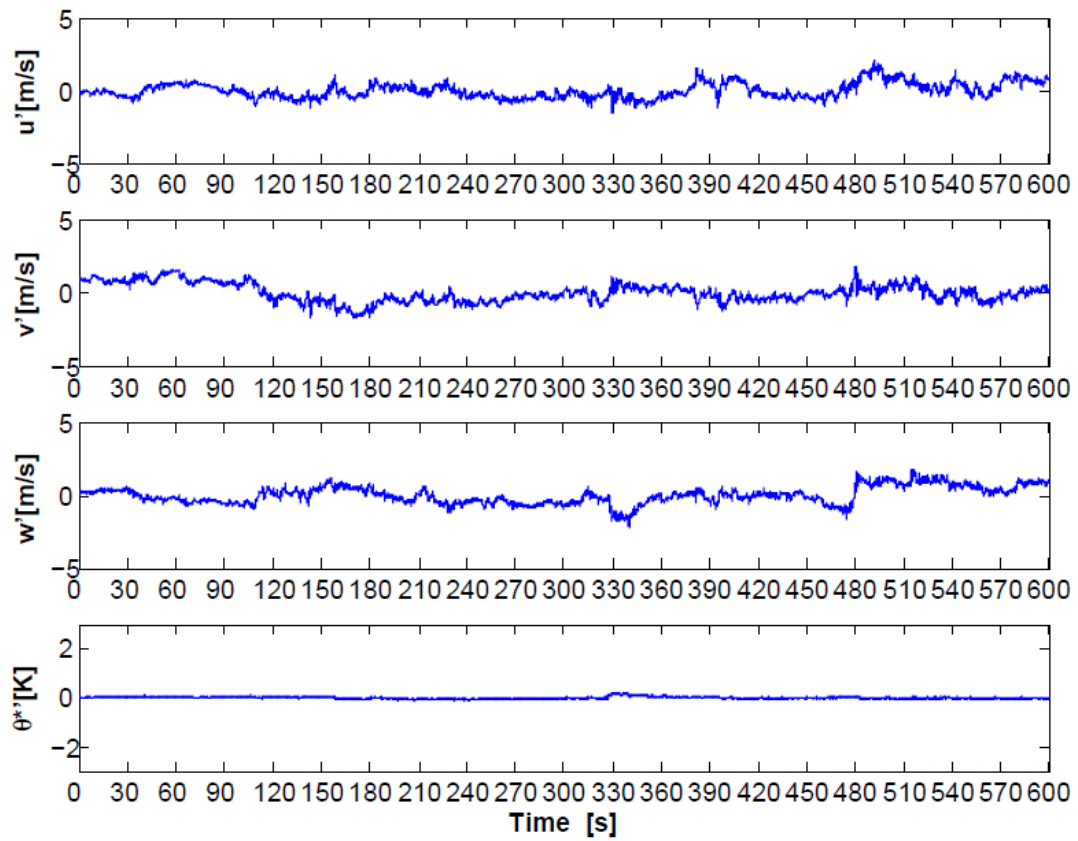


Figure VI-79 Turbulent fluctuations at 152m AGL.

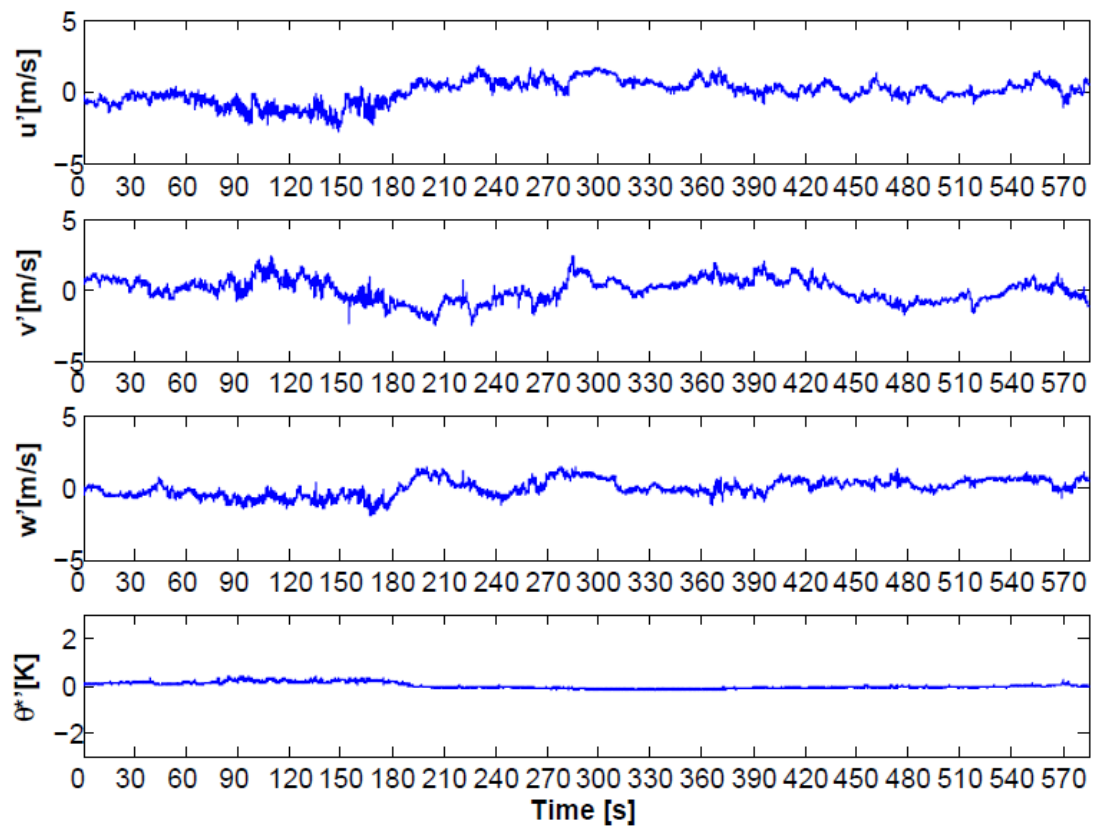


Figure VI-80 Turbulent fluctuations at 183m AGL.

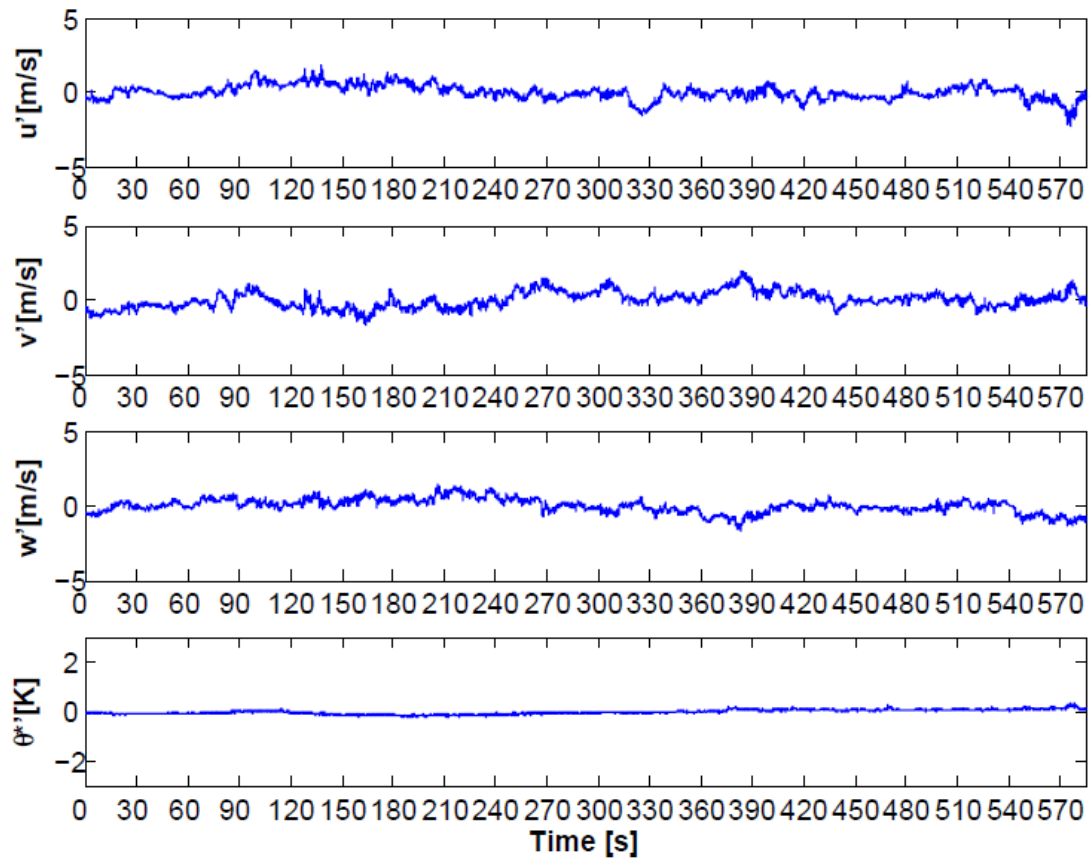


Figure VI-81 Turbulent fluctuations at 213m AGL.

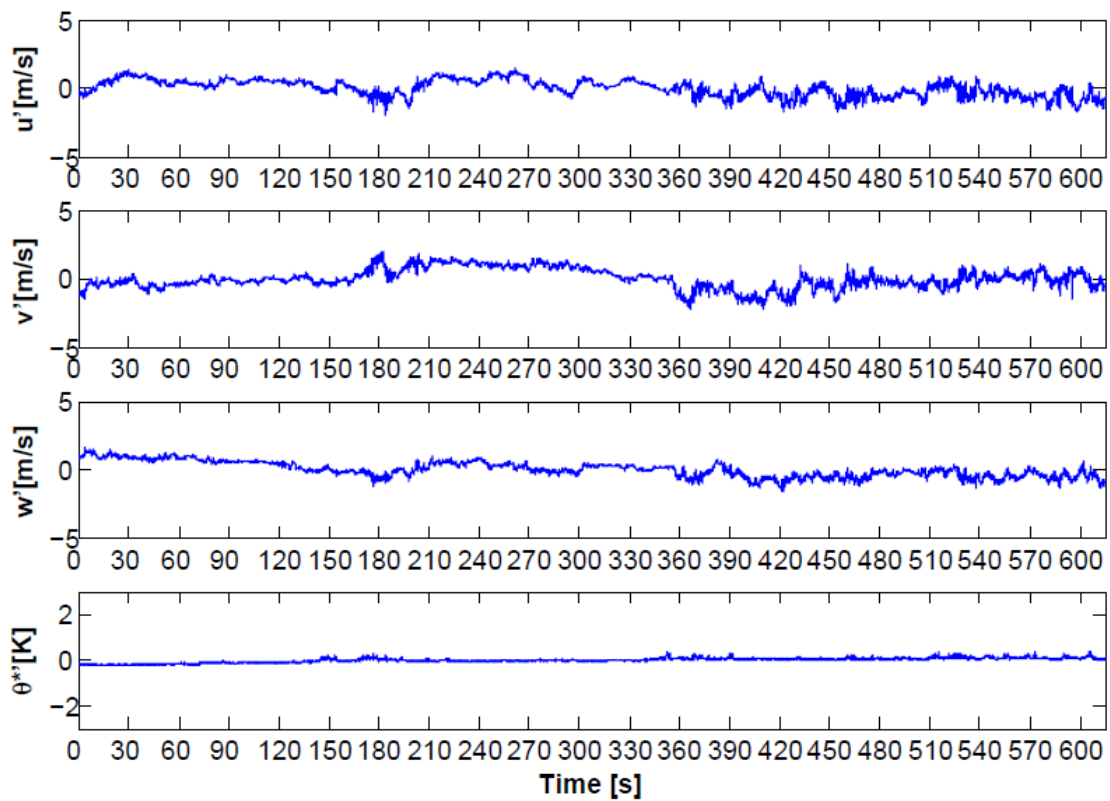


Figure VI-82 Turbulent fluctuations at 245m AGL.

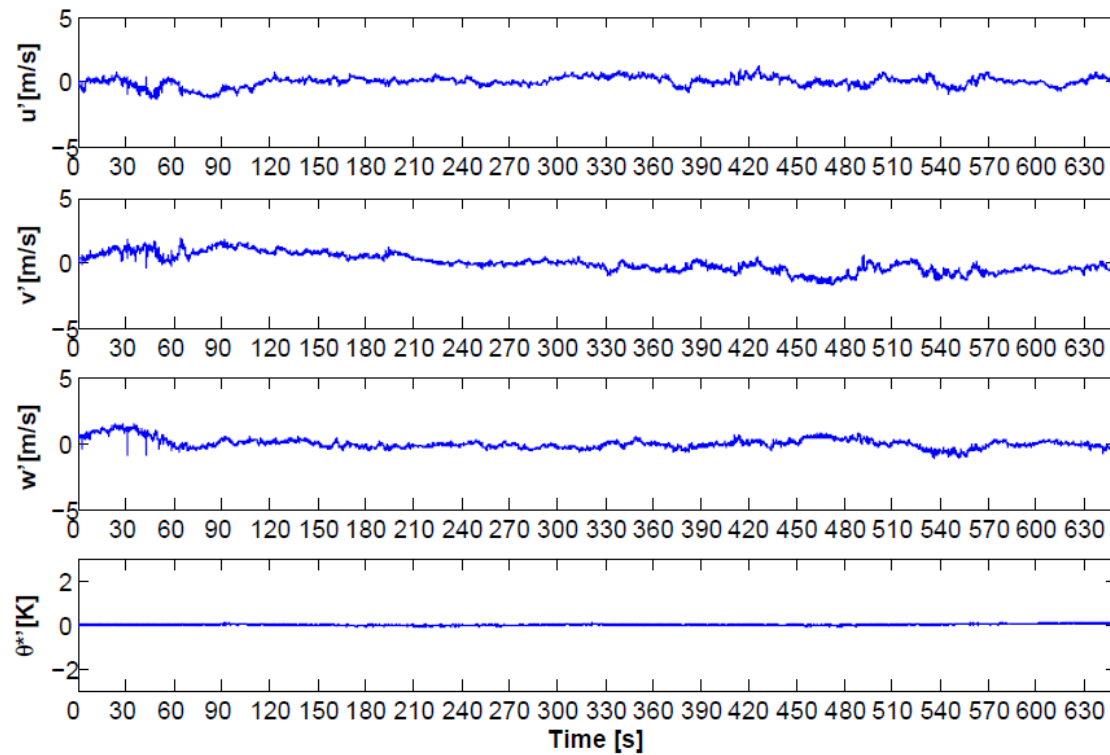


Figure VI-83 Turbulent fluctuations at 309m AGL.

VII.16.2. Turbulent statistics

The resulting standard deviations of θ^* and w' are shown compared to that measured by Ogawa (Ogawa Y., 1986) in figure VII-68 and VII-69.

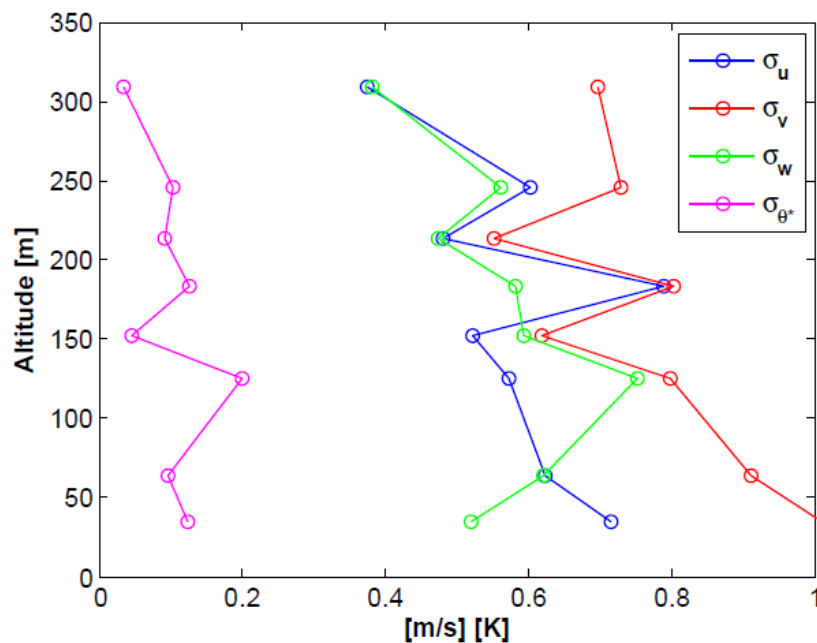


Figure VI-84 Standard deviations of the turbulent components over altitude; 7/9/2010 10:30-12:45 UTC+1.

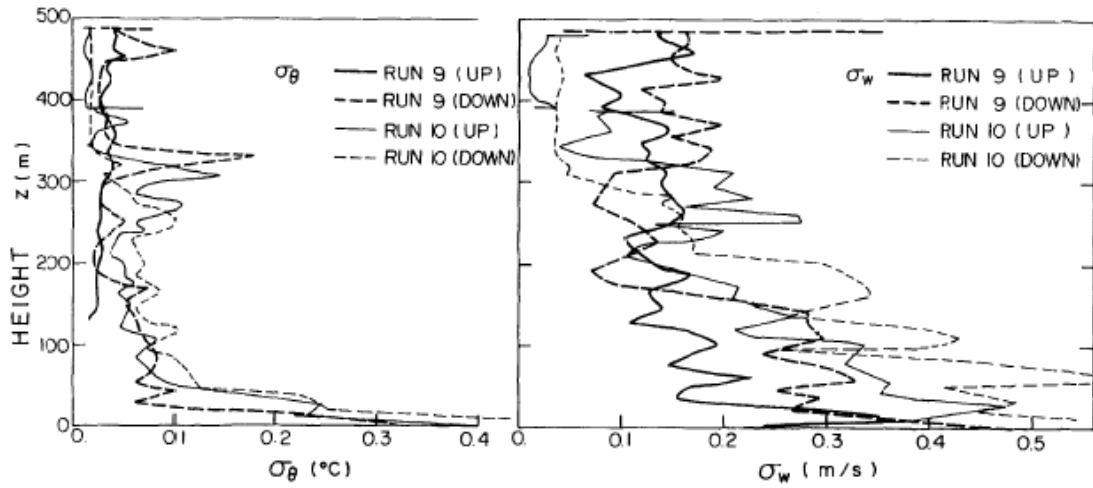


Figure VI-85 Standard deviations over altitude on 11 June 1982: Run 9 up (9:00-9:44) and down (9:44-10:42); run 10 up (11:00-12:40) and down (12:40-13:20); time EDT; (Ogawa Y., 1986).

The thermal deviation is much smaller than the dynamic standard deviation in both the experiments. At $z=183$ m, σ_u and σ_v are a very similar (Fig. VII-68). The σ_v reaches a value very close to unity at $z=34$ m; this means that the thermal convection is very intense in the North-South direction at this altitude.

We observe that the standard deviations of temperature are quite similar to each experiment over altitude, but the measurements about the downwind component (w), made on 7/9/2010, shows sensibly higher turbulence than that of Ogawa (run 10 up).

Turbulent statistics show larger value at low altitudes where the turbulence represents the principal transport process in every case.

VII.16.3. Turbulent fluxes

Figure VII-70 and VII-71 shows the $\overline{w'g'}$ and the $\overline{u'w'}$ profiles.

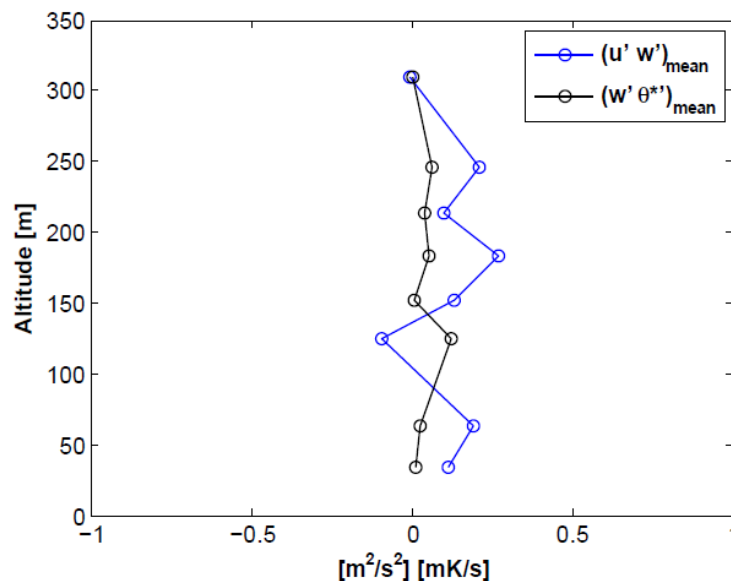


Figure VI-86 Vertical eddy fluxes profiles; 7/9/2010, 10:30-12:45 UTC+1.

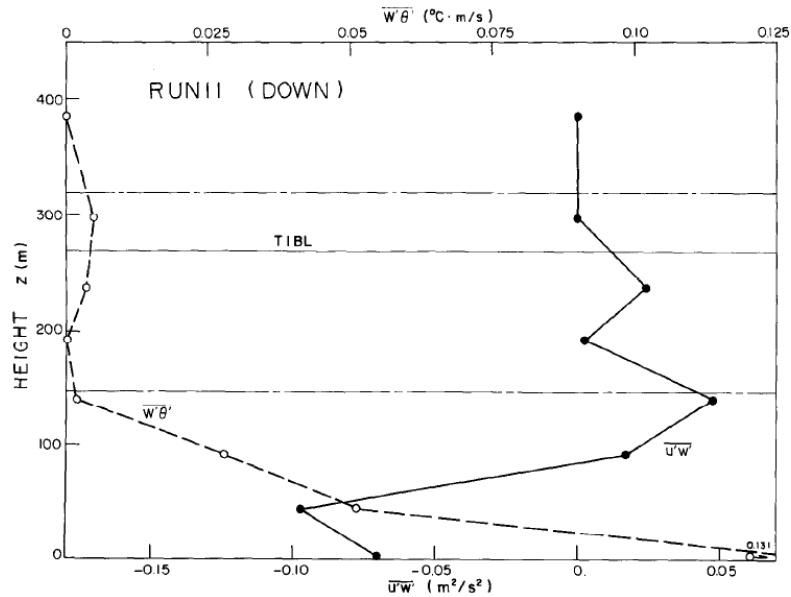


Figure VI-87 Vertical eddy fluxes measured on 11 June 1982, 14:44-16:36 EDT; Thermal internal Boundary Layer (TIBL); (Ogawa Y., 1986)

The $\overline{w'\theta'}$ profile, measured in Caserta and by Ogawa, had always very close and positive values. Particularly they decrease with altitude.

The same observation applies to $\overline{u'w'}$ except at respectively $z = 124\text{m}$ (Fig. VII-70) and $z < 100\text{m}$ (Ogawa, Fig. VII-71), where the values are negative.

At high altitude (up to 300m) the turbulent cross-correlations assume zero value (we are over TIBL).

Figure VII-72 show an example of linear correlation coefficient calculation between u' and w' .

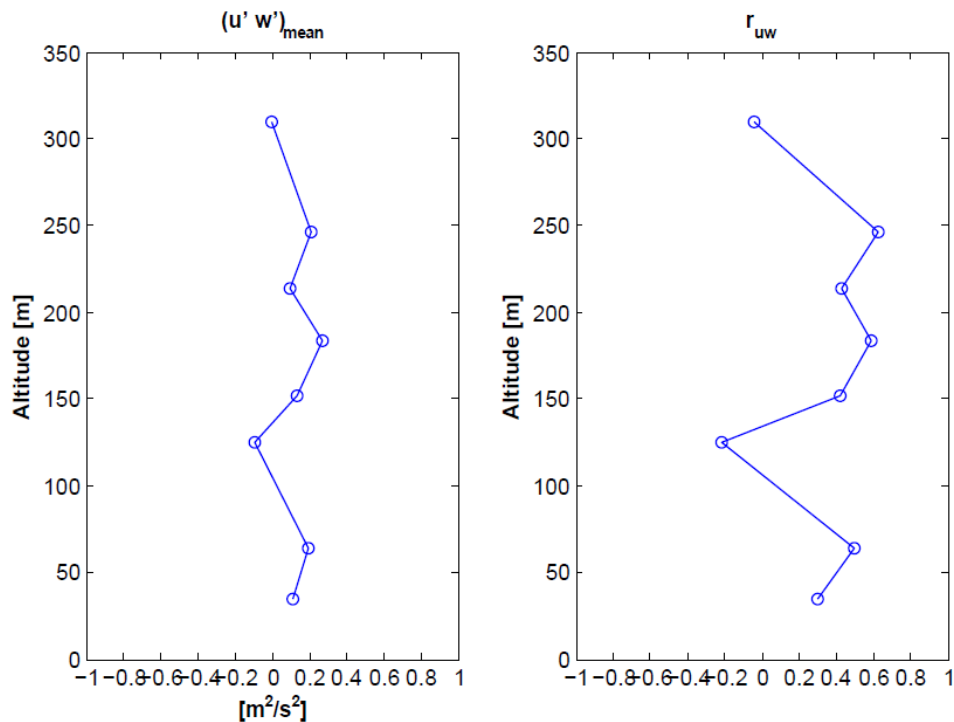


Figure VI-88 Linear correlation coefficient of u' and w' ; 7/9/2010, 10:30-12:45 UTC+1.

VII.16.4. Turbulent kinetic energy

As expected, the TKE decrease over altitude (Fig. VII-73).

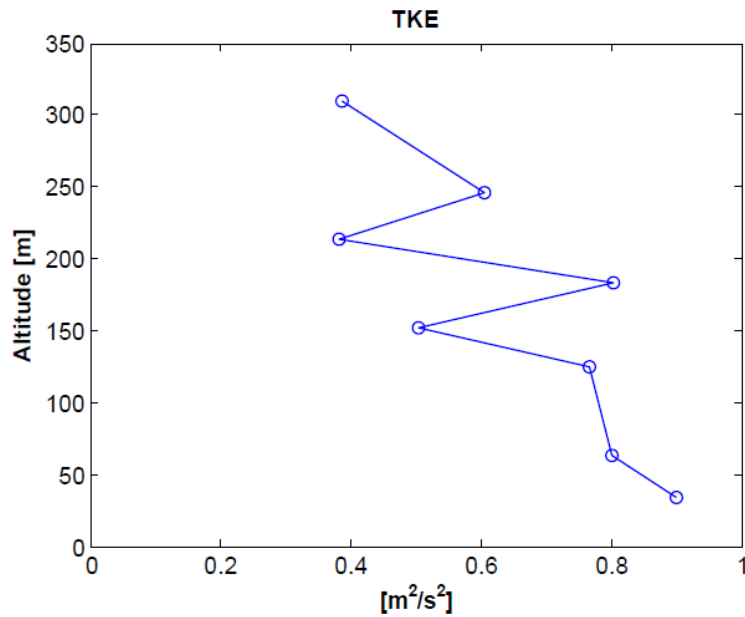


Figure VI-89 TKE profile; 7/9/2010, 10:30-12:45 UTC+1.

VII.16.5. Turbulent power density spectra

This section shows the spectra of u' , v' , w' and θ^* , as the scientific literature commonly reported. In order to smooth the fluctuations in the original signal, a moving average filter was used, before the spectra calculation. The temperature spectra can be compared to that reported in figure VII-78 (Roth, 2000). U is the mean horizontal (crosswind and longitudinal) wind intensity.

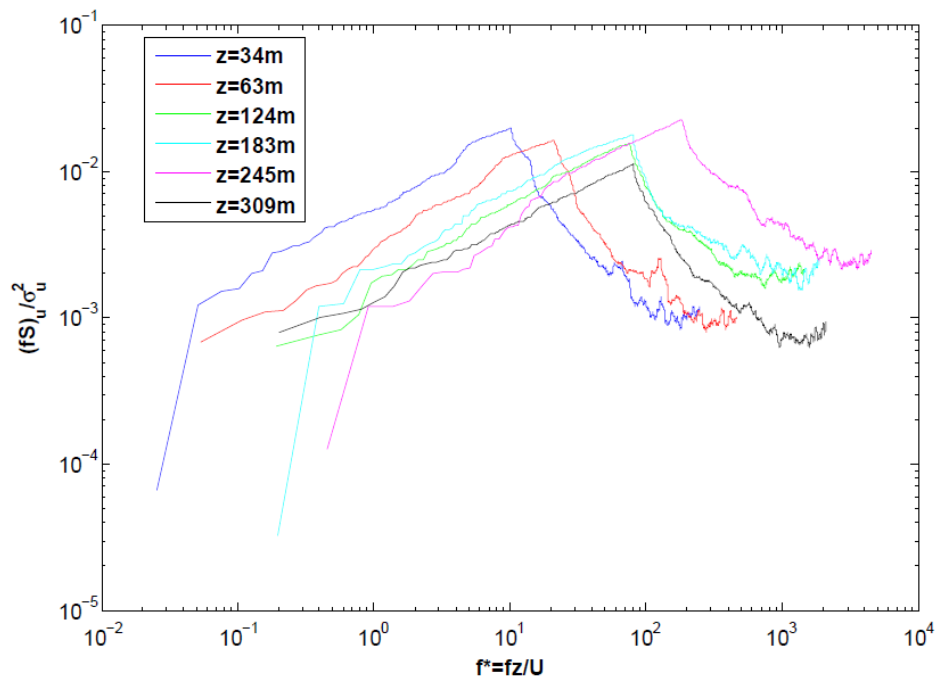


Figure VI-90 Normalized power spectra density of turbulent longitudinal component (u) of wind over altitude; 7/9/2010, 10:30-12:45 UTC+1.

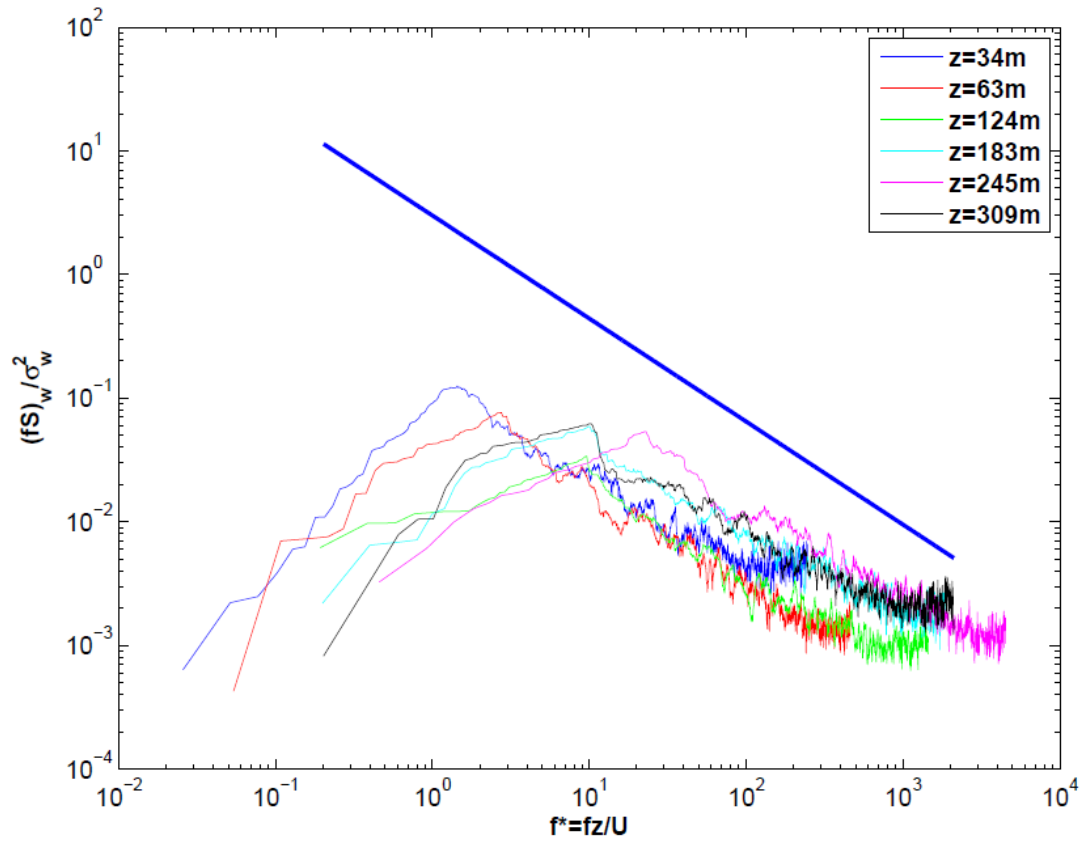


Figure VI-91 Normalize power density spectra of turbulent vertical component (w) of wind over altitude; $-2/3$ power law is shown in bleu; 7/9/2010, 10:30-12:45 UTC+1.

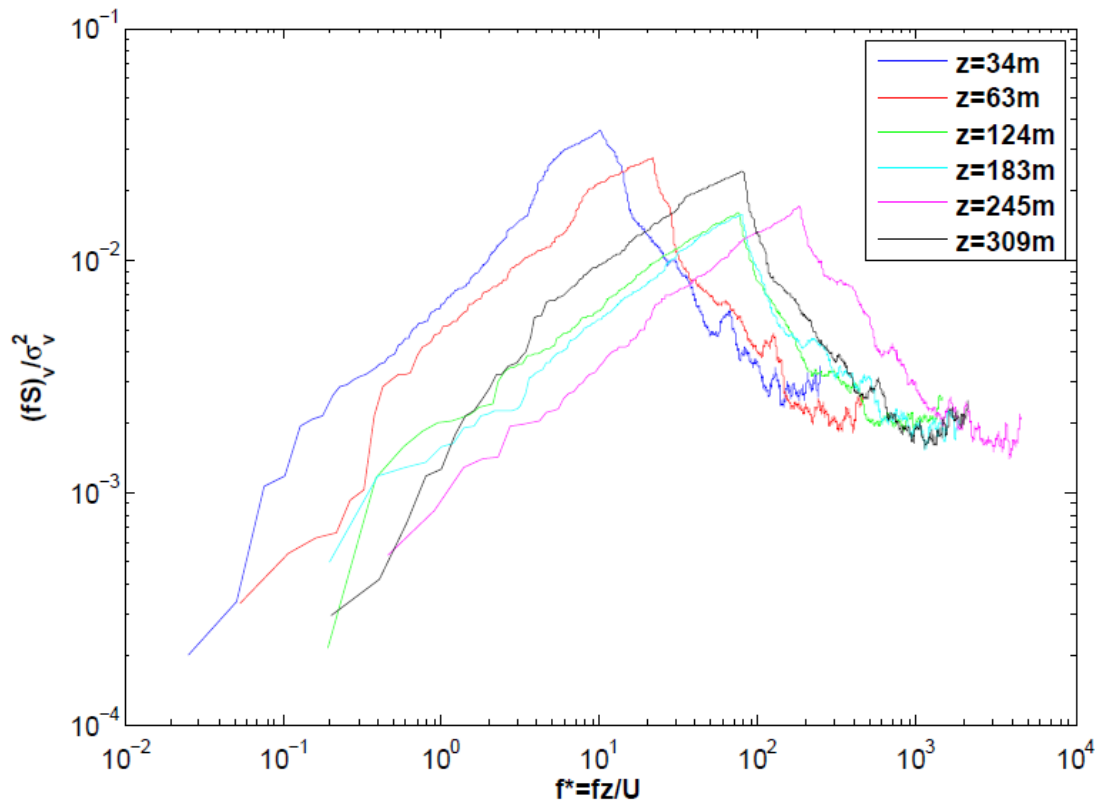


Figure VI-92 Normalized power density spectra of crosswind component (v) over altitude; 7/9/2010, 10:30-12:45 UTC+1.

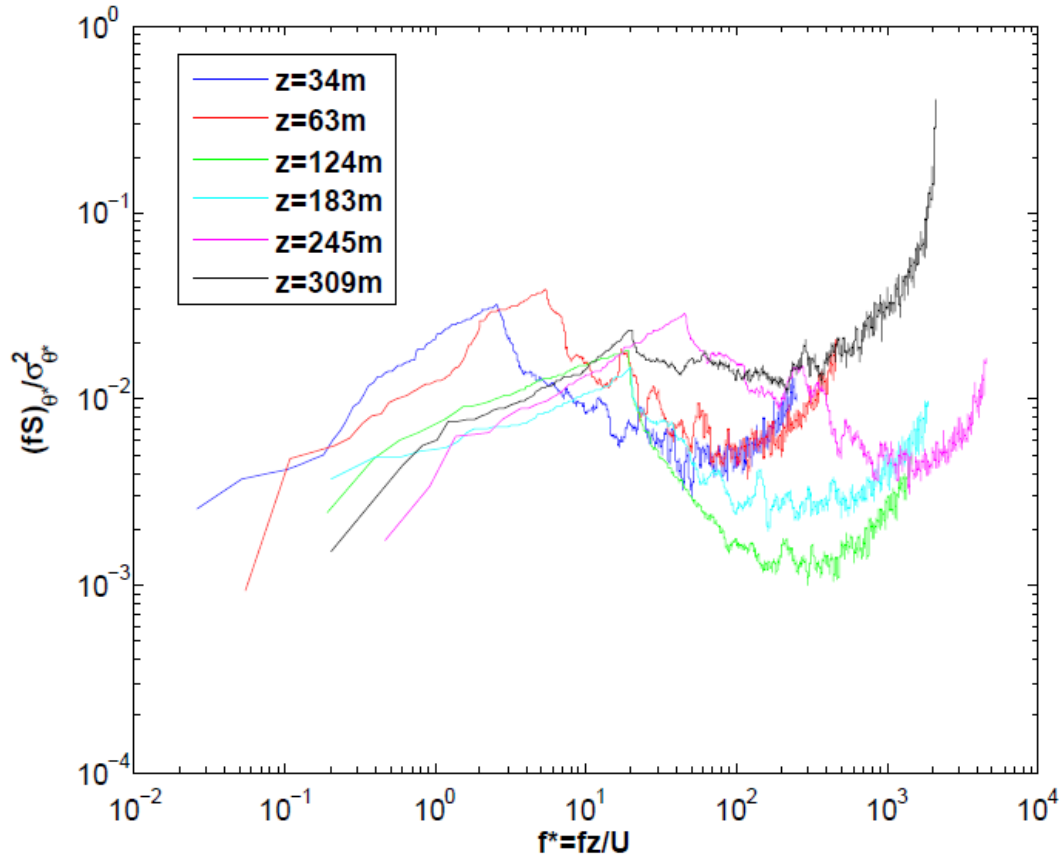


Figure VI-93 Normalized power density spectra of sonic virtual potential temperature (θ_v^*) over altitude; 7/9/2010, 10:30-12:45 UTC+1.

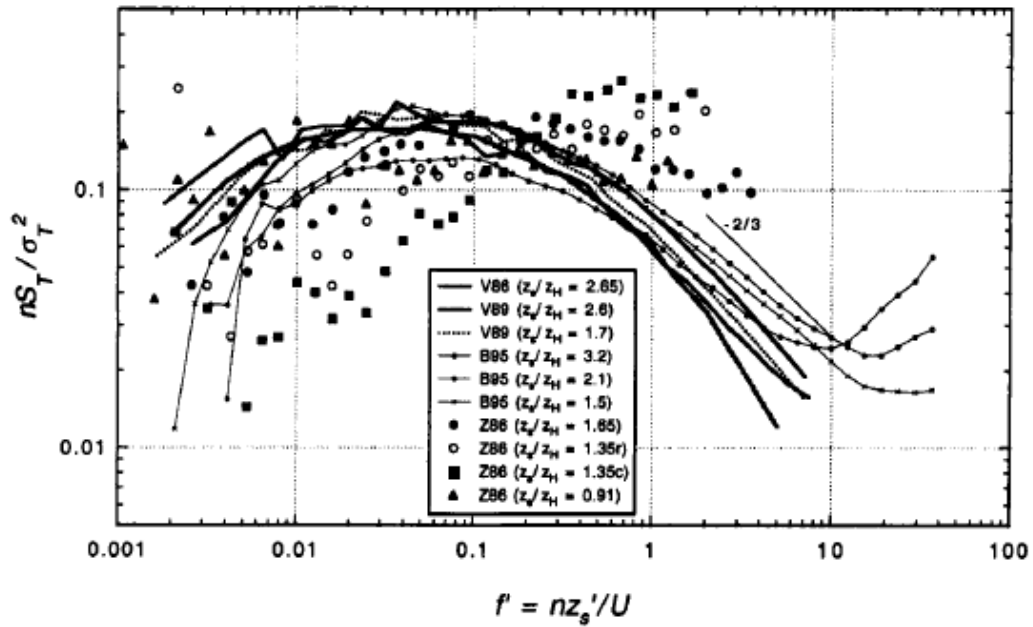


Figure VI-94 Normalized power density spectra of virtual potential temperature (Roth, 2000).

The high sampling frequency allows to analyze better the faster turbulent phenomena.

Conclusions

The beauty and the livability of our Mediterranean cities depends strictly from the capacity of us to preserve them, following sustainable development.

The will to improve the quality of life, in terms of comfort, must take in to account the worst effect it has.

Unfortunately we do not know completely the consequences of our actions on the environment where we live.

Scientific literature has demonstrated that we are longer to understand particularly the dispersion mechanisms of air pollutants when UHI, sea/land breezes and valley flows interact to each other, since no research had been organized to study this.

The PhD thesis has illustrated the development of a kytoon station available to improve the knowledge about this topic.

Lots of vertical profiles can be obtained, such as:

- *Wind components (longitudinal, crosswind and downwind);*
- *Static, potential and virtual potential temperature;*
- *Specific humidity;*
- *Bulk Richardson number;*
- *Concentration of CO, O₃, NO₂, C₆H₆;*
- *Turbulent fluctuation components and their standard deviation, power density spectra;*
- *Turbulent kinetic energy;*
- *Vertical kinematic eddy heat flux and U-momentum;*
- *Linear correlation coefficients.*

The station tested near the center of Caserta city (Italy) on 7th, 13th, 15th, 16th, 17th September 2010 has shown its potentiality and its originality : no kytoon station described in literature has be founded to measure simultaneously well concentration of four air pollutants and a fully and accurate characterization of turbulent spectra and statistics.

Symbols

A, B	[]	Generic variables, $A \neq B$
a', b'	[]	Generic perturbation component
C	[m/s]	Speed of sound
C_6H_6	[$\mu\text{g}/\text{m}^3$]	Concentration of Benzene
CO	[mg/m^3]	Concentration of Carbon Monoxide
f, F	[1/s] = [Hz]	Frequency
Lat	[°]	Latitude (WGS-84)
$Long$	[°]	Longitude (WGS-84)
NO_2	[$\mu\text{g}/\text{m}^3$]	Concentration of Nitrogen Dioxide
O_3	[$\mu\text{g}/\text{m}^3$]	Concentration of Ozone
p	[Pa]	Absolute pressure
P	[s]	Sampling period
p_0	[Pa]	Reference pressure (standard air condition)
q	[g/kg]	Specific Humidity
r_{AB}	[]	Linear correlation coefficient between A and B
R_f	[]	Flux Richardson Number
RH	[%]	Relative Humidity
Ri	[]	Gradient Richardson Number
Ri_B	[]	Bulk Richardson Number
r_L	[g/kg]	Liquid-water mixing ratio
r_{sat}	[g/kg]	Water-vapor saturation mixing ratio
s	[m]	Space or position
S	[m^2/s]	Power Spectral density (Spectrum)
T	[°C] or [K]	Static temperature
t	[s]	Time
U	[m/s]	Longitudinal component of wind
U	[m/s]	Mean horizontal wind
u'	[m/s]	Longitudinal turbulent perturbation
V	[m/s]	Transverse or crosswind component
\mathbf{V}	[m/s]	Velocity vector
v'	[m/s]	Crosswind, turbulent perturbation
W	[m/s]	Vertical or Down component of wind
w'	[m/s]	Vertical wind, turbulent perturbation
z	[m]	Altitude (WGS-84)
α	[°]	Pitch (Euler angle DEV-NED)
ϕ	[°]	Roll (Euler angle DEV-NED)
μ	[]	Statistic Mean of a generic variable
θ	[°C] or [K]	Potential temperature
θ_v	[°C] or [K]	Virtual potential temperature
θ_v'	[°C] or [K]	Virtual potential temperature, turbulent perturbation
σ	[]	Standard Deviation
ψ	[°]	Yaw (Euler angle DEV-NED)

Super/Subscripts

*	Sonic/Friction
–	Average/...
anm	.../anemometer referenced
wind	.../wind
GPS	.../GPS referenced (WGS-84)
DEV	.../IG 500N device coordinate system
NED	.../Nord Est Down coordinate system
s.l.	.../Sea level

Abbreviations

AGL	<i>Altitude above Ground level</i>
AHRS	<i>Attitude and Heading Reference System</i>
AoA	<i>Angle of Attach</i>
APRS	<i>Automatic Reporting Position System</i>
BL	<i>Boundary Layer</i>
CAT	<i>Clear Air Turbulence</i>
DCM	<i>Direct Cosine Matrix</i>
DEV	<i>AHRS device coordinate system</i>
dof	<i>Degree of Freedom</i>
ENAC	<i>Ente Nazionale Per l'Aviazione Civile</i>
ENAV	<i>Ente Nazionale di Assistenza al Volo</i>
GPS	<i>Global Positioning System</i>
IMU	<i>Inertial Measurement Unit</i>
INS	<i>Inertial Navigation System</i>
MEMS	<i>Micro Electro Mechanic System</i>
ML	<i>Mixed Layer</i>
MLH	<i>Mixed Layer Height</i>
NED	<i>Nord Est Down reference system</i>
N-E-S-W	<i>North, East, South, West</i>
PBL	<i>Planetary Boundary Layer</i>
R.M.S.	<i>Root Mean Square</i>
RASS	<i>Radio Acoustic Sounding System</i>
RL	<i>Residual Layer</i>
SBL	<i>Stable Boundary Layer</i>
SODAR	<i>SONic Detection And Ranging</i>
SVG	<i>Servizio Volontario Giovanile</i>
TIBL	<i>Thermal Internal Boundary Layer</i>
TKE	<i>Turbulent Kinetic Energy</i>
TSR	<i>Time since last reset</i>
UHI	<i>Urban Heat Island</i>
WGS-84	<i>World Geodetic System 1984</i>

Bibliography

Al-Jiboori M. H., Xu, Y., Qian, Y. Velocity spectra over different terrains [Journal] // Atmospheric Science Letters. - [s.l.] : Royal Meteorological Society, 2001.

Arnfield J.A. Two decades of urban climate research: a review of turbulence, exchanges of energy and water, and the urban heat island [Journal] // International Journal of Climatology. - [s.l.] : Royal Meteorological Society, 2003. - Vol. 23. - pp. 1-26.

Bastin S. and Drobinski P. Temperature and wind velocity oscillations along a gentle slope during sea breeze events [Journal] // Boundary Layer Meteorology. - [s.l.] : Springer, 2005. - Vol. 114. - pp. 573-594.

Burns A. Power spectra of low level atmospheric turbulence measured from an aircraft [Report] : papers / Ministry of aviation ; London's Ministry of aviation. - London : Her Majesty's stationery office, 1964. - p. 69. - C.P. No 733.

Busch N.E. and Panofsky, H.A. Recent spectra of atmospheric turbulence [Journal] // Turbulent spectra. - 1968.

Clements W.E., Archuleta J.A. and Gudiksen P.H. Experimental design of the 1984 ASCOT field study [Journal] // Journal of applied meteorology. - 1989. - Vol. 28.

Crosman Erik T. and Horel, John D. Sea and Lake Breezes: A Review of Numerical Studies [Journal] // Boundary-Layer Meteorology. - [s.l.] : Springer, 2010. - Vol. 137. - pp. 1-29.

Edmilson D. [et al.] Interactions of an urban heat island and sea-breeze circulations during winter over the metropolitan area of São Paulo, Brazil [Journal] // Boundary Layer Meteorology. - [s.l.] : Springer, 2007. - Vol. 122. - pp. 43-65.

Finkele K. Inland and offshore propagation speeds of a sea breeze from simulations and measurements [Journal] // Boundary Layer Meteorology. - [s.l.] : Kluwer Academic Publishers, 1998. - 87. - pp. 307-329.

Grachev A. Free convection frequency spectra of atmospheric turbulence over the sea [Journal] // Boundary-Layer Meteorology. - [s.l.] : Kluwer Academy Publisher, 1994. - Vol. 69. - pp. 27-42.

Hinkel K.M., Nelson, F.E., Klene, A.E., Bell, J.H. The urban heat island in winter at Barrow, Alaska [Journal] // International Journal of Climatology. - [s.l.] : Wiley InterScience, 2003. - Vol. 23. - pp. 1889-1905.

Hongstrom U. J.C.R. Hunt and A.S. Smedman Theory and measurements for turbulence spectra and variances in the atmosphere neutral surface layer [Journal] // Boundary Layer Meteorology. - [s.l.] : Kluwer Academy Publisher, 2002. - Vol. 103. - pp. 101-124.

- Jerevic A. and Grisogono, B.** The critical bulk Richardson number in urban areas: verification and application in a numerical weather prediction model [Journal] // Tellus. - Singapore : Blackwell Munksgaard, 2006. - A : Vol. 58. - pp. 19-27.
- Kaimal J.C., Wyngard, J.C. and Izumi Y. and Cote', O.R.** Spectral characteristics of surface-layer turbulence [Journal] // Quart. J. R. Met. SOC.. - 1972. - Vol. 98. - pp. 563-589.
- Kaiser R. and Fedorovich E.** Turbulence Spectra and Dissipation Rates in a Wind Tunnel Model of the Atmospheric Convective Boundary Layer [Journal] // Journal of the atmospheric sciences. - [s.l.] : American Meteorological Society, February 15, 1999. - Vol. 55. - pp. 580-594.
- Launiainen J.** Derivation of the relationship between the obukhnov stability parameter and the bulk richardson number for flux-profile studies [Journal] // Boundary Layer Meteorology. - [s.l.] : KluwerAcademi Publishers, 1995. - 76. - pp. 165-179.
- Leuzzi G and Monti P.** Numerical modelling of flow and dispersion in Rome area [Conference] // Int. Conf. on Harmonisation within Atmospheric Dispersion Modelling for Regulatory Purposes.
- Li Wei [et al.]** Turbulence spectra and surface fluxes in the atmospheric surface layer over the Loess Plateau [Report]. - 2005. - p. 5.
- Lovejoy S. and Schertzer D.** Towards a new synthesis for atmospheric dynamics: Space–time cascades [Journal] // Atmospheric Research. - [s.l.] : Elsevier, 2010. - Vol. 96. - pp. 1-52.
- MacCready Paul B. Jr** Structure of atmospheric turbulence [Journal] // Journal of meteorology. - December 1953. - Vol. 10. - pp. 434-449.
- Maletto A., McKendry, I.G. and Strawbridge, K.B.** Profiles of particulate matter size distributions using a balloon borne lightweight aerosol spectrometer in the planetary boundary layer [Journal]. - [s.l.] : Elsevier-Pergamon, 2003. - Vol. 37. - pp. 661-670.
- Met Office** Small-scale wind energy technical report [Report]. - 2008.
- Neumark S. Tech.Sc.D., F.R.Ae.S.** Equilibrium configuration of flying cables of captive balloons, and cable derivatives for stability calculations [Report] / Ministry of aviation. - London : Her Majesty's stationery office, 1963. - p. 40. - R.A.E. Report No. Aero 2653.
- Ogawa Y. and Ohara, T.** Observation of the turbulent structure in the planetary boundary layer with a kytoon-mounted ultrasonic anemometer system [Journal] // Boundary Layer Meteorology. - [s.l.] : D.Reidel Publishing Co., 1982. - Vol. 22. - pp. 123-131.
- Ogawa Y. Ohara T., Wakamatsu S., Diosey P.G. and Uno I.** Observation of lake sea breeze penetration and subsequent development of the thermal internal layer for the Nanticoke II shoreline diffusion experiment [Journal]. - [s.l.] : D.Reidel Publishing Company, 1986. - 35 : Vol. Boundary Layer Meteorology. - pp. 207-230.
- Ohara T. Wakamatsu S. and Uno I.** Observed Structure of Land Head in the Tokyo Metropolitan Area [Journal] // Journal of applied meteorology. - [s.l.] : American Meteorological Society, August 1989. - Vol. 28. - pp. 693-704.

- Oke T.R. and East, C.** The urban boundary layer in Montreal [Journal] // Boundary Layer meteorology. - 1971. - Vol. 1. - pp. 411-437.
- Panelli M. and Cardone G.** Development of kytoon for meteorological and chemical pollutants measurement in mediterranean urban climate [Conference] // XX AIDAA. - Milano : [s.n.], 2009. - p. 20.
- Rankin A.M. and Wolf, E.** Aerosolo profiling Using a Tethered Balloon in coastal Antartica [Journal]. - Journal of Atmospheric and oceanic technology : American Meterological Society, 2002. - Vol. 19. - pp. 1978-1985.
- Roth M.** Review of atmospheric turbulence over cities [Journal] // Q. J. R. Meteorol. SOC. - Singapore : [s.n.], 2000. - Vol. 126. - pp. 941-990.
- Roulet Yves-Alain** Validation and application of an urban turbulence parameterisation scheme for mesoscale atmospheric models. - 2004.
- Sailor D.** The Urban Heat Island (UHI) – Causes, Impacts, and Mitigation Strategies. - 2007.
- Salmond J.A. and McKendry I.G.** A review of turbulence in the very stable nocturnal boundary layer and its implications for air quality [Journal] // Progress in Physical Geography. - [s.l.] : Edward Arnold Ltd, 2005. - 2 : Vol. 29. - pp. 171-188.
- Schotz S. and PanoFsky, H.A.** Wind Characteristics at the boulder atmospheric observatory [Journal] // Boundary Layer Meteorology. - [s.l.] : D.Reidel Publishing Co., 1980. - Vol. 19. - pp. 155-164.
- Shafran P.C., Seaman, N.L. and Gayno, G.A.** Evaluation of numerical predictions of boundary layer structure during the Lake ozone study [Journal] // Journal of Applied Meteorology. - [s.l.] : American Meteorological Society, March 2000. - Vol. 39. - pp. 412-426.
- Sharan M., Aditi, T.V.B.P.S.R.K.** On the bulk Richardson number and flux-profile relations in an atmospheric surcafe layer under weak wind stable conditions [Journal] // Atmospheric Environment. - [s.l.] : Elsevier-Pergamon, 2003. - 37. - pp. 3681-3691.
- Silbert M.N.** Description and Performance Characteristics of a captive airfoil balloon system used in the initial phase of the Aeropalynologic Survey Project [Report] / Wallops Flight center ; NASA. - 1967. - pp. 145-162.
- Stull R.B.** An introduction to Boundary Layer Meteorology [Book]. - Vancouver : Springer, 1988. - 2009.
- Tijm A. B. C., Holtslag, A. A. M. and Van Delen, A.J.** Observations and Modeling of the Sea Breeze with the Return Current [Journal] // Monthly Weather Review. - [s.l.] : American Meteorological Society, May 1999. - Vol. 127. - pp. 625-640.
- Tjernstorm M.,Jensen, M., Oncley,S. and Persson, O.** The AOE2001 meteorological experiment in the high artic [Report] / Deparment of meteorology ; Stockholm university. - Stockholm : [s.n.], 2001. - p. 4.
- Tropea C., Yarin,A.L. and Foss,J.F.** Atmospheric Measurements [Book]. - [s.l.] : Springer, 2007.

Van Der Hoven I. Power spectrum of horizontal wind in the frequency range from 0.0007 to 900cycles per hour [Journal] // Journal of meteorology. - 1957. - Vol. 14. - pp. 160-164.

Van Dijk A., Moene, A.F., de Bruin, H.A.R. The principles of surface flux physics: theory, pratice and description of the ECPACK library [Report] : 2004/1 / Meteorology and Air Quality Group ; Wageningen University. - Wageningen, the Netherlands : [s.n.], 2004. - p. 99.

Weber R. O. Remarks on the definition and estimation of friction velocity [Journal] // Boundary-Layer Meteorology. - [s.l.] : Kluwer Academic Publishers, 1999. - Vol. 93. - pp. 197-209.

Weber S. and Kordowski K. Comparison of atmospheric turbulence characteristics and turbulent fluxes from two urban sites in Essen, Germany [Journal] // Theor Appl Climatol. - [s.l.] : Springer-Verlag, 2010. - Vol. 102. - pp. 61-74.

Wilczak J.M., Oncley,S.P. and Stage,S.A. Sonic Anemometer tilt correction algorithms [Journal] // Boundary layer meteorology. - [s.l.] : Kluwer Academic Publisher, 2001. - Vol. 99. - pp. 127-150.

Winston Jeeva J. On the structures of sea-breeze fronts observed near the coastline of Thumba, India [Journal] // Boundary layer meteorology. - [s.l.] : Kluwer Academic Publishers, 1992. - Vol. 59. - pp. 111-124.

Zhang H. Chen J. and Park S.U. Turbulence structure in unstable conditions over various surfaces [Journal] // Boundary Layer Meteorology. - [s.l.] : Kluwer Academy Publisher, 2001. - Vol. 100. - pp. 243-261.

Zoumakis N.M. and Kelessis, A.G. The dependence of the bulk richardson number on stability in the surface layer [Journal] // Boundary Layer meteorology. - [s.l.] : Kluwer Academic Publishers, 1991. - 57. - pp. 407-414.

Appendix A: Sensor and equipment datasheets

Follows the list of instruments and equipment datasheets of:

- Gill Windmaster 3D Sonic Anemometer; <http://www.gill.co.uk>
- Vaisala HMP50 thermohygrometer; <http://www.vaisala.com>
- Unitec Sens3000 air pollutant sensor; <http://www.unitec-srl.com>
- Sbg IG 500N INU sensor; <http://www.sbg-system.com>
- Datexel DAT 3017-V multiplexer; <http://www.datexel.it>
- Icop Vortex86 CPU AIO board; <http://www.icop.com.tw>
- Big Red Bee Beeline GPS; <http://www.bigredbee.com>
- Gottifredi Maffioli DSK 75 Ultra tether lines; <http://www.gottifredimaffioli.com>
- Honda EU 30is generator; <http://power.hondaitalia.com/industry/>

WindMaster™

3-Axis Ultrasonic Anemometer



Key Features

- Precision 3-axis sonic anemometer
- 20Hz Output Rate (32Hz Optional)
- 0-45m/s wind speed
- 0-359° wind direction
- U, V, W Vector Outputs
- Aluminium/Carbon Fibre Construction
- Sonic temperature output
- Optional custom calibration

The Gill WindMaster™ is a precision anemometer offering three-axis wind measurement data. This instrument will monitor winds speeds of 0-45 m/s and provides sonic temperature, speed of sound and U, V & W vector outputs at 20Hz (32Hz optional). This 3D anemometer is of aluminium/carbon fibre construction and is ideal for the understanding of turbulent flows, surface energy balance and scalar fluxes. Each WindMaster™ is calibrated with a Gill wind tunnel test to provide optimum performance.

This 3D sonic anemometer is ideally suited to the measurement of air turbulence around bridges, buildings, wind turbine sites, building ventilation control systems, meteorological and flux measurement sites.



Wind Speed

Range	0 - 45 m/s
Resolution	0.01 m/s
Accuracy*	<1.5% RMS @12 m/s
Accuracy*	<1% RMS @12 m/s (Custom)

Direction

Range	0 - 359°
Resolution	0.1°
Accuracy	2° @12 m/s
Accuracy	0.5° @12 m/s (Custom)

Sonic Temperature

Range	-40°C to +70°C
Resolution	0.01°C

Speed of Sound

Range	300-370 m/s
Resolution	0.01 m/s
Accuracy	< ±0.5% @ 20°C

Measurement

Internal sample rate	20 Hz or 32 Hz
Output Parameters	1, 2, 4, 8, 10, 16, 20 & 32 (Option) Hz
Units of Measure	m/s, mph, kph, knots, ft/min
Formats	UVW, Polar or NMEA
Averaging	Flexible 0-3600 s

Digital Output

Communication	RS232, 422, 485
Baud Rates	2400 - 115200
Format	ASCII

Analogue Outputs - Optional

Resolution 12 bits or 14 bits	4 channels available
Selectable Range	User selectable full scale wind speed
Output type	0-20mA, 4-20mA, 0-5 V, ±2.5 V, ±5 V

Analogue Inputs - Optional

Resolution 12 bits or 14 bits	Up to 4 single ended or 2 differential
Input Type	±5 V

Power Requirement

Anemometer	9-30 VDC (25mA @ 12 VDC)
------------	--------------------------

Mechanical

Weight	1.0 kg
Size	750mm x 240mm

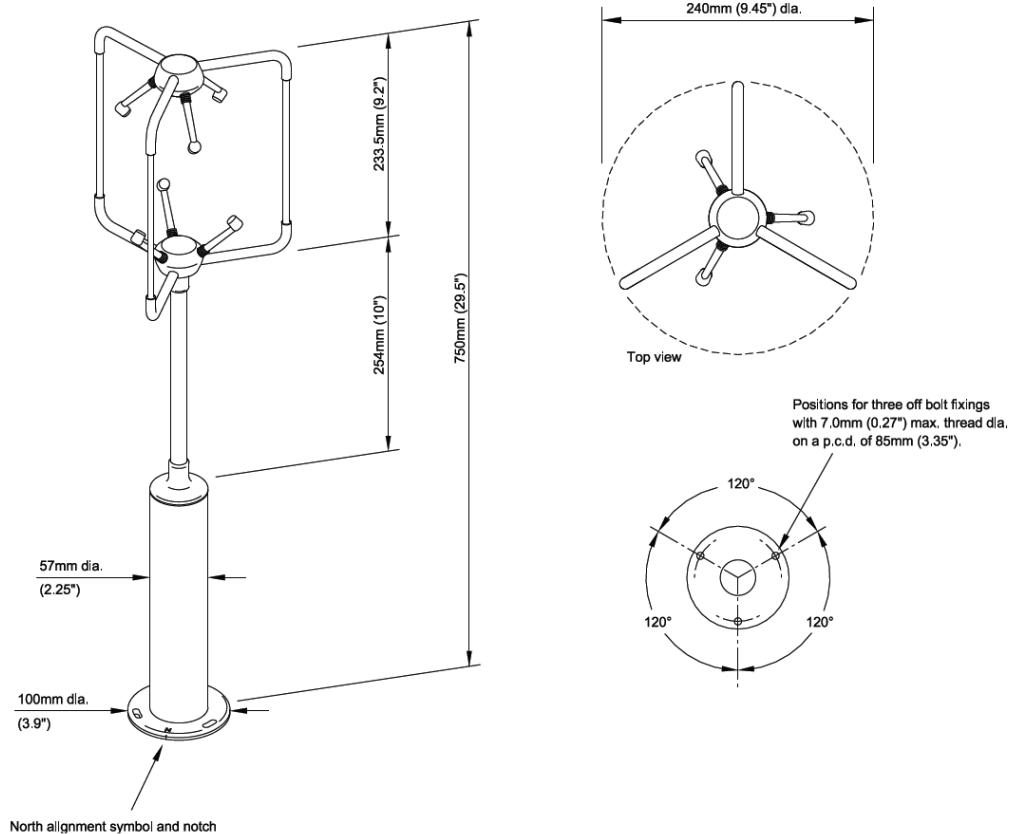
Environmental

Protection Class	IP65
Operating Temp	-40°C to +70°C
Humidity	< 5% to 100% RH
Precipitation	300mm/hr
EMC	BS EN 61000 - 6 - 3 (Emissions) BS EN 61000 - 6 - 2 (Immunity)

*Accuracy spec applies for wind speed, and for wind incidence up to ±30° from the horizontal

Typical Applications

- Power Lines
- Bridges
- Viaducts
- Building ventilation control systems
- Measurement Masts
- Skyscrapers
- Wind Turbine Test Sites
- Meteorological & Flux measurement sites



This product is in continuous development and therefore specifications may be subject to change without prior notice.



Gill Instruments Ltd
Saltmarsh Park
67 Gosport Street
Lymington
Hampshire
SO41 9EG, UK

T: +44 (0) 1590 613 500
F: +44 (0) 1590 613 501
E: anem@gill.co.uk

www.gill.co.uk



Copyright © Gill Instruments 2010

D1304

Gill Instruments Ltd

Reg No. 3154453 Registered Office: The George Business Centre, Christchurch Road, New Milton, BH25 6QJ



P.O. Box 26, FI-00421 Helsinki, FINLAND
Tel: +358 9 894 91
Fax: +358 9 8949 2485
Email: industrialsales@vaisala.com
www.vaisala.com/HMP50

HMP50 Miniature Humidity and Temperature Probe for OEM Applications



The HMP50 features good measurement performance in a small, rugged and simple probe.

Features/Benefits

- Miniature-size humidity transmitter
- Very low power consumption
- Short power-up time
- Measurement range 0 ... 98 %RH and -10 ... +60 °C (+14 ... +140 °F)
- Cable detachable with standard M8 quick connector
- Rugged metal housing
- Interchangeable Vaisala INTERCAP® Sensor
- Optional outputs and cable lengths

The Vaisala INTERCAP® Humidity and Temperature Probe HMP50 is a simple and cost effective humidity transmitter suitable for volume applications or integration into other manufacturers' equipment.

The HMP50 is ideal for a variety of applications such as

- glove boxes
- greenhouses
- fermentation chambers
- data loggers

Installation flexibility

The probe cable has a screw-on quick connector for ease of installation. Two different cable lengths are available, and customers can also use any M8 series cable of their choice.

Low current consumption

Because of its very low current consumption and short power-up time, the HMP50 is well suitable for battery-powered applications.

Several outputs available

The temperature measurement is optional. Three standard voltage outputs are available.

For the RH-only model, a current interface output is available. It can be used to build a 4 ... 20 mA loop-powered current output with external components (the optional current converter kit).

Rugged design

The aluminum body of the HMP50 is IP65-classified. The sensor is protected by a membrane filter and plastic grid, or optionally a stainless steel filter.

No need for recalibration

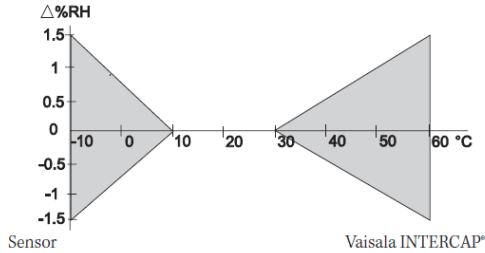
The Vaisala INTERCAP® Sensor is interchangeable. Instead of recalibrating the instrument, the user can easily replace the sensor.

Technical Data

Performance

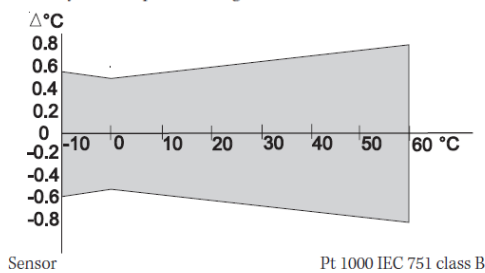
Relative humidity

Measurement range 0 ... 98 %RH
 Typical accuracy at +20 °C (+68 °F) 0 ... 90 %RH ±3 %RH
 90 ... 98 %RH ±5 %RH
 Stability ±2 %RH over 2 years
 Temperature dependence



Temperature (optional)

Measurement range -10 ... +60 °C (+14 ... +140 °F)
 Typical accuracy at +20 °C ±0.6 °C (±1.1 °F)
 Accuracy over temperature range

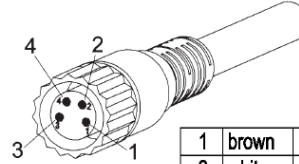


Operating environment

Environmental temperature
 operating -10 ... +60 °C (+14 ... +140 °F)
 storage -40 ... +60 °C (-40 ... +140 °F)
 Environmental relative humidity
 operating 0 ... 100%RH
 Electromagnetic compatibility Complies with EMC standard EN61326-1, Generic Environment

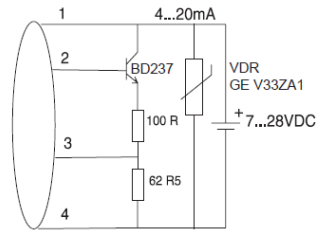
Inputs and outputs

Operating voltage 7 ... 28VDC
 for 0 ... 5 VDC output model 8 ... 28 VDC
 Current consumption 2 mA typical
 Settling time at power-up 150 ms
 Outputs
 (equals 0 ... 100% RH) 0 ... 1 VDC
 and 0 ... 2.5 VDC
 -10 ... +60 °C) 0 ... 5 VDC
 current interface
 External loads
 0 ... 1/0 ... 2.5V $R_{i,min}$ 10kohm
 0 ... 5 $R_{i,min}$ 50kohm



1	brown	+VDC 7... 28 VDC
2	white	+ 0...1/2.5/5 V 0...100 %
3	blue	- VDC
4	black	0...1/2.5/5 V -40...+60 °C

Circuit diagram for 4 ... 20 mA loop-powered current output with current interface.



Mechanics

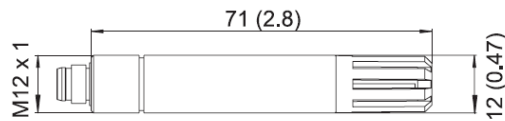
Materials
 body chrome coated aluminium
 grid/filter chrome coated ABS plastic
 cable polyurethane
 Housing classifications IP65
 Body thread M12x1 / 10 mm
 Grid thread M11x1 / 5 mm
 Cable connector 4-pin M8 (IEC 60947-5-2)
 Cable lengths 0.3 and 3 m
 Weight 25 g (with 0.3 m cable)

Options and accessories

Vaisala INTERCAP® sensor 15778HM
 Vaisala INTERCAP® sensor with membrane 15872HM
 Sensor protection
 plastic grid DRW010522
 membrane filter DRW010525
 stainless steel sintered filter HM46670SP
 Current output converter kit 26182HM
 Plastic M12 installation nuts, pair 18350SP
 Connection cable M8
 0.3 m HMP50Z032
 3 m HMP50Z300

Dimensions

Dimensions in mm (inches)



INTERCAP® is a registered trademark of Vaisala.
 Specifications subject to change without prior notice.
 ©Vaisala Oyj





THICK FILM SOLID STATE SENSORS FOR ENVIRONMENT

Each cell is provided with a thick film sensor for the measurement of one of the following parameters:

CO, NO₂, O₃, C₆H₆, CH₄

The sensible surface of the sensor is a semiconductor oxide made of nano-particles of the size of 200 µm. The first reaction which happens on the surface of the sensor is the absorption of the atmospheric oxygen and the consequent charge transfer from the semiconductor to the oxygen molecule. The second reaction is related to the specific gas to be measured, which while linking to the oxygen molecule allows the electrons to be released in the conduction band of the semiconductor. Taking the current signals from the sensor, the direct concentration of the specific gas in atmosphere can be measured. Selectivity and precision are reached using special semiconductor oxides with appropriate filters.

The output analog signal from the sensor needs to be converted into concentration using a known function.

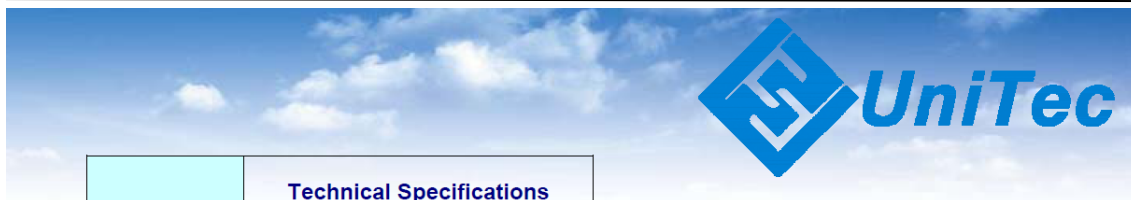


FEATURES:

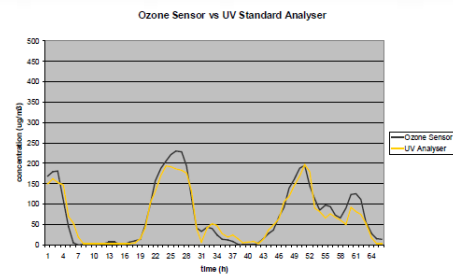
- ⇒ **Air quality monitoring of CO – NO₂ – O₃ – C₆H₆– CH₄**
- ⇒ **AFFORDABLE PRICE**
- ⇒ **THICK FILM SOLID STATE SENSORS at ppb levels**
- ⇒ **Anodized aluminium case**
- ⇒ **Embedded fan**



*SENS3000
thick film
sensor unit*



	Technical Specifications
Solid state thick film sensors	CO – NO ₂ – O ₃ – C ₆ H ₆ – CH ₄
Analog Output:	0-5 Vcc (not linear: calibration curve provided)
Precision:	< 2% F.S.
Power supply:	+12 Vcc, -12 Vcc,
Response	<3 s (T90)
Operating temperature	-20°C - +50°C
Relative Humidity	5-95% (non condensating)
Power consumption:	150 mA
Dimensions:	55 (diam) x 94 (h) mm
Weight:	220 gr
Execution:	Aluminum anodized cylindrical enclosure



Sensor	Range (@0°C 1 atm)	Accuracy	Resolution
Carbon monoxide (CO)	0-100 mg/m ³ 0-80 ppm	+/- 0,5 mg/m ³	0,1 mg/m ³
Nitrogen dioxide (NO₂)	0-500 µg/m ³ 0-400 ppb	+/- 10 µg/m ³	0,1 µg/m ³
Ozone (O₃)	20- 500 µg/m ³ 10- 200 ppb	+/- 10 µg/m ³	1,0 µg/m ³
Benzene (C₆H₆)	0-100 µg/m ³ 0-30 ppb	+/- 1 µg/m ³	0,1 µg/m ³
Methane (CH₄)	0- 300 µg/m ³ 0- 400 ppb	+/- 10 µg/m ³	1 µg/m ³

IG-500N

Redefine motion limits...

GPS aided Orientation Sensor



The IG-500N is the world smallest GPS enhanced Attitude and Heading Reference System (AHRS). With its embedded Extended Kalman Filter, the IG-500N delivers unmatched precision for attitude and position measurements in very high dynamic conditions.

All In one: the IG-500N

The IG-500N includes a MEMS based Inertial Measurement Unit (IMU), a GPS receiver and a pressure sensor. It provides precise drift-free attitude and position, even in long time turns.

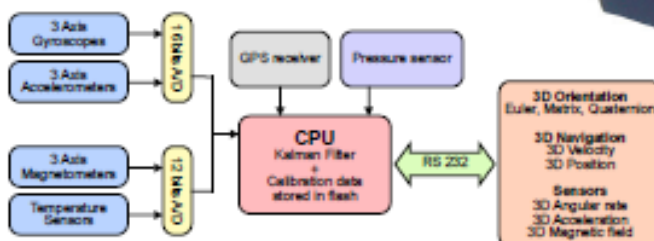
This miniature Inertial Navigation System (INS) runs a real time, on board, Extended Kalman Filter that computes orientation, position and velocity data at high update rates, up to 100 Hz.

The attitude accuracy is also improved, compared to traditional AHRS, by removing transient accelerations measured by the GPS receiver.

Easy and fast integration

SBG Systems has designed a powerful and easy to use Development Kit for this product. In just a few seconds, you can start evaluating and configuring your new device. Integrating the IG-500N in your application is even easier.

Simplified Block Diagram



Key Features

- GPS enhanced 3d velocity, position and orientation at high update rate (100 Hz)
- Accurate attitude even in high G maneuvers
- Precise UTC referenced output
- Embedded 4Hz GPS receiver & barometric sensor
- Wide inertial sensors range options
- Calibrated over full temperature range -40 to 85°C for bias, gain, misalignments, cross-axis and gyro-g
- Advanced and easy to use magnetometers compensation procedure for soft and hard iron
- Communication protocols : RS-232, CAN and USB
- Very compact and lightweight design (44 grams)
- Very low power design down to 550 mW
- Robust and high precision aluminum enclosure

Fields of use

- Unmanned vehicles
- Vehicle motion analysis
- Aerospace
- Robotics
- Marine industry



Tel: +33 (0)1 80 88 45 00 • Mail: contact@sbg-systems.com • Web: www.sbg-systems.com

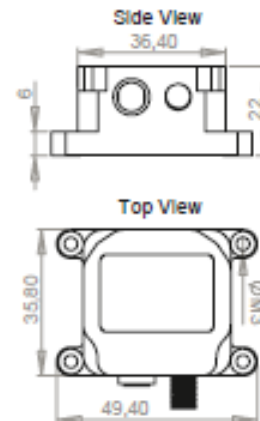


IG-500N*Redefine motion limits...*

Technical Specifications

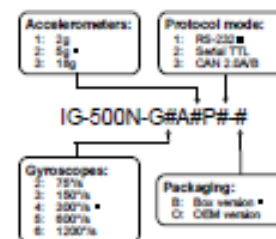
Parameter	Specification	Remarks
Attitude		
Sensing range	360° in all axes	
Static accuracy	± 0.5° (Pitch, Roll) ± 1° (Heading)	Stabilized Kalman Filter Homogenous magnetic field
Dynamic accuracy	± 1.0° RMS	Under good GPS availability
Repeatability	< 0.2°	
Resolution	< 0.05°	
Output frequency	0 to 500 Hz 0 to 100 Hz	Calibrated sensors only Sensors, attitude, velocity, position
Standard Sensors		
	Accelerometers	Gyroscopes
Measurement range	± 5 g	± 300 °/s
Non-linearity	< 0.2% of FS	< 0.1% of FS
Bias stability	± 5 mg	± 0.5 °/s
Scale factor stability	< 0.1%	< 0.05%
Noise density	0.25 mg/√Hz	0.05 °/s/√Hz
Alignment error	< 0.1°	< 0.1°
Bandwidth	50 Hz	40 Hz
Sampling rate	10 000 Hz	10 000 Hz
		1 000 Hz
GPS Receiver		
Receiver type	L1 frequency, C/A Code, 16-Channels, 4 Hz	
Position accuracy	2.0 meters 2.5 meters 5.0 meters	with SBAS support CEP (Horizontal accuracy) SEP (Vertical accuracy)
Acquisition time	< 3.5 s / 34 s	Hot start / Cold start
Tracking sensitivity	-158 dB	
Pressure Sensor		
Resolution	6 Pa	
Pressure accuracy	± 50 Pa ± 200 Pa	Relative Absolute
Long term stability	100 Pa	Over 12 months
Update rate	9 Hz	
Communication		
Output modes	Euler angles, Quaternion, Matrix, 3d velocity, 3d position, Calibrated sensor data, Raw sensor data	Each output can be enabled or disabled by the user
Interface options	Serial (RS-232 or TTL 3.3V) CAN 2.0A/B up to 1 Mbit/s USB using provided USB to UART	
Serial data rate	9 600 to 921 600 bps	User selectable
Physical		
Dimensions OEM	27x30x14 mm	
Dimensions box	36x48x22 mm	
Weight OEM	10 grams	
Weight box	44 grams	
Specified temperature	-40 to 85°C	Non-condensing environment
Storage temperature	-40 to 85°C	
Shock limit	1 000g (Powered), 2 000g (Unpowered)	Shocks can affect performance
Electrical		
Operating voltage	3.3 V to 30 V	
Power consumption	550 mW @ 5.0 V	High efficiency DC/DC converter
Start-up time	< 1 s	Valid data

Mechanical drawing



All dimensions are in millimeters

Product code options



■ standard product options

Rev 1.9 Specifications are subject to change without notice.

SBG Systems s.a.s. • 3bis, chemin de la Jonchère • 92500 Rueil Malmaison • FRANCE





Via monte Nero, 40/B – 21049 TRADATE (VA) ITALY
Tel: +39 (0)331841070 Fax: +39 (0)331841950 - e-mail: datexel@datexel.it - www.datexel.it



UNI EN ISO 9001:2000

**Modulo I/O distribuito
4 canali ingresso +/-10V
comunicante su rete RS-485**

DAT 3015-V



CARATTERISTICHE

- Acquisizione dati remota su Bus di campo
- Comunicazione tipo Master/Slave su rete RS-485
- Protocollo MODBUS RTU/ASCII o protocollo ASCII
- 4 canali di ingresso
- Ingresso per tensione fino a +/-10V
- Allarme Watch-Dog
- Configurabile da terminale remoto
- Isolamento galvanico a 2000 Vca sulle tre vie
- Elevata precisione
- EMC conforme - Marchio CE
- Adatto al montaggio su binario DIN conforme a EN-50022

DESCRIZIONE GENERALE

Il dispositivo DAT 3015-V converte fino a 4 segnali analogici applicati in ingresso in unità ingegneristiche in formato digitale. I dati sono trasmessi con protocollo MODBUS RTU/ASCII su rete RS-485 (è disponibile il modello con interfaccia RS-232).

Agli ingressi è possibile collegare segnali in tensione fino a +/- 10V.

Attraverso l'uso di un convertitore a 16 bit, il dispositivo garantisce una elevata precisione ed una misura molto stabile sia nel tempo che in temperatura.

Al fine di garantire la sicurezza dell'impianto, il dispositivo è fornito di due sistemi di timer Watch-Dog.

L'isolamento a 2000 Vca tra ingresso, alimentazione e linea seriale RS-485 (o RS-232) elimina tutti gli effetti dovuti ai loops di massa eventualmente presenti, consentendo l'uso del dispositivo anche nelle più gravose condizioni ambientali.

Il DAT 3015-V è conforme alla direttiva CEE/336/89 sulla compatibilità elettromagnetica.

Esso è alloggiato in un contenitore plastico di 17,5 mm di spessore adatto al montaggio su binario DIN conforme allo standard EN-50022.

PROTOCOLLI DI COMUNICAZIONE

Nel modulo DAT 3015 è stato implementato il protocollo **MODBUS RTU/ASCII**: protocollo standard di comunicazione diffuso nel bus di campo; permette di interfacciare la serie DAT3000 direttamente alla maggior parte dei PLC ed ai pacchetti SCADA presenti sul mercato.

Per le impostazioni di comunicazione, fare riferimento alle istruzioni riportate sul Manuale Operativo.

ISTRUZIONI DI IMPIEGO

Prima di installare il dispositivo, leggere attentamente la sezione "Istruzioni per l'installazione".

Se non si conosce l'esatta configurazione di un modulo, può risultare impossibile stabilire una comunicazione con esso; connettendo il morsetto INIT al morsetto GND (massa), all'accensione l'apparato sarà automaticamente impostato nella configurazione di default (vedi Manuale Operativo).

Collegare l'alimentazione, il bus seriale, gli ingressi analogici come illustrato nella sezione "Collegamenti".

Il LED "PWR" cambia stato in funzione della condizione di funzionamento del dispositivo: fare riferimento alla sezione "Segnalazione luminosa" per verificare il funzionamento del dispositivo.

Per la fase di configurazione e calibrazione fare riferimento alle istruzioni riportate sul Manuale Operativo.

Per facilitare la manutenzione o la sostituzione di un dispositivo, è possibile rimuovere i morsetti già cablati anche con l'impianto funzionante.

SPECIFICHE TECNICHE (Tipiche a 25 °C e nelle condizioni nominali)			
Tipo ingressi	Min	Max	
Tensione 10 V	-10 V	+10 V	
			Calibrazione ingressi (1) +/- 10 mV
			Linearità (1) +/-0,1%
			Impedenza di ingresso > 100 KΩ
			Deriva termica (1) Fondo Scala ± 0,005 % / °C
			Influenza della R di linea (1) V < 8 uV/Ohm
			Tempo di risposta 0,5 ÷ 1 sec.
			Trasmissione dati (seriale asincrona) Velocità massima 38,4 Kbps Distanza massima 1,2 Km
			Tempo di riscaldamento 3 minuti
			(1) riferiti allo Span di ingresso (differenza tra Val. max. e Val. min.)
			Alimentazione Tensione di alimentazione 10 .. 30 Vcc Consumo di corrente 30 mA @ 24 Vcc Protezione invers. polarità 60 Vcc max
			Tensione di isolamento Ingresso – RS485 2000 Vca 50 Hz, 1 min. Alim. – Ingresso 2000 Vca 50 Hz, 1 min. Alim. – RS485 2000 Vca 50 Hz, 1 min.
			Temperatura e Umidità Temperatura operativa -10°C .. +60°C Temp. di immagazzinaggio -40°C .. +85°C Umidità (senza condensa) 0 .. 90 %
			Contenitore Materiale Montaggio Peso 150 g. circa
			EMC Immunità Emissione EN 61000-6-2 EN 61000-6-4

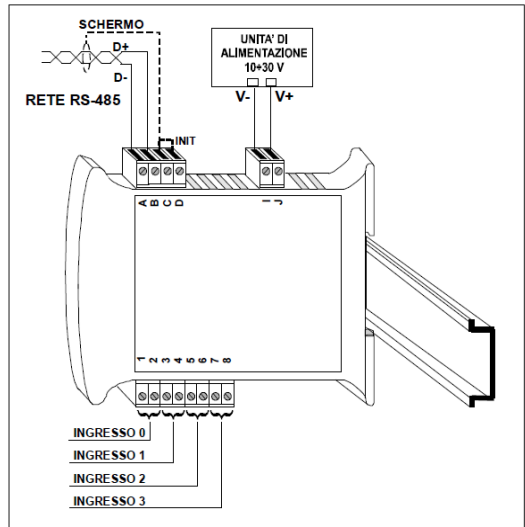
ISTRUZIONI PER L' INSTALLAZIONE

Il dispositivo DAT 3015-V è adatto al montaggio su binario DIN in posizione verticale.
Per un funzionamento affidabile e duraturo del dispositivo seguire le seguenti indicazioni.

Nel caso in cui i dispositivi vengano montati uno a fianco all' altro distanziarli di almeno 5 mm nei seguenti casi:
- Temperatura del quadro maggiore di 45 °C e tensione di alimentazione elevata (>27Vcc).

Evitare che le apposite feritoie di ventilazione siano occluse da canaline o altri oggetti vicino ad esse.
Evitare il montaggio dei dispositivi al di sopra di apparecchiature generanti calore; si raccomanda di montare il dispositivo nella parte bassa dell'installazione, quadro o armadio che sia.
Installare il dispositivo in un luogo non sottoposto a vibrazioni.
Si raccomanda inoltre di non far passare il cablaggio in prossimità di cavi per segnali di potenza e che il collegamento sia effettuato mediante l' impiego di cavi schermati.

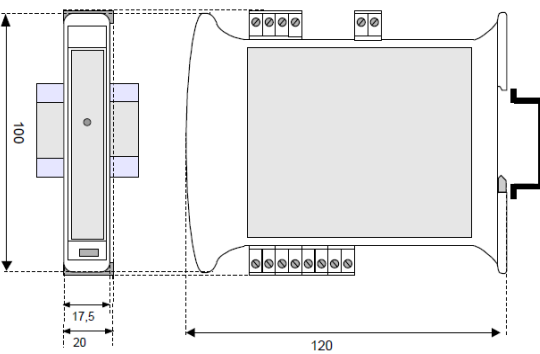
CABLAGGIO



SEGNALAZIONE LUMINOSA

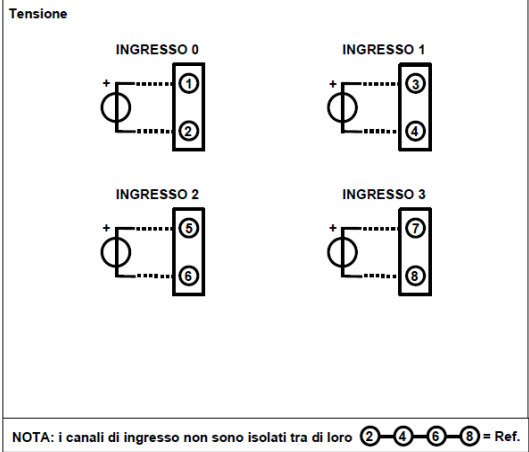
LED	COLORE	STATO	DESCRIZIONE
PWR	VERDE	ACCESO	Modulo alimentato
		SPENTO	Modulo non alimentato / Collegamento errato RS-485
		BLINK VELOCE	Comunicazione in corso (frequenza blink dipende da Baud-rate)
		BLINK LENTO	~ 1 sec. - Condizione di Allarme Watch-Dog

DIMENSIONI MECCANICHE (mm)

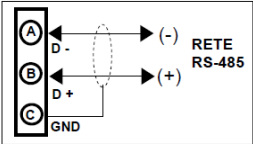


COLLEGAMENTI

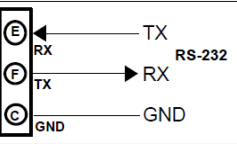
COLLEGAMENTI INGRESSI ANALOGICI



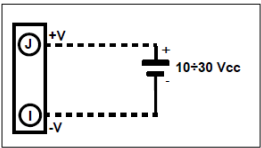
COLLEGAMENTI SERIALE RS-485



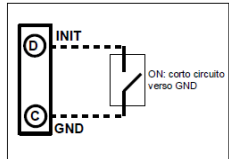
COLLEGAMENTI SERIALE RS-232



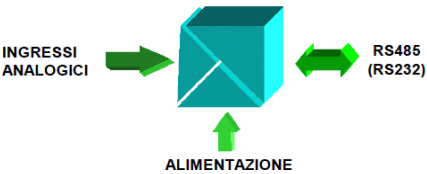
COLLEGAMENTI ALIMENTAZIONE



COLLEGAMENTO INIT



STRUTTURA ISOLAMENTI



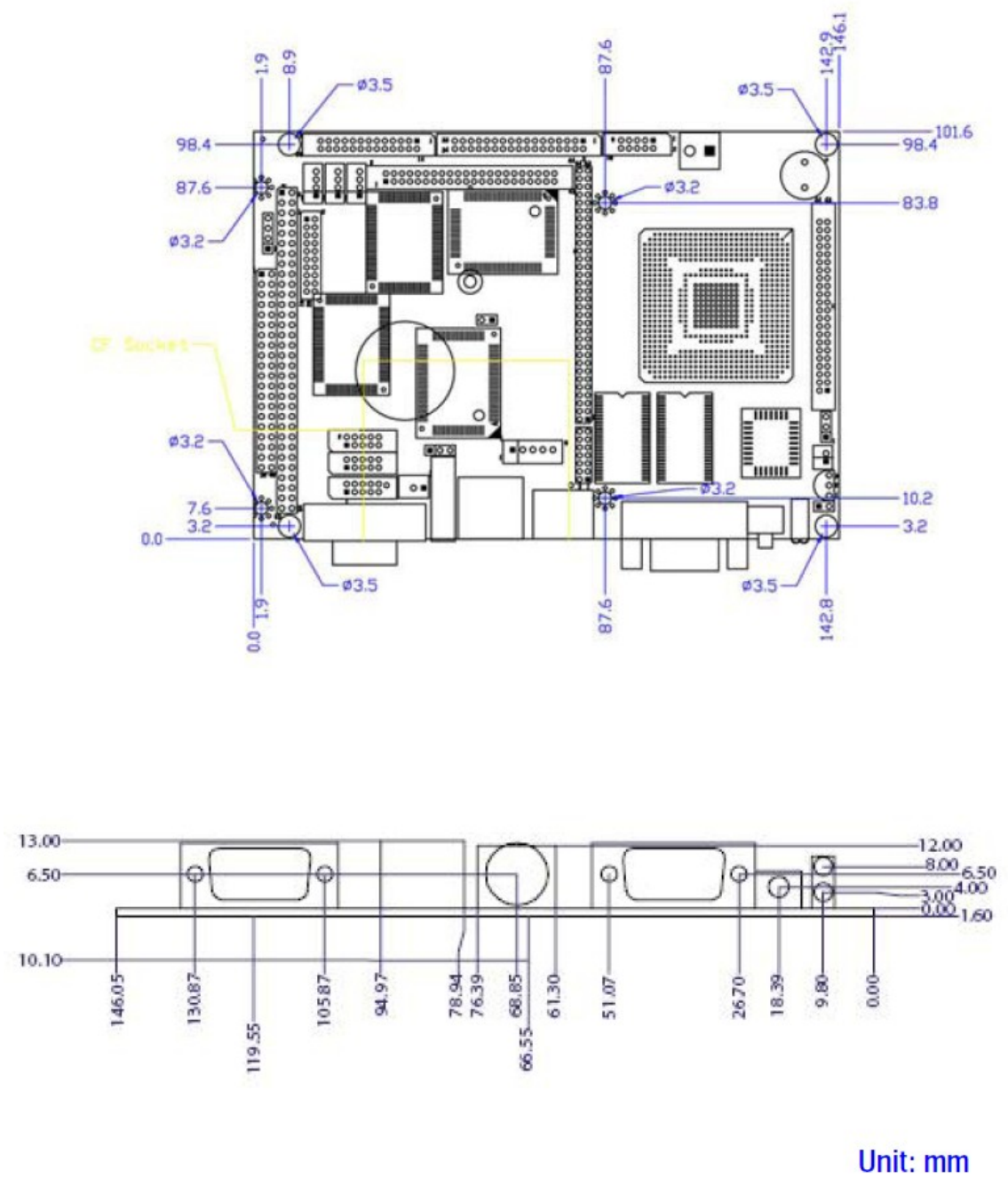
COME ORDINARE

In fase di ordine è necessario specificare il tipo di protocollo (MODBUS) ed il tipo di interfaccia (RS485 o RS232).

DAT 3015-V / M / 485

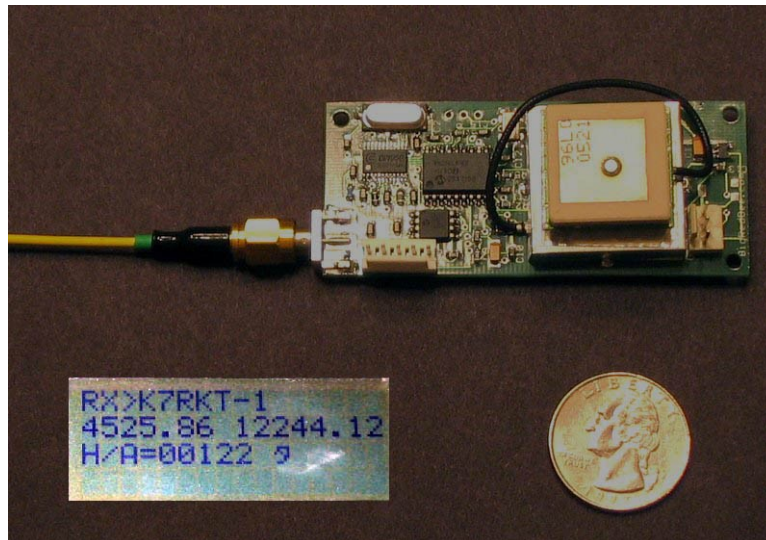
Tipo di protocollo: M: protocollo MODBUS.	Tipo di interfaccia: 485 : RS-485 232 : RS-232
--	--

■ = Richiesto
□ = Opzionale



Features	VORTEX86-6047-4S
Chipset	DM&P(SiS) Vortex86™ System-on-Chip CPU–166MHz (Low Voltage) Real Time Clock with Lithium Battery Backup
BIOS	AMI BIOS
System Memory	128MB SDRAM onboard
Bus Interface	PC/104 standard compliant 32-bit x-PCI interface, compatible with PCI Rev.2.2, PC 98/99
Watchdog Timer	Software programmable from 4ms to 1hour
VGA	AGP Rev.2.0 compliant Shared system memory up to 64MB (Default 8 MB) Support resolution up to 1,280x1,024 true colors VGA and TFT/LVDS Flat Panel interface support
LAN	Realtek 8100B 10/100Mbps Ethernet Controller Half/Full duplex capability
Audio	Fully compliant with AC97 V2.1 Hardware DirectSound accelerator
I/O Interface	<ul style="list-style-type: none"> ● Enhanced IDE port x1 ● RS232 port x 3 ● RS232/485 port x1 (RS485 with Auto Direction) ● Parallel port x1 ● FDD port x1 ● USB port x2 (USB 1.1 version) ● 16 bit GPIO port x1 ● 10/100Mbps Ethernet port x1

Connectors	<ul style="list-style-type: none"> ● 2.0mm Ø 44-pin box header for IDE x1 ● 2.0mm Ø 34-pin box header for FDD x1 ● 2.0mm Ø 26-pin box header for Printer x1 ● 2.0mm Ø 10-pin box header for RS-232 x3 ● 2.0mm Ø 20-pin header for GPIO x1 ● 2.0mm Ø 10-pin box header for USB x1 ● 2.0mm Ø 44-pin box header for LCD connector x1 ● 2.0mm 4-pin wafer for Line-in/Line-out/MIC-in x3 ● 2.54mmØ 3-pin header for RS-485 x1 ● 2.54mm 2-pin header for Reset x1 ● 2.54mm 4-pin header for +12V, -12V, -5V DC-in x1 ● External 15-pin D-Sub female connector for VGA x1 ● External 9-pin D-Sub male connector for RS-232 x1 ● External RJ-45 connector for Ethernet x1 ● External Mini DIN socket for Keyboard/Mouse x1 ● Type I/II Compact Flash slot x1
Flash Disk Support	<ul style="list-style-type: none"> ● 44-pin IDE Flash Disk(EmbedDisk 16MB or above) ● Type I/II CF Card
Power Requirement	Single Voltage +5V @1.06A
Dimension	102mm X 144mm (4.01" x 5.67 inches)
Weight	190g
Operating Temperature	-20°C ~ +70°C



- Completely integrated: RF transmitter, GPS and RF antennas, GPS Module, and battery all in one small package.
- Optional Digital Telemetry Package: hardware G-switch for launch detect, up to 4 digital inputs
- Lithium-Poly battery lasts for more than 8 hours.
- Transmits on ANY frequency in the 70cm band (in 125 hz steps) (33cm band optional) APRS compatible -- uses standard decoding hardware
- Integrated active GPS patch antenna -- external antenna available
- Battery Backup for GPS module enables quick GPS lock times
- Power Management: User programmable transmit rates
- Compatible with existing BeeLine Serial / USB Adapters and Chargers
- Optional SMA RF antenna connection
- Field - upgradeable firmware
- Range: 20 miles line of site.
- Flight data stored in non-volatile memory -- compatible with Google Earth
- 1.25" x 3", weighs about 2 ounces, and fits in a 38mm body tube (or a 54mm nose cone)
- Transmits latitude, longitude, altitude, course and speed.

DSK 75 Ultra

Grazie alla sua costruzione a treccia singola e all'esclusivo trattamento a caldo HTR messo a punto da Gottifredi Maffioli, il quale enfatizza le eccellenti proprietà meccaniche del Dyneema® SK 75 (UHMW-PE), questa cima dalle straordinarie prestazioni offre la miglior sintesi di leggerezza, resistenza e durata. L'elevato carico di rottura, l'allungamento estremamente ridotto ed il comportamento a creep notevolmente migliorato, si accoppiano alla straordinaria resistenza all'abrasione, alla leggerezza e all'impermeabilità tipiche di questa fibra, dando così vita ad un prodotto senza compromessi, le cui prestazioni durano nel tempo. Uno speciale trattamento di resinatura superficiale ne migliora infine la maneggevolezza e la tenuta, rendendone inoltre più agevoli le operazioni di impiombatura e ricopertura.



Caratteristiche Tecniche:

Costruzione:	Treccia singola
Materiale:	Dyneema® SK 75 con trattamento HTR
Colori:	bianco, giallo, grigio e nero (altri colori disponibili su richiesta)
Diametri:	produzione standard da 2 a 16 mm (diametri superiori su richiesta)
Uso consigliato:	semplicemente tutto (per l'uso negli stopper o sui verricelli è richiesta una calza di protezione)

Proprietà meccaniche e fisiche:

Diametro [mm]	2	3	3.5	4	5	6	7	8	9	10	12	14	16
Carico di Rottura [kgf]*	450	900	1350	1825	2750	3850	5950	6950	8475	11000	14100	17150	21750
Peso Lineare [g/m]	2.35	4.70	7.05	9.35	13.9	18.4	27.4	31.9	41.5	50.8	73.8	87.7	120

Valori soggetti a variazioni senza preavviso

* I valori riportati in tabella sono stati misurati in condizioni di laboratorio su campioni nuovi con entrambe le terminazioni impiombate. Nonostante ciò, riduzioni fino al 25% del carico di rottura possono verificarsi per effetto di impiombature male eseguite o troppo corte. La presenza di nodi può provocare cali della resistenza della fune di oltre il 50%. Al fine di preservare le proprietà del prodotto ed evitare rotture inattese, il carico di lavoro della fune non deve mai eccedere il 20% dei valori esposti nella tabella dei carichi di rottura sopra riportata. Inoltre, a causa delle proprietà fisiche del Dyneema®, il prodotto oggetto di questa scheda non deve essere utilizzato in ambienti con temperatura superiore a 50°C. Sotto carico, non dovrebbe altresì venire a contatto con alcuna superficie tagliente. In nessun caso Gottifredi Maffioli S.p.A. o i suoi fornitori saranno responsabili per qualsiasi danno derivante dall'uso improprio del prodotto in questione: qualunque utilizzo del prodotto che violi anche solo in parte o temporaneamente le indicazioni riportate in questa nota, è da considerarsi improprio e illegittimo. Dyneema® è un marchio registrato di DSM High Performance Fibers.



GOTTFREDI MAFFIOLI



EU 30 is

Alternatore corrente Alternata

Potenza massima	3 KVA
Potenza racc. uso continuato	2.8 KVA
Frequenza	50 Hz
Tensione	230 V
Stabilità di tensione momentanea	10 V
Stabilità di tensione media	6 V
Stabilità di tensione tempo di stabiliz.	3 V
Stabilità di tensione sta. sotto carico	+/- 1 V
Stabilità di frequenza momentanea	1 Hz
Stabilità di frequenza media	1 Hz
Stabilità di frequenza tempo di stabiliz.	1 Hz
Stabilità di frequenza sta. sotto carico	+/- 0,1 Hz
Regolatore automatico di tensione	Inverter

Alternatore corrente continua

Potenza massima	120 W
Tensione	12 V
Intensità	3 - 10 A

Alternatore

Livello di isolamento	IP 23
-----------------------	-------

Rumorosità gruppo

Potenza acustica	90 db
Pressione acustica	70 db
Livello sonoro a 7m	58 db

Motore

Modello	GX 200 Kg
Tipo - Cilindrata	4 tempi - 196 cc - Monocilindrico cc
potenza max KW-CV g/m	4,8/6,5 3600
Raffreddamento	aria
Valvole in testa	OHV
Avviamento autovolgente	si
Avviamento elettrico	si
Aria / choke	manuale
Accensione	TRANSIST.
Dispositivo antidisturbo	si
Capacità serbatoio	13 l

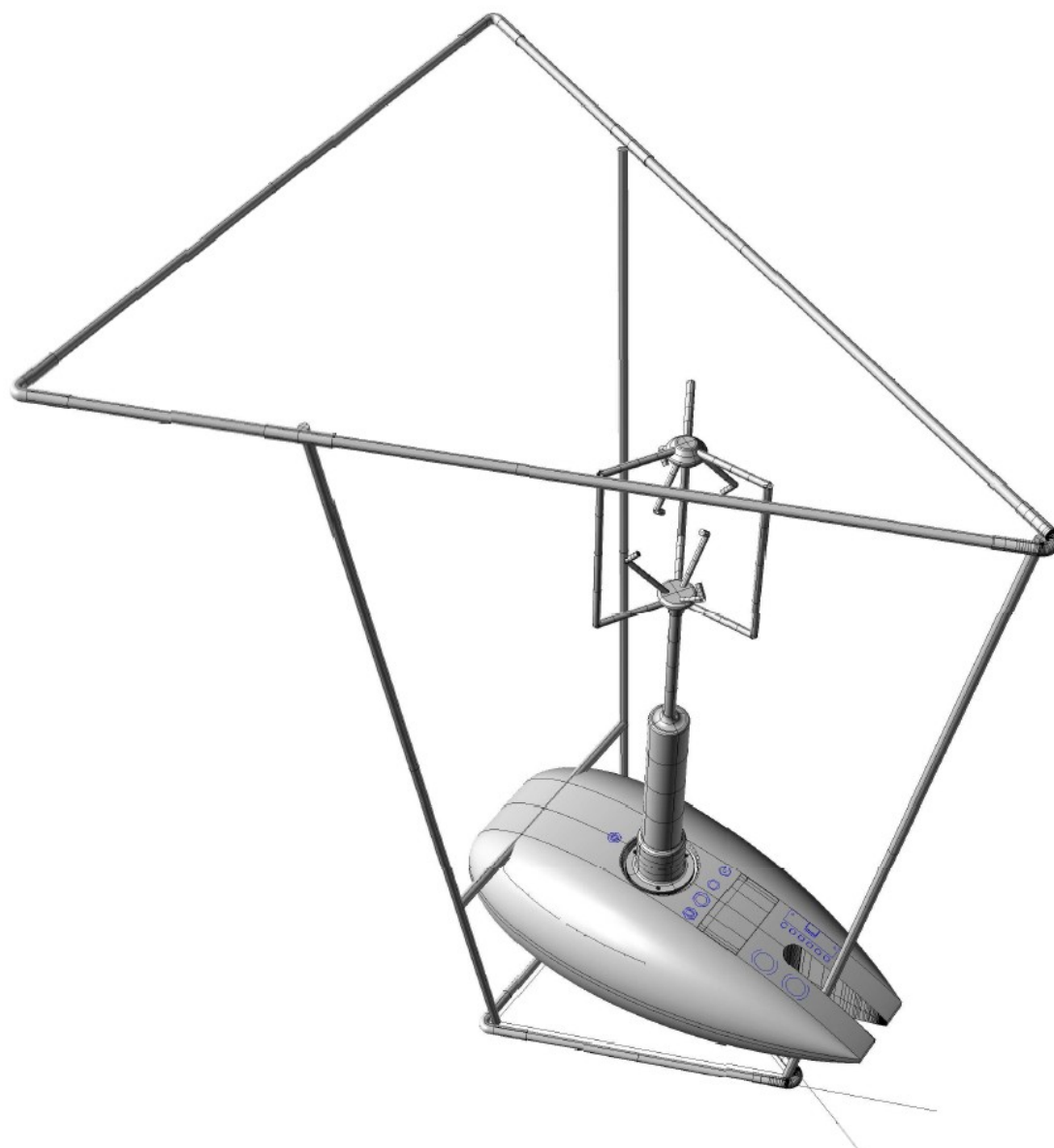
Equipaggiamento

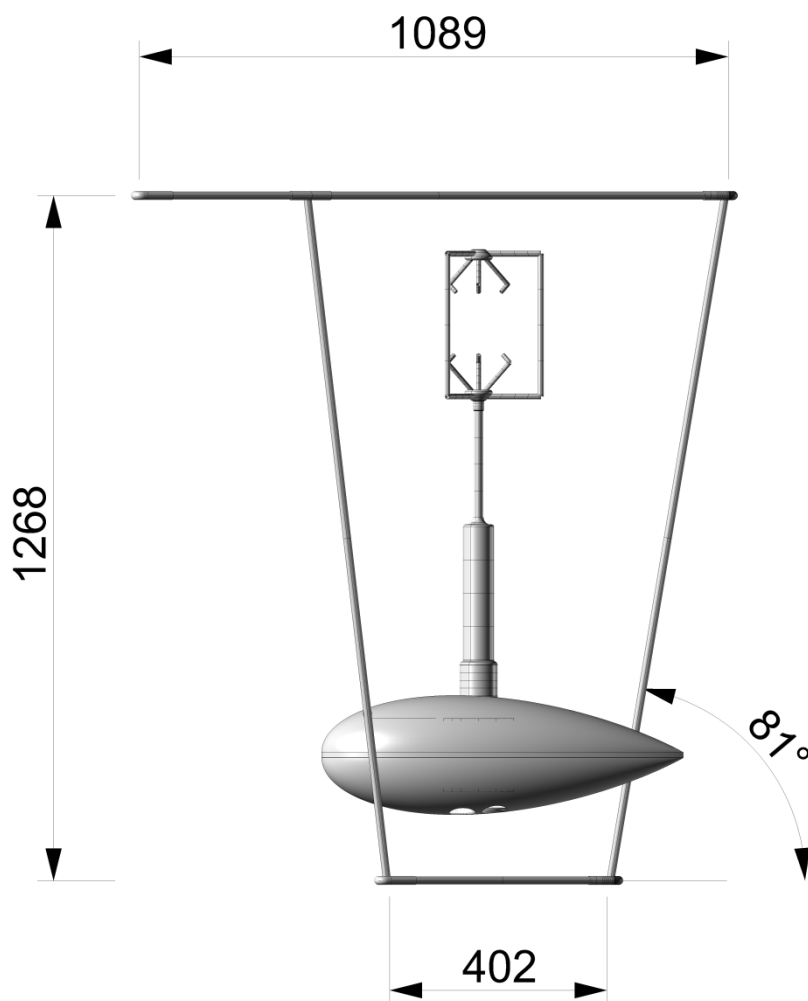
Disgiuntore termico C.A.	si
Disgiuntore termico C.C.	si
Oil Alert(dispositivo controllo livello olio motore)	si
Econimizzatore	si
Indicatore livello di carburante	si
Ruote	si
Batteria	si
Kit per collegamento in parallelo	optional

Dimensioni e peso

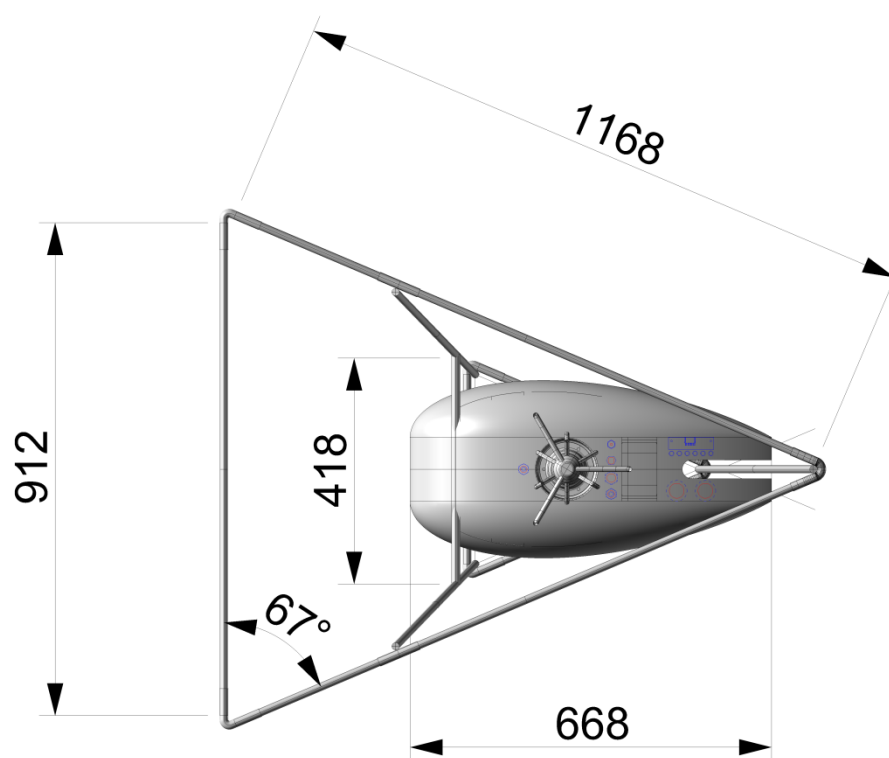
Dimensioni (lung. X larg. X alt.)	655 x 480 x 570 mm
Peso a secco / in ordine di marcia	61 / 66 Kg

Appendix B: CATFISH gondola drawings

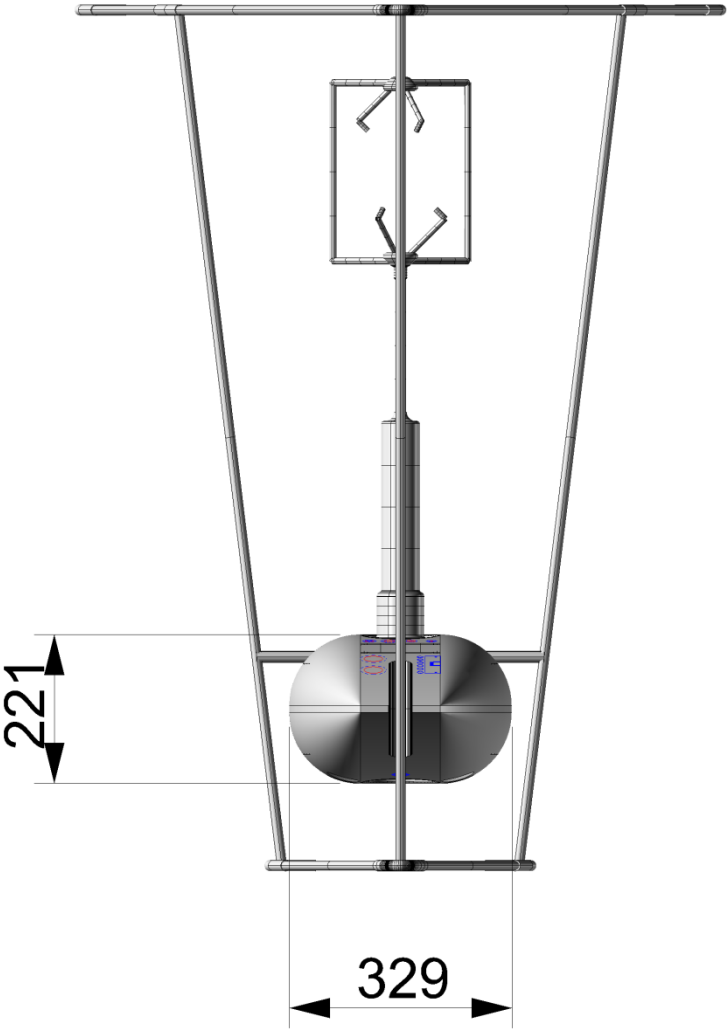




Dimension are in mm .



Dimension are in mm .



Dimension are in mm .

Appendix C: IG 500 N Configuration Document¹¹.

Di seguito sono riportati i programmi richiesti:

Prg.Acquisizione , nel quale si esegue:

- Check strumenti ; Sullo schermo compare la lista delle strumentazioni e di fianco il risultato del test: valore “OK” nel caso affermativo; “ERRORE” nel caso negativo. Se possibile nel secondo caso descrivere la causa dell’errore a mezzo di messaggi di warning, tipo: “VERIFICARE COLLEGAMENTI”, etc..Come si procede nel caso di test negativo.
- Controllo spazio della memoria: se la memoria è piena far comparire messaggio di warning “MEMORIA PIENA” , e la procedura si interrompe ; altrimenti far comparire il valore della dimensione ancora disponibile della memoria, tipo: “15MB MEMORIA LIBERA”;
- Controllo carica delle batterie: visualizza l’autonomia delle batterie e chiede all’utente se si vuol procedere o meno presa visione dei valori di carica della batteria e di spazio di memoria libera;
- Numerazione automatica dei test di volo con numero progressivo (ex. Test0001) Viene visualizzato il nome del test sullo schermo all’accensione della strumentazione.
- Configurazione IG500: vedi modulo Mod.ConfigGet.IG500
- Inizio acquisizione : solo quando il cavo di collegamento al PC sul quale vengono scaricati i dati, viene staccato.

Prg.Stop.Acquisizione : per sancire l’interruzione della prova.

Mod.ConfigGet.IG500

```
\\ Dichiarare le variabili      dyn_plat_mod   (uint8)
                                magn_decl      (float)
                                grav_cost      (float)
                                divider         (uint8)
                                kalman          (uint32)
                                gps_lev_arm_x   (float)
                                gps_lev_arm_y   (float)
                                gps_lev_arm_z   (float)
```

\\ I valori delle variabili sono estrapolate da un file testo chiamato *config_IG500*

//titolo: config_IG500

//File di configurazione di alcune variabili utilizzate nel modulo Mod.ConfigGet.IG500

```
SBG_GPS_MODEL_STATIONARY,dyn_plat_mod          (a)
2.4,magn_decl
9.81,grav_cost
2,divider
default,kalman                                  (b)
0,gps_lev_arm_x
0,gps_lev_arm_y
0.75,gps_lev_arm_z
```

¹¹ This is the original (in Italian) document that explain the configuration of *IG 500 N* device.

(a) i possibili valori delle variabili sono : SBG_GPS_MODEL_STATIONARY
SBG_GPS_MODEL_PEDESTRIAN
SBG_GPS_MODEL_AUTOMOTIVE
SBG_GPS_MODEL_SEA
SBG_GPS_MODEL_AIRBONE_1G
SBG_GPS_MODEL_AIRBONE_2G
SBG_GPS_MODEL_AIRBONE_4G

n.b. Se ci fossero errori di battitura nel file config_IG500 è necessario far comparire un warning; quindi far eseguire un controllo sulla variabile *dyn_plat_mod*

(b) i possibili valori delle variabili sono specificate nel seguito;
se, come nel file di esempio, compare il valore 'default', saltare il comando di configurazione (*SbgSetFilterAttitudeOptions*) che utilizza le variabili di sotto. In tal modo viene attivata la configurazione di default che le attiva tutte.

SBG_FILTER_OPTION_FILTER_ACCELERATIONS
SBG_FILTER_OPTION_FILTER_MAG_DISTORTIONS
SBG_FILTER_OPTION_ESTIMATE_GYRO_BIAS
SBG_FILTER_OPTION_ESTIMATE_ACCEL_BIAS
SBG_FILTER_OPTION_ENABLE_ATTITUDE

n.b. Se ci fossero errori di battitura nel file config_IG500 è necessario far comparire un warning; quindi far eseguire un controllo sulla variabile *kalman*

\\ Far comparire il messaggio "ATTENDERE 15 MINUTI (WARM-UP DELLA PIATTAFORMA INERZIALE) OPPURE PROCEDERE?" così da consentire che in prove successive alla prima, nelle quali il dispositivo è a regime, si perdano 15 minuti.

\\ Configurazione Piattaforma IG500:

```
sbgSetGpsOptions(SbgProtocolHandle, FALSE, dyn_plat_mod,  
...SBG_GPS_ENABLE_SBAS_DIFF_CORRECTION|SBG_ENABLE_SBAS_RANGING)  
sbgSetContinuousMode(SbgProtocolHandle, FALSE, TRUE, divider)  
sbgSetGpsLeverArm(SbgProtocolHandle, FALSE, [gps_lev_arm_x, gps_lev_arm_y,  
gps_lev_arm_z])  
sbgSetMagneticDeclination(SbgProtocolHandle, FALSE, magn_decl)  
  
sbgSetGravityMagnitude(SbgProtocolHandle, FALSE, grav_cost)  
  
sbgSetFilterAttitudeOptions(SbgProtocolHandle, FALSE, kalman)
```

\\ Far comparire il messaggio: “ASSICURARSI CHE IL DISPOSITIVO SIA FERMO PER PROCEDURA CALIBRAZIONE GIROSCOPI; PREMERE TASTO PER CONTINUARE”

sbgCalibGyroBias(SbgProtocolHandle, FALSE , SBG_CALIB_MEASURE)

sbgCalibGyroBias(SbgProtocolHandle, FALSE , SBG_CALIB_SAVE)

\\ Configurazione della maschera di output del dispositivo

sbgSetDefaultOutputMask(SbgProtocolHandle, FALSE, SBG_OUTPUT_GPS_POSITION|...
...SBG_OUTPUT_GPS_INFO|SBG_OUTPUT_GPS_NAVIGATION|SBG_OUTPUT_GPS_A
CCURACY|...

...SBG_OUTPUT_EULER|SBG_OUTPUT_GYROSCOPES|SBG_OUTPUT_TIME_SINCE_
RESET|...

...SBG_OUTPUT_BARO_PRESSURE|SBG_OUTPUT_POSITION|SBG_OUTPUT_VELOCI
TY|...

...SBG_OUTPUT_NAV_ACCURACY|SBG_OUTPUT_TEMPERATURES)

\\ Si richiede di immagazzinare i dati importati dal dispositivo in forma di una stringa di 134 bytes

	<i>Numero variabili</i>	Dimensione (byte)
SBG_OUTPUT_GPS_POSITION	3	12
SBG_OUTPUT_GPS_INFO	3	6
SBG_OUTPUT_GPS_NAVIGATION	4	16
SBG_OUTPUT_GPS_ACCURACY	4	16
SBG_OUTPUT_EULER	3	12
SBG_OUTPUT_GYROSCOPES	3	12
SBG_OUTPUT_TIME_SINCE_RESET	1	4
SBG_OUTPUT_BARO_PRESSURE	1	4
SBG_OUTPUT_POSITION	3	24
SBG_OUTPUT_VELOCITY	3	12
SBG_OUTPUT_NAV_ACCURACY	2	8
SBG_OUTPUT_TEMPERATURES	2	8
totale	32	134

Supponendo una frequenza di campionamento di 50 Hz ne risulta una velocità di trasmissione di 50(Hz) x 134 (bytes) = 6700 bytes/s = 53.6 kbps = 6.7 kb/s

Per un ora di acquisizione (3600 s) risulta un file di 23,5Mb.

NOTA BENE

Un esempio di programma funzionante di acquisizione e configurazione del dispositivo IG-500 SDK è presente nella cartella:

SBG-Systems \ IG-500 SDK \ Software Development \ Examples \ ig500Continuous \ src \
ig500Continuous.c

Appendix C: *IG 500N* configuration document

Si può partire da quello e aggiungere le righe di comando necessarie per soddisfare I requisiti di sopra.

Inoltre nella directory:

SBG-Systems \ IG-500 SDK \ Software Development \ Examples \ ig500Continuous \ lib \ include \ sbgCom









































Sono presenti tutte le funzioni utilizzate nel file esempio e da cui sono state estratte le righe di comando riportate di sopra; la maggior parte sono nella cartella PROTOCOL.

Si richiede la possibilità di selezionare le variabili da registrare, impostando una variabile booleana nel file di configurazione del dispositivo IG500 (*config_IG500*).


















































Appendix D: Weather forecast

Taken from: www.ilmeteo.it


















































14th September 2010

Ora	Tempo	T (°C)	Vento (km/h)	Precipitazioni	Percepita	Umidità	UV	Quota 0°C
	 Segnala il tempo!	 Webcam	 Video	 Foto				
07.00	 sereno	16.3°	 ENE 14 / max 23 moderato	– assenti –	17°C	96 %	0	3110m
08.00	 poco nuvoloso	18.1°	 NE 15 / max 23 moderato	– assenti –	19°C	87 %	0.5	3110m
09.00	 poco nuvoloso	20.6°	 ENE 17 / max 23 moderato	– assenti –	21°C	70 %	1.6	3110m
10.00	 poco nuvoloso	22.4°	 ENE 17 / max 22 moderato	– assenti –	23°C	60 %	3.2	3130m
11.00	 sereno	24.5°	 ENE 14 / max 21 moderato	– assenti –	25°C	54 %	4.9	3140m
12.00	 poco nuvoloso	25.7°	 ENE 14 / max 22 moderato	– assenti –	27°C	48 %	6	3190m
13.00	 poco nuvoloso	26.5°	 ENE 14 / max 22 moderato	– assenti –	27°C	45 %	6.2	3250m
14.00	 poco nuvoloso	27.1°	 ENE 15 / max 23 moderato	– assenti –	28°C	42 %	5.7	3300m
15.00	 poco nuvoloso	27.4°	 ENE 16 / max 23 moderato	– assenti –	28°C	41 %	4.6	3320m
16.00	 poco nuvoloso	27.3°	 ENE 15 / max 22 moderato	– assenti –	28°C	41 %	3.1	3330m
17.00	 sereno	26.8°	 ENE 15 / max 21 moderato	– assenti –	27°C	41 %	1.5	3320m
18.00	 sereno	25.9°	 ENE 14 / max 21 moderato	– assenti –	27°C	43 %	0.3	3290m
19.00	 sereno	23.8°	 ENE 13 / max 22 moderato	– assenti –	24°C	50 %	0	3250m
20.00	 sereno	22°	 ENE 14 / max 24 moderato	– assenti –	23°C	55 %	0	3280m
21.00	 sereno	20.6°	 ENE 15 / max 24 moderato	– assenti –	21°C	62 %	0	3340m
22.00	 sereno	19.5°	 ENE 14 / max 23 moderato	– assenti –	20°C	66 %	0	3410m
23.00	 sereno	18.6°	 ENE 14 / max 23 moderato	– assenti –	19°C	70 %	0	3460m
24.00	 sereno	17.8°	 ENE 13 / max 22 moderato	– assenti –	18°C	74 %	0	3480m

15th September 2010

Ora	Tempo	T (°C)	Vento (km/h)	Precipitazioni	Percepita	Umidità	UV	Quota 0°C
24.00	 sereno	17.8°	 <u>ENE 13 / max 22</u> moderato	-- assenti --	18°C	74 %	0	3480m
01.00	 sereno	17.1°	 <u>ENE 12 / max 21</u> moderato	-- assenti --	18°C	77 %	0	3480m
02.00	 sereno	16.4°	 <u>NE 12 / max 20</u> moderato	-- assenti --	17°C	80 %	0	3490m
03.00	 sereno	15.9°	 <u>NE 12 / max 19</u> moderato	-- assenti --	16°C	83 %	0	3490m
04.00	 sereno	15.4°	 <u>NE 12 / max 19</u> moderato	-- assenti --	16°C	85 %	0	3490m
05.00	 sereno	15°	 <u>NE 12 / max 19</u> moderato	-- assenti --	15°C	87 %	0	3500m
06.00	 sereno	14.6°	 <u>NE 12 / max 18</u> moderato	-- assenti --	15°C	88 %	0	3510m
07.00	 sereno	14.3°	 <u>NE 12 / max 18</u> moderato	-- assenti --	15°C	89 %	0	3520m
08.00	 sereno	16.4°	 <u>NE 12 / max 16</u> moderato	-- assenti --	17°C	79 %	0.5	3540m
09.00	 sereno	19.8°	 <u>NE 12 / max 14</u> moderato	-- assenti --	20°C	64 %	1.8	3570m
10.00	 sereno	22.2°	 <u>NE 11 / max 13</u> moderato	-- assenti --	23°C	54 %	3.4	3610m
11.00	 sereno	24.1°	 <u>NE 9 / max 10</u> debole	-- assenti --	25°C	48 %	5	3640m
12.00	 sereno	25.6°	 <u>NE 5 / max 7</u> debole	-- assenti --	27°C	43 %	6.3	3650m
13.00	 sereno	26.6°	calma	-- assenti --	27°C	40 %	6.6	3660m
14.00	 sereno	27.3°	 <u>W 4</u> debole	-- assenti --	27°C	38 %	6.1	3670m
15.00	 sereno	27.7°	 <u>WSW 8</u> debole	-- assenti --	28°C	37 %	4.8	3670m
16.00	 sereno	27.5°	 <u>WSW 12</u> moderato	-- assenti --	28°C	38 %	3.1	3680m
17.00	 sereno	26.9°	 <u>WSW 14</u> moderato	-- assenti --	27°C	40 %	1.5	3680m
18.00	 sereno	25.7°	 <u>WSW 15 / max 17</u> moderato	-- assenti --	27°C	45 %	0.3	3690m
19.00	 sereno	23.3°	 <u>W 14 / max 18</u> moderato	-- assenti --	24°C	55 %	0	3700m
20.00	 sereno	21.3°	 <u>W 11 / max 17</u> moderato	-- assenti --	22°C	66 %	0	3720m
21.00	 sereno	20.1°	 <u>W 9 / max 15</u> debole	-- assenti --	21°C	73 %	0	3740m
22.00	 sereno	19.1°	 <u>W 7 / max 13</u> debole	-- assenti --	20°C	79 %	0	3780m
23.00	 sereno	18.4°	 <u>W 6 / max 11</u> debole	-- assenti --	19°C	84 %	0	3820m
24.00	 sereno	17.8°	 <u>W 5 / max 10</u> debole	-- assenti --	18°C	88 %	0	3830m

16th September 2010



















































Ora	Tempo	T (°C)	Vento (km/h)	Precipitazioni	Percepita	Umidità	UV	Quota 0°C
24:00	 sereno	17.2°	 SSW 4 / max 8 debole	-- assenti --	18°C	89 %	0	3920m
01:00	 sereno	16.7°	 SSW 4 / max 8 debole	-- assenti --	17°C	91 %	0	3930m
02:00	 sereno	16.4°	 SSW 3 / max 8 debole	-- assenti --	17°C	92 %	0	3930m
03:00	 sereno	16.1°	 SSW 3 / max 8 debole	-- assenti --	17°C	93 %	0	3920m
04:00	 sereno	15.8°	 SSW 2 / max 6 debole	-- assenti --	16°C	94 %	0	3900m
05:00	 sereno	15.6°	calma	-- assenti --	16°C	95 %	0	3900m
06:00	 sereno	15.4°	 ESE 3 / max 4 debole	-- assenti --	16°C	96 %	0	3910m
07:00	 sereno	15.3°	 E 4 / max 5 debole	-- assenti --	16°C	97 %	0	3930m
08:00	 sereno	17.9°	 E 5 / max 6 debole	-- assenti --	18°C	92 %	0.5	3970m
09:00	 sereno	20.7°	 ESE 3 / max 5 debole	-- assenti --	21°C	82 %	1.7	3980m
10:00	 sereno	22.8°	 S 3 / max 5 debole	-- assenti --	23°C	74 %	3.3	3980m
11:00	 sereno	24.7°	 SW 8 / max 10 debole	-- assenti --	25°C	67 %	4.9	3980m
12:00	 sereno	25.9°	 SW 13 / max 16 moderato	-- assenti --	27°C	60 %	6.1	3990m
13:00	 sereno	26.5°	 SW 16 / max 20 moderato	-- assenti --	28°C	57 %	6.5	3980m
14:00	 sereno	26.7°	 SW 18 / max 21 moderato	-- assenti --	28°C	56 %	6	3980m
15:00	 sereno	26.5°	 SW 18 / max 22 moderato	-- assenti --	28°C	55 %	4.7	3990m
16:00	 sereno	26.1°	 SW 18 / max 22 moderato	-- assenti --	27°C	56 %	3	4000m
17:00	 sereno	25.3°	 SW 17 / max 21 moderato	-- assenti --	27°C	58 %	1.4	4000m
18:00	 sereno	24.3°	 SW 15 / max 19 moderato	-- assenti --	25°C	62 %	0.2	4000m
19:00	 sereno	22.6°	 SW 12 / max 17 moderato	-- assenti --	23°C	70 %	0	4000m
20:00	 sereno	21°	 SW 9 / max 15 debole	-- assenti --	22°C	79 %	0	4000m
21:00	 sereno	19.9°	 SW 8 / max 13 debole	-- assenti --	20°C	87 %	0	3980m
22:00	 sereno	19.2°	 SSW 6 / max 12 debole	-- assenti --	20°C	92 %	0	3980m
23:00	 sereno	18.6°	 SSW 5 / max 10 debole	-- assenti --	19°C	95 %	0	3960m
24:00	 sereno	18.2°	 SSW 5 / max 10 debole	-- assenti --	19°C	96 %	0	3950m

17th September 2010Comune di **Caserta** (CE) - CAP 81100

Casa.it - Trovala a Caserta

Meteo Giornaliero  **Giovedì 16**  **Venerdì 17**  **Sabato 18**  **Domenica 19**  **Lunedì 20**  **Martedì 21**  **Mercoledì 22** **Fino al 30 Settembre»**
 **novità**

Previsioni Priorarie **Previsioni Orarie** Sperimentali Bollettino PDF Opzioni Altri dati Meteo

Ora	Tempo	T (°C)	Vento (km/h)	Precipitazioni	Percepita	Umidità	UV	Quota 0°C
24:00	 sereno	18°	 SSW 7 / max 12 debole	-- assenti --	19°C	95 %	0	4050m
01:00	 sereno	17.7°	 SSW 7 / max 13 debole	-- assenti --	18°C	95 %	0	4070m
02:00	 sereno	17.4°	 SSW 7 / max 13 debole	-- assenti --	18°C	96 %	0	4090m
03:00	 poco nuvoloso	17.1°	 SSW 6 / max 12 debole	-- assenti --	18°C	96 %	0	4070m
04:00	 nubi sparse	17.1°	 S 5 / max 11 debole	-- assenti --	18°C	96 %	0	4050m
05:00	 nubi sparse	17.4°	 S 4 / max 10 debole	-- assenti --	18°C	96 %	0	4050m
06:00	 nubi sparse	17.3°	 SSE 4 / max 10 debole	-- assenti --	18°C	96 %	0	4070m
07:00	 nubi sparse	17.3°	 SSE 5 / max 10 debole	-- assenti --	18°C	96 %	0	4100m
08:00	 nubi sparse	19.5°	 SSE 5 / max 8 debole	-- assenti --	20°C	90 %	0.4	4150m
09:00	 nubi sparse	22°	 SSE 6 / max 8 debole	-- assenti --	23°C	81 %	1.4	4190m
10:00	 nubi sparse	23.6°	 S 7 / max 10 debole	-- assenti --	24°C	75 %	2.8	4240m
11:00	 poco nuvoloso	25°	 SSW 10 / max 14 moderato	-- assenti --	25°C	69 %	4.1	4220m
12:00	 nubi sparse	25.9°	 SSW 13 / max 17 moderato	-- assenti --	27°C	62 %	4.3	4230m
13:00	 nubi sparse	26.3°	 SSW 14 / max 18 moderato	-- assenti --	28°C	58 %	5.6	4300m
14:00	 sereno	26.8°	 SW 14 / max 18 moderato	-- assenti --	28°C	54 %	6	4380m
15:00	 sereno	27.1°	 SW 15 / max 19 moderato	-- assenti --	28°C	52 %	4.7	4420m
16:00	 sereno	26.9°	 SW 14 / max 18 moderato	-- assenti --	28°C	51 %	3	4450m
17:00	 sereno	26.4°	 SSW 14 / max 18 moderato	-- assenti --	27°C	53 %	1.4	4470m
18:00	 poco nuvoloso	25.4°	 SSW 12 / max 17 moderato	-- assenti --	27°C	57 %	0.3	4490m
19:00	 sereno	23.4°	 SSW 10 / max 15 debole	-- assenti --	24°C	66 %	0	4500m
20:00	 sereno	21.6°	 SSW 8 / max 14 debole	-- assenti --	22°C	77 %	0	4500m
21:00	 poco nuvoloso	20.5°	 S 6 / max 13 debole	-- assenti --	21°C	85 %	0	4500m
22:00	 nubi sparse	19.8°	 S 6 / max 12 debole	-- assenti --	20°C	90 %	0	4500m
23:00	 nubi sparse	19.3°	 SSE 6 / max 11 debole	-- assenti --	20°C	93 %	0	4500m
24:00	 nubi sparse	19°	 SSE 5 / max 11 debole	-- assenti --	19°C	94 %	0	4470m

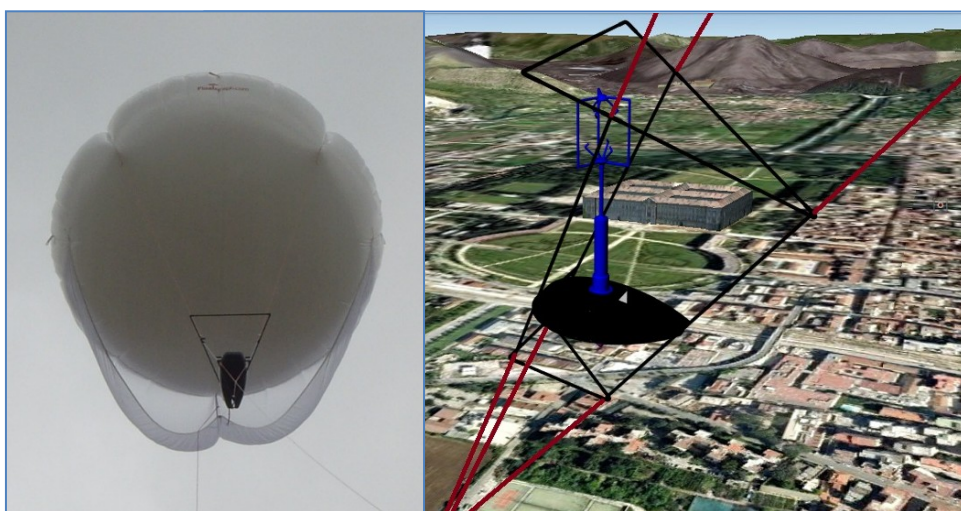
Appendix E: Failure Analysis¹²

UNIVERSITÀ DEGLI STUDI DI NAPOLI

FEDERICO II

DIPARTIMENTO DI INGEGNERIA

AEROSPAZIALE



FEDERICO II- KYTOON STATION OPEARTING MANUAL UPDATE Revisione 1

PHD'S STUDENT	TUTOR OF THE PROJECT
Prepared	Revision
<i>Eng. Mario Panelli</i>	<i>Prof. Eng. Gennaro Cardone</i>

¹² This is the original document (In Italian) given to the ENAC and ENAV in order to obtain the NoTAM.

1. SCOPO

L'obiettivo di questo documento fornire all'ENAC nuove informazioni (richieste nella riunione del 17/06/2010) per il rilascio delle autorizzazioni necessarie per il rilascio del NOTAM.

Come è indicato da FAR PART 101 il pallone del DIAS per tipologia, dimensioni e massa non è classificabile come un aeromobile ai fini del Codice della Navigazione e pertanto non è soggetto ad omologazione e non deve rispondere ad uno specifico regolamento tecnico con l'eccezione delle norme che regolano gli ostacoli alla navigazione aerea.

Al fine di dimostrare comunque che i voli del pallone del DIAS non presentano rischi né per la navigazione aerea e per eventuali terzi presenti nell'area di lancio, nel seguito sarà riportato una Failure Analysis effettuata mediante l'analisi dei *Factor of Safety and probability of failure* dei vari componenti del sistema (pallone, cavo di ritegno, argano) dove i diversi *Factor of Safety* saranno confrontati con quelli richiesti dalla [3] per la certificazione aeronautica di palloni frenati con persone a bordo. Sarà inoltre presentata una Functional Hazard Assessment [8]. relativa al sistema in oggetto. Verrà infine verificata la conformità con le specifiche di segnalazione dell'ostacolo [5].

2. ACRONIMI

FA	<i>Failure Analysis</i>
ENAC	<i>Ente Nazionale Aviazione Civile</i>
FHA	<i>Functional Hazard Assessment</i>

3. APPLICABILITÀ

Il documento in oggetto è applicabile alla KYTOON STATION del DIAS per rilevamento meteorologico e chimico dell'Università Federico II di Napoli [1].

4. DOCUMENTI DI RIFERIMENTO

- [1] *Federico II Kytoon-Station, Manuale Operativo*
- [2] *Minuta riunione pallone frenato, 17/6/2010 (allegata)*

EASA Documents

- [3] EASA CS 31 TGB "*Certification Specification For Manned Tethered Gas Balloon For Passenger Transport*"

FAA Documents

- [4] *FAR PART 101 "Moored Balloons, Kites, Unmanned Rockets And Unmanned Free Balloons"*
- [5] *FAA AC 70/7460-1K "Obstruction Marking and Lighting"*
- [6] *FAA AC23.1309-1C "Equipements Systems, And Installations in Part 23 Airplanes"*

NASA Documents

- [7] *Fault Tree Handbook with Aerospace Applications ver. 1.1, 2002*

5. DESCRIZIONE GENERALE

Il sistema sotto esame è costituito dagli elementi visibili in figura 1 ed elencati di sotto:

- 1) Pallone;
- 2) Briglie di collegamento tra il pallone e il cavo di ritegno principale
- 3) Gondola portastrumenti: elemento nel quale sono integrati gli strumenti; quest'ultima è connessa alle briglie. La struttura e i supporti della gondola sono realizzati in maniera che quest'ultima non è soggetta al tiro del cavo di ritegno
- 4) Cavo di tenuta principale: elemento di collegamento tra l'argano e il resto del sistema;
- 5) Argano: è l'elemento che determina e controlla il moto di salita e discesa dell'aerostato. (esso è composto da un motore elettrico, da una riduttore e da un inverter di comando motore). l'energia elettrica viene fornita da un gruppo elettrogeno.

Dettagli maggiori sugli elementi che costituiscono la stazione sono presenti nel manuale operativo [1].

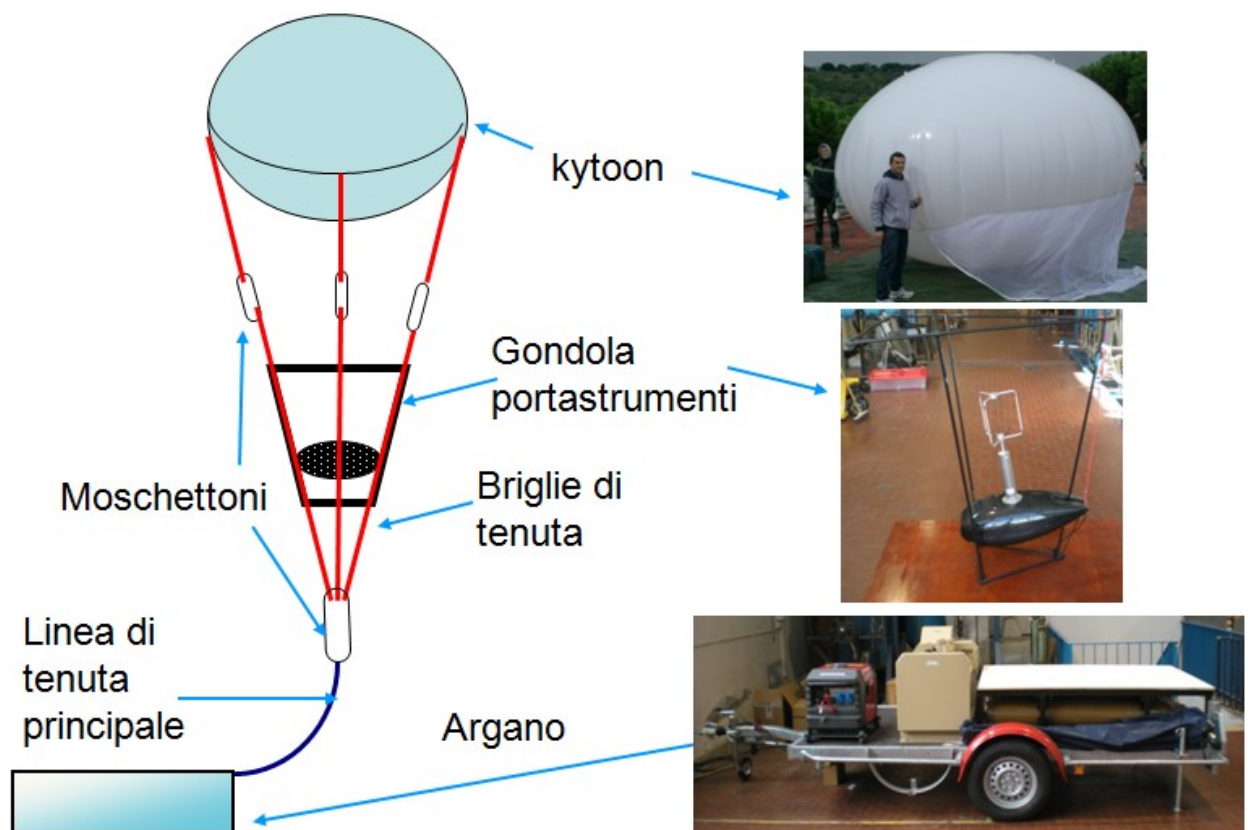


Fig. 1 Kytoon-Station: schema e foto.

5.1 Condizioni operative

Gli esperimenti previsti nell'ambito del progetto di ricerca verranno condotti nei regimi di brezza e di correnti di pendio tipici dell'area di Caserta (regime meteo: *fresh breeze*, *velocità max vento 10.7 m/s*); non si effettuano voli in condizioni di tempo variabile e con pioggia/temporali. La zona di lancio viene appositamente scelta secondo i criteri definiti nel manuale utente [1]

Nel seguito sarà anche valutata capacità del sistema (carichi e safety factor) nel regime meteo di Tempesta (*Storm*, velocità max vento 24.4 m/s) anche se *questa non è da considerarsi condizione operativa*.

6. SAFETY FACTORS and PROBABILITY OF FAILURE

6.1 Service Loads

In accordo con la EASA CS 31TGB sono stati identificati i **SERVICE LOADS** (carichi in condizioni di esercizio) ed è stato verificato che i limits loads (service loads* prescribed factor safety) siano compatibili con i materiali e le configurazione adottate.

La valutazione dei carichi (come richiesto da [3]) è stata fatta con misure sperimentali ad hoc (test in galleria del vento e misure sul campo realizzate dalla casa costruttrice del pallone). I valori di carico per il pallone SKYDOC #18 al variare della velocità del vento riportate in figura 1 sono forniti dal produttore del pallone SKYDOC LCC

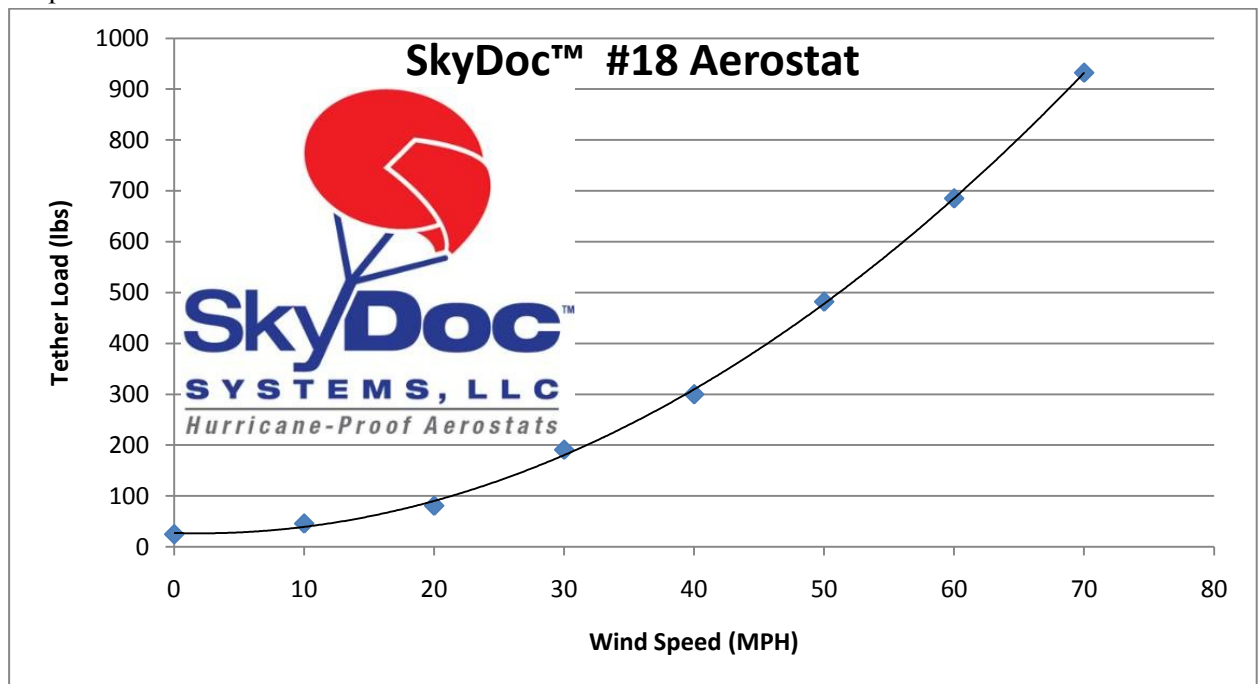


Fig. Tiro del pallone SKYDOC 18 misurato in Galleria del vento (fonte SKYDOC LCC)

il service load viene identificato dalle le condizioni limite di utilizzo di *fresh breeze*.

La resistenza aerodinamica e la forza ascensionale del pallone in condizioni meteo *fresh breeze* da luogo ad **service load** sul cavo di ritegno di **0.553 kN**. Il tiro massimo, in condizioni di meteo *storm*, sul cavo di ritegno è 2.52 kN.

6.2 RIGGING

6.2.1 Cavo di ritegno

la soluzione adottata da SKYDOC LLC in accordo con Il DIAS è un cavo di ritegno in DYNEMA DSK75 ULTRA da 3.5mm di diametro che prevede un carico di rottura di 14 kN. **Al fine di non introdurre riduzioni del carico utile del cavo di ritegno tutte le connessioni sono realizzate senza utilizzare nodi ma con impiombature.**

Il coefficiente di sicurezza (Factor of safety) in condizioni di *service load* risulta essere pari a **25,31** mentre in condizioni di *storm* è di 5,3. E' stata inoltre calcolata (con un metodo montecarlo) la **Probability of Failure** che risulta **1.3E-11 in service load** e 5.8E-9 in condizioni di *storm*.

La norma EASA CS 31 TGB prescrive per il Rigging (in assenza di duplicazione del cavo di ritegno) un factor of safety di 5.25 in service load.

Per i voli diurni, dovendo raggiungere il pallone durante gli esperimenti un quota più bassa (300 m) è possibile, al fine di incrementare il coefficiente di sicurezza, utilizzare un cavo di ritegno sempre in

DYNEMA DSK75 ULTRA da 5.0mm di diametro con carico di rottura di 29kN. L'utilizzo del cavo da 5mm se richiesto da ENEC da luogo a un coefficiente di sicurezza (Factor of safety) in condizioni di service load di **52,44** e in condizioni di storm è di 11,5. La **Probability of Failure** risulta in questo caso di **4.79E-12 in service load** e 1.13E-10 in condizioni di storm.

6.2.2 Briglie e sistemi di sgancio (moschettoni)

Al fine di aumentare la sicurezza intrinseca del sistema le briglie sono realizzate con DYNEMA DSK75 ULTRA da 5.0mm (tenendo conto che il peso del payload introduce un lieve aumento dei carichi) Il coefficiente di sicurezza (Factor of safety) in condizioni di *service load* risulta essere pari a **76.11** mentre in condizioni di storm è di 27.97. La **Probability of Failure** risulta in questo caso di **3.58E-12 in service load** e 1.13E-11 in condizioni di storm

I sistemi di sgancio/aggancio pallone/cavo di ritegno (sono 3) hanno un carico di rottura di 14.7 kN per cui presentano un Factor of safety di **38.58** in *service load* e 14.18 in condizioni di storm. La **Probability of Failure** risulta in questo caso di **6.45E-12 in service load** e 5.67E-11 in condizioni di storm

La norma EASA CS 31 TGB prescrive per il Rigging (in assenza di duplicazione del cavo di ritegno) un factor of safety di 5.25 .

6.3 Pallone

La membrana pallone del DIAS è realizzata in DUREFLEX PS8000. I data sheet tecnico è riportato in appendice. La SKYDOC LCC raccomanda una pressione di gonfiaggio del pallone di 500 Pa che considerato lo spessore della membrana (6 mils=0.1524mm) e le dimensioni del pallone da luogo ad uno sforzo di trazione massimo nella membrana di 5.47MPa. Il coefficienti di sicurezza risulta esser quindi di **12.59**. La **Probability of Failure** risulta in questo caso di **7.79E-11**.

Le variazioni di quota e di temperatura danno luogo ad un aumento di volume. Con una variazione + 300 metri ed una aumento di +30 °C si ha una aumento di volume dell'elio del 14% ed una allungamento della membrana del 4.5%. L'allungamento della membrana non induce incrementi del valore di tensione grazie all'elevato allungamento a rottura del materiale (450%). Il Safety factor sull'allungamento del materiale è **100**. Un peculiarità del DUREFLEX PS8000 è un elevata Tear resistance (113.7 N/mm2). Questa proprietà insieme all'elevato allungamento danno luogo a una probabilità di rottura del materiale per cause accidentali (urti, sovraccarichi etc) praticamente trascurabile.

La SKYDOC ha sviluppato una soluzione tecnica che scarica Il tiro del cavo di ritegno su tre attacchi distribuiti sulla superficie dell'emisfero superiore del pallone in questo modo le tensioni indotte nella membrana sono pari a 0,1 MPa in condizioni di operative (fresh breze) e 0.48 MPa in condizioni Storm. Nelle zone degli attacchi i la sigma totale massima è 5.57 Mpa [5.47 (pressione)+ 0.1 (tiro)] in condizioni operative e 5.95 Mpa (5.47(pressione) + 0.48 (tiro)). Il coefficiente di sicurezza nelle zone degli attacchi risulta essere **12.37** in condizioni operative e 11.58 in condizioni Storm. La **Probability of Failure** risulta in questo caso di **8.33E-11 in service load** e 1.11E-10 in condizioni di *storm*.

La norma EASA CS 31 TGB prescrive per la membrana e per i carichi indotti dal cavo di ritegno un factor of safety uguale a 5.

6.4 Argano

Il sistema argano è realizzato con un motore trifase con potenza utile all'asse di 2HP (1490 W), una scatola di riduzione 1:60 ed un Inverter vettoriale per variare la velocità di recupero. La scatola di riduzione, l'Inverter ed il gruppo elettrogeno sono stati dimensionati con un coefficiente di sicurezza 1.5 rispetto alla potenza motore. La velocità massima di recupero è di 20m/min (0,33 m/s). La potenza di recupero risulta quindi in condizioni operative pari a 276.5 W e di 840W in condizioni Storm. I coefficienti di sicurezza per il sottosistema argano sono riportati in tabella

	<i>Service Load (Fresh Breeze)</i>		<i>Storm</i>	
	Factor of safety	Probability of Failure	Factor of safety	Probability of Failure
Motore	5.38	5.70E-013	1.77	5.89E-5
Scatola di riduzione	8.08	1.09E-014	2.66	2.20e-8
Inverter	8.08	1.09E-014	2.66	2.20e-8
Gruppo elettrogeno	8.08	1.09E-014	2.66	2.20e-8

La norma EASA CS 31 TGB prescrive (tranne per rigging e membrana pallone paragraphs (b) and (c) EASA CS 31TGB.25) un factor o f safety uguale a 1.5.

7. FUNCTIONAL HAZARD ASSESSMENT

L'FHA è un esame sistematico dei sistemi che consente di identificare le classi di avaria degli stessi in: MINOR, MAJOR, HAZARDOUS e CATHASTROPHIC, così come riportato nel regolamento AC23.1309-1C. Inoltre la FHA illustra i metodi con i quali la condizione di avaria viene trattata al fine di diminuire il livello di classificazione.

Come già detto, una applicazione diretta di tali regolamenti non è possibile in quanto l'oggetto di analisi non è un aeromobile con passeggeri ed equipaggio. Pertanto le definizioni di classi di avaria date deve essere debitamente interpretata alla luce della nuova situazione.

Allo scopo nel seguito si riporta la definizione data dalla regolamentazione e successivamente si riporta la proposta modifica, nella quale i passeggeri sono sostituiti dai civili non operanti nelle operazioni di lancio e ritiro dell'aerostato.

Descrizione	Risultato sulla sicurezza
Catastrophic	Condizione che causa una grave conseguenza per gli occupanti oppure la morte dell'equipaggio che causa la perdita dell'aeroplano
Hazardous	<p>Condizione di avaria che può ridurre la capacità del velivolo o dell'equipaggio di fronteggiare determinate situazioni operative come:</p> <ul style="list-style-type: none"> • Elevata riduzione del margine di sicurezza o delle funzionalità del velivolo; • Agitazione fisica che non consente all'equipaggio di svolgere il proprio compito in maniera accurata e completa; • Ferimento o morte di un passeggero non facente parte dell'equipaggio. <p>La condizione "hazardous" deve essere "estremamente remota", ovvero non prevista nella vita operativa di un singolo velivolo, ma possibile considerando l'intera vita operativa di tutta la flotta di quel tipo di velivolo.</p>
Major	Il fattore di sicurezza e le funzionalità del velivolo diminuiscono, c'è un significativo incremento del carico di lavoro per l'equipaggio e sono possibili ferimenti dello stesso.
Minor	<p>Questa condizione di avaria non reduce in maniera significativa la sicurezza del velivolo, e coinvolge l'equipaggio in azioni comprese nel programma di addestramento.</p> <p>Il margine di sicurezza e le funzionalità del velivolo diminuiscono in maniera non significativa e l'aumento del carico di lavoro per l'equipaggio non è eccessivo (es: variazione del piano di volo).</p>
No Safety Effect	La condizione così classificabile non inficia la sicurezza del velivolo e non aumenta in alcun modo il carico di lavoro dell'equipaggio.

Tab. 1. Definizioni di Classi di Avaria 7

Descrizione	Risultato sulla sicurezza
Catastrophic	Condizione che causa gravi danni per i civili a terra e pericolo di morte per l'equipaggio di terra (gruppo di persone impegnate nel lancio)
Hazardous	<p>Condizione di avaria che può ridurre la capacità dell'aerostato o dell'equipaggio di terra di fronteggiare determinate situazioni operative come:</p> <ul style="list-style-type: none"> • Elevata riduzione del margine di sicurezza o delle funzionalità dell'aerostato; • Agitazione fisica che non consente all'equipaggio di terra di svolgere il proprio compito in maniera accurata e completa; • Ferimento o morte di un civile non facente parte dell'equipaggio di terra. <p>La condizione "hazardous" deve essere "estremamente remota", ovvero non prevista nella vita operativa dell'aerostato.</p>
Major	Il fattore di sicurezza e le funzionalità dell'aerostato diminuiscono, c'è un significativo incremento del carico di lavoro per l'equipaggio di terra e sono possibili ferimenti dello stesso.
Minor	<p>Questa condizione di avaria non riduce in maniera significativa la sicurezza dell'aerostato, e coinvolge l'equipaggio di terra in azioni comprese nel programma di addestramento.</p> <p>Il margine di sicurezza e le funzionalità diminuiscono in maniera non significativa e l'aumento del carico di lavoro per l'equipaggio non è eccessivo.</p>
No Safety Effect	La condizione così classificabile non inficia la sicurezza dell'aerostato e non aumenta in alcun modo il carico di lavoro dell'equipaggio di terra.

Tab. 2. Definizioni di Classi di Avaria per Kytoon Station

l'FHA si divide in tre passi fondamentali:

- 1) acquisire una sufficiente conoscenza del sistema soggetto all'analisi per definire:
 - I limiti del sistema
 - L'interfacce con l'equipaggio di terra
 - Gli input richiesti per correggere la situazione creatasi
- 2) determinare le conseguenze sull'aerostato derivanti dall'avaria della funzione in oggetto
- 3) determinare le condizioni di sicurezza richieste per ovviare/limitare l'avaria suddetta [7]

Le valutazioni sono effettuate in accordo con la seguente procedura:

- Individuazione delle funzioni associate con l'impianto oggetto dello studio;
- Individuazione e descrizione dell'avaria associata a queste funzioni;
- Determinazione degli effetti di tale avaria;
- Classificazione degli effetti della condizione di avaria sull'aerostato [7];
- Individuazione dei metodi utilizzati per garantire la rispondenza al regolamento.

8.1 Titoli delle colonne: descrizione

<i>Function</i>	Breve descrizione della funzione analizzata
<i>FC</i>	Codice ad essa associata
<i>Functional Failure</i>	Avaria associata alla funzione analizzata
<i>Most Critical Condition</i>	Fase del volo più critica possibile
<i>Effect of Functional Failure on other systems</i>	Effetti dell'avaria su altri impianti installati sull'aerostato
<i>Effect of failure condition on aerostat/crew</i>	Effetti dell'avaria sul velivolo, equipaggio e passeggeri considerando la situazione più critica possibile
<i>Functional failure classification in most critical condition</i>	Classificazione della situazione nella condizione più critica possibile
<i>Remarks/Verification</i>	Effetti dell'avaria, procedure per la risoluzione della stessa, metodi di analisi

8.2 FHA: Breakdown delle parti principali dell'aerostato

Si riportano nel seguito le principali funzioni considerate nel seguente documento:

1. **Frenatura a terra del sistema:** si intende la funzione di vincolare il sistema aerostato-gondola con il terreno (tipico per i così detti "palloni frenati");
2. **Controllo del sistema:** si intende la capacità di controllare il moto del sistema (up/down);
3. **Perdita forza di galleggiamento:** si verifica alla rottura della membrana del pallone

8. OSTACOLO ALLA NAVIGAZIONE AEREA

Come già illustrato i palloni frenati sono da considerarsi come ostacoli alla navigazione aerea. A tal scopo la *FAA AC 70/7460-1K* prevede una parte specifica per questi ultimi (*CHAPTER 11. MARKING AND LIGHTING MOORED BALLOONS AND KITES* pag. 29)

Per il volo diurno *FAA AC 70/7460-1K* richiede la segnalazione del cavo con "markers" da applicare ogni 15 metri. La circolare fissa le dimensioni minime dei markers ed il loro colore. Il sistema del DIAS è conforme a queste specifiche come riportato nel manuale operativo [1]

Pur non essendo richiesta alcuna segnalazione particolare sul pallone, al fine di aumentare la visibilità di quest'ultimo sono state realizzate su quest'ultimo bande di colore arancione (*Tear-drop-striped pattern*) come richiesto dalla *AC 70/7460-1K* per *Spherical water storage tanks*. Se richiesto da ENAC saranno applicate durante il volo.

9. RISPONDENZA

Il presente report illustra che:

I coefficienti di sicurezza utilizzati nel dimensionamento dei vari sottosistemi sono conformi alla normativa **EASA CS 31 TGB**

Le *possibili failure* del sistema (FHA riportata in appendice) sono state analizzate e la loro probabilità è conforme alla normativa **FAA AC23.1309-1C**

Il soddisfacimento della normativa *FAA AC 70/7460-1K "Obstruction Marking and Lighting"* per *condizioni di volo diurne*

APPENDICE A

FHA del sistema Kytoon Station

Appendix E: FA Kytoon station

<i>Id</i>	<i>FUNCTION</i>	<i>FC</i>	<i>FUNCTIONAL FAILURE</i>	<i>MOST CRITICAL CONDITION</i>	<i>EFFECT OF FUNCTIONAL FAILURE ON OTHER SYSTEMS</i>	<i>EFFECT OF FAILURE ON AEROSTAT/CREW</i>	<i>FUNCTIONAL FAILURE CLASSIFICATION IN MOST CRITICAL CONDITION</i>	<i>REMARKS/VERIFICATION</i>	<i>PROBABILITY OF FAILURE</i>
1	Frenatura a terra del sistema	1.1	Rottura cavo di tenuta principale	In prossimità della quota massima (300m)	Nessuna	il cavo si rompe in estremità, alla quota massima. Il payload cade con una velocità di 5 m/s nell'area dell'involucro di volo.	Hazardous	l'aerostato non più vincolato verrà fatto discendere attivando la valvola per lo sgonfiamento di emergenza nel range prescritto nel manuale operativo; se trasportato dal vento la sua posizione sarà monitorata tramite la telemetria GPS di cui dispone la gondola portastrumenti.	1.30E-11
		1.2	Rottura briglie di tenuta	In prossimità della quota massima (300m)	Nessuna	Vedi sopra.	Hazardous	Vedi sopra	3.58E-12
2	Controllo del sistema	2.3	Motore/scatola riduzione dell'argano	Tutte	Nessuna	Non è possibile continuare la salita o il ritiro dell'aerostato	Major	Si procede alla sostituzione del motore con quello di riserva, alimentabile sia da gruppo di potenza centrale (gruppo elettrogeno) che da batteria di riserva. In alternativa si procede con recupero manuale del pallone	5.70E-13
		2.4	Inverter/gruppo elettrogeno	Tutte	Motore dell'argano	Non è possibile continuare la salita o il ritiro dell'aerostato	Major	Si sostituisce alla alimentazione del gruppo elettrogeno l'alimentazione della batteria e si necessita il cambio di motore (in quanto è un trifase a corrente alternata mentre quello di riserva è in corrente continua). In alternativa si procede con recupero manuale del pallone	1.09E-14
3	Perdita forza di galleggiamento	2.3	Rottura membrana pallone o danneggiamento attacchi carico	Tutte	Nessuna	Il pallone perde quota lentamente. L'avaria è segnata dalla telemetria della posizione e	Minor	Si procede al recupero del pallone mediante riavvolgimento rapido del cavo di ritegno	8.33E-11

Appendix E : FA kytoon station

			membrana			della quota di cui dispone la gondola porta strumenti			
--	--	--	----------	--	--	--	--	--	--

APPENDICE B

Resoconto di riunione 17/06/2010

Oggetto: Innalzamento pallone frenato per rilevamenti in atmosfera da parte dell'Università di Napoli – Federico II.

Sono presenti presso la D.A. di Napoli
per l'Università di Napoli – Prof. Cardone;
per l'Aeronautica Militare - Comando Aeroporto Grazzanise – magg. Iazzetta;
per l'ENAV De Simone e Perfetto
per ENAC – Bronzone Scialla, Sepe e Marino;

L'incontro di oggi è stato indetto al fine valutare l'impatto sulle attività aeronautiche derivante dall'innalzamento di un pallone frenato da parte dell'Università di Napoli per fini di ricerca e rilevamento dati per impatto ambientale.

Sono stati valutati gli aspetti salienti correlati all'attività che l'Università di Napoli intende attuare e che si identificano principalmente in:
aspetti legati alla sicurezza del volo del pallone frenato;
aspetti legati alla sicurezza della navigazione aerea derivante dall'ostacolo rappresentato dal pallone;
definizione della competenza civile o militare in funzione del sito d'innalzamento del pallone e del CTR (Militare o Civile) in cui ricade.

Relativamente al primo punto si è chiarito che il pallone in oggetto non è classificabile aeromobile ai fini del Codice della Navigazione e pertanto non è soggetto ad omologazione e non deve rispondere ad uno specifico regolamento tecnico. Tuttavia l'ENAC ribadisce la necessità di produrre un documento di Failure Analysis onde accertare un adeguato livello di sicurezza del pallone con il suo carico aggiuntivo sottostante costituito da equipaggiamento elettronico di rilievo e memorizzazione dati. Il documento consegnato oggi dal prof. Cardone "Operating Manual" contiene le procedure operative che includono alcuni concetti di failure analysis che però non rispondono a quanto richiesto in una precedente riunione con ENAC e quindi è necessario produrre un documento separato. Ad ogni buon fine Enac chiede di poter visionare il sistema "pallone, fune e verricello" prima del volo.

Relativamente alle problematiche rappresentate dall'ostacolo rispetto alla navigazione aerea si chiarisce che le stesse sono molteplici e riguardano principalmente:

- impatto con le procedure di volo;
- modalità di segnalazione dell'ostacolo;
- modalità di comunicazione ai piloti dell'innalzamento dell'ostacolo (NOTAM).

L'ENAV in relazione all'impatto che il pallone potrebbe avere sulle procedure di volo informa che sul proprio sito internet è disponibile un servizio di valutazione dell'ostacolo da erigere che è propedeutico al rilascio delle autorizzazioni degli enti competenti.

ENAV analizza ogni aspetto della problematica e trasferisce le proprie valutazioni agli Enti che dovranno richiedere l'eventuale emissione di NOTAM.

In tal senso è preferibile che l'Università ripresenti la richiesta d'innalzamento del pallone frenato usufruendo preventivamente del servizio reso via internet da ENAV.

Analogamente l'A.M. rappresenta che se l'ostacolo dovesse ricadere in ambito di propria competenza, l'intera problematica dovrà essere analizzata dal CIGA di Pratica di Mare con procedure analoghe a quelle utilizzate dall'ENAV.

Sarà cura del richiedente produrre un documento che evidenzi il soddisfacimento dei requisiti normativi applicabili, correlati alla segnalazione dell'ostacolo e della fune di collegamento al suolo, alle limitazioni operative, alle modalità di esercizio, riportando con chiarezza la normativa di riferimento (Annesso ICAO, Circolari, ecc.).

E' altresì concordato che si procederà in prima istanza a valutare il pallone e l'equipaggiamento collegato per le sole operazioni diurne, rimandando ad un successivo momento il suo impiego operativo anche per attività notturne.

A chiusura dell'incontro è stato concordato che l'Enac rimane in attesa di nuova documentazione da produrre da parte dell'Università di Napoli, mirata ad ottemperare alle richieste emerse nel corso della riunione.

Napoli, 17/06/2010